

NORTHWESTERN UNIVERSITY

Buried Organic-Inorganic Interfaces in Biological Minerals

A DISSERTATION

SUBMITTED TO THE GRADUATE SCHOOL
IN PARTIAL FULFILLMENT OF THE REQUIREMENTS

for the degree

DOCTOR OF PHILOSOPHY

Field of Materials Science and Engineering

By

Lyle Matthew Gordon

EVANSTON, ILLINOIS

January 2014

© Copyright Lyle M. Gordon 2014

All Rights Reserved

ABSTRACT

Buried Organic–Inorganic Interfaces in Biological Minerals

Lyle Matthew Gordon

Biological organisms exhibit extraordinary control over the structure and properties of biomineralized tissues, creating architectures from smoothly curving single crystals to tough, lightweight self-repairing skeletal elements. An organic matrix is thought to play a critical role in selectively forming and templating metastable mineral precursors and directing its transformation into the final polymorph. Biology's precise control over polymorph and morphology far exceeds current synthetic capabilities. Here we report the use of complementary microscopy and spectroscopy techniques including atom probe tomography (APT), X-ray absorption spectroscopy and electron paramagnetic resonance spectroscopy to map the chemistry and structure of buried interfaces in biological minerals at the nanoscale to improve our understanding of these biomineralization processes.

APT of the magnetite cusp of the chiton tooth revealed that magnesium and sodium are selectively bound to occluded organic matrix fibers. Using XAS and EPR in combination with an *in vitro* model; we further demonstrated the acidic organic matrix complexes iron during mineralizing, enabling selective formation of the metastable precursor ferrihydrite prior to the transformation to magnetite.

Extending APT to bone and dentin, we observed that some of the collagen fibers also exhibited selective binding of ions, implying that an additional, chemical level of hierarchy is present. Surprisingly, segregation to grain boundaries was not observed, questioning the current platelet model for bone-type biominerals.

APT and XAS of tooth enamel revealed that the majority of the magnesium was segregated in grain boundary precipitates of Mg-substituted amorphous calcium phosphate (Mg-ACP). Additionally, unlike many other mineralized tissues, the residual organic molecules were not occluded within the apatite crystals. Interestingly, the metastable Mg-ACP precipitates were found to be responsible for the rapid acid etching of enamel and provide pathways for fluoride diffusion. On the surface of rodent enamel, the Mg-ACP phase was replaced with a mixture of metastable ferrihydrite and amorphous iron phosphate, which renders the enamel mechanically harder than regular enamel, but also hardens it against acid attack, providing inspiration to develop new prophylactics and treatments for dental caries.

Beyond biominerization, the application of APT was extended to new classes of materials, including hybrid organic–inorganic nanoparticles and tricalcium silicate.

ACKNOWLEDGEMENTS

This work would not have been possible without the help of many people. First and foremost, I would like to thank my advisor, Professor Derk Joester for his guidance, support, the opportunity to pursue this unique project, and the confidence in me to allow me freedom to explore many different research areas.

My sincere thanks also go to my committee members, Professor Phillip Messersmith, Professor Vinayak Dravid and Dr. Tom Kelly for their support and guidance. In addition, I would also like to thank Tom for his long term interest in my project and constant optimism towards my new and exciting applications of atom probe tomography. I would also like to thank Professor David Seidman for helpful discussions over the years.

I would like to thank all the members of the Joester group and many of my colleagues at Northwestern, including Minna Krejci for introducing me to X-rays, tolerating me sitting beside her in the office and during the long nights of beamtime, and her guidance and friendship; Ching-Hsuan Wu and Chantel Testerman for many helpful discussions and Chantel's assistance interpreting X-ray spectroscopy data; Dan Schreiber for his assistance with atom probe tomography; and Mike Cohen, for taking over my project, whom I look forward to having great success continuing atom probe tomography of biominerals and many other unique and exciting materials. I would also like to thank all the members of the Joester group who came before me for setting up the lab.

Without the dedicated staff and scientists at the Northwestern core-facilities and National Labs none of this work would have been possible. In particular, I would like to thank Dieter Isheim for his assistance with atom probe tomography and his dedication to NUCAPT; Ben Myers for his endless help with FIB and SEM; Jinsong Wu and Shuyou Li for help with TEM; Keith MacRenaris for help with ICP-MS; Charlene Wilke for her sectioning skills; Jerry Carsello, Amy Sarjeant and Charlotte Stern for help with XRD; Carla Shute for assistance polishing samples and many conversations; Qing Ma and David Vine of

Argonne National Lab and Tom Regier of the Canadian Light Source for their assistance with synchrotron X-ray absorption spectroscopy. I would also like to thank the members of the Cameca Scientific Instruments staff, in particular Dan Lawrence and Rob Ulfig for their help with atom probe tomography and sample preparation.

Lastly, I would like to my family for their love and support, my mom for her constant encouragement, and for being proud of me and my brother for his support, excellent television show recommendations, many of which got me through numerous exam periods and stressful times and his writing/editing help over the years. I would especially like to thank Christina, for her love, support, her patience throughout my PhD, especially for spending another year in cold Chicago waiting for me to finish, and her very gracious help throughout the writing process, including this dissertation.

Funding for this project was provided by the National Science Foundation (NSF DMR-0805313 and DMR-1106208), the Northwestern University Materials Research Center (NSF-MRSEC DMR-1121262), the International Institute for Nanotechnology, and the Canadian National Sciences and Engineering Research Council, through a graduate fellowship.

Portions of this work were performed at the DuPont-Northwestern-Dow Collaborative Access Team (DND-CAT) located at Sector 5 of the Advanced Photon Source (APS). DND-CAT is supported by E.I. DuPont de Nemours & Co., The Dow Chemical Company and Northwestern University. Use of the APS, an Office of Science User Facility operated for the U.S. Department of Energy (DOE) Office of Science by Argonne National Laboratory, was supported by the U.S. DOE under Contract No. DE-AC02-06CH11357, the Canadian Light Source, which is supported by the Natural Sciences and Engineering Research Council of Canada, the National Research Council of Canada, the Canadian Institutes of Health Research, the Province of Saskatchewan, Western Economic Diversification Canada, and the University of Saskatchewan, the Northwestern University Center for Atom Probe Tomography (NUCAPT) support-

ed by NSF-MRI (DMR-0420532) and ONR-DURIP (N00014-0400798, N00014-0610539, N00014-0910781), the Optical Microscopy and Metallography Facility, the Biological Imaging Facility, the Integrated Molecular Structure Education and Research Center, the J. B. Cohen X-Ray Diffraction Facility supported by the NSF- MRSEC (DMR-1121262), the Quantitative Bioelemental Imaging Center generously supported by NASA Ames Research Center NNA06CB93G, the Northwestern University Atomic and Nanoscale Characterization and Experimental Center (NUANCE) and the Nanoscale Integrated Fabrication, Testing, and Instrumentation Facility (NIFTI) supported by NSF-NSEC, NSF-MRSEC, the Keck Foundation, the State of Illinois, and Northwestern University.

CONTENTS

Abstract 3

Acknowledgements 5

Contents 9

List of Tables 11

List of Schemes 11

List of Figures 13

1 Introduction 17

- 1.1 *Motivation* 17
- 1.2 *Matrix-Mediated Biominerization* 17
- 1.3 *Metastable Precursors* 20
- 1.4 *Overview of Thesis* 22

2 Model Systems 25

- 2.1 *The Chiton Radula* 25
- 2.2 *Bone and Dentin* 28
- 2.3 *Tooth Enamel* 31

3 Summary of Key Characterization Methods 37

- 3.1 *Atom Probe Tomography* 37
- 3.2 *X-ray Absorption Spectroscopy* 40

4 Buried Organic–Inorganic Interfaces in the Chiton Tooth 45

- 4.1 *Introduction* 45
- 4.2 *Results and Discussion* 48
- 4.3 *Conclusion* 60
- 4.4 *Materials and Methods* 61

5 Polymorph Selectivity in The chiton Tooth 67

- 5.1 *Introduction* 67
- 5.2 *Results and Discussion* 70
- 5.3 *Conclusion* 83
- 5.4 *Materials and Methods* 84

6 Atom Probe Tomography of Apatites and Bone-Type Mineralized Tissues 93

- 6.1 *Introduction* 93
- 6.2 *Results and Discussion* 97
- 6.3 *Conclusion* 114
- 6.4 *Materials And Methods* 115

7 Amorphous Intergranular Phases Control the Properties of Tooth Enamel 121

- 7.1 *Introduction* 121
- 7.2 *Results and Discussion* 125
- 7.3 *Conclusion* 145
- 7.4 *Materials and Methods* 146

8 Atom Probe Tomography of Ferritin 157

- 8.1 *Introduction* 157
- 8.2 *Results and Discussion* 159
- 8.3 *Conclusion* 163
- 8.4 *Materials and Methods* 164
 - 8.4.1 Sample Preparation 164
 - 8.4.2 APT Methods 164

9 Early Hydration of Tricalcium Silicate 167

- 9.1 *Introduction* 167
- 9.2 *Results and Discussion* 170
- 9.3 *Conclusion* 173
- 9.4 *Materials and Methods* 173

10 Constraining Atom Probe Tomography Reconstructions of Crystalline Oxides 177

- 10.1 *Introduction* 177
- 10.2 *Results and Discussion* 179
- 10.3 *Conclusion* 196
- 10.4 *Materials and Methods* 197

11 Future Outlook 201

- 11.1 *Mechanisms of Biominerization in the Chiton Tooth* 201
- 11.2 *Structure of Apatites and Bone-Type Mineralized Tissues* 202
- 11.3 *Intergranular Phases in Tooth Enamel* 204
- 11.4 *Ferritin and Hybrid Organic-Inorganic Nanoparticles* 205
- 11.5 *Early Hydration of Tricalcium Silicate* 206
- 11.6 *Atom Probe Tomography Reconstructions of Crystalline Oxides* 208

References 209

LIST OF TABLES

Table 4.1: Atomic and molecular ions identified in chiton teeth from APT mass spectra. 51

Table 5.1: Pre-edge fitting results 73

Table 5.2: EXAFS shell-by-shell fitting results 76

Table 5.3: In vitro reaction conditions and relative yield of different polymorphs 82

Table 6.1: Ions identified in Apatite Spectra 105

Table 6.2: APT Compositional Measurements of Apatites 105

Table 6.3: Identified organic ions and unknown ions in bone and dentin APT spectra 111

Table 7.1: Enamel composition 133

Table 7.2: EXAFS shell-by-shell fitting results 139

LIST OF SCHEMES

Scheme 9.1: Simplified Portland Cement Clinker Formation 167

LIST OF FIGURES

- Figure 1.1: Examples of matrix mediated biomineralization 18
Figure 1.2: STEM of synthetic calcite occluded with an agarose gel 20
Figure 1.3: Comparison of single crystals of geological and biological calcite 21

Figure 2.1: Chiton shell plates and girdle 26
Figure 2.2: Radula μ CT 26
Figure 2.3: The stages of mineralization of the chiton radula 27
Figure 2.4: Mineralization progress 27
Figure 2.5: Chiton tooth elemental distribution 28
Figure 2.6: The seven hierarchical levels of organization of the bone family of materials 31
Figure 2.7: Hierarchical structure of rodent enamel 33
Figure 2.8: Apatite crystal structure 34

Figure 3.1: Focused ion beam APT sample preparation 38
Figure 3.2: APT schematic 40
Figure 3.3: X-ray absorption spectra 42
Figure 3.4: XAS experimental setup 43

Figure 4.1: Chiton radula and tooth structure 46
Figure 4.2: Chiton tooth magnetite and occluded organic fibers 48
Figure 4.3: LAADF STEM of chiton tooth magnetite 49
Figure 4.4: APT mass-spectra 50
Figure 4.5: APT TOF m/z spectra 52
Figure 4.6: Chitin thin film reference standard 52
Figure 4.7: 3D Reconstructions and Proxigrams 54
Figure 4.8: Fiber bundle 56
Figure 4.9: Isodensity surfaces used to calculate proxigrams 57
Figure 4.10: Manganese concentration proxigrams 57
Figure 4.11: Model of a chiton tooth organic fiber 59

Figure 5.1: Stages of tooth mineralization along the radula of *K. tunicata* 69
Figure 5.2: XANES spectra of chiton teeth and reference compounds 71
Figure 5.3: X-ray absorption spectroscopy 72

- Figure 5.4: EXAFS spectra of chiton teeth and reference compounds 75
Figure 5.5: Shell-by-shell EXAFS fits based on theoretical scattering paths and reference spectra 76
Figure 5.6: X-band EPR spectra of chiton teeth and *in vitro* reaction products 79
Figure 5.7: Electron paramagnetic resonance spectra 80
Figure 5.8: Characterization of *in vitro* reaction products 81
Figure 5.9: XANES and EXAFS spectra of *in vitro* reaction products 83

Figure 6.1: Apatite crystal structure 95
Figure 6.2: Fluorapatite XRD 98
Figure 6.3: Hydroxylapatite XRD 98
Figure 6.4: Chlorapatite XRD 99
Figure 6.5: Reflectance FT-IR 99
Figure 6.6: Raman Spectroscopy 100
Figure 6.7: The influence of APT experimental run-time parameters on data quality 101
Figure 6.8: APT spectra of synthetic and geological apatites 104
Figure 6.9: $P_xO_y^+$ and FeO_x^+ relative abundances 106
Figure 6.10: Relative abundance of Ca^+ containing ions 107
Figure 6.11: Dentin and Bone APT Spectra 110
Figure 6.12: 3D reconstruction of a sample of elephant tusk dentin 113

Figure 7.1: Hierarchical structure of rodent enamel 124
Figure 7.2: Rat mandible 124
Figure 7.3: Controlled lactic acid etching of enamel 126
Figure 7.4: Etched sintered synthetic polycrystalline apatite. 127
Figure 7.5: Un-etched polished enamel surface 127
Figure 7.6: Enamel nanoindentation 129
Figure 7.7: APT mass to charge ratio spectra 131
Figure 7.8: Correlative TEM imaging of enamel APT sample 132
Figure 7.9: Atom-probe tomography 3D reconstructions 132
Figure 7.10: Mg *K*-edge X-ray absorption spectroscopy 136
Figure 7.11: Fe *K*-edge X-ray absorption spectroscopy 138
Figure 7.12: Linear combination fitting 141
Figure 7.13: Fe *K*-edge XAS Pre-edge comparison 141
Figure 7.14: Thermal stability of pigmented enamel 142

- Figure 7.15: Raman spectroscopy of enamel. 143
- Figure 7.16: P K-edge XANES 144
- Figure 7.17: P-K edge Photoelectron Emission Microscopy 145
- Figure 8.1: X-ray crystal structure of ferritin 158
- Figure 8.2: High-resolution TEM of ferritin 158
- Figure 8.3: Method for fabricating ferritin atom probe tomography sample tips. 160
- Figure 8.4: APT spectra of ferritin 161
- Figure 8.5: Ferritin APT reconstruction and proxigrams 162
- Figure 8.6: 1D concentration profile along tip z-axis 163
- Figure 9.1: Cement Hydration 169
- Figure 9.2: C3S APT Spectra 171
- Figure 9.3: Hydrated C3S APT Concentration Profiles 172
- Figure 9.4: Slices through Hydrated C3S reconstruction 172
- Figure 10.1: Overview of geological and biological magnetic 179
- Figure 10.2: Detector histogram of biogenic chiton tooth magnetite sample 181
- Figure 10.3: Lattice reconstructions 182
- Figure 10.4: Laue backscatter X-ray diffraction, radial pole projections and APT detector histograms 183
- Figure 10.5: SDM Alignment Optimization 185
- Figure 10.6: $\langle 111 \rangle$ zSDM from $\langle 111 \rangle$ oriented tip 186
- Figure 10.7: $\langle 111 \rangle$ zSDM from $\langle 110 \rangle$ oriented tip 186
- Figure 10.8: Chiton Tooth zSDM 187
- Figure 10.9: Post-LEAP SEM 188
- Figure 10.10: Magnetite crystal structure, theoretical and measured SDM 189
- Figure 10.11 TEM micrograph down [100] of LP204-1 magnetite 191
- Figure 10.12: Reconstruction of LP-204-1 192
- Figure 10.13: LP-204-1 SDM 193
- Figure 10.14: Distorted reconstruction 193
- Figure 10.15: Magnetite ($\text{FeO} \cdot \text{Fe}_2\text{O}_3$) Trevorite ($\text{NiO} \cdot \text{Fe}_2\text{O}_3$) crystal structure 194
- Figure 10.16: Trevorite Fe-Fe and Ni-Ni zSDM 195
- Figure 10.17: Trevorite Fe-Ni zSDM 196
- Figure 10.18: SDM alignment coordinate system 198

1 INTRODUCTION

1.1 MOTIVATION

Biological organisms possess an unparalleled ability to control the structure and properties of mineralized tissues, creating, for example smoothly curving single crystals or tough, lightweight, self-repairing skeletal structures^{1,2}. Bottom-up biomineralization processes enable carefully orchestrated synthesis of complex tissues hierarchically patterned from single nanometers to hundreds of microns². Modern fabrication processes used to create synthetic industrial and laboratory materials pale in comparison, often requiring large amounts of energy and a combination of extensive top-down fabrication steps, controlled environments, high temperatures and high pressures.

Despite the potential of biomineralization processes, the mechanisms driving their formation are not fully understood. An improved understanding of the mechanisms involved in biomineralization has many applications in the fields of both crystal growth and patterning, potentially leading to advances in the design of novel materials for a wide range of applications from electronics to medicine. Furthermore, adopting the chemistries involved in biomineralization could provide promise for environmentally sensitive and “green” material synthesis. Herein we investigate the structure and chemistry of nanoscale buried interfaces in biological minerals to understand the unique processes of biomineralization.

1.2 MATRIX-MEDIATED BIOMINERALIZATION

Biominerlization frequently occurs within a complex environment consisting of organic macromolecules that control the nucleation and growth of inorganic minerals and interact with the forming mineral to create hierarchically ordered mineralized tissues². Additionally, some of the organic matrix is left occluded within the crystalline matrix during growth and contribute to the unique properties, including enhanced fracture toughness and wear resistance³⁻⁷. Examples of these highly organized biominerls include verte-

breathe bone, mollusk shells and chiton teeth (Figure 1.1a-c); in each case the organic matrix within the inorganic mineral is occluded within in the mature tissues (Figure 1.1d-f).

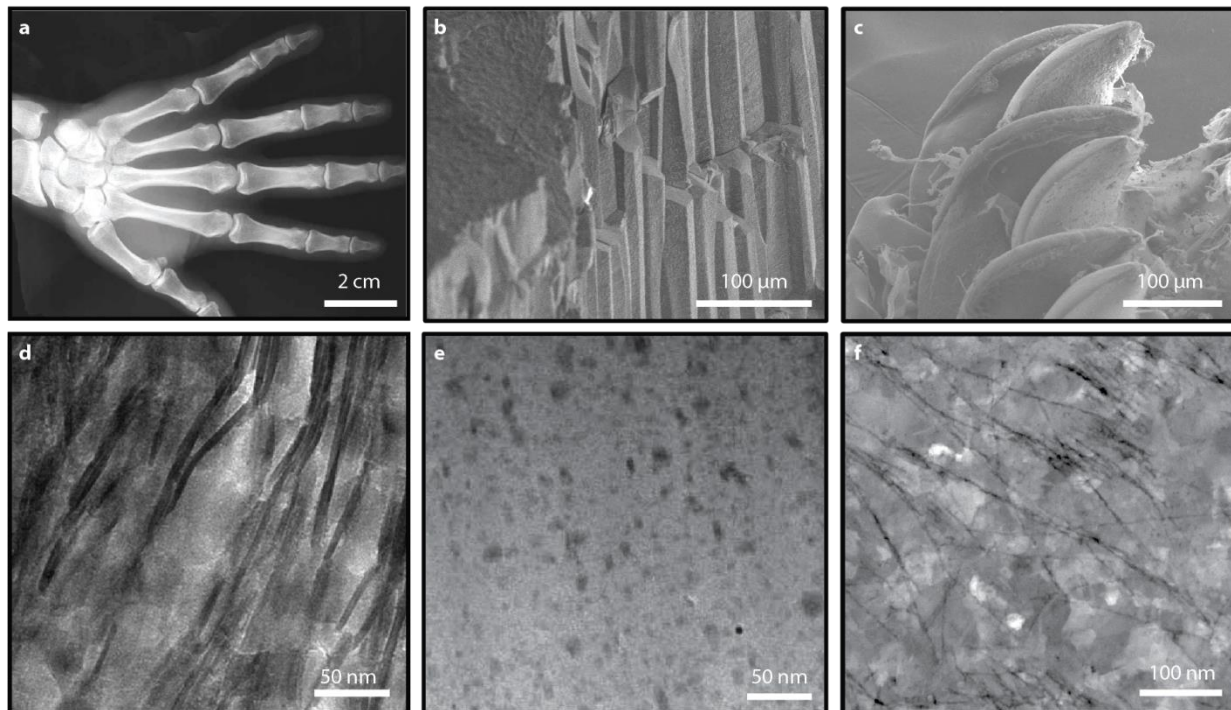


Figure 1.1: Examples of matrix mediated biomineralization

Transmission X-ray radiograph of (a) human hand bones (*Homo sapiens*), scanning electron micrographs of (b) columnar prismatic calcite single crystals from the rigid pen shell (*Atrina rigida*), and (c) chiton teeth along a section of the radula from an Eastern Beaded Chiton (*Chaetopleura apiculata*). Transmission electron micrographs visualizing (d) collagen fibrils and mineral platelets in bone, and (e) occluded intracrystalline proteins and polysaccharides in prismatic calcite single crystals, and (f) protein-decorated chitin fibers in nanocrystalline chiton tooth magnetite. Adapted from refs. ⁸⁻¹⁰.

Organic scaffolds in biominerals generally comprise a fibrous structural element, e.g., collagen in bone¹¹ or chitin in mollusks and crustaceans¹². Acidic macromolecules, such as the non-collagenous proteins in bone¹³, Aspartic acid-rich proteins in the bivalve prismatic layer¹⁴ and a variety of poorly characterized molecules in chiton teeth¹⁰, are usually associated with the fibrous scaffold. While these proteins may be

intrinsically disordered, their charge predisposes them to interact with the forming mineral¹⁵. They are thought to play a key role in controlling crystal polymorph and orientation. Additionally, ions such as Mg²⁺^(16,17), and polyphosphates¹⁸ are known to be important modulators of mineralization processes. Numerous studies have also investigated the chemistry of the organic matrix such as the nature of the occluded proteins and polysaccharides and how the organic molecules might hypothetically interact with the forming mineral¹⁹⁻²⁴.

Additionally, there is an enormous amount of interfacial area between organic macromolecules and very small inorganic crystals, e.g. in bone, where 5 nm wide crystals of carbonated hydroxylapatite intercalate between collagen fibrils^{25,26}. The interactions across these interfaces are crucial for our understanding of bone mineralization, bone mechanics, and especially the loss of function associated with pathological conditions such as osteoporosis. However, we currently do not completely understand the nature of the organic-inorganic interface or even the exact ordering of the mineral nanocrystals at the required level.

Characterization of the buried organic scaffold frequently requires wet chemical demineralization and drying that can result in structural artifacts and the loss of diffusive species. Removal of either the mineral or organic renders it impossible to analyze the interface between the two. Both Nudelman²⁷ and Evans²³ relied upon chemical demineralization to investigate the organic scaffold buried in the mollusk shell prismatic calcite and the chiton tooth, respectively. These studies were able to capture the physical structure of the buried organic matrix, however, since they removed the surrounding mineral the mineral-organic interface was no longer left in its native state²⁸. As an alternative to demineralization, Sone and coworkers turned to cryogenic transmission electron microscopy (cryo-TEM)²⁹ and visualized a fibrous network in the forming limpet tooth, similar to that observed in demineralized chiton teeth^{30,31}.

The structural complexity of buried organic-inorganic interfaces in synthetic and biogenic calcite single-crystals occluding organic macromolecules fibers was recently demonstrated by scanning transmission

electron microscopy (STEM) and tomography (Figure 1.2)³². However, even this advanced imaging modality does not reveal the chemical complexity of the sample in terms of the localization of different chemical species in the scaffold or the mineral. While high-resolution elemental mapping by electron microscopy is in principle possible, resolution and sensitivity are very much limited by the susceptibility of biological materials to beam damage. Advanced characterization techniques are needed to directly probe the structure and chemistry of the buried organic—inorganic interfaces without removing either phase.

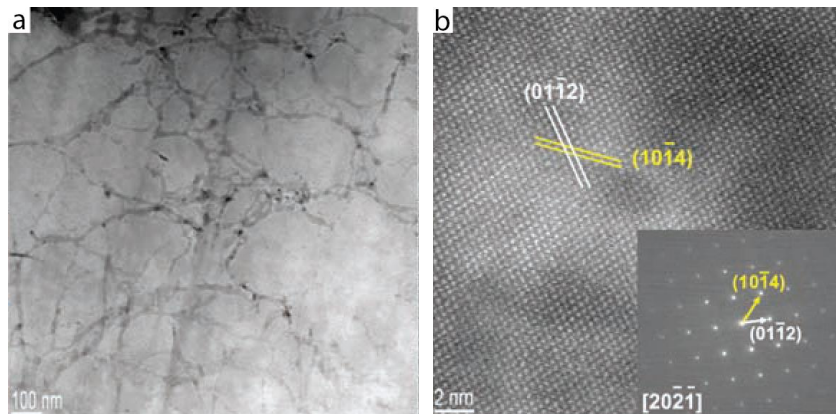


Figure 1.2: STEM of synthetic calcite occluded with an agarose gel

(a) Annular dark field STEM image of a thin section cut from a calcite crystal incorporating agarose fiber. Dark fibers (low atomic number) traverse the bright inorganic calcite (high atomic number) (b) High resolution STEM lattice image viewed down the [2021] zone axis of calcite. (Inset) A SAED pattern of the cut section. The examined area (diameter of 800 nm) contains both crystal and fibers. Adapted from ref.³².

1.3 METASTABLE PRECURSORS

Classical crystal growth near equilibrium most often results in neatly faceted crystals expressing certain surfaces that minimize their overall surface energy (Figure 1.3a). In contrast biological minerals exhibit smoothly curving surfaces and seemingly no relationship to the underlying crystal structure (Figure 1.3b).

It has been proposed that the ability of biological organism's to synthesize complex shaped mineralized tissues with seemingly no relationship to the underlying crystal structure of the mineral relies on the judicious use of metastable precursors³³. The isotropic nature of highly disordered and amorphous solids potentially enables the fabrication of complex morphologies more easily than crystalline materials, whose shapes are governed by the underlying structure of its atomic lattice³⁴. The strategy to form crystalline structures from transient metastable precursors, rather than direct crystal nucleation followed by classical ion-by-ion crystal growth from a supersaturated solution has been identified in a range of biominerals^{33,34}. For example, transient minerals have been identified in a number of phyla including amorphous calcium carbonate (ACC) in echinoderm spicules and mollusk shells to crustacean cuticles^{35,36} to amorphous calcium phosphates in forming vertebrate bone³⁷ and tooth enamel³⁸.

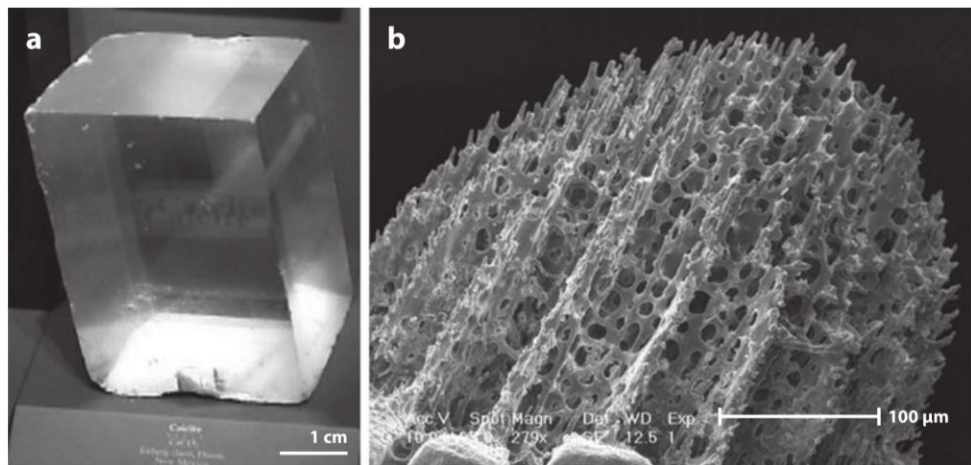


Figure 1.3: Comparison of single crystals of geological and biological calcite

The comparison illustrates the dramatic difference between a geological calcite single crystal (**a**) displaying the characteristic crystallographic facets formed by ion-by-ion crystal growth and (**b**) a biological single crystal calcite sea urchin spine formed via the transformation of amorphous calcium carbonate. Adapted from ref. ³⁴.

In contrast to traditional wasteful top-down industrial and laboratory manufacturing techniques, bottom-up biomineral synthesis takes advantage of metastable precursors to rapidly and efficiently create materials with carefully controlled complex microstructures³⁴. Taking inspiration from the biological systems biomimetic synthetic materials processing approaches are being developed to fabricate large single crystals with complex patterned microstructures based on metastable precursors³⁹⁻⁴³.

Stabilization of metastable precursors against crystallization has frequently been ascribed to organic matrix macromolecules, in particular acidic macromolecules, and inorganic additives present during mineralization⁴⁴, including Aspartic acid-rich proteins in the bivalve prismatic layer⁴⁵. However, no direct evidence of interactions between the forming mineral or soluble ionic species and these molecules has been found. Confinement within small volumes, for example in lipid vesicles³⁹⁻⁴¹ and protein nanocages⁴⁶, both widely observed in biological organisms has also been found to stabilize metastable precursors.

In addition to amorphous calcium carbonates and calcium phosphates, ferrihydrite, a metastable disordered iron oxyhydroxide is present as a transient precursor to minerals such as magnetite, the predominant mineral making up the chiton tooth⁴⁷ and magnetosomes in magnetotactic bacteria⁴⁸. Ferrihydrite is also encapsulated in ferritins and related proteins, which provide a nearly universal form of iron for transport and storage in biology⁴⁶. Surprisingly, ferrihydrite is not expected to form from bioavailable ferrous iron under physiological conditions⁴⁹. It is suspected that the organic matrix and possibly even acidic macromolecules present throughout the organic matrix are responsible for forming stable ferrihydrite prior to the transformation into magnetite²¹⁻²³.

1.4 OVERVIEW OF THESIS

This thesis describes the investigation into the structure and chemistry of buried interfaces in model mineralized tissues using advanced structural and chemical characterization tools (Chapter 2 -3). These investigations have provided new insight into the unique mechanisms by which biological organisms control

mineral nucleation and growth and the role of nanoscale structural and chemical heterogeneity on the final physiochemical properties of the composite tissue in iron oxide (Chapters 4 - 5) and calcium phosphate biominerals (Chapters 6 - 7). Development of novel sample preparation and analysis methods to study biological minerals has enabled novel application of atom probe tomography (Chapter 8 - 10).

1.4.1 Model Systems and Characterization Methods

The work presented in this dissertation focuses on characterizing three widely studied model biomineral systems: the chiton radula, vertebrate bone and dentin, and tooth enamel. These model systems are described in more detail in Chapter 2. Application of advanced characterization tools (Chapter 3) to study these systems has led to new insight that will potentially lead to advances in the design and production of novel biomimetic materials and medical therapies, including treatments for bone diseases and tooth decay.

1.4.2 Iron Oxides

Beyond the ubiquitous mineralized iron oxyhydroxide core of the iron transport and storage protein ferritin, iron oxides are formed by a number of specialized organisms for use as highly-abrasion resistant teeth or magnetoreception. Of particular interest has been the chiton radula, a rasping tongue-like organ with hundreds of hard, highly wear-resistant teeth. The chiton radula is described in detail in Chapter 2.1. Using Atom probe tomography (APT) it was possible to dissect the ultra-hard magnetite teeth atom by atom and characterize the nanoscale structure and chemistry of the buried organic—inorganic interfaces (Chapter 4). APT investigation led to the discovery of the metal binding capability of the acidic organic matrix molecules buried within the magnetite of the fully formed teeth. Continued investigation of the earliest stages of formation of the chiton tooth by X-ray absorption and electron paramagnetic resonance spectroscopy identified iron-organic complexes with these same acidic matrix molecules and demonstrated that these complexes are necessary for selectively forming the metastable precursor ferrihydrite (Chapter 5).

1.4.3 Calcium Phosphates

Calcium phosphates form the basis of a wide range of biological minerals including vertebrate teeth and bones. Application of APT to characterize the chemistry and isotope ratios in synthetic and geological apatite provided the knowledge necessary to study biological systems. Chapter 6.2.4 details the preliminary investigation into the structure of bone and dentin, the hierarchical collagen-mineral composite material that make up the major component of vertebrate bones and teeth (described in more detail in Chapter 2.2). The structure of tooth enamel is discussed in Chapter 2.3. Finally, Chapter 7 describes the investigation of the structure and chemistry of amorphous Mg- and Fe- substituted intergranular phases in tooth enamel with APT and X-ray absorption spectroscopy and their influence on the physiochemical properties of the tissue.

1.4.4 Novel Applications of Atom Probe Tomography

Due to the traditional use of atom probe tomography to study electrically conductive predominately metallic materials, analysis of dielectric materials, in particular, hybrid organic—inorganic composites, such as biological minerals, has required the development of new atom probe sample preparation and analysis techniques. In particular, the focused ion beam for sample preparation allows fabrication of tips from materials not amenable to electrochemical etching and the use of a focused ultraviolet laser to thermally excite non-electrically conductive samples. Taking advantage of these new developments we have applied APT to novel systems. Two of which are discussed in this dissertation, the iron storage and transport protein ferritin, a core shell iron oxide-organic composite nanoparticle (Chapter 8) and tricalcium silica (alite) the primary reactive and component of Portland cement (Chapter 9). In addition to developments leading to novel applications, three dimensional APT reconstructions of biogenic magnetite was performed largely based on reconstruction parameters established for metallic and semiconducting materials; Chapter 1 discusses the validation of the reconstruction parameters for oxides with a set of chemically and microstructurally well-characterized reference materials (Chapter 1).

2 MODEL SYSTEMS

This chapter describes the structure and relevance to biominerization, medicine and materials synthesis of the three widely studied model biomineral systems discussed throughout this dissertation.

2.1 THE CHITON RADULA

Chitons are a widespread group of marine mollusks characterized by the eight dorsal shell plates (Figure 2.1)⁵⁰. Most chitons feed on algae by grazing on rocks, using their extremely hard, wear resistant, and self-sharpening teeth^{1,51,52}. Chiton teeth are arranged in rows along a rasping tongue-like organ called the radula (Figure 2.2 and Figure 2.3). Remarkably, the radula acts as a conveyor-belt, on one end the tooth consists entirely of an organic matrix composed of the polysaccharide α -chitin (poly- β -1,4-N-acetylglucosamine) and several proteins^{22,23}. As the tooth progresses towards the other end of the radula (~1 row/day), it remodels and mineralizes, in several stages, first, the iron oxide is deposited and then the softer core mineral is deposited (Figure 2.4 and Figure 2.5). Each phase occludes the preformed organic matrix during mineralization.

Developmental that can be differentiated based on the color that originates from the iron mineral present (Figure 2.3). Stage I teeth are colorless and are therefore often referred to as un-mineralized scaffolds. They primarily comprise α -chitin, proteins, and water. Stage II teeth are brown, containing predominately ferrihydrite (for a recently proposed structure and stoichiometry, $\text{Fe}_{8.2}\text{O}_{8.5}(\text{OH})_{7.4}\cdot 3\text{H}_2\text{O}$, see Ref. ⁵³). In stage III, transformation of ferrihydrite to magnetite (Fe_3O_4) results in a gradual change from brown to black. Stage IV teeth are completely black as the cusp reaches its final density of magnetite. After the cusp has been completed, the tooth is filled in with a softer mineral or mixture of minerals specific to the species. The presence of all stages of development in a single organism along the radula thus allows comparison of different stages of the tooth development in the same animal simply by analyzing sequential rows of teeth.



Figure 2.1: Chiton shell plates and girdle

Dorsal view of the chiton *Chaetopleura apiculata*. Grid is 5x5 mm.

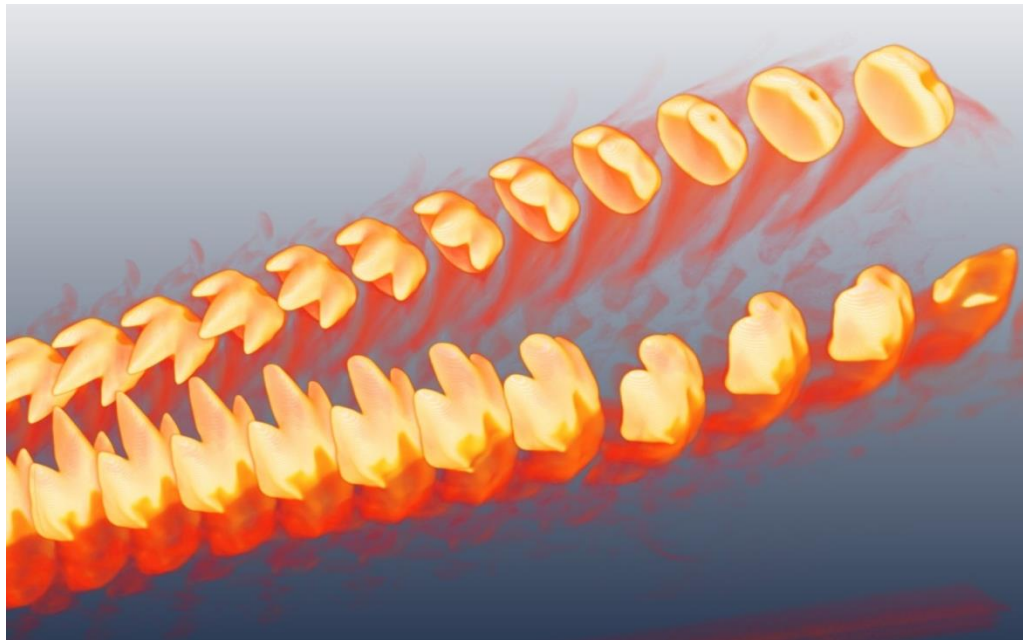


Figure 2.2: Radula μCT

X-ray micro-computed tomography of the fully mineralized working end of the radula of the chiton *K. tunicata*. Note the heavily worn teeth at the front (right side) of the radula from constant abrasion on rocks that are ready for replacement.

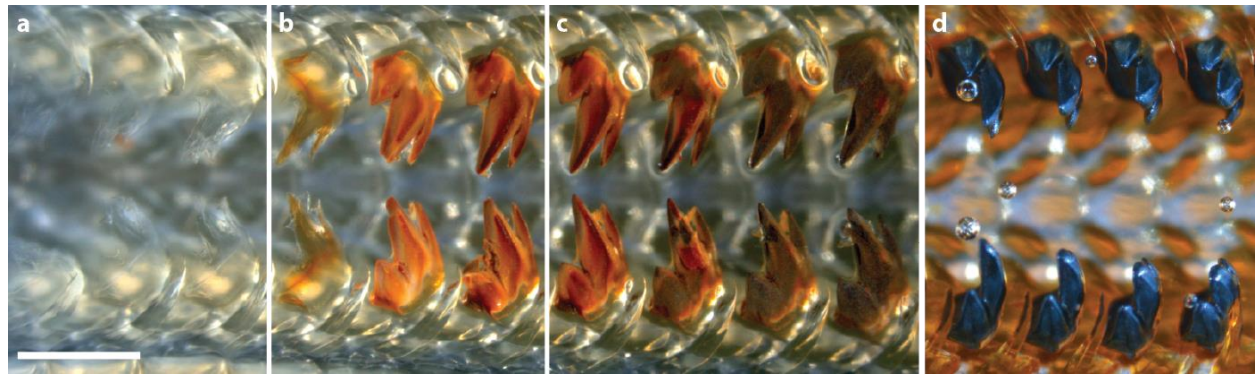


Figure 2.3: The stages of mineralization of the chiton radula

Stages of mineralization of the radula of the chiton *Katharina tunicata*. Unmineralized (a), ferrihydrite (b), transformation of ferrihydrite to magnetite (c) and the final fully mineralized black magnetite teeth. Scale bar represents 500 µm.

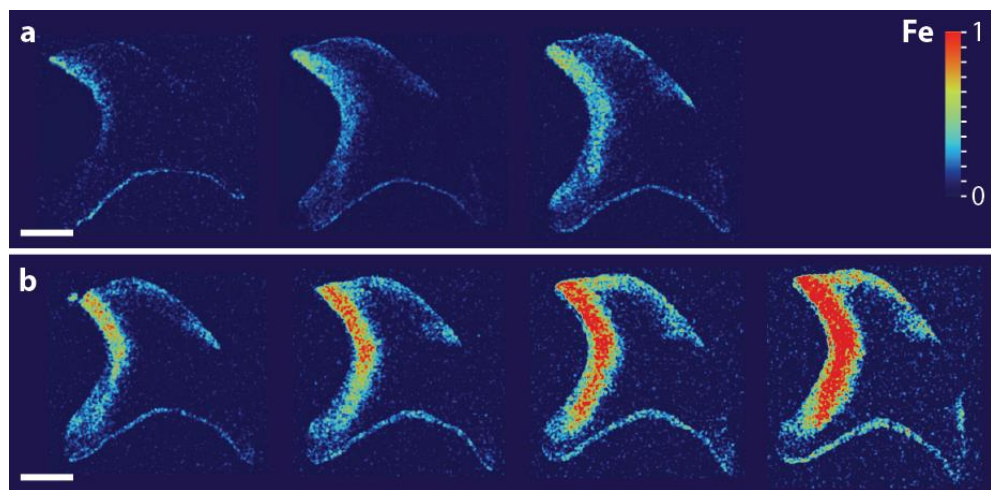


Figure 2.4: Mineralization progress

Iron concentration from *K. tunicata* tooth cross sections maps generated by SEM-EDS of longitudinal tooth cross sections in stage II (a) and III (b). Iron concentration was normalized to the highest value. Scale bar represents 100 µm.

Similar to vertebrate teeth, mature chiton teeth consist of a softer core capped by a harder outer layer (Figure 2.5)¹. The mineral present in the core depends on the species and often contains high-levels of phosphate, either as amorphous iron phosphate or calcium-rich apatite. Additional layers of minerals such as lepidocrocite [γ -FeO(OH)] may also be present. Overall, the architecture of a hard, abrasion resistant cap and a more compliant core is reminiscent of vertebrate teeth. The outstanding fracture toughness and wear resistance of the tooth results from the organic-inorganic interfaces over multiple levels of hierarchy (i.e. intra- and inter-crystalline) that deflect and arrest cracks⁵².

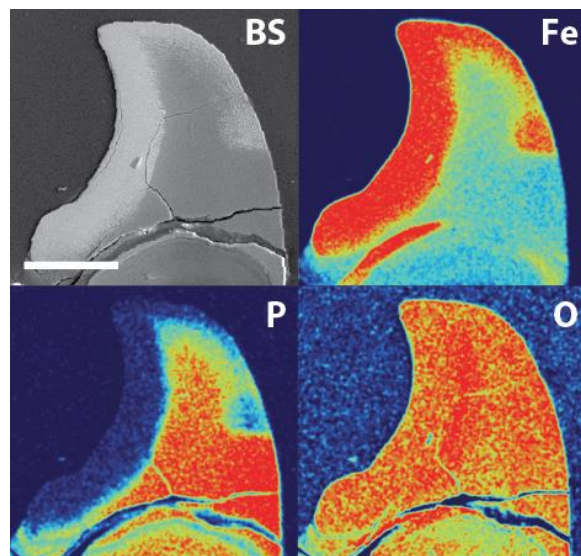


Figure 2.5: Chiton tooth elemental distribution

Cross section of a stage IV fully mineralized tooth from the chiton, *K. tunicata*, by SEM in backscattered electron (BS) contrast and SEM-EDS elemental maps showing a Fe/P/O-rich core (amorphous iron phosphate) and Fe/O-rich cap (magnetite). Scale bar represents 100 μ m.

2.2 BONE AND DENTIN

Bone is a composite material composed of carbonated hydroxyapatite (cHAp), proteins and water found in forming the rigid endoskeleton of vertebrates⁵⁴. The mechanical properties of bone are the result of complex hierarchical organization over multiple length scales (Figure 2.6)⁵. The formation of this tissue

begins with the deposition of an organic matrix, composed primarily of triple helical collagen fibrils and non-collagenous proteins, which control and template the nucleation and growth of nanoscale cHAp platelets⁵⁴. The chemical properties of bone are strongly influenced by the extensive interfacial area between the nanoscale mineral particles and the surrounding organic matrix. Understanding the synthesis and properties of bone requires detailed characterization of the numerous nanoscale buried organic—inorganic interfaces. Furthermore, the economic costs of bone diseases in North America exceed hundreds of billions of dollars each year and there is a significant demand for the development of new treatment strategies⁵⁵. Numerous bone diseases, such as osteoporosis and osteogenesis imperfecta, have no cure and make the patients' bones extremely susceptible to fracture⁵⁵.

The mineral phase of bone best resembles OH-deficient OHAp substituted with significant carbonate (5-8 wt %) and smaller levels of Na⁺ and Mg²⁺ (0.5-1.0 wt %), of which the Mg is likely associated with the crystal surfaces⁵⁶⁻⁵⁹. Approximately 1 wt % of the composite is citrate (C₆H₅O₇³⁻) that may be associated with the mineral surface and/or the collagen fibrils that constitute the majority of the organic fraction^{60,61}. Presence of various organic and inorganic impurities at the surface is suspected to strongly influence the chemical properties of the composite. Based on analysis of mineralizing tendons and bones and fully formed bone where the organic fraction has been removed, the poorly crystalline mineral is thought to be present in irregular platelets approximately 50 nm long, 25 nm wide and 2-5 nm thick^{62,63}. In forming bone and mineralizing tendon, these platelets are roughly aligned with their crystallographic c-axis parallel to collagen fibrils.⁶⁴ Within a fibril, platelets are generally parallel to each other. However, with increasing age, as the amount of intrafibrillar and interfibrillar mineral increases and platelets grow, the orientation of platelets with respect to each other becomes less homogenous^{8,65,66}. Recent electron microscopy results suggests that the majority of the mineral is in fact present in platelets shaped crystals, however, much of the mineral is present outside the collagen fibrils^{8,65,67}. This indicates that crystallization within gap-regions in the self-assembled collagen fibrils is not solely responsible for the platelet crystal mor-

phology. Further high-resolution analysis is needed to elucidate the complex nanoscale structure and chemistry of bone.

Elephant tusk dentin is a highly organized bone-like structure with a similar architecture composed of nanoscale mineral platelets and collagen fibers, however, the collagen fibers are highly organized parallel to each other and also aligned with the tusk axis presenting a simpler model sample for study than bone where the collagen fiber organization is more complex^{65,67,68}. The mechanism of mineral nucleation within the matrix, the composition of the mineral platelets and the exact juxtaposition of organic matrix proteins and the mineral remains an unanswered question despite tremendous progress in electron microscopy and tomography²⁵.

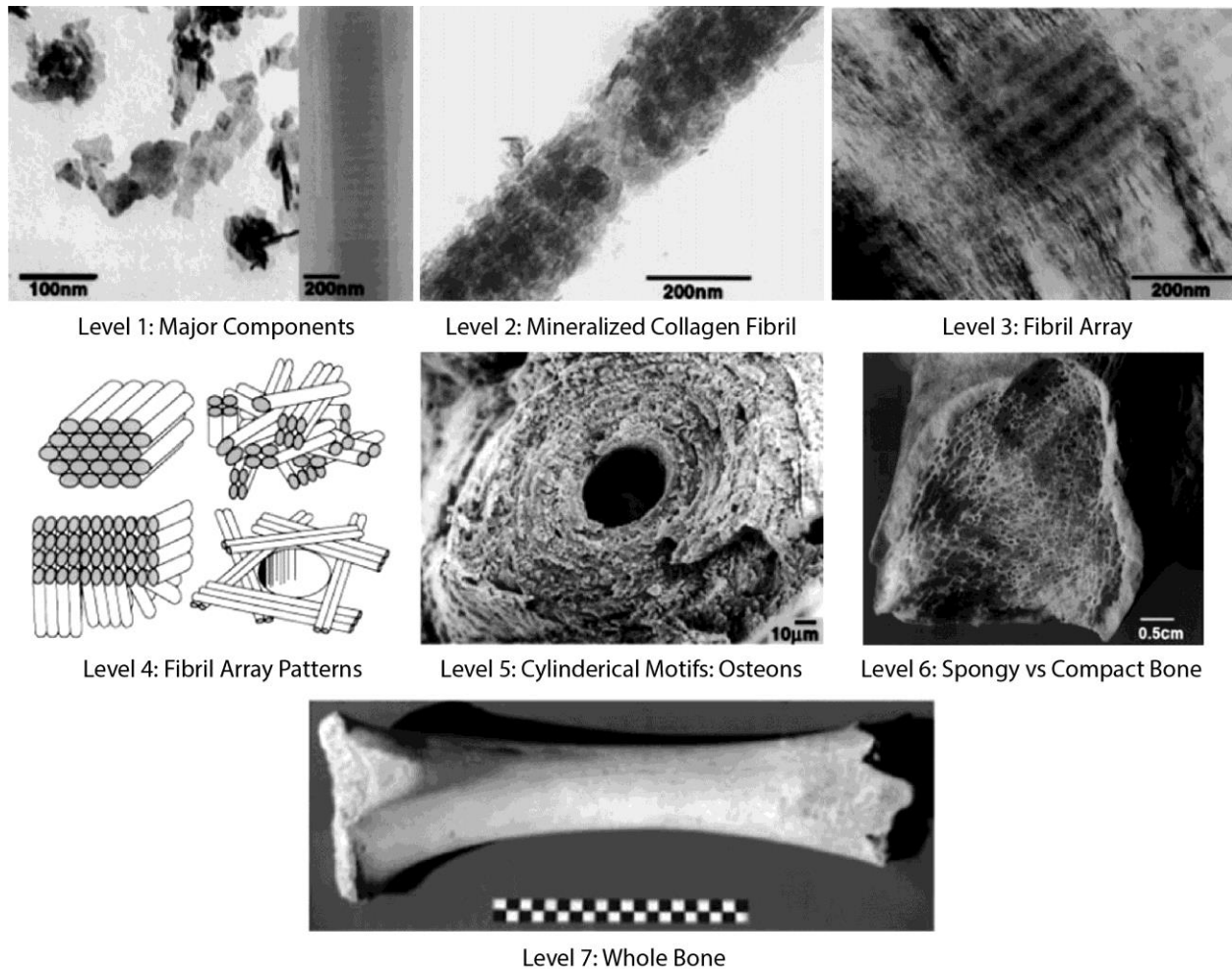


Figure 2.6: The seven hierarchical levels of organization of the bone family of materials

Level 1: Isolated crystals from human bone (left side) and part of an unmineralized and unstained collagen fibril from turkey tendon observed in vitreous ice in the TEM (right side). Level 2: TEM micrograph of a mineralized collagen fibril from turkey tendon. Level 3: TEM micrograph of a thin section of mineralized turkey tendon. Level 4: Four fibril array patterns found in the bone family of materials. Level 5: SEM micrograph of a single osteon from human bone. Level 6: Light micrograph of a fractured section through a fossilized (about 5500 years old) human femur. Level 7: Whole bovine bone (scale: 10 cm). Adapted from ref. ⁶⁹.

2.3 TOOTH ENAMEL

Tooth decay, also known as dental caries, is the most ubiquitous infectious disease in humans and severely affects quality of life⁷⁰. The pathophysiology of dental caries involves the development of a bacterial

biofilm that produces a highly acidic environment, resulting in the dissolution of the underlying tissue. Enamel, the outermost covering of the tooth, is the most susceptible to caries. With nearly \$91.5 billion dollars being spent on dental services in 2006 in the US alone, there is no question that a significant demand exists for improved dental treatments⁷⁰. Currently, treatments involve the use of polymeric resins or alloys, which act as seals for replacing damaged tissue. This approach is far from ideal, as the resins can fail and introduce complications such as infection, loosening, lack of tissue integration, wear, and damage to surrounding healthy tissue. One of the largest challenges of working with teeth is that, unlike other mineralized tissues such as bone, the outermost enamel layer is acellular and lacks the capability to self-regenerate. Despite decades of research on enamel, the complex nanoscale structure and chemistry of the tissue is still not fully understood. As a result, understanding the structure and chemistry of enamel is a fundamental milestone for preventing and properly treating dental caries.

Enamel, the hardest tissue in the vertebrate body, is composed of 98% carbonated hydroxylapatite (OHAp) crystallites along with 1-2% organic molecules and water. Enamel is formed by highly specialized cells, known as ameloblasts and the process of mineralization occurs in the extracellular milieu. The tissue has a complex composite inorganic-organic architecture with several levels of hierarchy⁷¹. The remarkable hierarchical structure of enamel and the included organic molecules enable substantially improved mechanical properties, such as toughness and wear resistance, compared to synthetic HA, which would shatter under the typical forces seen during mastication. On the nanoscale, hundreds of thousands of high aspect-ratio crystallites are organized into three to five micron wide bundles, called rods, which are woven together in a complex pattern. Between the rods are regions composed of poorly aligned crystallites enriched with proteinaceous material.

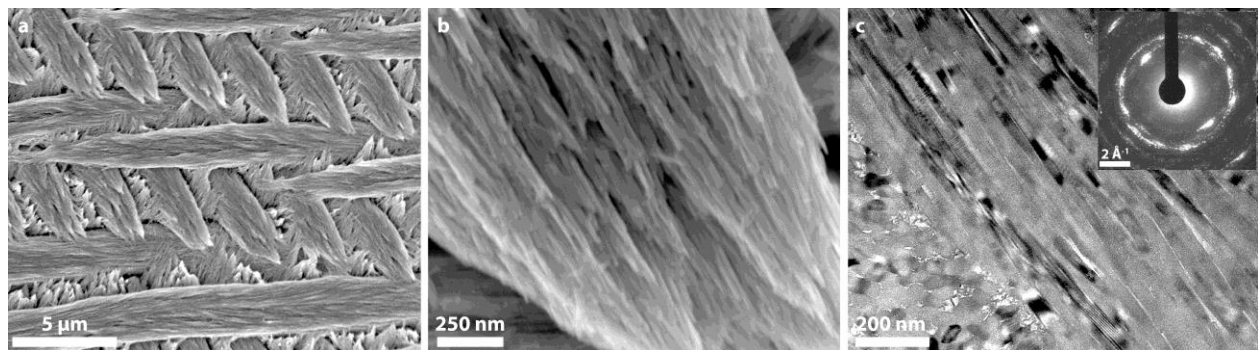


Figure 2.7: Hierarchical structure of rodent enamel

a Low-magnification scanning electron micrograph (SEM) of acid etched mouse enamel surface revealing the woven layers of 3 to 5 μm rods (scale bar 20 μm). **b** higher magnification SEM image showing that each rod is in turn composed of thousands of high-aspect ratio carbonated hydroxylapatite nanocrystals (scale bar 250 nm), **c**, bright-field transmission electron micrograph through a singly rod showing the high-aspect ratio nanocrystals (scale bar 200 nm), the inset selected area electron diffraction patterns reveals the crystals are co-oriented along their crystallographic c-axis (scale bar 2 \AA^{-1}).

The OHAp unit cell (Figure 2.8) has a monoclinic lattice belonging to space group $P2_1/b$. The lattice can be described based on four distinct crystallographic sites: (1) tetrahedral sites for six P^{5+} -ions, in 4-fold coordination with oxygen, (2) $\text{Ca}[1]$ sites for four of the Ca^{2+} ions, (3) $\text{Ca}[2]$ sites for the six other Ca^{2+} ions (arranged such that they form a channel along the c-axis) and (4) the channel site, occupied by an OH ion in the case of OHAp⁵⁶. The structure and physiochemical properties of enamel are strongly affected by the incorporation of numerous impurities into the mineral phase. The most relevant changes relate to the ability of enamel to resist acid dissolution. The mineral makeup of enamel consists primarily of apatite, specifically OHAp with the prototypical formula $\text{Ca}_{10}(\text{PO}_4)_6(\text{OH})_2$. However, many of the Ca, OH and PO_4 lattice sites are vacant or are occupied by different chemical impurities. Cationic (Na^+ , Mg^{2+}) and anionic impurities (Cl^- , F^-) primarily substitute for Ca^{2+} or OH⁻, respectively. Carbonate ions, common in biogenic apatite, are found to occupy both the OH (A-type) and the PO_4 site (B-type). The impurities with the most substantial effects on the mineral are fluoride, magnesium, sodium, and carbonate ions. Fluoride

ride—unlike Mg^{2+} , Na^+ and CO_3^{2-} , which increase enamel solubility—has been observed to substantially reduce enamel solubility⁴.

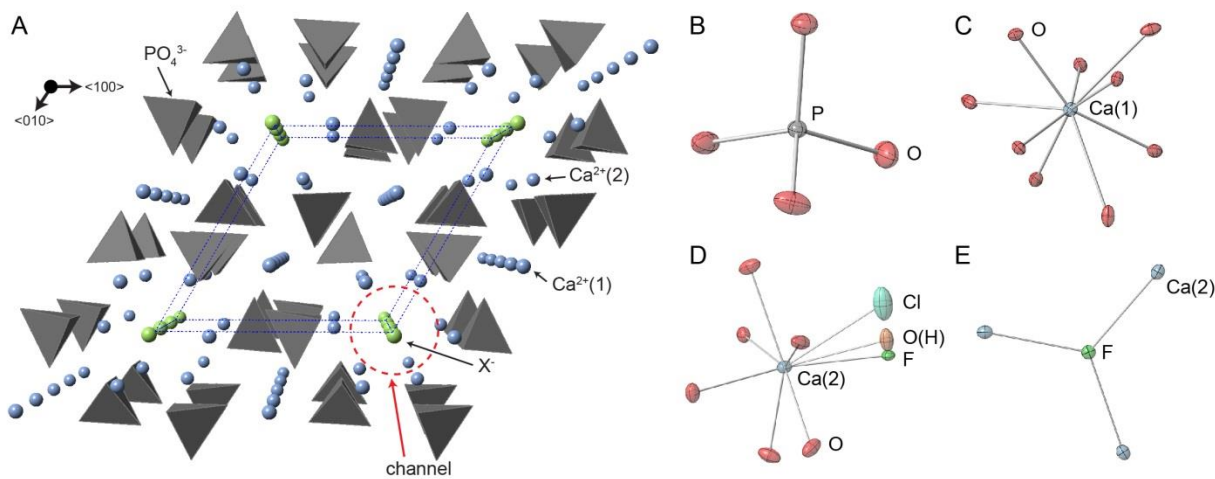


Figure 2.8: Apatite crystal structure

A) The apatite unit cell with four distinct crystallographic positions (sites): six tetrahedral phosphates (B); four Ca(1) coordinated by nine oxyanions (C); six Ca(2) coordinated by six oxyanions and one channel ion (D); and two channel sites, which are occupied by F⁻, OH⁻, or Cl⁻ and are coordinated by three Ca(2) (E)⁵⁶. The Ca(2) site shows the channel ion positions from the FAp, ClAp and OHAp crystal structures⁷². While unit cell parameters change slightly and the symmetry of the crystal is affected by the position of the channel ion, the structures are highly similar. Thermal ellipsoids were rendered according to the atom-specific anisotropic thermal parameters at 80% probability level.

Due to the ability of fluoride ions to reduce enamel solubility and consequently the incidence of caries, fluoride is now commonly added to drinking water and toothpastes as a means⁷³. However, there is still debate as to whether systemic or topical fluoride exposure reduces caries⁷⁴, as well as on the role of systemic fluoride in dental and skeletal fluorosis⁷⁵. Fluoridation for caries prevention is extremely widespread; the fluorine distribution in enamel has been examined at the macro- and microscopic scales by numerous methods, and it is clear that the majority of the fluorine is concentrated at the surface of the enamel^{76,77}. However, the exact nature of the fluorine incorporation into the complex three-dimensional

structure of enamel at the nanoscale is not yet understood. Researchers have proposed that fluorine accumulates at structural defects, or that non-apatitic fluorine rich phases (such as fluorapatite or fluorite) form within enamel; however, no direct evidence has yet been observed⁷⁶. A better understanding of enamel fluoride is necessary to improve fluoride delivery for treatment of dental caries.

Magnesium is sparingly soluble in OHAp (less than 0.5 wt%)^{78,79}; however, it occurs in substantial concentrations in the enamel (0.5 – 1 wt%)⁷⁹. It has been suggested that therefore the majority of the Mg must be present either at defects, on the surfaces of the individual crystallites (i.e., at grain boundaries and triple junctions) or as a second high-Mg non-apatitic phase (such as dolomite, huntite or whitlockite⁷⁹) Although the specifics of the Mg incorporation have been studied for decades, the exact distribution and crystallography of the Mg-rich regions are not yet known. Additionally, the nanoscale distributions of sodium and carbonate ions, which are both soluble in the OHAp lattice, are not well understood.

The majority of our understanding of enamel structure and chemistry is based on bulk compositional analysis, ion- and electron-probe microanalysis, and transmission electron microscopy (TEM). Although these tools have provided valuable information on the structure of enamel, they have a limited ability to probe compositional variations of important ions in nanometer and sub-nanometer volumes. Toward the goal of improved treatment and prevention of dental caries, it is necessary to characterize the structure and chemistry of enamel at the nanoscale to increase our understanding of apatite mineral chemistry, specifically in complex heterogeneous nanostructured systems.

3 SUMMARY OF KEY CHARACTERIZATION METHODS

This chapter provides an overview of the central microscopic and spectroscopic techniques used to characterize the biological minerals described throughout this dissertation. Together these methods provide new information into the mechanisms of biomineralization and the unique physiochemical properties of the resulting mineralized tissues.

3.1 ATOM PROBE TOMOGRAPHY

Atom probe tomography (APT) is a unique microscopy tool capable of characterizing the structure and chemistry of the sample with sub-nanometer spatial resolution and parts-per-million chemical sensitivity in three-dimensions by directly probing the location and chemical identity of the atoms within a small sample of material⁸⁰⁻⁸². APT has been instrumental in characterizing the nanoscale structures for a range of materials, including metals and semiconductors^{80,83-86}. APT has historically been used predominately in metallurgy, however, recent technological advances, in particular, the advent of focused ion beam sample preparation and ultraviolet lasers to thermally excite the sample, have enabled the study of insulating, organic and biological specimens^{80,87-95}.

The atom-probe is the only technique which is capable of producing a sub-nanometer scale three-dimensional map of the position and chemical identity of the atoms in the sample. This high resolution information makes it possible to develop an atomistic picture of the inorganic-organic composite structure and the interfaces buried within mineralized biological tissues^{10,96}.

The atom probe evolved from a combination of a field ion microscope and a time-of-flight (TOF) mass spectrometer^{97,98}. The specimen atoms are individually field evaporated from the surface of a sharp tip by the application of an extremely high electric field on the order of $20\text{-}40 \text{ V}\cdot\text{nm}^{-1}$. To achieve the necessary electric field intensity the sample is a needle-shaped specimen with a radius of curvature on the order of tens of nanometers. Traditionally, metallic specimens have been prepared by electrochemical etching⁹⁹.

However, with the recent applicability of APT to non-metallic materials more versatile sample preparation techniques were needed. The focused ion beam (FIB) has enabled site-specific preparation of a wide range of materials¹⁰⁰⁻¹⁰². FIB APT sample preparation (Figure 3.1) relies on *in situ* lift-out of segments of the material of interest with a micromanipulator based on protocols for FIB transmission electron microscopy sample preparation developed in the semi-conductor industry.

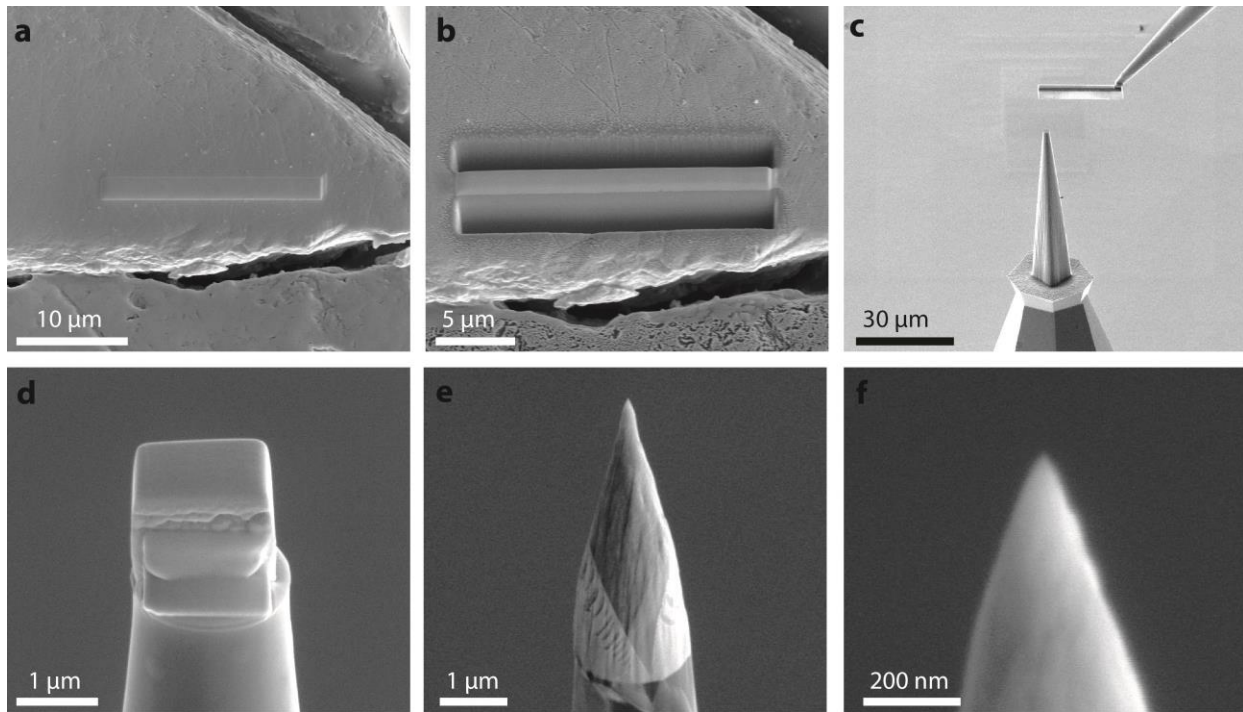


Figure 3.1: Focused ion beam APT sample preparation

(a) First a layer of platinum is deposited over a region of interest on the polished cross-section using the ion beam. (b) A wedge of material below the Pt strap is cut out on three sides. (c) The wedge is attached to an *in-situ* nano-manipulator using FIB deposited Pt before cutting the final edge free. (d) Individual segments are cut from the wedge and sequentially affixed to the tops of Si posts in an array. (e) Each tip is shaped and sharpened using annular milling patterns of decreasing inner and outer diameters¹⁰³. The majority of the amorphized surface region and implanted gallium ions in the tip surface is removed by a final low energy ion milling step.

Under the applied field, the application of a periodic high-voltage or thermal pulse to the specimen initiates evaporation events at a specific time, enabling TOF determination^{83,104}. Unlike conventional microscopes where a lens magnifies an image of the sample, in APT the sample surface itself acts as a high magnification point-projection lens where each ion is projected outward from the approximately hemispherical surface during controlled field evaporation. This results in a magnification of about 10^6 times. Following a rapid laser heating (thermal pulse) or high-voltage pulse one or multiple positively charged ions field ionize and evaporate from the tip and travel along the electric field lines and through a conical local electrode towards a negatively charged detector, where their impact position and TOF are determined. The TOF measurement enables mass-to-charge state ratio (m/z) measurement and therefore determination of the chemical identity of the ion. The x - y position of the ion is determined by back-projecting the impact position on the detector the hemispherical emitter surface. Emitted ions travel along electric field lines to the detector. Unlike a simple gnomonic/radial projection the observed angles on the detector are compressed compared to the expected angle. An image compression factor is introduced into the calculation that accounts for the material and geometry dependent changes to the electric field lines. The z position is determined based on the order of evaporation; specifically the z position for each ion is incremented by the ionic volume of the ion divided by the current surface area of the reconstruction (based on the radius). The instantaneous tip radius is determined based on the evaporation voltage divided by the product of the evaporation field of the material and an instrument and sample dependent field factor. A curvature correction is subsequently applied to correct for the flat detector and the spherical emitter surface^{83,105}. For further details on the reconstruction algorithms the reader is referred to Larson et al. and the references therein¹⁰⁶. APT analyzes volumes on the order of 10^5 nm³ with a spatial resolution that is generally better than 0.4 nm and can be below 0.1 nm under certain conditions¹⁰⁷.

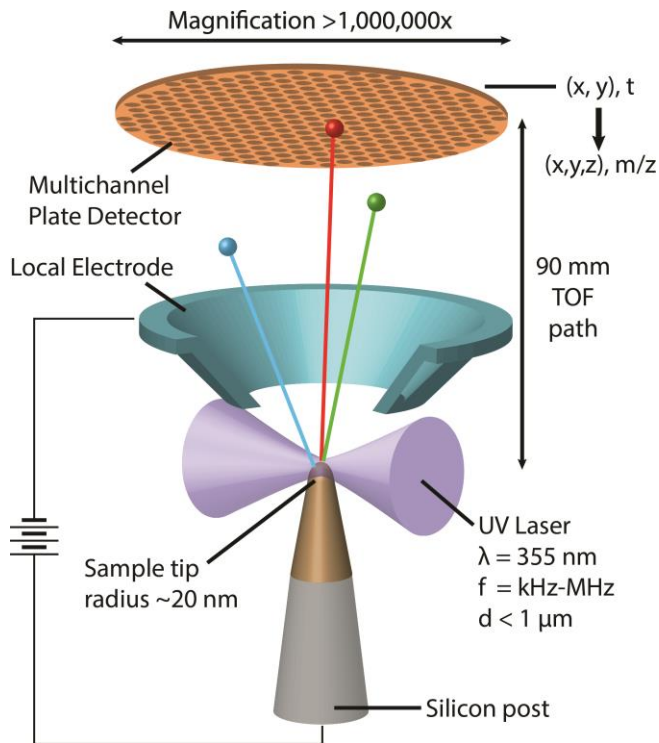


Figure 3.2: APT schematic

Focused ion beam prepared sample with a tip radius of 20-100 nm is mounted on a Si support. Electric field is applied between the sample and the local electrode. Periodic laser pulses repeatedly thermally evaporate surface ions which project along the field lines through the conical electrode towards the detector where their TOF and impact position are recorded. Figure courtesy of Prof. Derk Joester.

3.2 X-RAY ABSORPTION SPECTROSCOPY

APT provides a three dimensional chemical map with sub-nanometer resolution and parts per million chemical sensitivity. However, the resolution is only adequate to resolve crystal structures in certain materials and the nature of the field evaporation process precludes straightforward interpretation of the local chemical and bonding environment of ions within the material.

X-ray absorption spectroscopy (XAS) provides a sensitive probe of the local environment around specific atoms in the sample¹⁰⁸. Unlike X-ray diffraction based methods that are limited to long-range ordered crystalline materials, XAS is suitable for characterizing disordered and amorphous materials exhibiting

only short or medium range order. XAS is based on the energy dependence of X-ray absorption at and above an element's binding energy. Above the binding energy, X-ray absorption is influenced by the interference between photoelectrons ejected from the absorbing atom and those backscattered by its neighbors. By tuning the energy of the incident X-rays to a specific binding energy, XAS provides information about the structure surrounding an element of interest.

Resulting spectra are separated into two regions for analysis—the near edge, and the far edge (Figure 3.3). The X-ray absorption near edge structure (XANES) is typically treated qualitatively, and provides information on the oxidation state of the absorbing atom and the symmetry of the surrounding near neighbor atoms. Pre-edge features are often observed and provide further insight into symmetry and coordination environment around the absorbing atom. The extended X-ray absorption fine structure (EXAFS) yields quantitative information about the short range order. Theoretical scattering factors are calculated using a model compound. The calculated values are then used to construct a model of photoelectron scattering paths, the model parameters are refined to fit the experimental data. These fitted parameters provide the coordination numbers, as well as the identity and bond lengths of neighboring atoms.

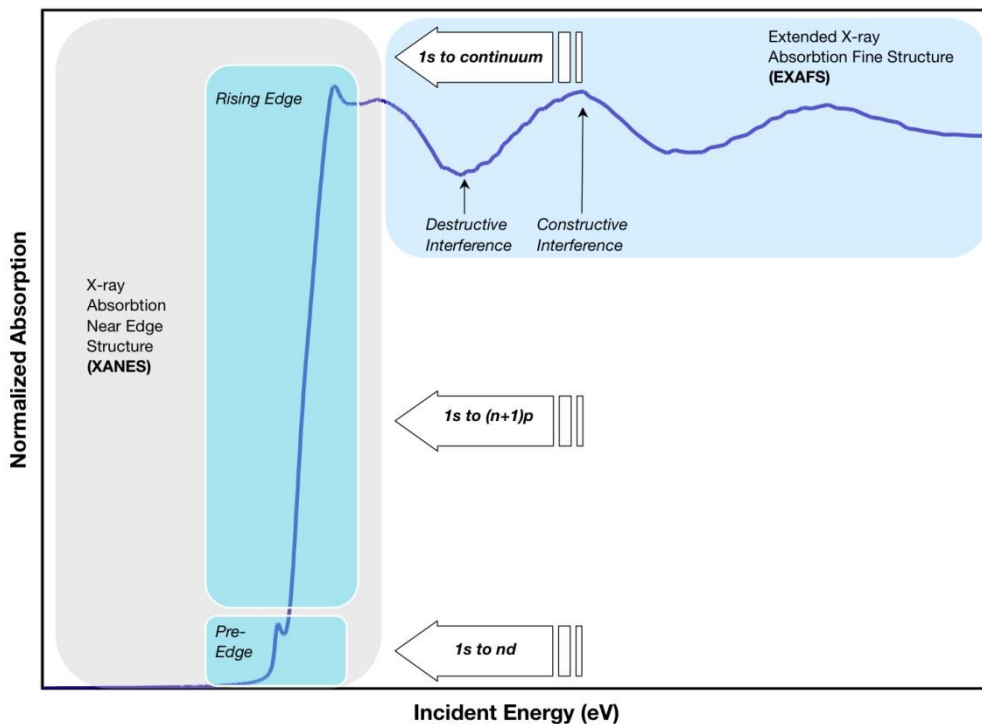


Figure 3.3: X-ray absorption spectra

Spectra are separated into two regions for analysis—the near edge (XANES), and the far edge (EXAFS). Pre-edge features are often observed and provide further insight into symmetry and coordination environment. Figure courtesy of M. Blank, Stanford University.

Measuring X-ray absorption across an elemental absorption edge requires a tunable X-ray source. While lab sources can in certain cases be satisfactory, XAS is typically performed at a synchrotron. The synchrotron provides an intense and tunable X-ray beam. High photon flux enables measurements on dilute samples. The majority of high-energy synchrotron XAS beamlines utilize two-crystal monochromators suitable for energies above about 4 keV. This provides access to the *K*-edges of elements heavier than potassium, however lighter element edges are inaccessible. Accessing the *K*-edges of lighter elements, in particular, light biologically-relevant metals (i.e. Na, Mg) requires specialized beamlines. Only recently have these elements become accessible with modern grating monochromators which provide sufficient flux at the required energies¹⁰⁹. Furthermore, the low energy X-rays are rapidly absorbed in air requiring

experiments to be performed under vacuum. Measurement of concentrated samples at high energies can be performed simply by directly measuring the ratio of the intensity of the incident to the transmitted beam (Figure 3.4); however, sensitivity is very poor when dilute samples are measured. Alternatively, the X-ray fluorescence emission from the element of interest can be measured as a function of incident beam energy where the absorption coefficient, $\mu(E)$, is proportional to I_f/I_0 (Figure 3.4). Fluorescence is also suitable for samples too thick or non-uniform for direct transmission measurements, particularly at low incident beam energies. While providing much greater sensitivity, down to a few parts per million, thicker or more concentrated samples can cause self-absorption effects and high-fluorescence X-ray flux can saturate detectors.

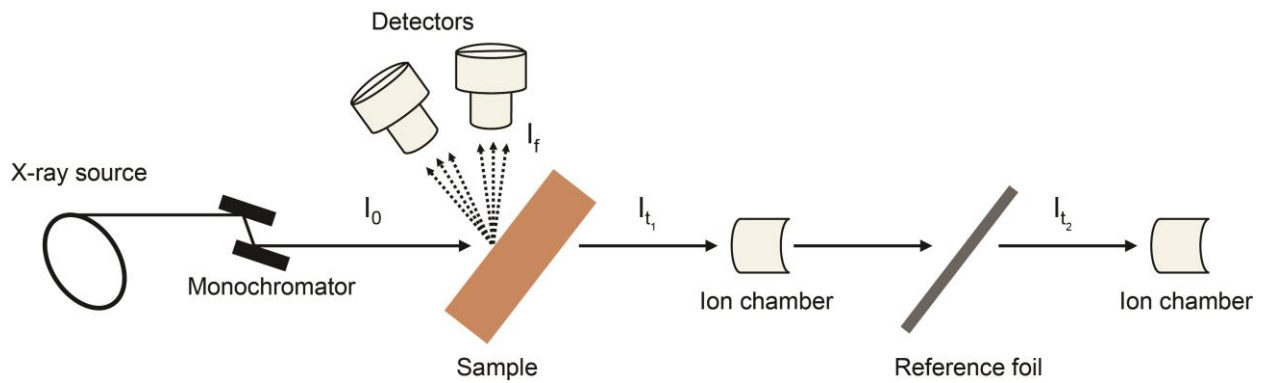


Figure 3.4: XAS experimental setup

X-ray absorption is measured in transmission or fluorescence geometry, a reference foil for internal monochromator energy calibration can be inserted after the sample. High-flux and tunable X-ray energy requirements typically necessitates performing measurements at a synchrotron. Gas ionization chambers are used for hard X-ray transmission measurements and multiple energy dispersive solid-state detectors are used to measure X-ray fluorescence intensity.

4 BURIED ORGANIC-INORGANIC INTERFACES IN THE CHITON TOOTH

This chapter discusses the application atom-probe tomography to characterize hybrid organic—inorganic materials and the insight these experiments provided into the chemistry of the buried interfaces between the inorganic mineral and the occluded organic fibers within the magnetite cusp of the chiton tooth. Alok Tayi assisted in the preparation of chitin thin film reference standards for APT.

Parts of the work have been published in the following article:

Gordon, L. M. & Joester, D. Nanoscale chemical tomography of buried organic-inorganic interfaces in the chiton tooth. *Nature* **469**, 194-197 (2011).

4.1 INTRODUCTION

Biological organisms possess an unparalleled ability to control the structure and properties of mineralized tissues, creating, for example smoothly curving single crystals or tough, lightweight self-repairing skeletal elements¹. In many biominerals, an organic matrix interacts with the forming mineral, controls its morphology and polymorph, and is occluded during mineralization^{3,110,111}. The remarkable functional properties of the resulting composites, such as the outstanding fracture toughness and wear resistance, can be attributed to buried organic-inorganic interfaces at multiple levels of hierarchy¹¹². Analyzing and controlling such interfaces at the nanometer length scale is critical also in emerging organic electronic and photovoltaic materials¹¹³. However, the structural and chemical complexity of buried organic-inorganic interfaces is a great challenge to state-of-the-art imaging techniques. Here we show that pulsed laser atom-probe tomography (APT) reveals three-dimensional (3D) chemical maps of organic fibers with a diameter of 5-10 nm in the surrounding, nano-crystalline magnetite (Fe_3O_4) mineral in the chiton tooth. Remarkably, most fibers co-localize with either sodium or magnesium. Furthermore, clustering of these cations in the fiber indicates a structural level of hierarchy previously undetected. Our results demonstrate that in the chiton tooth, individual organic fibers have different chemical compositions, and thus likely different

functional roles in controlling fiber formation and matrix–mineral interactions. APT is uniquely able to detect this chemical/structural heterogeneity by virtue of its unparalleled 3D spatial resolution and sensitivity across the periodic table. We anticipate that the quantitative analysis and visualization of nano-scale interfaces by laser-pulsed APT will contribute greatly to our understanding not only of biominerals (e.g. bone, dentin, and enamel), but also to that of synthetic organic/inorganic composites such as organic photovoltaic materials and polymer nano-composites.

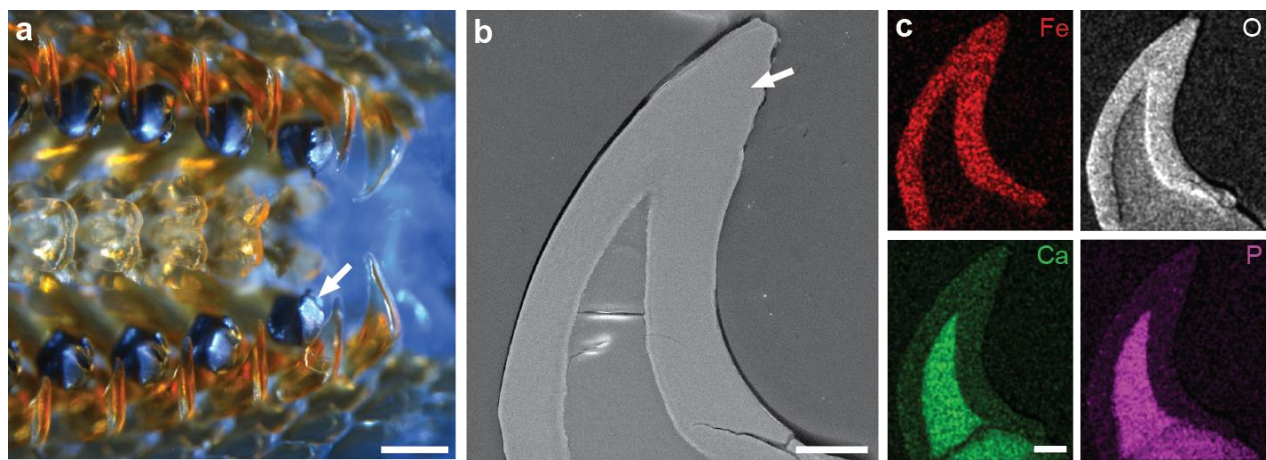


Figure 4.1: Chiton radula and tooth structure

a, Reflected light optical micrograph of the tip of a *C. apiculata* radula, with 4 rows of fully mineralized teeth (arrow). Scale bar: 200 μm . **b**, SEM image of polished cross-section of a tooth, with approximate site where samples for APT and TEM were extracted (arrow). Scale bar: 50 μm . **c**, SEM-EDS elemental maps of cross-section (b) show of a Ca/P/O-rich core (apatite) and Fe/O rich cap (magnetite). Scale bar: 20 μm .

Organic scaffolds in biominerals generally comprise a fibrous structural element, e.g., collagen in bone¹¹ or chitin in mollusks and crustaceans¹². Acidic macromolecules, such as the non-collagenous proteins in bone¹³ and Asprich proteins in the bivalve prismatic layer¹⁴, are usually associated with the fibrous scaffold. While these proteins may be intrinsically disordered, their charge predisposes them to interact with the forming mineral¹⁵. They are thought to play a key role in controlling crystal polymorph and orientation. Additionally, ions such as Mg²⁺^(16,17), and polyphosphates¹⁸ are known to be important modulators of

mineralization processes. Consequently, understanding the biological control over mineral growth and the resulting functional properties critically depends on characterizing buried organic/inorganic interfaces.

Characterization of the organic scaffold frequently requires wet chemical demineralization and drying that can result in structural artifacts and loss of diffusive species. Removal of either mineral or organic also renders it impossible to analyze the interface between the two. The structural complexity of buried interfaces in a synthetic calcite single-crystal occluding agarose fibers was only recently demonstrated by scanning transmission electron microscopy (STEM) and tomography³². However, even this advanced imaging modality does not reveal the chemical complexity of the sample in terms of the localization of different chemical species in the scaffold or the mineral. While high-resolution elemental mapping by electron microscopy is in principle possible, resolution and sensitivity are very much limited by the susceptibility of biological materials to beam damage.

We demonstrate herein that atom-probe tomography (APT), an established technique in metallurgical and semiconductor research^{80,114}, is uniquely capable of chemical tomography of nanoscale buried organic-inorganic interfaces. In particular, we investigate the nano-crystalline magnetite cap (Fe_3O_4 , Figure 4.1) of the chiton tooth, a classical model system for studying matrix-mediated mineralization¹. Chiton teeth are arranged in rows along the radula (rasping tongue). Similar to vertebrate teeth, mature chiton teeth consist of a softer core (apatite or iron phosphate) capped by a hard magnetite layer¹. Depending on the species, the capping may cover the whole tooth or just the leading edge, and other mineral phases (e.g. lepidocrocite) may be present. The outstanding fracture toughness and wear resistance of the tooth results from the organic-inorganic interfaces over multiple levels of hierarchy that deflect and arrest cracks⁵². Remarkably, the radula acts as a conveyor-belt on which an organic matrix scaffold composed of semi-crystalline α -chitin (poly- β -1,4-N-acetylglucosamine) and protein is first deposited²². As the maturing tooth progresses along the radula (~1 row/day), the scaffold is remodeled and filled in with mineral, which occludes the organic matrix in the process. All stages of tooth development are thus present in one animal.

4.2 RESULTS AND DISCUSSION

Samples for TEM and APT were prepared from polished sagittal cross-sections of teeth of the Eastern Beaded Chiton (*Chaetopleura apiculata*). Focused ion beam (FIB) lift out techniques were used to prepare electron-transparent samples from the leading edge of the tooth cap. The identity of the mineral (magnetite) was confirmed by selected-area electron diffraction (SAED, Figure 4.2). Annular dark-field (ADF) STEM reveals numerous dark (weakly scattering) fibrous structures on a bright (strongly scattering) background with dimensions similar to those observed in demineralized chiton teeth (Figure 4.2 & Figure 4.3, $d = 7.6 \pm 2.4$ nm)²². The carbonaceous nature of the fibers was confirmed by carbon K-edge electron energy-loss spectroscopy (EELS).

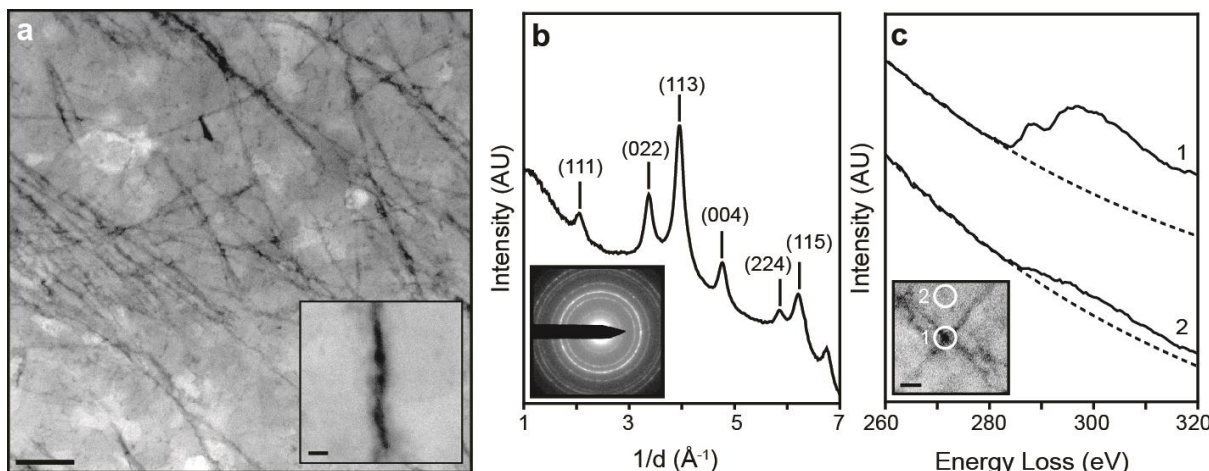


Figure 4.2: Chiton tooth magnetite and occluded organic fibers

a, HAADF-STEM image of chiton tooth magnetite showing dark (low-Z) fibrous structures with a length >1 μm and a diameter of $\sim 5\text{--}10$ nm embedded in the nanocrystalline magnetite (for LAADF STEM see Figure 4.3). Scale bar: 100 nm. (Inset) Detail of fiber. Scale bar: 10 nm **b**, Radially integrated SAED pattern from chiton tooth cusp, labeled planes correspond to magnetite. (Inset) 2D SAED pattern. **c**, Carbon-K edge electron energy-loss (EEL) spectra recorded at fiber intersection (1) and off-fiber (2) demonstrate that fibers are carbon-rich and likely correspond to the chitin observed in un- and de-mineralized chiton teeth. Scale bar: 20 nm.

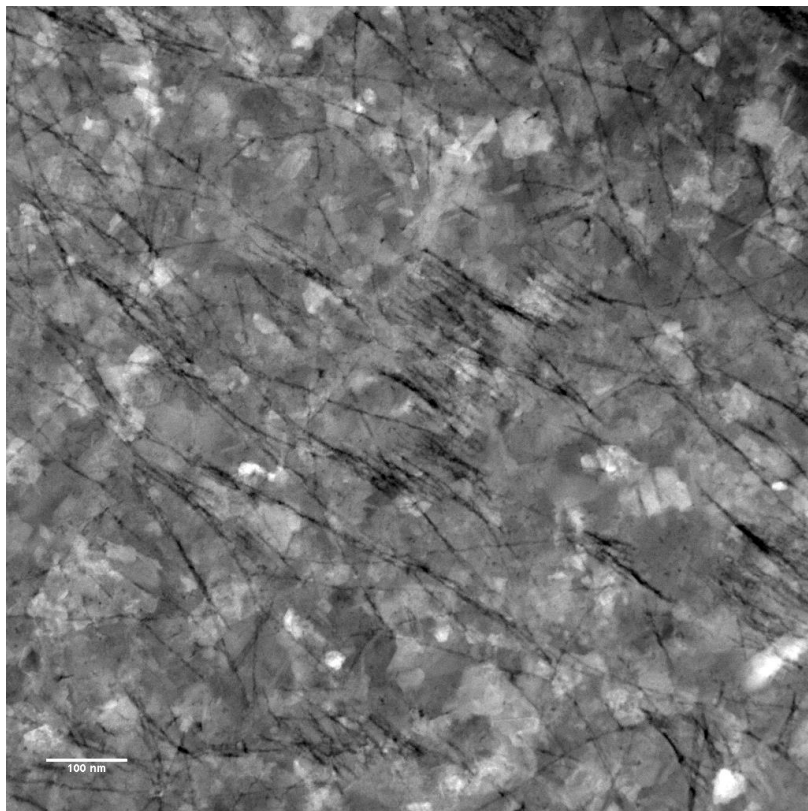


Figure 4.3: LAADF STEM of chiton tooth magnetite

Low angle annular dark field STEM image of chiton tooth magnetite showing long occluded organic fibers crossing numerous nanosized grains in the magnetite. Scale bar 100 nm.

An atom probe is a point projection microscope where, in the presence of a very high electric field, individual or molecular ions sequentially field-evaporate from a sharp tip and are projected onto a 2D position-sensitive detector⁸⁰. The mass-to-charge ratio (m/z) and thus the chemical identity of each ion are determined by time-of-flight (TOF) mass-spectrometry using timed picosecond laser pulses to trigger evaporation events. The sequence and location of ions impinging on the detector enables reconstruction of the 3D structure of the sample. APT analyzes volumes on the order of 10^5 nm^3 with sub-nanometer spatial resolution⁸⁰. The recent development of ultraviolet-laser pulsing greatly increases the scope of the technique to include high resistivity materials and organics.

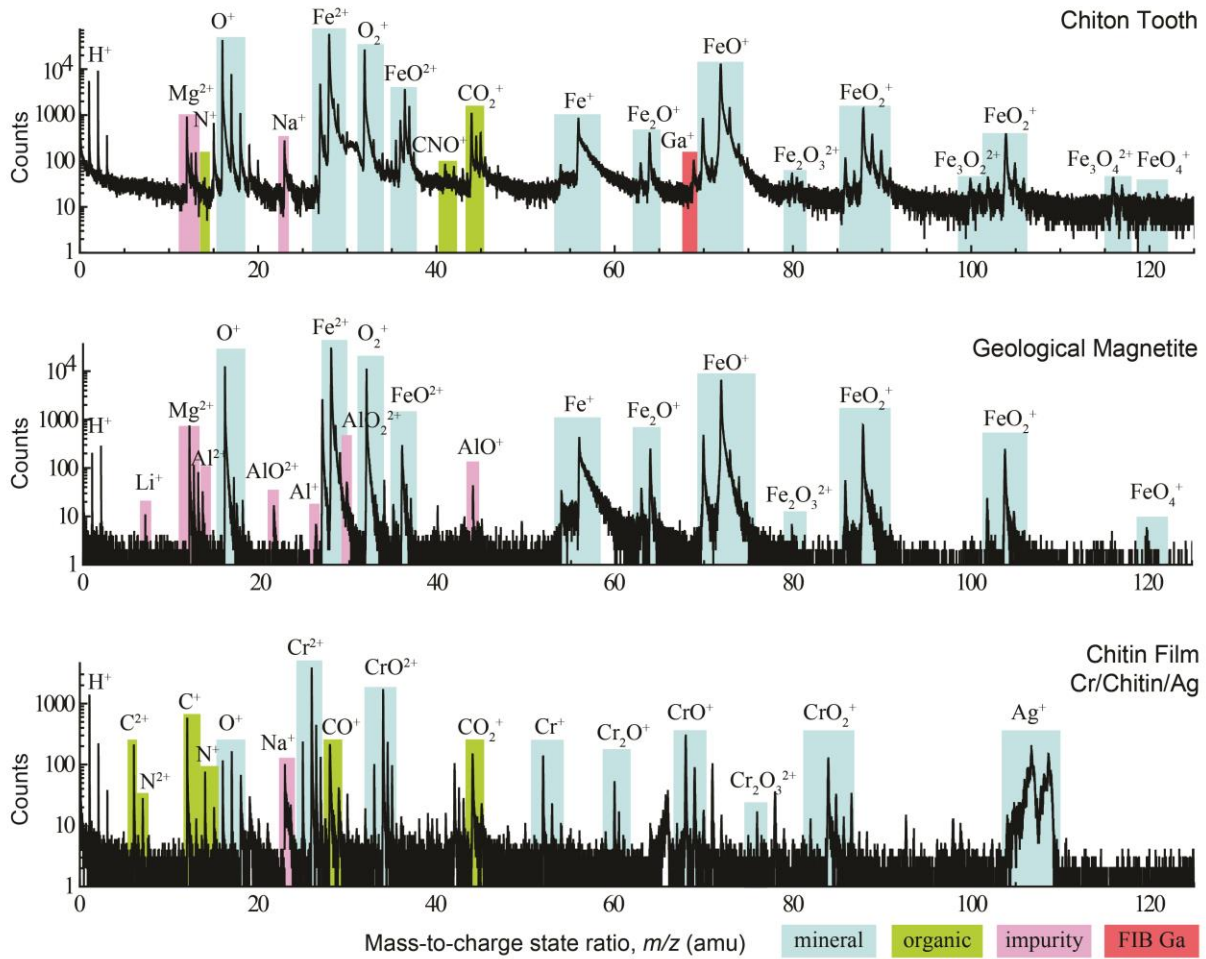


Figure 4.4: APT mass-spectra

Annotated APT mass spectrum from chiton tooth, geological magnetite single crystal and chitin thin-film samples.

In APT mass spectra of samples from the chiton tooth cusp, magnetite-derived iron, oxygen, and iron oxide molecular ions prevail (Table 4.1), similar to spectra of geological magnetite (Figure 4.4 and Ref. ⁹⁵). Typical for oxides, *ca.* 25% of the oxygen evaporates as O_2^{2+} , which cannot be differentiated from O^+ ^(90,95,115). The measured Fe/O ratio for both the biological (0.97 ± 0.15) and geological magnetite (1.13 ± 0.08) is thus higher than the theoretical value of 0.75. APT mass spectra also contain molecular fragments with m/z values corresponding to C/N/O-containing ions (Table 4.1, Figure 4.5), which are not present in

spectra of geological magnetite. While ions such as C^+ and C^{2+} are also found in metal carbides, there is no precedence for carbide formation under physiological conditions. In addition, other ions frequently associated with carbides such as C_n^+ , C_n^{2+} ($n > 1$), and FeC^+ were not detected. However, samples prepared from chitin thin films (Figure 4.6) yield a similar series of molecular ions, confirming that these ions originate from the organic scaffold within the tooth (Figure 4.5). While there is some overlap between organic and mineral-derived ions, for example, $^{12}\text{C}^{16}\text{O}_2^+$ and $^{56}\text{Fe}^{16}\text{O}_2^{2+}$ at $m/z \approx 44$, analysis based on natural isotopic abundances allows identification and quantification.

Table 4.1: Atomic and molecular ions identified in chiton teeth from APT mass spectra.

	Identified Ions
Magnetite	O^+ , O_2^+ , Fe^{2+} , Fe^+ , FeO^{2+} , FeO_2^{2+} , Fe_2O^{2+} , $\text{Fe}_2\text{O}_3^{2+}$, $\text{Fe}_3\text{O}_4^{2+}$, FeO_n^+ , $n = 1-4$
Organic Matrix	C^{2+} , C^+ , CO^+ , CO_2^+ , N^+ , NH^+ , NO^+ , NO^{2+} , CNO^+
Other Ions	Mg^{2+} , Na^+ , Mn^{z+} , MnO_n^{z+} , $n = 1-3$, $z = 1,2$

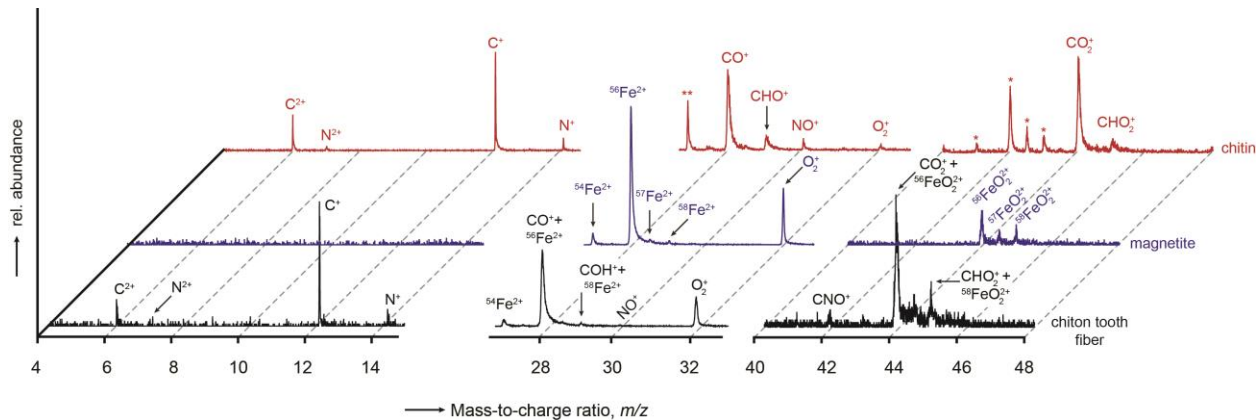


Figure 4.5: APT TOF m/z spectra

Typical spectra of organic fibers (black), the surrounding magnetite (blue), and a chitin thin film (red). Note presence of characteristic chitin-derived atomic and molecular ions (C⁺, C₂⁺, N⁺, N₂⁺, CO⁺, CO₂⁺) in the chiton tooth fiber but not in the surrounding magnetite. Spectral overlap between species (e.g. CO₂⁺ and 56FeO₂²⁺) derived from organics and magnetite can be detected by analysis of natural abundance of Fe isotopes. Species originating from the substrate of the chitin thin film, CrO₂²⁺ (*) and 54Cr²⁺ (**), are indicated. To account for large differences in relative abundance, each m/z range is scaled separately.

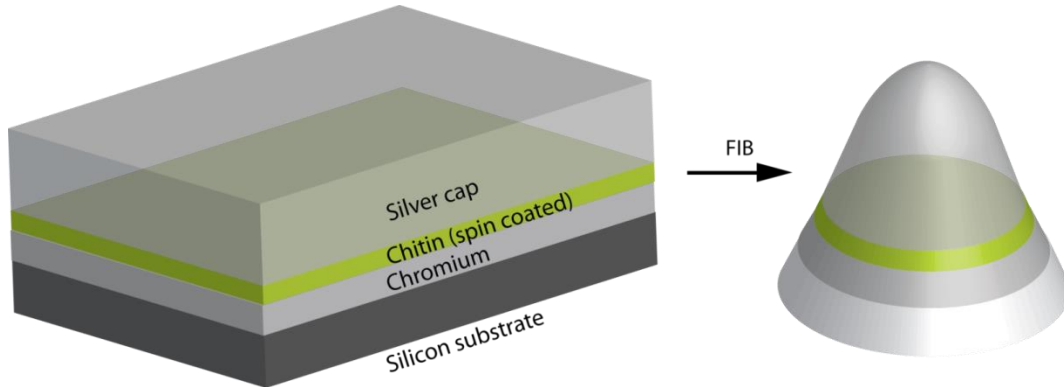


Figure 4.6: Chitin thin film reference standard

Standard consists of a chitin thin film spin coated from solution on a chromium coated silicon wafer. This chitin film is covered with a protective silver cap.

The relative fraction of iron-containing ions and organic ions in the overlapping peaks at 28 and 44 m/z was determined based on the known isotopic abundances of the four naturally occurring iron isotopes: three stable isotopes: ^{56}Fe (5.85%), ^{57}Fe (91.75%) and ^{58}Fe (0.28%) and ^{54}Fe (2.12%) with an extremely long half-life $>3.1 \cdot 10^{22}$ years. Since no organic fragment was identified which overlapped with either $^{54}\text{Fe}^{2+}$ at 27 m/z or $^{54}\text{FeO}_2^{2+}$ at 43 m/z the number of counts of the ^{54}Fe isotope was used to determine the expected number of counts in the overlapping peak containing the common ^{56}Fe isotope. The small peaks corresponding to ^{57}Fe and ^{58}Fe lie in the thermal tail region after the large ^{56}Fe peak and thus were not used in these calculations. For example, the number of counts after background subtraction in the $^{54}\text{FeO}_2^{2+}$ peak (43 m/z) in two samples was 205 and 616, respectively. Based on these values and the relative natural abundances of the iron isotopes the expected number of $^{56}\text{FeO}_2^{2+}$ ions in the two samples should be 3215 and 9661, respectively. The actual number of counts of $^{56}\text{FeO}_2^{2+}$ ions after background subtraction in both samples was, however, 11663 and 22810, respectively. This indicates that 60-70% of the counts in the peak at 44 m/z correspond to CO_2^+ not $^{56}\text{FeO}_2^{2+}$.

Demonstrating the unique sensitivity of APT across the entire periodic table, APT spectra reveal the presence of the light elements sodium and magnesium and trace amounts of manganese. While the role of Na in biomineralization is not well understood, Mg^{2+} has been shown to modulate mineralization processes, and Mg-binding motifs have been identified in acidic proteins^{17,116}. Mn, on the other hand, is a highly regulated, essential cofactor in many redox-active enzymes¹¹⁷ and may play a role in magnetite mineralization.

We used standard reconstruction algorithms to generate 3D tomograms (Figure 4.7). The organic matter-derived ions are clearly seen to originate from fibers occluded within the mineral. The total amount of carbon is less than what would be expected from crystalline chitin fibers. This may be a consequence of overlapping peaks in TOF spectra, preferential evaporation, or biological remodeling of fibers during mineralization¹¹⁸. Nevertheless, the fiber diameter (5-10 nm) closely resembles the organic fibers ob-

served in STEM images of the mineralized tooth (Figure 4.2). Furthermore, Na^+ and Mg^{2+} clearly co-localize with organic fibers (Figure 4.7). Surprisingly, no biologically relevant counter ions (e.g., chloride, phosphate, sulfate) could be detected. With chitin being neutral or, if partially deacetylated, slightly positively charged, the most likely scenario is that acidic proteins associated with the chitin scaffold bind the cations. Interestingly, within each fiber there appear to be small domains around which cations cluster (Figure 4.7). It is conceivable that these domains correspond to crystalline α -chitin domains that exclude acidic proteins and the cations associated with these.

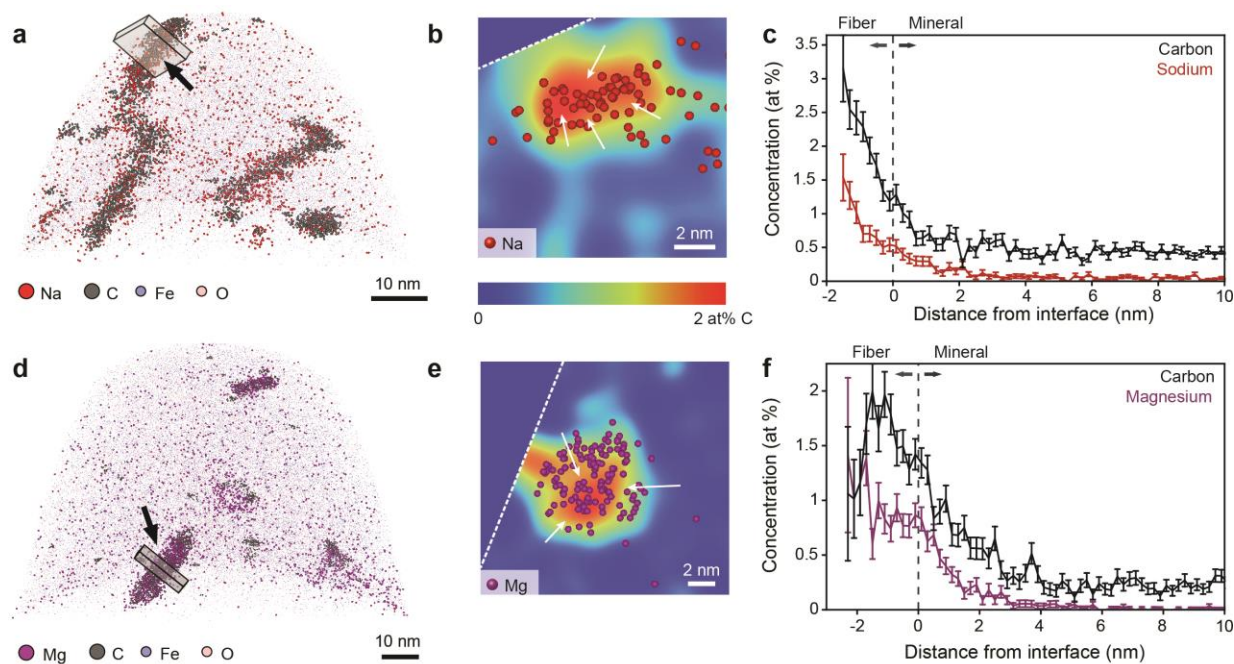


Figure 4.7: 3D Reconstructions and Proxigrams

a,b Two representative samples of samples containing organic fibers that bind Na^+ (**a-c**) or Mg^{2+} (**d-f**), exclusively. For clarity, only 5% of Fe/O ions are rendered; the edge of the field of view of the APT detector is marked (dashed line). Overlay of Na^+ (**b**, red spheres) and Mg^{2+} (**e**, magenta) ion positions on carbon concentration maps integrated over the boxed regions indicated in **a** and **d**. Note that some regions of the fibers are devoid of Na or Mg (arrows). Proximity histograms (error bars: $\pm 1\sigma$) of Na/C (**c**) and Mg/C (**f**) across the organic-inorganic interface of fibers indicated by arrows in **a** and **d**. Interfaces appear graded over 2-4 nm.

Unexpectedly, in some samples fibers only bind Na^+ (Figure 4.7a) while Mg^{2+} is bound exclusively in others (Figure 4.7d). This is despite the fact that these samples were taken within a few μm of each other. Both Mg^{2+} and Na^+ co-localize with fibers in fiber-bundles (Figure 4.8). There are many examples of proteins that selectively bind and/or transport cations; they frequently differentiate between ions based on their ionic radius, preferred coordination geometry, and hard/soft acid/base properties¹¹⁹. For example, the so-called DEAD box motif found in some acidic proteins from biominerals has been suggested to play a role in Mg^{2+} binding¹⁶. It is thus conceivable that in the chiton tooth scaffold, chitin-binding proteins with specificity for either Na^+ or Mg^{2+} are assembled with chitin into a fiber that shows selective binding. The cations themselves may be integrated as part of the assembly, or come in at a later stage. While we cannot yet provide accurate statistics of the relative frequency of Mg- and Na-binding fibers, it is clear that this unprecedented chemical heterogeneity requires extending the number of hierarchical levels to accurately describe the architecture of the chiton tooth. It is possible that similar differences in elemental distributions are present in other biominerals, e.g. bone or enamel, but have so far been overlooked.

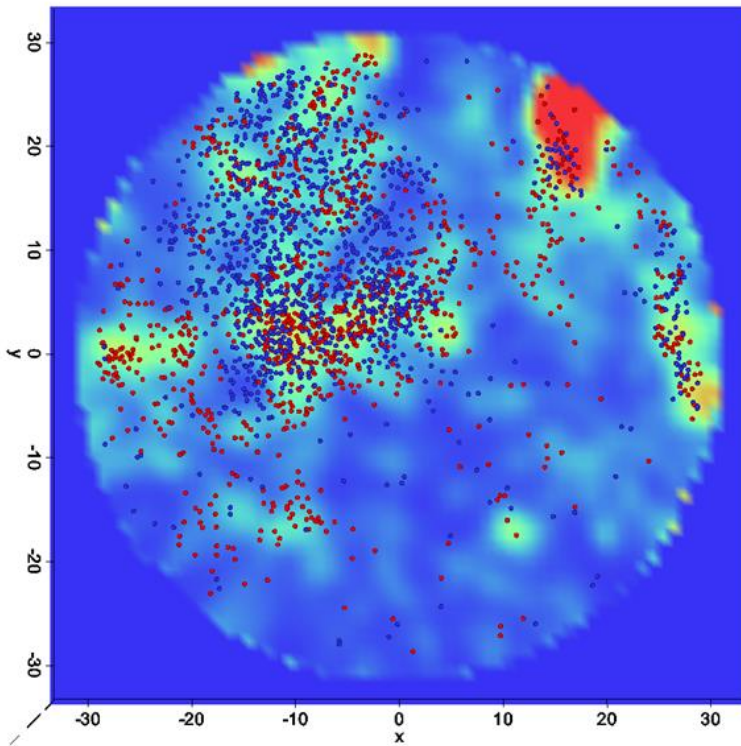


Figure 4.8: Fiber bundle

Colocalization of magnesium ions (blue spheres) and sodium ions (red spheres) within a fiber bundle. Both ions are observed to cluster near the organic fibers. The background shows the total carbon concentration averaged over the 5nm thick slice, scale goes from blue (0 at%) to red (3 at%). A number of clear regions of high carbon concentration correspond to the fibers visible in the 3D rendering. The scale bar is in nanometers.

Proximity histograms (proxigrams)¹²⁰ that give concentration as a function of distance to the fiber-mineral interface (defined by an isodensity surface at $1 \text{ C} \cdot \text{nm}^{-3}$, Figure 4.9) reveal that the interface is graded rather than sharp, creating a 2-4 nm wide region of interpenetrating mineral and organic material (Figure 4.7c,f). A graded or rough interface may improve mineral/organic adhesion and enhance mechanical load transfer and toughness. Furthermore, this results in a fundamentally different interface than that observed in single crystals of calcite grown in agarose gels, where high index planes at the interface create a sharp boundary³². Proxigrams in addition reveal a roughly two-fold increase of the manganese concentration in

the fibers (Figure 4.10). This raises the intriguing possibility that Mn-dependent enzymes, some of which may have chitin binding domains, catalyze the reductive transformation of ferrihydrite to magnetite.

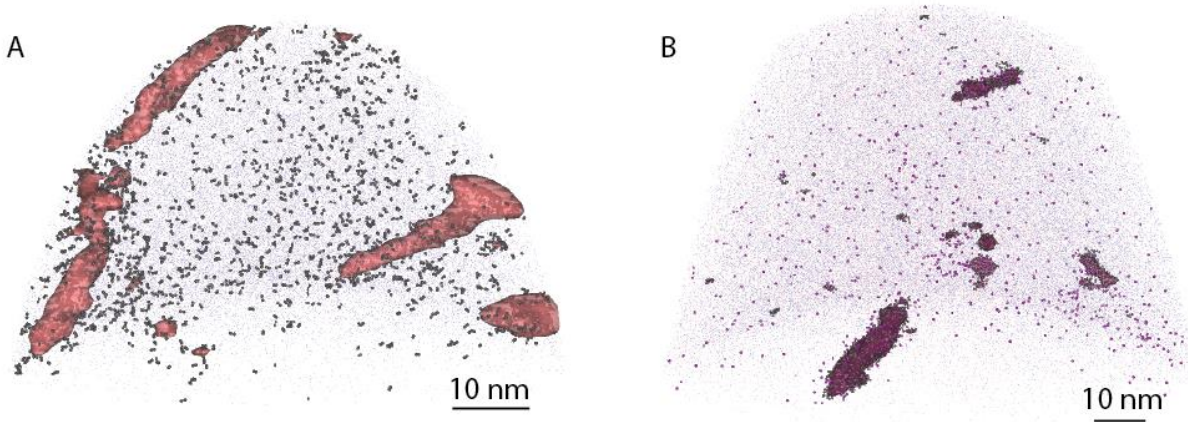


Figure 4.9: Isodensity surfaces used to calculate proxigrams

1 carbon atom per cubic nanometer isodensity surfaces. (A) Sodium binding fibers (B) Magnesium binding fibers. The voxel size used was 1 x 1 x 1 nm and the delocalization parameters were 3 nm in x and y and 1.5 nm in z.

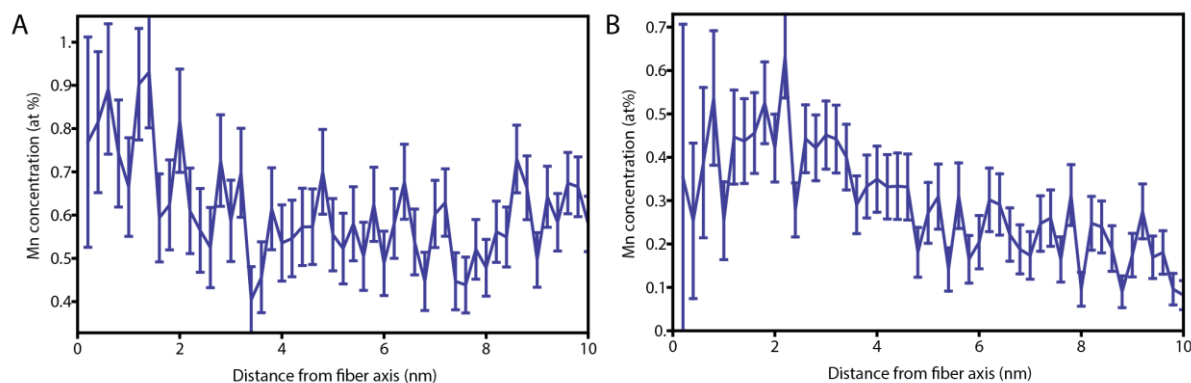


Figure 4.10: Manganese concentration proxigrams

For fibers shown in Figure 4.7a (a) and Figure 4.7d (b).

With the fiber-backbone being semi-crystalline α -chitin, it follows that there are crystalline domains and amorphous regions that connect them. It seems reasonable to assume that single strands or loops/coils of amorphous chitin create the rough fiber surface we observe (Figure 4.11). The distribution of Na^+ and Mg^{2+} suggests that chitin-binding proteins with selectivity for either or both cations decorate the fiber surface. They may also be present on the inside of the fiber, but are likely excluded from crystalline domains. Fiber-mineral interactions may be mediated by these cations or direct contacts between side chain carboxylates, amines, and hydroxyl groups and iron cations or oxy-anions on the mineral surface.

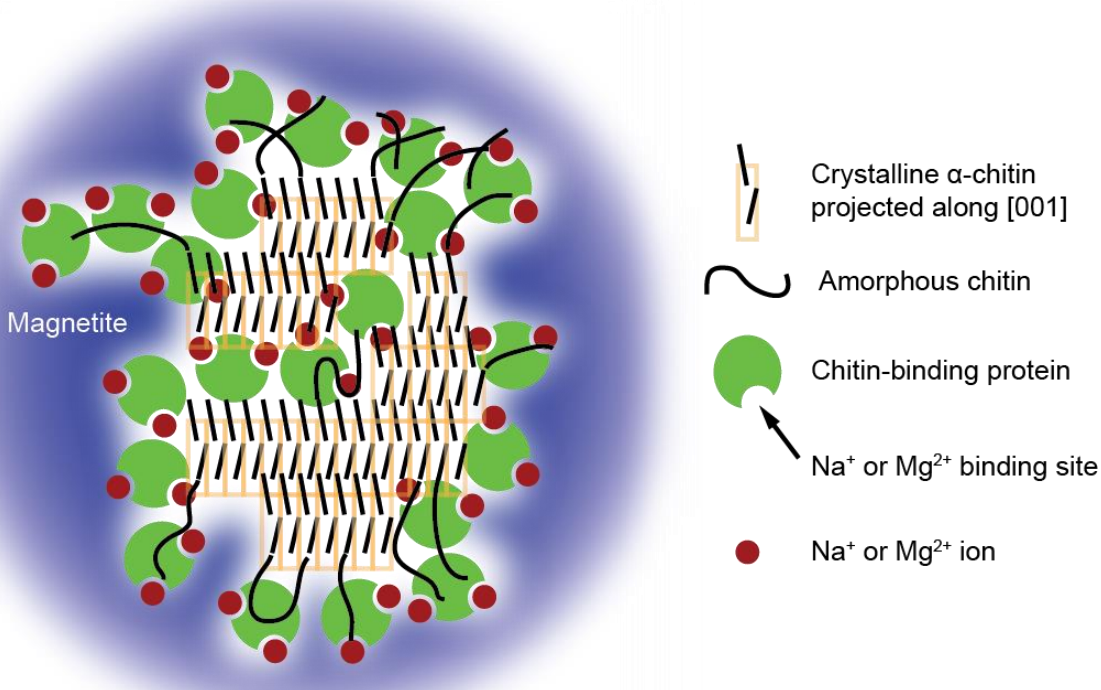


Figure 4.11: Model of a chiton tooth organic fiber

The backbone of the fiber consists of semi-crystalline α -chitin. In the crystalline domains, anti-parallel polysaccharide chains are arranged along the [001] direction and are aligned with the fiber axis. Amorphous chitin connects these domains and creates a rough fiber surface. Hypothetical chitin-binding proteins in addition have acidic domains that specifically bind Na^+ or Mg^{2+} . Fiber-mineral interactions may be mediated by these cations and/or acidic, basic, or hydroxyl side chains. At this time, it is not clear whether the magnetite-organic interface involves specific crystallographic planes, is extensively reconstructed, or even strongly disordered (amorphous).

Based on this model, it is conceivable that fibers decorated with cations with strongly different charge density (that of Mg^{2+} is 4-10 times greater, depending on the coordination number) differ in their functional roles. Modulation of colloidal properties such as the ζ -potential may be an important way to control fiber self-assembly and maintain the fiber diameter such that mineral overgrowth is not impeded. By inducing counter-ion condensation, the fiber chemistry could also influence where and when nucleation of

the mineral phase occurs, similar to what has been proposed for nacre organic matrix.¹²¹ Different strength and geometry of coordinative bonds mediated by Na^+ and Mg^{2+} will affect interactions within the organic matrix, between mineral and organic matrix and/or control the amount of water retained in the final structure. This could modulate the ability of organic matrix molecules to accommodate large strains by elastic uncoiling (“hidden length”), or control energy dissipation during plastic deformation (i.e. toughness) through the strength and number of sacrificial bonds¹²². Water is an important lubricant, and the incorporation of Mg^{2+} with its tightly bound water molecules may prevent the composite from becoming overly brittle or facilitate reforming sacrificial bonds after deformation, thus contributing to self-healing. Whether the chiton uses these effects to control mineral deposition and properties of the final composite and how we might adapt them to bio-inspired materials synthesis is the subject of our ongoing investigation.

4.3 CONCLUSION

In summary, using HAADF-STEM and ultraviolet-laser pulsed APT, we identified organic fibers in the magnetite layer of the chiton tooth that bind either Mg^{2+} or Na^+ , and fiber bundles in which both ions are present. This is the first account that shows direct proof of intra-crystalline organic fibers and demonstrates their chemical and structural heterogeneity at a sub-nanometer length scale in a biological material, or in fact any organic/inorganic composite. We furthermore demonstrate the presence of a graded fiber/mineral interface and find evidence for a role of Mn in magnetite biomineralization. APT dramatically expands the ability to characterize complex nano-composites and ideally complements state-of-the-art (S)TEM techniques. Of great importance to biomedical research, APT may soon give insight into the chemical nanostructure of bone, dentin, and enamel. Organic scaffolds in biominerals generally comprise a fibrous structural element, e.g., collagen in bone¹¹ or chitin in mollusks and crustaceans¹². Acidic macromolecules, such as the non-collagenous proteins in bone¹³ and Asprich proteins in the bivalve prismatic layer¹⁴, are usually associated with the fibrous scaffold. While these proteins may be intrinsically disor-

dered, their charge predisposes them to interact with the forming mineral¹⁵. They are thought to play a key role in controlling crystal polymorph and orientation. Additionally, ions such as Mg²⁺^(16,17), and polyphosphates¹⁸ are known to be important modulators of mineralization processes. Consequently, understanding the biological control over mineral growth and the resulting functional properties critically depends on characterizing buried organic/inorganic interfaces.

4.4 MATERIALS AND METHODS

4.4.1 Consumables

Unless otherwise specified, the following chemicals were used without further purification: MgCl₂, HCl, NaOH, ethanol, NaOCl (VWR, West Chester, PA); glutaraldehyde, Ultra-Smooth Carbon Adhesive Tabs (Electron Microscopy Sciences, Hatfield, PA); propylene oxide, Araldite 502, Conductive Liquid Silver Paint (Ted Pella, Redding, CA); Instant All Purpose Brush-On cyanoacrylate adhesive (Krazy Glue, Columbus, OH); EPO-TEK H2OE Conductive Silver Epoxy (Epoxy Technology, Billerica, MA); CarbiMet II SiC grinding paper, Metadi supreme polycrystalline aqueous diamond polishing suspension, Microcloth polishing cloths (Buehler, Lake Bluff, IL); Chitin (TCI America, Portland, OR); Hexafluoroisopropanol (Sigma-Aldrich, St. Louis, MO); Silver pellets, chromium-plated tungsten rods (Kurt J. Lesker Company, Clairton, PA). Unless otherwise noted, all solutions were prepared in ultra-pure water ($\rho = 18.2 \text{ M}\Omega\cdot\text{cm}$) prepared with a Barnstead Nanopure UF+UV (Thermo-Fisher Scientific, Waltham, MA). Artificial seawater (ASW) was prepared using Instant Ocean Sea Salt to a final salinity of 35 g·L⁻¹.

4.4.2 Chitin Tooth Isolation and Preparation

Eastern Beaded chitons, *Chaetopleura apiculata* (Say 1834), were acquired live from the Woods Hole Marine Biological Laboratory (Woods Hole, MA). Radulae were extracted by dissection after narcotization of the specimens in aqueous magnesium chloride (0.38 M, 20 min, 15 °C). Radulae were fixed in 3% glutaraldehyde in ASW overnight at 4°C. Samples were washed once in ASW and water and then dehy-

drated in a graded ethanol series in water (50, 70, 90, 100 vol %). Prior to resin infiltration the samples were transferred into propylene oxide. The samples were embedded in Araldite resin and polymerized overnight at 60°C. The embedded samples were ground using progressively finer grits of SiC grinding paper (400, 600, 800, 1200, and 2000 grit) and polished using polycrystalline aqueous diamond polishing suspensions (6, 3, 1.5, and 0.1 μm). The polished cross-sections secured to an aluminum stub with cyanoacrylate adhesive, coated with 25nm of Pt by magnetron sputtering with a turbo-pumped Desk III (Denton Vacuum, Moorestown, NJ) then grounded to the stub with conductive liquid silver paint.

4.4.3 Geological Magnetite Samples

Geological magnetite single crystals were acquired from ABCRox (Grand Junction, CO) and Commercial Crystal Laboratories, Inc. (Naples, FL). The ABCRox sample was cut along the (111) face with a low speed diamond saw (Buehler Isomet) ground using progressively finer grits of SiC grinding paper (400, 600, 800, 1200, and 2000 grit) and polished using polycrystalline aqueous diamond polishing suspensions (6, 3, 1.5, and 0.1 μm). The polished sample was secured to an aluminum stub using conductive silver epoxy. The Commercial Crystal Laboratories sample was purchased one-side polished with a (100) orientation and then secured to an aluminum stub with a conductive adhesive carbon tab.

4.4.4 Chitin Film Purification and Preparation

Crude chitin was purified by adapting previously published protocols¹²³⁻¹²⁵. The chitin was washed twice in water. The chitin was then stirred with HCl (1.5 M, 6 h, 25°C), then washed twice with water. The acid-treated chitin was further stirred with NaOH (1.5 M, 3 h, 25°C) and washed twice with water. The chitin was then treated with NaOCl (10%, 5 min, 25°C) then washed twice with water. The purified sample was then frozen in liquid nitrogen and lyophilized. The lyophilized chitin was dissolved at 1 mg/ml in hexafluoroisopropanol (HFIP). The following substrate preparation and spin coating steps were carried out in a nitrogen filled oxygen- and water-free glove box to minimize contamination of surfaces with organic materials from the atmosphere. Silicon wafers were first coated with a 28 nm layer of Cr by thermal

evaporation (MBraun, Garching, Germany) at a base pressure below 10^{-5} Pa. Deposit thickness was monitored using a quartz crystal monitor (Inficon, East Syracuse, NY). The thermal evaporator was vented with dry nitrogen and the coated substrates were transferred within the glove box to a spin coater (Specialty Coating Systems G3P-B, Indianapolis, IN) where they were spin coated with a chitin film from the HFIP solution at 3000 rpm. The spin-coated substrates then coated with 200nm of Ag at a base pressure below 10^{-5} Pa. The wafer was secured to an aluminum stub with a conductive adhesive carbon tab.

4.4.5 TEM Sample Preparation

Transmission electron microscopy (TEM) lamella were prepared from a polished cross section of the chiton tooth following established procedures with a DualBeam scanning electron microscope (SEM) and focused ion beam (FIB) instrument (Helios NanoLab, FEI, Hillsboro, OR)¹²⁶. First a strap of platinum (FIB-Pt) was deposited over a region of interest on the polished cross-section using the ion beam (30kV, 93pA) to locally decompose an organometallic precursor gas (methyl cyclopentadienyl trimethyl platinum [$C_5H_5Pt(CH_3)_3$]). Two trenches were then milled out (30kV, 6.5nA) on either side of a 2 μ m thick slice of material. The slice of material was cut free (30kV, 2.8nA) from the substrate on three sides leaving only small connecting bridge. An *in situ* tungsten nanomanipulator probe (Omniprobe) was attached to the free side of the substrate using FIB-Pt (30kV, 93pA). The remaining connection to the substrate was milled away (30kV, 93pA) and the probe was retracted with the sample. The sample was then welded to a copper TEM half-grid (Omniprobe) using FIB-Pt and the connection to the probe was milled away (30kV, 93pA). The lamella was successively thinned to ~100nm at 30 kV (93pA) at a 1-2° angle grazing incidence milling condition. The majority of the surface amorphization and gallium implantation was removed by low angle milling (~7°) at 5 and 2 kV (28pA) to thin the sample to approximately 60-80nm.

4.4.6 SEM and TEM

Elemental mapping of polished cross-sections was performed using energy dispersive X-ray spectroscopy (EDS) in the Dual-Beam SEM/FIB operating at 15 kV using a Quantax X-flash silicon drift detector

(Bruker AXS, Madison, WI). Selected area electron diffraction (SAED) patterns were acquired using a Hitachi H-8100 (Tokyo, Japan) operating at 200 kV. High angle annular dark field (HAADF) scanning TEM (STEM) images and electron energy loss spectra (EELS) were acquired using a JEOL 2100F (Tokyo, Japan) operating at 200 kV equipped with a Gatan electron energy loss spectrometer (Pleasanton, CA). EELS maps were acquired with a dwell time of 1 sec/pixel, a probe convergence angle of 10 mrad and a collection angle of 50 mrad. Pre-edge backgrounds were fit using a power law function.

4.4.7 APT Sample Preparation

Samples for APT were prepared using the SEM/FIB instrument using established protocols¹⁰⁰⁻¹⁰². First a layer of platinum was deposited over a region of interest (2 x 25 μm) on the polished cross-section using the ion beam (30kV, 93pA). For the geological samples where no sputtered or evaporated metal coating was present a protective 100nm layer of platinum was deposited first using the electron beam (5 kV, 5.5nA) before the ion beam was turned on. A wedge of material below the Pt strap was cut out on three sides. The wedge was attached to an in-situ nano-manipulator (Omniprobe, Dallas, TX) using FIB deposited Pt before cutting the final edge free. 1-2 μm wide segments were cut from the wedge and sequentially affixed to the tops of Si posts in an array (Cameca Scientific Instruments, Madison, WI) with FIB-Pt. Each tip was shaped and sharpened using annular milling patterns of increasingly smaller inner and outer diameters¹⁰³. The majority of the amorphized surface region and implanted gallium ions in the tip surface was removed by milling at 5 and 2 kV, 89pA.

4.4.8 APT Methods

Atom probe tomographic analyses were conducted in a Cameca local-electrode atom-probe (LEAP 4000XS) tomograph using a pulsed laser ($\lambda = 355\text{nm}$, 160-500 kHz, 40-75 pJ per pulse). The DC potential on a microtip during APT was controlled to maintain an evaporation rate between of either 0.0025 or 0.005 ions per laser pulse. The base temperature of the microtip was maintained at 40 or 60 K and the ambient vacuum pressure was $<10^{-8}\text{ Pa}$.

Three-dimensional reconstruction of APT data was performed using the IVAS atom-probe data visualization and analysis software (Cameca) using published algorithms, assuming a hemispherical tip shape^{83,105}. Standard reconstruction parameters were used with an electric field dependent radius (r). The average evaporation field (F_e) of the biogenic chiton tooth magnetite ($23.5 \text{ V}\cdot\text{nm}^{-1}$) was measured by acquiring either SEM or STEM images of microtips after APT analysis. Atomic volumes of Fe and O for the reconstruction were calculated based on published values of ionic radii and the known magnetite crystal structure^{127,128}. The atomic volume assigned to oxygen was increased to account for the oxygen deficiency in the measured stoichiometry. Proximity histograms¹²⁰ were calculated using a carbon isodensity surface (Figure 4.9) of 1 carbon atom per cubic nanometer and then extrapolating to the fiber axis.

4.4.9 APT 3D Renderings

Three-dimensional renderings of APT data were created in IVAS. The carbon containing ions (C^{2+} , CO_2^+ , CNO^+) were only rendered where the local density exceeded 0.75 nm^{-3} due to the spectral overlap between CO_2^+ and $^{56}\text{FeO}_2^{2+}$ in the magnetite. CO^+ was not rendered due to the overlap with $^{56}\text{Fe}^{2+}$. For clarity, only 5-10% of the background Fe and O ions were rendered.

4.4.10 APT 2D Concentration Plots

Two-dimensional concentration plots were created with a pixel size of 0.1nm . The 3D grid voxel size was $0.2 \times 0.2 \times 0.2 \text{ nm}$ and the delocalization parameters were 2.5 nm in x and y and 1.25 nm in z . The edge of the field of view (where the ions from the tip impact the local electrode) is marked with a white dashed line. The concentrations were averaged over a 3 nm thick region.

5 POLYMORPH SELECTIVITY IN THE CHITON TOOTH

This chapter discusses the mechanisms responsible for polymorph selectivity in the chiton tooth. Jessica K. Román, Dr. R. Michael Everly and Professor Jonathan J. Wilker in the Department of Chemistry at Purdue University were instrumental in verifying X-ray absorption spectroscopy measurements of chiton teeth and *in vitro* reaction products with electron paramagnetic resonance spectroscopy. Anaerobic experiments were performed in the laboratory of Prof. Yun Wang, Civil and Environmental Engineering, Northwestern University. Dr. Qing Ma, Argonne National Lab, assisted with X-ray spectroscopy measurements.

Parts of the work have been published in the following conference proceedings and prepared for submission in the following article:

Gordon, L. & Joester, D. Understanding the biological stabilization of ferrihydrite and its transformation to magnetite. *Bulletin of the American Physical Society* **58** (2013).

Gordon, L. M., Román , J. K., Everly, R. M., Cohen, M. J., Wilker, J. J. & Joester, D. On polymorph selection in the chiton tooth. *in preparation.*

5.1 INTRODUCTION

The use of metastable, disordered precursors is a widespread phenomenon in biominerization³⁴. This precursor strategy is thought to play a major role in the impressive ability of biological organisms to create intricately shaped, yet mechanically robust single crystals and construct hierarchical functional materials. Chitons, marine mollusks that graze on rocks, grow teeth that are extremely hard, wear resistant, and self-sharpening^{1,51}. These remarkable properties result from the deposition of nanocrystalline magnetite (Fe_3O_4) in a nanofibrous chitin scaffold of surprising chemical and structural complexity^{10,129}. The ability of chitons to synthesize monolithic nanocomposites of magnetite is critically dependent on infiltration of

the scaffold with metastable ferrihydrite^{47,130}. Here we show by a combination of X-ray absorption and electron paramagnetic resonance spectroscopy that, prior to the formation of ferrihydrite, the acidic organic matrix forms complexes with Fe(III). Parallel *in vitro* experiments demonstrate that such complexes are necessary and sufficient to ensure selective formation of phase-pure ferrihydrite under physiological conditions. Taken together, these results indicate that acidic macromolecules are integral to controlling ferrihydrite formation in the chiton tooth. At the same time, this biological approach to polymorph selection is not limited to specialized proteins and can be expropriated using simple chemistry, with exciting implications for bio-inspired material synthesis.

The chemistry of iron oxides is a particularly rich field with broad industrial applications, from magnetic nanoparticles for theranostics to ferrofluids and from catalysts to information storage^{131,132}. Surprisingly, fundamental aspects of the structure and phase transformations of iron oxides remain controversial and new evidence for non-classical nucleation and particle mediated growth pathways have recently come to light^{53,133-135}. The study of organisms that mineralize iron oxides has been a very powerful approach to gain deeper insight into the mechanisms by which iron oxide phase transformations can be controlled^{1,48,136}. Among these, the chiton radula has emerged as a model system for basic mechanisms of extracellular, matrix-mediated mineralization and for the design of abrasion resistant, self-sharpening functional materials⁵⁰.

The chiton radula is a ribbon-like rasping tongue with many rows of teeth that are designed to withstand the stresses of grazing on rocky substrates⁵¹. The magnetite tooth cusp of radular teeth is the hardest biomaterialized tissue known. Notwithstanding their abrasion resistance, teeth are subject to significant wear. Newly formed teeth replace worn ones every few days, moving along the radula as if on a conveyor belt. Therefore, all stages of tooth development can be simultaneously observed in one animal.

Developmental stages can be differentiated based on the color that originates from the iron mineral present (Figure 5.1). Stage I teeth are colorless and are therefore often referred to as un-mineralized scaffolds. They primarily comprise α -chitin, proteins, and water. Stage II teeth are brown, containing predominately ferrihydrite (for a recently proposed structure and stoichiometry, $\text{Fe}_{8.2}\text{O}_{8.5}(\text{OH})_{7.4}\cdot 3\text{H}_2\text{O}$, see Ref. ⁵³). In stage III, transformation of ferrihydrite to magnetite (Fe_3O_4) results in a gradual change from brown to black. Stage IV teeth are completely black as the cusp reaches its final density of magnetite. After the cusp has been completed, the tooth is filled in with a softer mineral or mixture of minerals specific to the species. The configuration of the cap is also species-dependent and layers of minerals such as lepidocrocite [$\gamma\text{-FeO(OH)}$] may be present. Overall, the architecture of a hard, abrasion resistant cap and a more compliant core is reminiscent of vertebrate teeth.

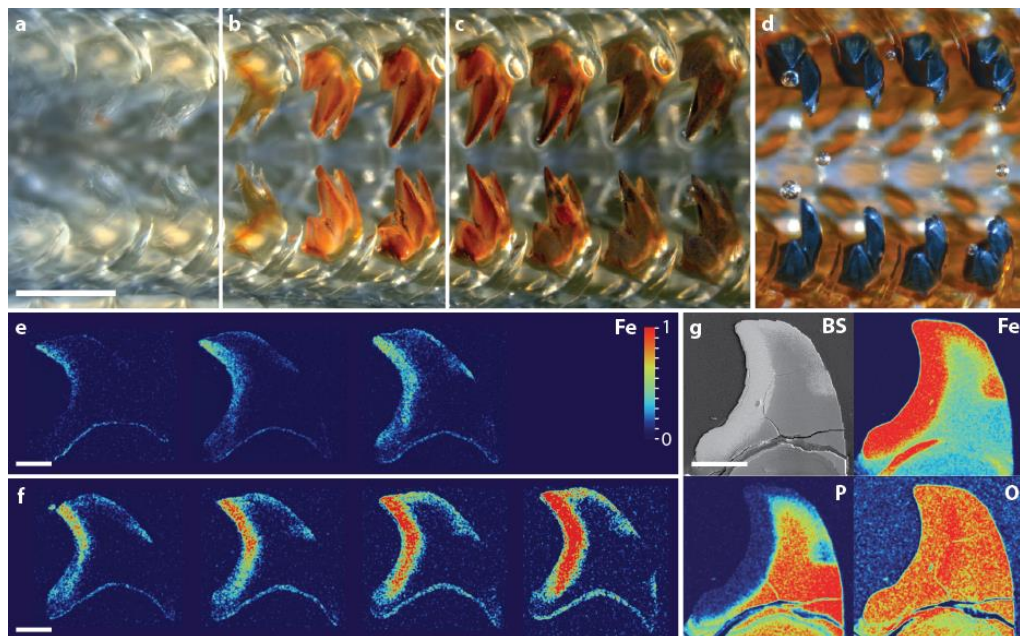


Figure 5.1: Stages of tooth mineralization along the radula of *K. tunicata*

a-d, Top down view in reflected light with representative rows of teeth from stage I (**a**), stage II (**b**), stage III (**c**) and stage IV (**d**). **e – f**, Iron concentration maps generated by SEM-EDS of longitudinal tooth cross sections in stage II (**e**) and III (**f**). Iron concentration was normalized to the highest value in (**f**). **g**, Cross section of a stage IV, fully mineralized tooth by SEM in backscattered electron (BS) contrast and SEM-EDS elemental maps showing a Fe/P/O-rich core (iron phosphate) and Fe/O-rich cap (magnetite). Scale bars represent 500 μm in **a – d** and 100 μm in **e – g**.

Two interconnected features of this biological material synthesis elude our synthetic capabilities. Unlike the biological process, where ferrihydrite is a precursor for a *monolithic* magnetite nano-composite with excellent mechanical properties, wet chemical synthesis results in nanodisperse powders instead. That ferrihydrite is formed at all is even more surprising. Under physiological conditions and in the absence of strong ligands, only Fe(II) is bioavailable. However, in the presence of oxygen at circumneutral pH, Fe(II) is rapidly oxidized to Fe(III). The latter immediately hydrolyzes to crystalline lepidocrocite or goethite [α -FeO(OH)], not metastable ferrihydrite. Wet chemical synthesis of ferrihydrite therefore requires conditions of extreme pH and/or rapid hydrolysis that are far outside the physiological range¹³¹. Clearly, the organism manipulates the reaction environment in some fashion to achieve its dual ends.

In other systems, acidic macromolecules are thought to play an important role in the transient stabilization of metastable, amorphous precursors of calcium carbonates and calcium phosphate^{34,137}. Acidic macromolecules are likewise found in the organic matrix of chiton teeth, and have been implicated in the unusual, selective decoration of chitin fibers with sodium or magnesium ions^{10,129}. However, the functional role of macromolecules in the chiton tooth organic matrix remains poorly understood^{50,138}. Herein, we investigate the role of the native organic matrix of the chiton tooth in the selective precipitation of metastable ferrihydrite under physiological conditions. Specifically, we use complementary spectroscopic techniques to interrogate structure and evolution of the chemical environment of iron in the matrix.

5.2 RESULTS AND DISCUSSION

5.2.1 *In Situ: The Chiton Radula*

Samples for spectroscopy were cleaned using Shaw's protocol to remove all weakly bound iron¹³⁹; all remaining iron is either present in insoluble (mineral) form or is strongly bound by the organic matrix. X-ray absorption near edge structure (XANES) spectra clearly show the evolution of the iron environment from ferrihydrite in stage II to magnetite in stage IV (Figure 5.2)¹⁴⁰. However, we find that teeth in the

'unmineralized' stage I not only show a distinct Fe *K*-edge, but also exhibit markedly different spectral features from ferrihydrite and magnetite (see Figure 5.3). Specifically, the intensity of a broad post-edge shoulder decreases in intensity. A pre-edge feature (~7114 eV) increases in intensity and the edge itself shifts to lower energy (Figure 5.2b). The latter shift is much more pronounced going from stage II to stage IV and is consistent with the partial reduction of Fe(III) in ferrihydrite to Fe(II) in magnetite.

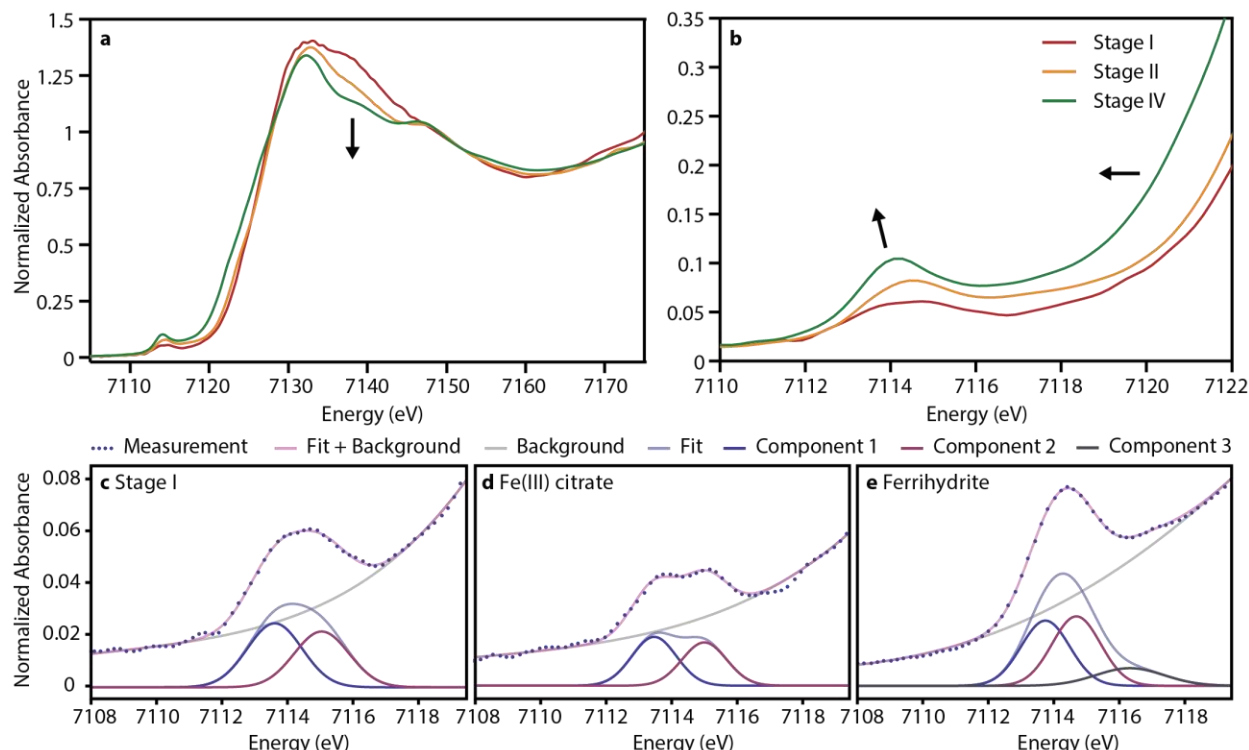


Figure 5.2: XANES spectra of chiton teeth and reference compounds

a. Normalized Fe *K*-edge spectra obtained from sections of *K. tunicata* radulae corresponding to stages I, II and IV. Radulae of ten specimens were pooled for each sample. Arrow denotes a post-edge feature that decreases in intensity with increasing maturity of the teeth. **b.** In this magnified pre-edge region, arrows highlight the increasing intensity of the pre-edge feature and the associated shift to lower energy of the pre-edge feature and the edge itself. **(c – e)** Pre-edge fits for **(c)** stage I teeth **(d)** Fe(III) citrate and **(e)** synthetic "2-line" ferrihydrite.

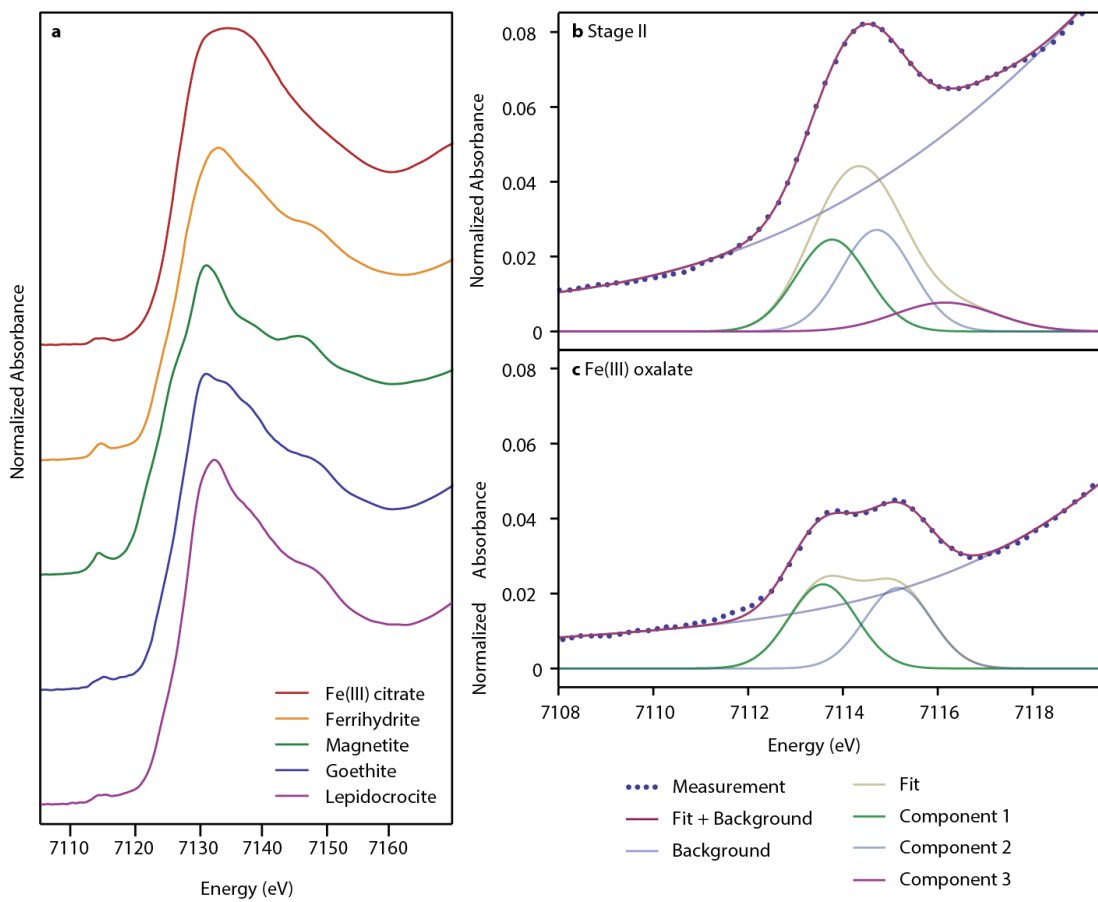


Figure 5.3: X-ray absorption spectroscopy

a, XANES spectra of reference standards: Fe(III) citrate, ferrihydrite, magnetite, goethite and lepidocrocite. **b – c**, Pre-edge fit for stage II and Fe(III) oxalate. Measurement shown as a dotted line overlaid with the fit plus the polynomial background in purple. Pre-edge fit in yellow and individual pre-edge components, 1, 2 & 3, in green, blue and purple, respectively. Fitted parameters are given in Table 5.1.

The pre-edge feature corresponds to a $1s \rightarrow 3d$ transition for which energy, splitting, and intensity distribution are sensitive to spin state, oxidation state, geometry, and bridging ligation^{141,142}. The marked increase in from stage I to stage IV is consistent with an increasingly distorted octahedral coordination environment of high-spin Fe(III) in ferrihydrite in stage II and the presence of tetrahedral Fe(II) in magnetite in stage IV¹⁴². Fitting the pre-edge region revealed that in stage I the crystal field splitting, $10Dq$ (1.4 eV),

is larger than what is observed in ferrihydrite and stage II (0.95 eV), and is much closer to values near 1.5 eV typically observed for octahedral, high-spin organic Fe(III) complexes such as iron citrate and oxalate (Figure 5.2 and Table 5.1)¹⁴¹. The shift of the peak intensity ratio of the individual components toward lower values from stage I to stage II is consistent with the decreasing covalency of the Fe-O bonds¹⁴¹. Finally, a third component (at ~1716 eV) arising from multiple scattering from distant Fe atoms is present in ferrihydrite and stage II but absent in stage I, indicating that there is little or no sharing of ligands by iron octahedra. This is strong evidence that iron is present in low nuclearity complexes, not in iron oxy-hydroxide minerals with extensive bridging ligation (high nuclearity)¹⁴¹.

Table 5.1: Pre-edge fitting results

Overall intensity, centroid, individual peak positions, crystal field splitting ($10 Dq$), individual peak amplitudes, and peak 2:1 ratio tabulated for reference compounds, chiton radula stage 1 and 2 samples and *in vitro* model samples.

Sample	Intensity	Centroid	Position (eV)			$10Dq$	Amplitude			Peak Ratio
			Peak 1	Peak 2	Peak 3		Peak 1	Peak 2	Peak 3	
Reference Samples										
Fh	0.043	7114.27	7113.78	7114.73	7116.37	0.95	0.025	0.027	0.0068	1.08
Fe(III) Cit-rate	0.021	7114.22	7113.51	7115.04	-	1.53	0.019	0.017	-	0.89
Chiton Radula Samples										
Stage I	0.032	7114.31	7113.64	7115.07	-	1.43	0.025	0.022	-	0.88
Stage II	0.044	7114.27	7113.77	7114.72	7116.96	0.95	0.025	0.027	0.0077	1.08
<i>In vitro model</i>										
5 mM citrate	0.032	7114.41	7113.83	7115.06	7116.1	1.23	0.024	0.021	0.0031	0.88
1 mM citrate	0.040	7114.22	7113.67	7114.72	7116.21	1.05	0.024	0.027	0.0064	1.13
1 mg/mL pAsp	0.034	7114.35	7113.74	7114.93	7116.53	1.19	0.023	0.024	0.0044	1.04
0.2 mg/mL pAsp	0.036	7114.28	7113.65	7114.8	7116.53	1.15	0.023	0.027	0.0060	1.17

This assessment was confirmed by an analysis of the extended X-ray absorption fine structure (EXAFS) of teeth in different stages. A pronounced beat pattern at 5 \AA^{-1} and 7.5 \AA^{-1} emerged in k -space spectra of

stage II and increased in intensity at stage IV (Figure 5.4a and Figure 5.5), but was not observed at stage I. These spectral changes mirror the emergence of the same beat going from Fe(III) citrate to ferrihydrite and then on to magnetite. Given that the higher frequency components originate from second shell, next-nearest neighbor Fe-Fe scattering, the absence of this peak in spectra of stage I and Fe(III) citrate is indicative of the iron being present in low nuclearity complexes¹⁴³. This trend is also apparent in real space spectra with a strong increase in the second shell (Fe-Fe) scattering amplitude with increasing maturity of teeth. Furthermore, the scattering amplitude from oxygen in the first shell decreases substantially in the same series, again closely mirroring the reference compounds (Figure 5.4b). The strong first shell scattering in stage I is a result of a less distorted octahedral coordination geometry, consistent once more with the presence of ligands that maintain iron in a complex¹⁴³. A quantitative analysis of the local environment of iron by fitting spectra with theoretical scattering paths was consistent with qualitative results (see Figure 5.5 and Table 5.2).

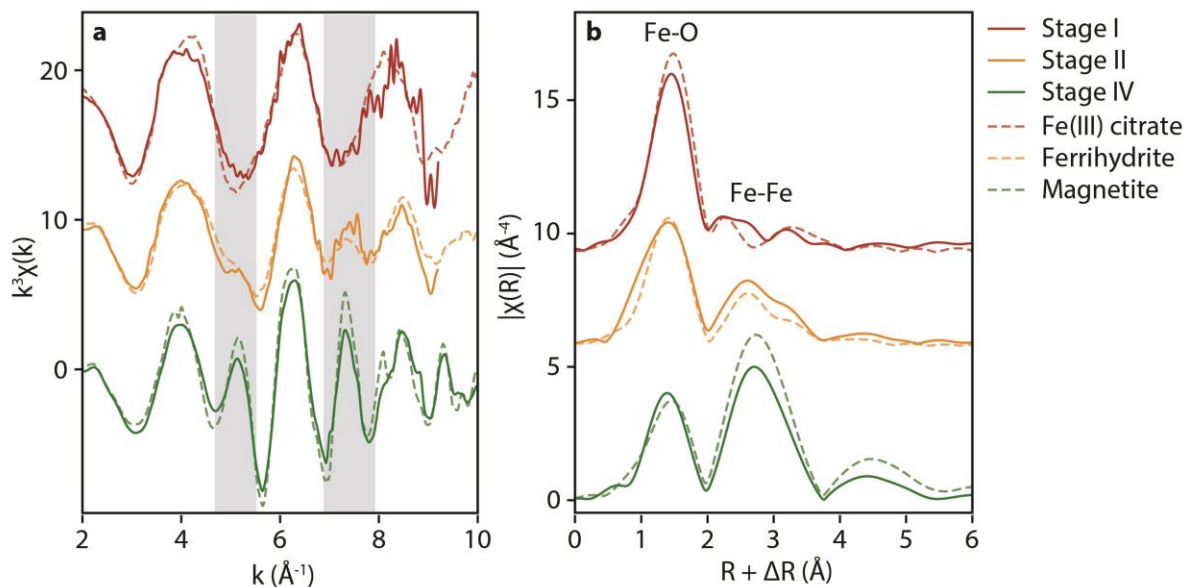


Figure 5.4: EXAFS spectra of chiton teeth and reference compounds

Sections corresponding to stages I, II, and IV were pooled from 10 animals. k^3 -weighted (a) k -space (b) real space spectra, each overlaid with the corresponding synthetic reference compound, i.e. Fe(III) citrate for stage I, ferrihydrite for stage II, and magnetite for stage IV. Spectra are offset for clarity. A consistent Fourier transform window (2.5 - 8.5\AA^{-1}) was used to facilitate comparison between spectra. The higher-frequency spectral components originating from second shell Fe-Fe scattering at 5\AA^{-1} and 7.5\AA^{-1} are highlighted in gray. Radius (R) is uncorrected for phase shift (ΔR).

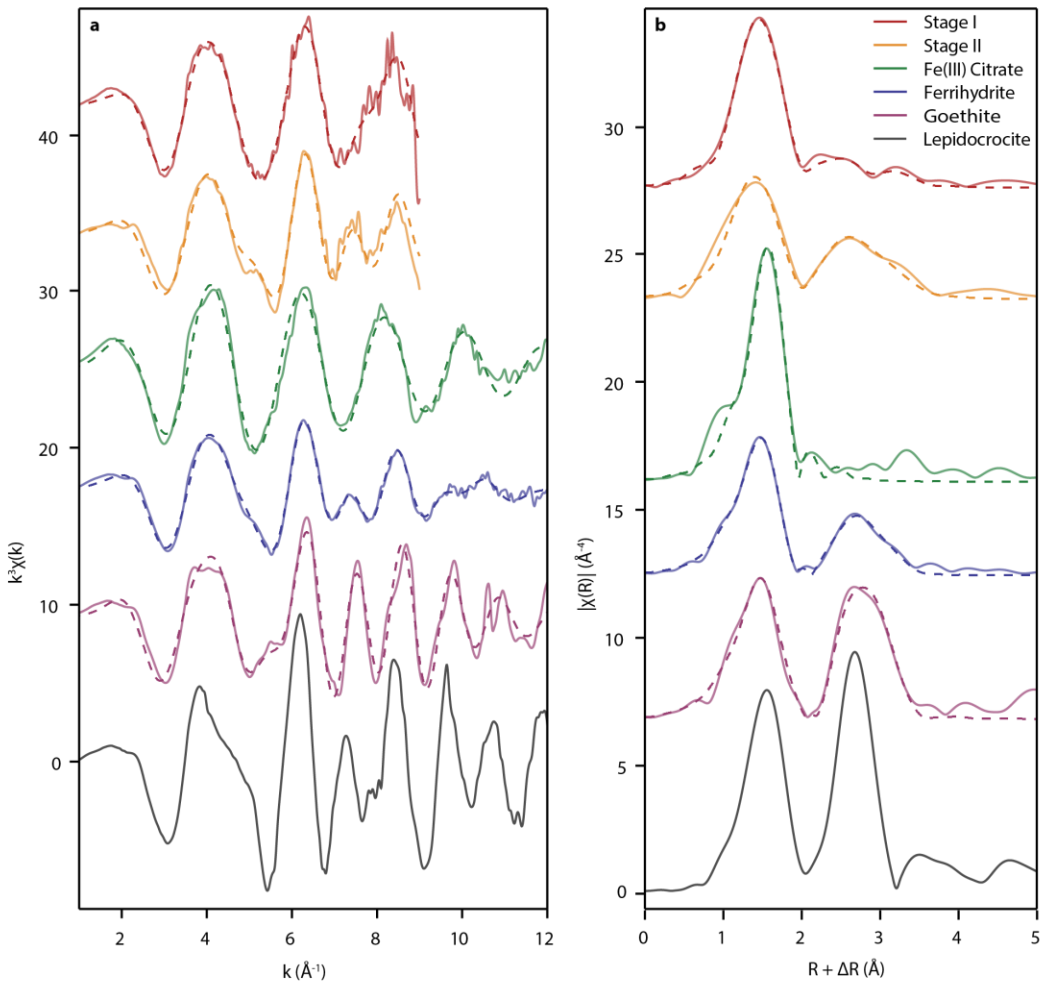


Figure 5.5: Shell-by-shell EXAFS fits based on theoretical scattering paths and reference spectra

a, k -space spectra. b, Real-space EXAFS spectra, uncorrected for phase shift. Measurements shown as solid lines, fits as dashed lines. Fitted parameters are given in Table 5.2. Lepidocrocite has a different local configuration around the iron atoms consisting of only face sharing FeO_6 octahedra and was not fit.

Table 5.2: EXAFS shell-by-shell fitting results

Radius, coordination number and σ^2 given for each fitted path. ΔE was fixed for individual paths but allowed to vary between samples. R -factors tabulated for Fe-O path, Fe-Fe paths and for all paths combined. Amplitude reduction factor (0.88) was fixed based on the fit to goethite. Bolded values are held constant in the fit and asterisks indicates values fixed based on crystal structure. Uncertainty in the last digits are given in parenthesis.

Sample	Path	R (Å)	CN	σ^2	ΔE (eV)	R-factor (%)
Reference Samples						
Goethite	Fe-O	1.991(6)	6	0.0035(4)	-5.5	0.4
	Fe-Fe ₁	3.01(1)	2	0.006(1)		0.8
	Fe-Fe ₂	3.21(4)	2	0.006(4)		
	Fe-Fe ₃	3.39(1)	4	0.004(1)		
	Fe-O-O _{MS}	3.4019	24	0.0035		
	All Paths					1.6
Fh	Fe-O	1.964(6)	4.9(4)	0.0108(8)	-5	0.05
	Fe-Fe ₁	3.06(1)	3.2(6)	0.017		0.3
	Fe-Fe ₂	3.43(1)	2.4(5)	0.013		
	Fe-O-O _{MS}	3.4	19.6	0.0108		
	All Paths					0.2
Ferric Citrate	Fe-O	2.012(9)	5.3(7)	0.006(1)	-0.9	0.5
Chiton Radula Samples						
Stage I	Fe-O	1.98(2)	5(1)	0.006(3)	-5	0.06
	Fe-Fe ₁	3.06(4)	3(2)	0.017		3.5
	Fe-Fe ₂	3.35(4)	2(1)	0.013		
	Fe-O-O _{MS}	3.45	19	0.006		
	All Paths					0.4
Stage II	Fe-O	1.96(3)	6(2)	0.012(6)	-6.5	0.5
	Fe-Fe ₁	3.01(4)	3(1)	0.017		1.3
	Fe-Fe ₂	3.42(3)	3(1)	0.013		
	Fe-O-O _{MS}	3.46	22	0.012		
	All Paths					0.4
In vitro Model Samples						
5mM citrate	Fe-O	1.988(5)	5.4(4)	0.0082(6)	-3.4	0.4
	Fe-Fe ₁	3.13(2)	2.6(7)	0.017		6.4
	Fe-Fe ₂	3.42(1)	2.4(6)	0.013		
	Fe-O-O _{MS}	3.407	21.6	0.0082		
	All Paths					0.95
1mM citrate	Fe-O	1.968(4)	5.3(2)	0.0110(5)	-5	0.08
	Fe-Fe ₁	3.06(1)	2.0(4)	0.017		1.9
	Fe-Fe ₂	3.42304	1.5(3)	0.013		
	Fe-O-O _{MS}	3.440	21.2	0.011		
	All Paths					0.23
1 mg/mL pAsp	Fe-O	1.99(1)	5.9(8)	0.012(2)	-3	0.8
	Fe-Fe ₁	3.07(2)	2.0(6)	0.017		5.6
	Fe-Fe ₂	3.42(2)	1.7(5)	0.013		
	Fe-O-O _{MS}	3.40	23.6	0.012		
	All Paths					1.4
0.2 mg/mL pAsp	Fe-O	1.974(4)	5.5(3)	0.0110(5)	-5.3	0.09
	Fe-Fe ₁	3.06(1)	2.5(4)	0.017		1.9
	Fe-Fe ₂	3.43(1)	2.1(3)	0.013		
	Fe-O-O _{MS}	3.429	22	0.011		
	All Paths					0.34

As a complementary technique to XAS, we chose electron paramagnetic resonance (EPR) spectroscopy for its sensitivity to the oxidation state and local environment of paramagnetic nuclei such as Fe(III)¹⁴⁴. EPR spectra of stage I teeth exhibit a narrow resonance at $g \approx 4.2$, consistent with a mononuclear high-spin Fe(III) iron complex (Figure 5.6). Note that at a peak-to-peak line width of 56 G, the resonance is ~2.2 times broader than the corresponding resonance in the spectrum of [Fe(EDTA)]⁻ (Figure 5.7). This may indicate that Fe(III) in stage I is present in complexes with a range of slightly different local chemical environments, consistent with iron bound by one or more matrix macromolecules in a variety of geometries. However, we cannot exclude that low-nuclearity complexes are also present. This resonance is significantly weaker in stage II, where a broad resonance at a lower g -factor dominates spectra, consistent with the presence of mineralized iron oxyhydroxides, including ferrihydrite (Figure 5.7). In stage IV, the only feature present is an extremely broad resonance typical for magnetite that has previously been observed for mature teeth of the chiton *Cryptochiton stelleri*¹⁴⁵. It is possible that the iron complexes are still present, but that the large amount of mineralized iron masks their presence.

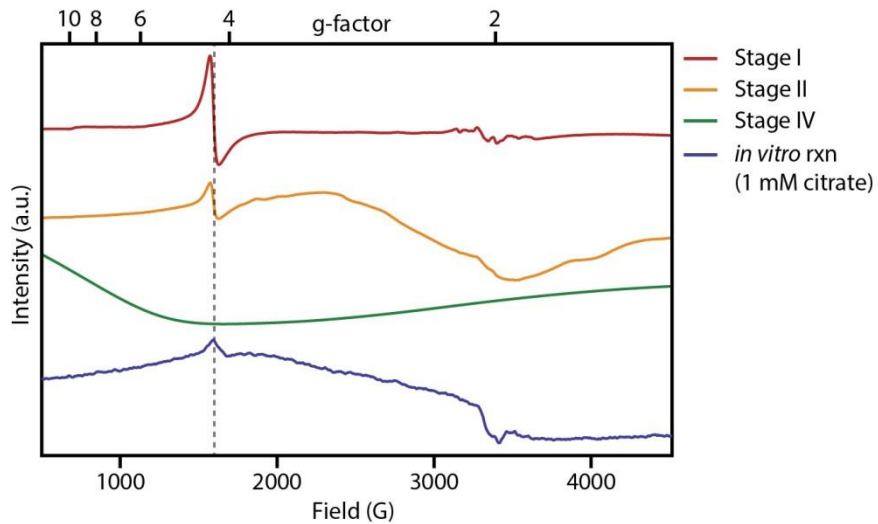


Figure 5.6: X-band EPR spectra of chiton teeth and *in vitro* reaction products

A narrow resonance at $g \approx 4.2$ (dashed line), corresponding to high-spin mononuclear Fe(III), was observed in stage I and II chiton teeth. Broad resonances in stage II and IV are consistent with mineralized iron oxides/oxyhydroxides. Note the similarity of stage II spectra to spectra of ferrihydrite precipitated *in vitro* in the presence of citrate as a model ligand. Biological samples were pooled from radulae extracted from two specimens. In vitro produce conditions: 5 mM Fe^{2+} + 1 mM citrate.

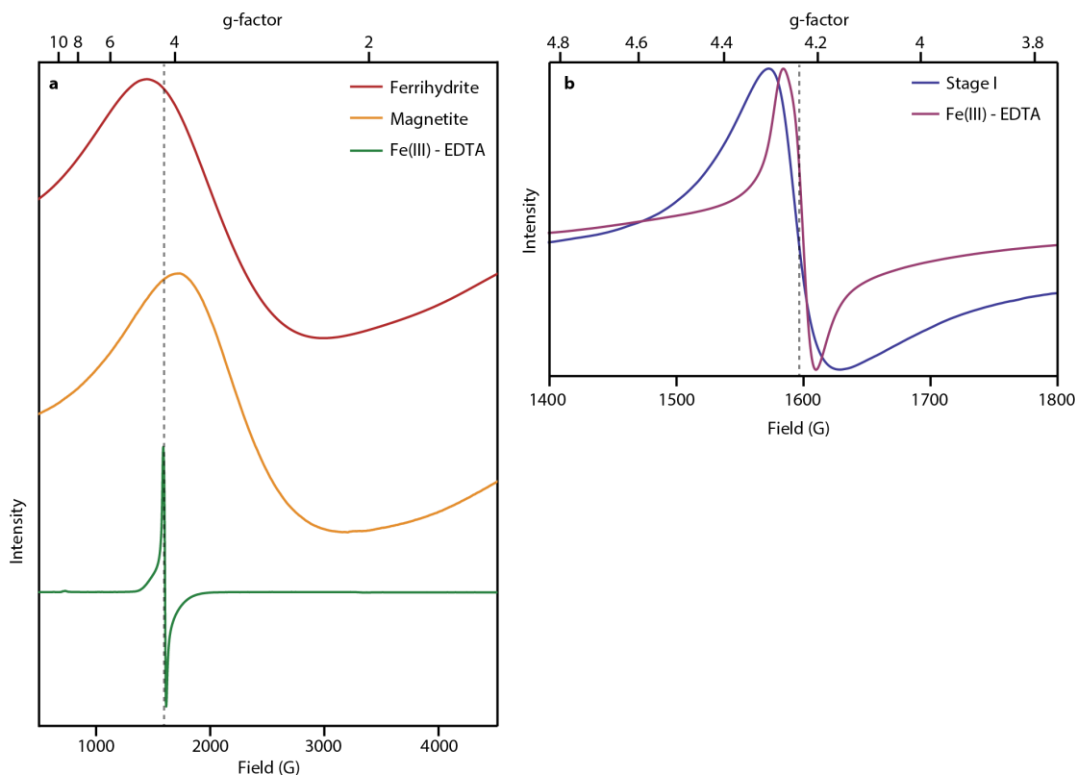


Figure 5.7: Electron paramagnetic resonance spectra

a, EPR spectra of reference standards: ferrihydrite, magnetite, and Fe(III)-EDTA complex. Spectra are offset for clarity. b, Magnified EPR spectra of stage I chiton radula overlaid with the EPR spectra of the Fe(III)-EDTA complex, illustrating the broader resonance in stage I compared to Fe(III)-EDTA. A $g \approx 4.2$ value corresponding to high-spin mononuclear Fe(III) is indicated with dashed lines.

5.2.2 *In vitro: Model Compounds*

Having confirmed that in stage I teeth, Fe(III) occurs predominantly in low-nucularity complexes, we probed the possible functional role of such complexes *in vitro* (Figure 5.8 and Table 5.3). When an anaerobically prepared solution of FeCl_2 in HEPES buffer was oxidized in air, orange, crystalline lepidocrocite precipitated. The buffer, itself a sulfonic acid, a primary alcohol, and a tertiary amine, is thus inert. Lepidocrocite was the predominant product also (by linear combination fitting of EXAFS spectra) when bovine serum albumin (BSA), a moderately acidic protein with substantial metal binding capacity ($\text{p}I =$

5.7, 98 Glu/Asp residues), was present, and in hydrogels formed from reconstituted chitin. However, when either the chelator citric acid, or poly(aspartic acid), a model compound for highly acidic proteins, were present as ligands, brown colloidal dispersions were formed instead. X-ray diffraction patterns of these colloids are identical to those of “2-line” ferrihydrite (Figure 5.8a). Fe *K*-edge EXAFS spectra reveal that the local environment of iron in the colloids closely resembles that of synthetic ferrihydrite and of iron in stage II chiton teeth (Figure 5.8b-c cf. Figure 5.4a-b). In EPR spectra of colloids formed in the presence of citric acid, a narrow resonance at $g \approx 4.2$ reveals that low-nuclearity, high-spin Fe(III) complexes are present in addition to ferrihydrite (Figure 5.6); the resulting spectra are quite similar to those of stage II chiton teeth.

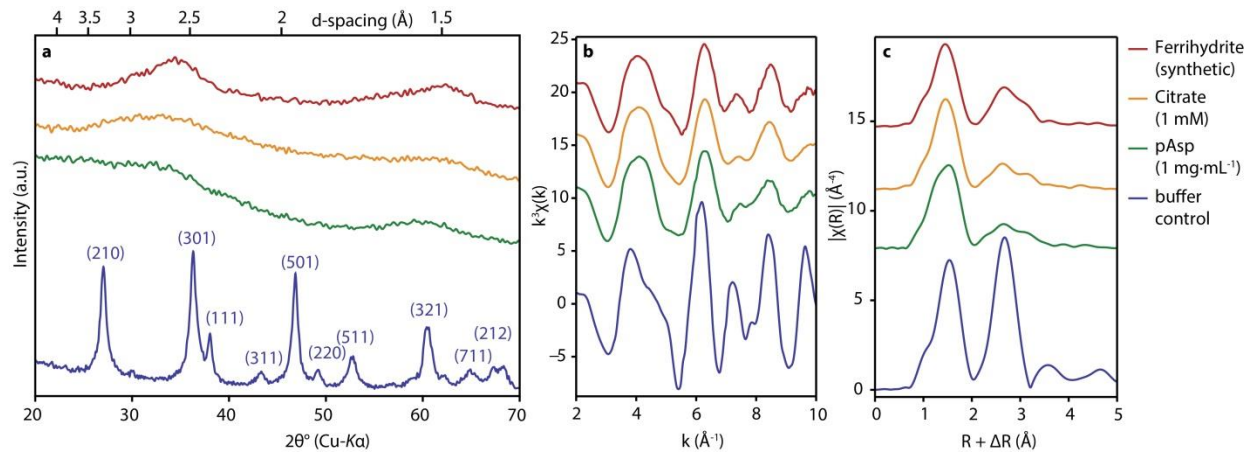


Figure 5.8: Characterization of *in vitro* reaction products

Representative powder X-ray diffraction (XRD) patterns (a), *k*-space EXAFS (b), real space EXAFS (c). In vitro oxidation of Fe(II) under physiological conditions (HEPES buffer, pH 7.2) in the presence of citrate or pAsp gives ferrihydrite. Lepidocrocite is formed in the absence of ligands.

Table 5.3: In vitro reaction conditions and relative yield of different polymorphs

Yields were determined by linear combination fitting to k^3 weighted EXAFS spectra (2-12 Å⁻¹). Deviations from a component sum of 100 % were typically < 5%. Quality of fit (R-factor) < 4% for all fits. Calculated fit uncertainties < 5 %. ^{a)} Note that values of 5% and smaller may not be significant. ^{b)} Ligand concentration calculated based on 98 Glu/Asp residues per BSA, ^{c)} equivalent Asp monomer concentration in pAsp (2-11 kg mol⁻¹) solution.

Ligand	Concentration (mM)			Relative amount (%)		
	Ligand	HEPES	Fe ²⁺	Lepidocrocite	Ferrihydrite	Fe(III) complex
Buffer control	0	100	5	98	0	2 ^a
BSA (1 mg·mL⁻¹)	1.5 ^b	100	5	84	16	1 ^a
Chitin gel (1 mg·mL⁻¹)	-	5	100	83	12	5 ^a
Citrate	1	100	5	0	82	18
Citrate	5	100	5	3 ^a	52	46
pAsp (0.2 mg·mL⁻¹)	1.8 ^c	100	5	20	71	9
pAsp (1 mg·mL⁻¹)	8.8 ^c	100	5	0	69	31

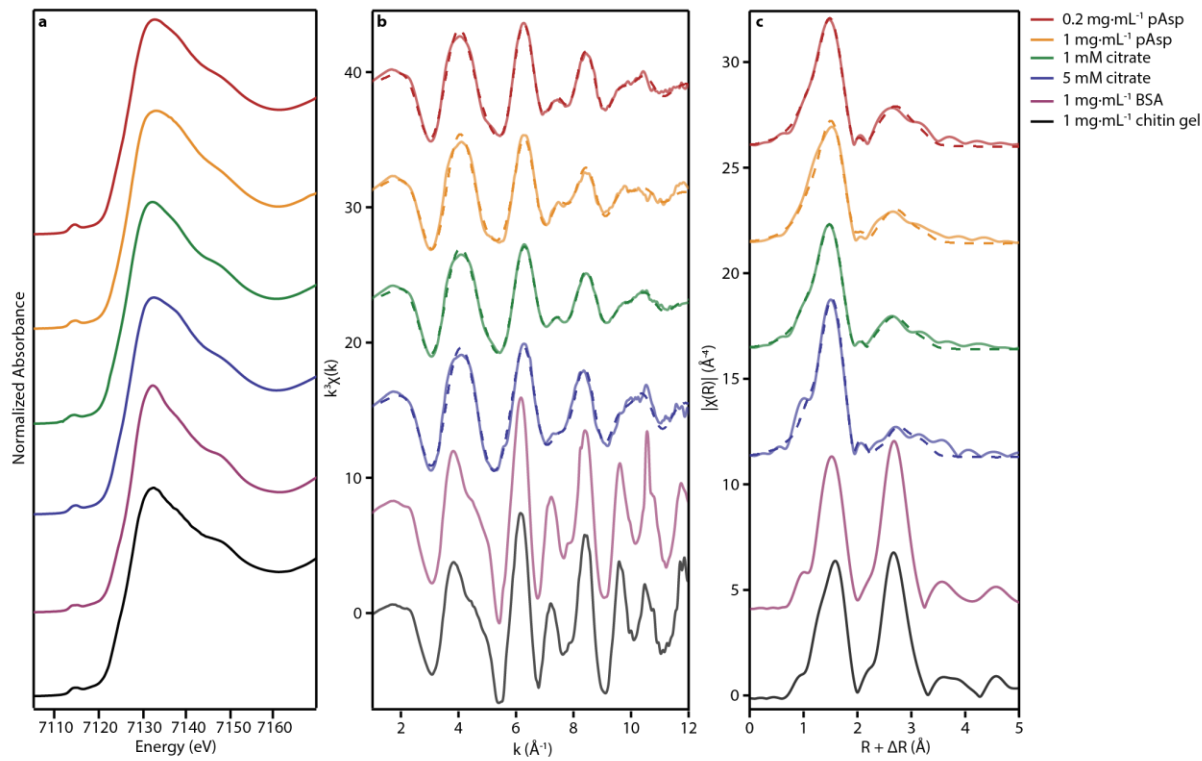


Figure 5.9: XANES and EXAFS spectra of *in vitro* reaction products

a, XANES spectra. b, k-space EXAFS spectra. c, Real-space EXAFS spectra, uncorrected for phase shift. Measurements shown as solid lines, fits as dashed lines. Spectra are offset for clarity. Fitted parameters are given in Table 5.2. Samples matching crystalline lepidocrocite ($1 \text{ mg}\cdot\text{mL}^{-1}$ BSA and $1 \text{ mg}\cdot\text{mL}^{-1}$ chitin gel) were not fit.

5.3 CONCLUSION

These results confirm suppression of lepidocrocite formation in the presence of certain organic acids¹⁴⁶, and clearly indicate that the presence of acidic macromolecules in the chiton scaffold is necessary and sufficient for the selective precipitation of ferrihydrite. The formation of low-nuclearity complexes of iron with carboxylate ligands is most likely an important aspect of this mechanism. Chitin fibers decorated with Fe(III) complexes could heterogeneously nucleate ferrihydrite, and at the same time limit growth to small nanoparticles¹⁴⁷. This is consistent with the formation of a stable colloid of ferrihydrite in the pres-

ence of pAsp. Preventing uncontrolled aggregation and thus maintaining very high surface areas may be important to ensure the subsequent formation of monolithic magnetite in the chiton tooth.

Patterning of the chitin scaffold with acidic macromolecules might be a straightforward way for chitons to achieve the remarkable degree of spatial control over the mineral polymorphs evident within their teeth, for instance the deposition of a thin layer of lepidocrocite below the magnetite cusp in some species¹. Graded interfaces might be constructed in a similar fashion. Given that the organism also controls the binding of sodium and magnesium to the chitin fibers¹⁰, it appears that fine-tuned control over counter ion binding is an important aspect of the mechanisms by which the chiton controls mineralization.

Ferrihydrite encapsulated in ferritins and similar proteins is a universal transport and storage form of iron in biology¹³⁶ and has further been implicated as a precursor in the formation of magnetosomes⁴⁸. Interestingly, it has been suggested that Fe(III) bound to the nucleation sites of ferritin and an acidic protein in magnetosomes is integral to ferrihydrite formation within these nano-sized containers^{48,136,148}. Compared to these systems, where the geometry and location of complexes is tightly controlled, those formed in the organic matrix of the chiton tooth appear to be structurally less uniform. This simpler, more flexible chemistry may be a consequence of the much larger amount of ferrihydrite that the chiton needs to precipitate in the tooth, or possibly be due to the dual role of acidic macromolecules that need to create a mechanically strong interface between chitin fibers and magnetite mineral in the mature tooth. Given that chiton teeth are the hardest and most wear resistant biominerals, understanding this material has profound implications for biologically inspired material syntheses.

5.4 MATERIALS AND METHODS

5.4.1 Consumables

Unless otherwise specified, the following chemicals were used without further purification: 2-[4-(2-hydroxyethyl)piperazin-1-yl]ethanesulfonic acid (HEPES), potassium hydroxide (KOH), sodium hydrox-

ide (NaOH), ethanol, chlorine bleach (NaOCl) (VWR, Radnor, PA); Glycerol, Ethylenediaminetetraacetic acid (EDTA), tribasic sodium citrate ($\text{Na}_3\text{C}_6\text{H}_5\text{O}_7$), Fe(III) nitrate nonahydrate ($\text{Fe}(\text{NO}_3)_3 \cdot 9\text{H}_2\text{O}$), ferrous chloride tetrahydrate ($\text{FeCl}_2 \cdot 4\text{H}_2\text{O}$), microcrystalline cellulose, 2000-11000 mol. wt. poly(aspartic acid) (Sigma-Aldrich, St. Louis, MO); hydrochloric acid (Mallinckrodt Chemicals); magnetite (Fe_3O_4), Fe(III) citrate ($\text{FeC}_6\text{H}_5\text{O}_7$), Fe(III) oxalate ($\text{Fe}_2(\text{C}_2\text{O}_4)_3$) (Alfa Aesar, Ward Hill, MA); glutaraldehyde (Electron Microscopy Sciences, Hatfield, PA.), instant all-purpose brush-on cyanoacrylate adhesive (KrazyGlue, Columbus, OH); hexafluoroisopropanol (HFIP) (Oakwood Products Inc. West Columbia, SC.; chitin (TCI America, Portland, OR) Unless otherwise specified, all solutions were prepared with ultra-pure water ($\rho = 18.2 \text{ M}\Omega \cdot \text{cm}$) produced by a Barnstead Nanopure NanoDiamond UF+UV purification unit (Thermo Scientific, Hanover Park, IL). Artificial seawater was prepared using Instant Ocean sea salt (Spectrum Brands, Blacksburg, VA) to a final salinity of $35 \text{ g} \cdot \text{L}^{-1}$.

Chitin was purified following Gordon and Joester¹⁰. Briefly, the crude chitin was washed with water, stirred with HCl (1.5M, 6h, 25°C) and washed with water. The acid-treated chitin was further stirred with NaOH (1.5M, 3h, 25°C) and washed with water. The chitin was then treated with NaOCl (10%, 5min, 25°C) and washed with water. The purified chitin suspension was frozen in liquid nitrogen and lyophilized.

5.4.2 Reference materials

Synthetic lepidocrocite was kindly provided by Dr. Colleen Hansel (Woods Hole Oceanographic Institution, Woods Hole, MA). “2-line” ferrihydrite was synthesized based on a modification of the protocol given by Cornell and Schwertman¹³¹. An aqueous solution of $\text{Fe}(\text{NO}_3)_3$ (100 mL, 0.2 M) was rapidly titrated to pH 7 with an aqueous solution of KOH (1 M). The resulting red-brown precipitate was washed extensively with water by vacuum filtration, frozen in liquid nitrogen, and lyophilized. The lyophilized powder was ground with an agate mortar and pestle. Goethite was synthesized based on the protocol given by Cornell and Schwertman¹³¹. Briefly, aqueous KOH (5M, 68mL) was rapidly added to a stirred solu-

tion of $\text{Fe}(\text{NO}_3)_3$ (1M, 38mL) in a polyethylene container, the mixture was diluted to 750 mL with water, sealed, and heated to 70 °C for 5 days. The resulting brown precipitate was washed extensively with water by vacuum filtration and dried under vacuum. Dried powder was ground in an agate mortar and pestle. Phase purity of all reference materials was verified by powder X-ray diffraction.

5.4.3 *Chiton radula*

Black Katy chiton specimens (*Katharina tunicata*, Wood 1815, Mollusca: Polyplacophora) were acquired from the UC Davis Bodega Marine Laboratory (Bodega Bay, CA) and KLM Bioscientific (San Diego, CA). Radulae were extracted and washed with a pressurized jet of water, as per Shaw et al., to remove adhering cellular material and free iron¹³⁹.

Radulae for SEM and X-ray microcomputed tomography were fixed in 3 vol % glutaraldehyde in artificial sea water overnight at 4 °C. Samples were washed once each in artificial sea water and water and then dehydrated in a graded ethanol series in water (50, 70, 90 and 100 vol %). Radulae for XAS and EPR were washed and dissected into four stages based on color as per the description given by Lowenstam¹. Stage I was colorless and contained 8-9 rows of teeth, stage II was reddish-brown and contained 3 rows, stage III was brown-black and contained 30 rows, stage IV was black and contained the remaining ~20 rows. The dissected segments were air-dried and ground in an agate mortar and pestle. A rare earth magnet was used to separate the magnetite from dried powdered stage IV radula from the nonmagnetic core phosphate mineral. Radula segments from multiple animals were pooled for XAS (10 animals) and EPR (2 animals) measurements.

5.4.4 *Bulk precipitation*

Buffer containing 100 mM HEPES adjusted to pH 7.2 with NaOH was prepared and stored under nitrogen in an anaerobic glove box (MBraun, Garching, Germany) maintained below 0.1 ppm O₂. 5 mM FeCl₂ and organic additives (0.1 or 1 mg/mL poly(aspartic acid) or 1 or 5 mM sodium citrate) were added to the

buffer before use. The solution was then removed from the anaerobic chamber and air was bubbled through the solution overnight. The resulting precipitate was subsequently dialyzed for 3 days in repeated changes of water, frozen in liquid nitrogen and lyophilized. The lyophilized powders were ground with an agate mortar and pestle.

5.4.5 *Hydrogel precipitation*

Reconstituted chitin gels were prepared dissolving the purified lyophilized chitin at 1 mg·mL⁻¹ in HFIP, then droplets (3 µL) of the solution were individually pipetted into ethanol where they gelled. Gels were exchanged with buffer (5 mM HEPES, pH 7.2, 2h on a rotator) and then loaded with Fe(II) by incubation overnight in 100 mM FeCl₂ (in buffer, 5 mM HEPES, pH 7.2) in an anaerobic chamber. Gels were quickly rinsed with iron-free buffer and then placed into a fresh solution of buffer (5 mM HEPES, pH 7.2). Gels in buffer solution were then removed from the anaerobic chamber and air was bubbled through the solution overnight. The oxidized gels were washed with water and dried in air. Dried gels were ground with an agate mortar and pestle.

5.4.6 *Powder X-ray diffraction*

Samples were suspended in acetone and dispersed on the surface of an off-axis cut quartz single crystal “zero-background” plate (MTI Technologies, Richmond, CA). Remaining acetone was allowed to evaporate. Samples were analyzed with a Scintag diffractometer with a Cu X-ray source operating at 40 kV and 20 mA. Diffracted intensity was recorded between $2\theta = 5^\circ$ - 90° with a step size of 0.05° and a dwell time of 2 seconds per step. An energy dispersive X-ray detector was used to count only diffracted Cu-K α X-rays and exclude Fe X-ray fluorescence.

5.4.7 *Scanning electron microscopy (SEM) and energy dispersive X-ray spectroscopy (EDS)*

For SEM, fixed and ethanol dehydrated radulae were transferred into propylene oxide, then embedded in Araldite resin (Huntsman Advanced Materials, Everberg, Belgium) and polymerized overnight in air at

60 °C. Embedded samples were oriented and re-embedded in Epo-tek 301 epoxy resin (Epoxy Technology, Billerica, MA). Re-embedded samples were ground using progressively finer grits of Buehler Carbi-Met SiC grinding paper (400, 600, 800 and 1,200 grit) and polished using Buehler MetaDi aqueous diamond polishing suspensions (3 and 1 µm) and Buehler MasterPrep aqueous alumina suspension (0.05 µm) with Buehler Trident and Chemomet polishing cloths, respectively (Lake Bluff, IL).

Polished cross-sections were secured to an aluminum SEM stub with cyanoacrylate adhesive, coated with carbon by ion-beam sputtering with a South Bay Technology IBS/e (San Clemente, CA), then grounded to the stub with conductive silver paste (Ted Pella). SEM-EDS was performed with an FEI Helios Nanolab (Hillsboro, OR) operating at 10-20 keV with 10-20 nA probe current. The SEM was equipped with an energy dispersive silicon drift detector (Bruker, Berlin, Germany) with an ultrathin window (Moxtek AP3.3, Orem, UT). Tooth cross sections were individually scanned for 5-10 minutes each. Qualitative iron concentration maps were produced based on total detected Fe-K α fluorescence X-ray counts per pixel.

5.4.8 Fe-K edge X-ray absorption spectroscopy (XAS)

Powdered samples that adhered well to Kapton tape (3M 7419, St. Paul MN), were spread uniformly and multiple layers of tape were stacked to optimize X-ray absorption. Poorly adhering powders were diluted with microcrystalline cellulose (Sigma-Aldrich 310697) and pressed into a pellet with a diameter of 13 mm and a thickness of ~200 µm. EXAFS measurements were conducted at beam line 5-BM-D part of the Dupont-Northwestern-Dow collaborative access team at the Advanced Photon Source at Argonne National Laboratory. The energy of the Si(111) two-crystal monochromator was calibrated by assigning an energy of 7112 eV to the first zero-crossing of the second derivative (inflection point) of the absorption edge of an iron foil measured in transmission. The monochromator was detuned to eliminate harmonics. Absorption spectra of all samples except stage I and stage II were recorded at the Fe-K edge in transmission by simultaneously measuring the incident and transmitted flux with two ion chambers (FMB-Oxford

IC Spec). An iron foil was placed behind the second ion chamber before the third ion chamber and measured simultaneously with each sample for energy calibration. Due to reduced concentration and sample volume absorption spectra from stage I and stage II, samples were recorded by measuring the total Fe-K α fluorescence yield with two Vortex ME-4 four element silicon drift detectors (Hitachi High-Technologies Science America, Northridge, CA) placed close to the sample. Background was collected from -150 eV to -20 eV (relative to the edge) with steps of 5 eV, XANES was collected from -20 eV to +35 eV ($k = 3 \text{ \AA}^{-1}$) with steps of 0.1 eV. EXAFS data were collected from +35 eV to +750 eV ($k = 3 \text{ \AA}^{-1} - 14 \text{ \AA}^{-1}$) with a $k^{1.5}$ weighted count time and a k -increment of $.05 \text{ \AA}^{-1}$. A base count time of 1 second and a final count time of 10 seconds was used. Between 2 and 16 scans were collected for each sample and averaged. No beam-induced changes were observed when comparing sequential spectra.

5.4.9 Pre-edge analysis

A 4th order polynomial was fit to the main edge before and after the pre-edge to estimate the pre-edge baseline. Gaussian components were fit to each pre-edge spectrum using the nonlinear optimization routine NMinimize implemented in Mathematica (Wolfram Research, Champaign, IL). The width of the two main pre-edge Gaussians were set to be equal for each fit but allowed to vary between fits. The third feature which does not arise from 1s→3d transitions was fit with an independent width¹⁴².

5.4.10 EXAFS

The absorption data were normalized, background subtracted using AUTOBK, and converted to k-space using Athena¹⁴⁹. A constant edge energy (E_0) of 7128 eV was used. $\chi(k)$ data were weighted by k^3 and Fourier transformed over the k range $2.5-12 \text{ \AA}^{-1}$ applying a Hanning window with a sill width of 3 \AA^{-1} . Due to reduced signal to noise ratios in the spectra from the stage I and II chiton radula, a reduced k range of $2.5-8.5 \text{ \AA}^{-1}$ was used. Theoretical photoelectron scattering amplitudes and phase shifts based on the crystal structure of goethite¹⁵⁰ were calculated using FEFF6¹⁵¹. The amplitude reduction factor ($S_0^2 = 0.88$) was determined based on a fit to the reference goethite spectra with coordination numbers constrained

based on the crystal structure¹⁵⁰. Shell-by-shell fitting of the EXAFS data was performed in Fourier filtered k -space (q) using Artemis¹⁴⁹ following a protocol similar to that of Mikutta¹⁵². For each sample, first, the Fe-O path (0.9-2 Å) was fit, including an energy shift parameter (E_0) which was maintained constant for the Fe-Fe and Fe-O-O scattering paths. Then two Fe-Fe scattering scatterings paths (2.2-3.4 Å) were fit. Constant σ^2 values (0.017 Å² and 0.013 Å², respectively) were used based on a fit to reference “2-line” ferrihydrite. A triangular Fe-O-O multiple scattering path within the FeO₆ was included with radius, coordination number, and σ^2 constrained based on first Fe-O path fit, specifically: $R_{\text{Fe}-\text{O}-\text{O}} = R_{\text{Fe}-\text{O}}(1 + \sqrt{2}/2)$; $CN_{\text{Fe}-\text{O}-\text{O}} = 4CN_{\text{Fe}-\text{O}}$; $\sigma^2_{\text{Fe}-\text{O}-\text{O}} = \sigma^2_{\text{Fe}-\text{O}}$. Only the first Fe-O path was fit for Fe(III) citrate and Fe(III) oxalate complexes.

5.4.11 Linear combination fitting

Least squares linear combination fitting¹⁵³ of k^3 -weighted EXAFS spectra over a k -range of 2-12 Å⁻¹ was performed with Athena¹⁴⁹. Fe(III) citrate was used as a model compound for organically coordinated Fe(III). All fitted fractions were recalculated to 100%. Quality of fit determined with the R-factor, defined as $\frac{\sum_i (data_i - fit_i)^2}{\sum_i data_i^2}$.

5.4.12 Electron paramagnetic resonance (EPR)

Liquid samples were prepared using standard anaerobic Schlenk techniques under an argon atmosphere. In a typical preparation for the *in vitro* precipitate, a solution of 8:1 deionized water:glycerol was added to a 250 mL Schlenk flask and sparged with argon for at least 30 min. The *in vitro*-prepared colloidal dispersion (5 mM total Fe) was added to the solution in a 1:9 ratio, yielding a 0.5 mM final Fe concentration.

An Fe-EDTA standard solution (0.5 mM final concentration) was prepared as per Bou-Abdallah and Chasteen¹⁴⁴. Briefly, a solution of Fe(NO₃)₃ in dilute HCl (pH≈2.00, 14.4 µL, 17.8 mM) was added to EDTA in 3:1 (v/v) water:glycerol (pH ≈ 2.00, 500 µL, 1.80 mM). This solution was sparged with argon for 20 minutes prior to measurements.

For liquid samples, EPR tubes were evacuated and flushed with argon prior to sample addition. Samples were transferred via syringe through the EPR cap under an argon atmosphere. After addition, the cap was sealed with parafilm (Pechiney Plastic Packaging Company, Chicago, IL) to maintain an inert atmosphere. Solid samples were placed in the EPR tube prior to being flushed with argon and sealed.

X-band spectra were obtained on a Bruker EMX spectrometer. All data presented were collected at 15 K with a sweep width of 4500 Gauss, center field of 2500 Gauss, microwave frequency of 9.47 GHz, microwave power of 5.024 mW, and modulation frequency of 100 KHz. A modulation amplitude of 8.00 G was used on all sample except for Stage III samples which were measured at 5.00 G amplitude. Stage I, Stage II, and iron citrate spectra were measured with a gain of 25200. Due to signal/receiver saturation, the remaining samples required a reduced gain of 100 to obtain suitable spectra. Every sample was run with a minimum of nine scans, although twenty-five scans were used for most.

6 ATOM PROBE TOMOGRAPHY OF APATITES AND BONE-TYPE MINERALIZED TISSUES

This chapter discusses the application of atom-probe tomography to study synthetic, geological, and biological apatite minerals, a class of calcium phosphate minerals with wide-ranging geological, industrial and biological importance. Lawrence Tran, an undergraduate student in the laboratory assisted in the preparation of single crystal reference samples. Prof. Neal Blair (Northwestern University) performed the reflectance FTIR measurements and Prof. Jill Pasteris (Washington University in St. Louis) performed the Raman spectroscopy.

Parts of the work have been published in the following article:

Gordon, L. M., Tran, L. & Joester, D. Atom Probe Tomography of Apatites and Bone-Type Mineralized Tissues. *ACS Nano* **6**, 10667-10675 (2012).

6.1 INTRODUCTION

Nanocrystalline biological apatites constitute the mineral phase of vertebrate bone and teeth. Beyond their central importance to the mechanical function of our skeleton, their extraordinarily large surface acts as the most important ion exchanger for essential and toxic ions in our body. However, the nanoscale structural and chemical complexity of apatite-based mineralized tissues is a formidable challenge to quantitative imaging. For example, even energy-filtered electron microscopy is not suitable for detection of small quantities of low atomic number elements typical for biological materials. Herein we show that laser-pulsed atom probe tomography, a technique that combines sub-nanometer spatial resolution with unbiased chemical sensitivity, is uniquely suited to the task. Common apatite end members share a number of features, but can clearly be distinguished by their spectrometric fingerprint. This fingerprint and the formation of molecular ions during field evaporation can be explained based on the chemistry of the apatite channel ion. Using end members for reference, we are able to interpret the spectra of bone and dentin

samples, and generate the first three-dimensional reconstruction of $1.2 \cdot 10^7$ atoms in a dentin sample. The fibrous nature of the collagenous organic matrix in dentin is clearly recognizable in the reconstruction. Surprisingly, some fibers show selectivity in binding for sodium ions over magnesium ions, implying that an additional, chemical level of hierarchy is necessary to describe dentin structure. Furthermore, segregation of inorganic ions or small organic molecules to homophase interfaces (grain boundaries) is not apparent. This has implications for the platelet model for apatite biominerals.

Nanocrystalline apatite is the mineral phase in bone, dentin and enamel. It provides stiffness, strength, wear resistance, and forms part of a hierarchical, high-toughness, low-density composite with collagen and other proteins¹⁵⁴⁻¹⁵⁶. The biomineral in vertebrate bone and teeth resembles hydroxyapatite (OHAp), one of the apatite end members. The other common end members are fluorapatite (FAp), and chlorapatite (ClAp). OHAp, ClAp and FAp share the same general composition $\text{Ca}_{10}(\text{PO}_4)_6(\text{OH},\text{F},\text{Cl})_2$ ^{157,158} and exhibit a nearly identical crystal structure (Figure 6.1)¹⁵⁹. Substituents in the apatite lattice alter the structure and stoichiometry, introduce vacancies, modulate physiochemical properties of the mineral, and are of importance for applications from biomaterials to phosphors and high-energy lasers^{160,161}.

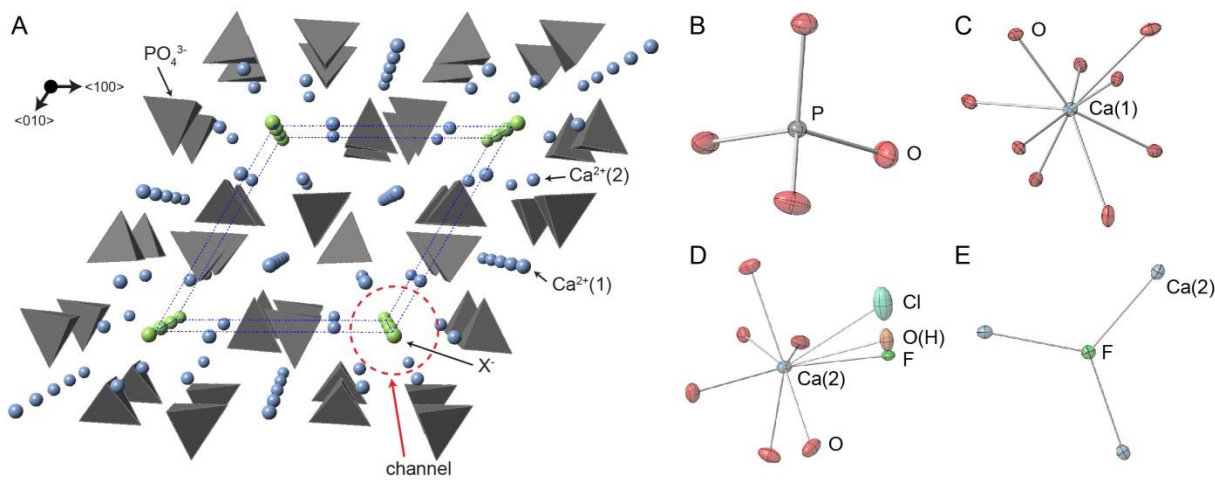


Figure 6.1: Apatite crystal structure

A) The apatite unit cell with four distinct crystallographic positions (sites): six tetrahedral phosphates (B); four Ca(1) coordinated by nine oxyanions (C); six Ca(2) coordinated by six oxyanions and one channel ion (D); and two channel sites, which are occupied by F⁻, OH⁻, or Cl⁻ and are coordinated by three Ca(2) (E)⁵⁶. The Ca(2) site shows the channel ion positions from the FAp, ClAp and OHAp crystal structures⁷². While unit cell parameters change slightly and the symmetry of the crystal is affected by the position of the channel ion, the structures are highly similar. Thermal ellipsoids were rendered according to the atom-specific anisotropic thermal parameters at 80% probability level.

While apatite is sparingly soluble at physiological pH, the bone mineral surface (>500,000 m² in an average human) is in rapid exchange with ionic species present in solution, thus acting as a sorbent and ion-exchanger in contact with body fluids⁵⁹. Bone apatite is substituted with significant amounts of carbonate and provides a reservoir of essential ions for biological functions, including calcium, magnesium and sodium^{20,56,61,78,162-164}. Certain species (e.g. F⁻, Al³⁺, Sr²⁺, bisphosphonates) accumulate in bone, where they can alter mineral solubility and crystallite size, interfere with collagen-mineral bonding, and affect bone cells. This can be advantageous, e.g. fluoride reducing the susceptibility of enamel to caries¹⁶⁵, or detrimental, as in skeletal fluorosis¹⁶⁶ or in aluminum-induced bone disease¹⁶⁷.

Despite the importance of the interfacial processes occurring at the surface of apatite nanocrystals, our understanding of structure, chemical composition, and bonding across the interface is rather limited. This is at least in part due to the small length scale, complex three-dimensional structure, and hard/soft hybrid nature that complicate quantitative imaging. Despite recent progress in atomic resolution elemental mapping by electron energy loss spectroscopy (EELS) or energy dispersive X-ray spectroscopy (EDS) in scanning transmission electron microscopy (STEM), the resolution and chemical sensitivity in biological minerals are greatly limited by the susceptibility of these materials to electron beam damage. Furthermore, many physiological ions with low atomic number have unfavorable spectroscopic properties that can make quantification very difficult or impossible.

We have recently shown, that atom probe tomography (APT), an imaging mass spectrometry technique, may rise to the challenge^{10,168}. APT is based on the phenomenon of field evaporation, where ions successively desorb from a microtip in the presence of an electric field⁸³. The chemical identity of each ion is determined by time-of-flight mass spectrometry. APT is capable of simultaneously mapping the structure and composition of nanoscale volumes (10^5 - 10^6 nm 3) with sub-nanometer spatial resolution and parts-per-million (ppm) chemical sensitivity^{80,83}. The advent of laser-pulsed APT has widened the scope of the technique to include a range of dielectric materials, including a small number of biological and geological minerals^{10,169-172}. We show here that APT is well suited for the analysis of apatite-based materials by investigating spectral features of synthetic and geological apatite end members. We then expand our spectral analysis to vertebrate bone and dentin as examples for apatite-mineralized tissues that contain a range of inorganic substituents and organic molecules. Finally, we discuss preliminary data showing that APT captures the fibrous nature of the collagenous organic matrix and reveals additional detail regarding the chemical nanostructure of homo-phase and hetero-phase interfaces.

6.2 RESULTS AND DISCUSSION

6.2.1 Characterization of Synthetic and Geological Apatite

Crystallinity and phase purity of synthesized apatite single crystals were verified by X-ray diffraction (Figure 6.2 - Figure 6.4), Reflectance Fourier transform infrared spectroscopy (Figure 6.5) and Raman spectroscopy (Figure 6.6). Powder and single crystal X-ray diffraction patterns are consistent with simulations based on published crystal structures for fluor-, chlor- and hydroxylapatite⁷². Geological fluorapatite X-ray diffraction reflections exhibit a different intensity distribution than the simulated random powder mixture indicative of preferred orientation of the crystallites in the sample following mechanical grinding of the single crystal specimen. Reflectance FTIR spectra recorded from polished crystal surfaces are consistent with literature spectra and peak positions indicate pure end-member apatites¹⁷³. Raman spectroscopy on single crystal facets and polished crystal surfaces are similar consistent with reference spectra for synthetic and geological apatite end-members. The characteristic PO₄ v₁, v₂, v₃, and v₄ vibrational modes were evident in all the spectra. The OH stretch was observed only in the hydroxylapatite spectra confirming the absence of hydroxyls in the other end-members. High temperature synthesis of chlorapatite in air could result in the formation of trace amount of undetected oxyapatite, where oxygen occupies the channel site¹⁷⁴.

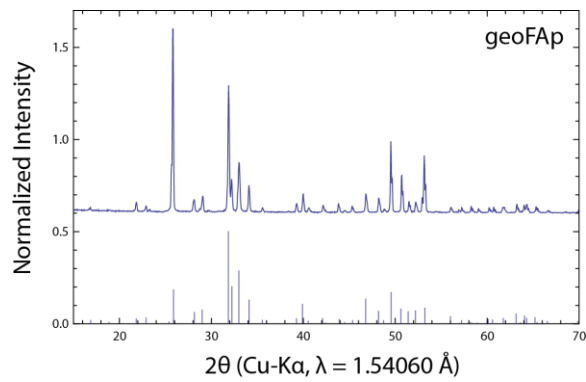


Figure 6.2: Fluorapatite XRD

Geological Fluorapatite powder X-ray diffraction (top) and simulated reflections based on published crystal structures (bottom)⁷². Intensity mismatch between experimental and simulated spectra likely results from preferred orientation of the crystallites in the sample. Spectra are offset for clarity.

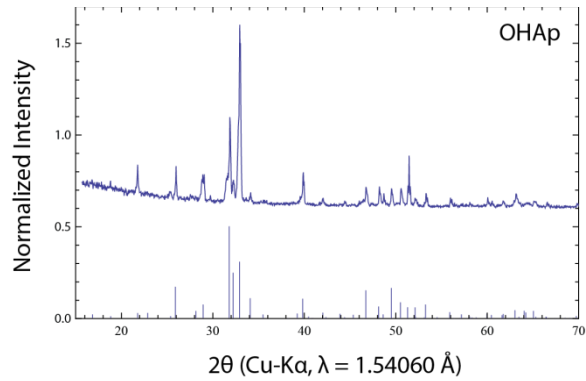


Figure 6.3: Hydroxylapatite XRD

Hydroxylapatite powder X-ray diffraction (top) and simulated reflections based on published crystal structures (bottom)⁷². Spectra are offset for clarity.

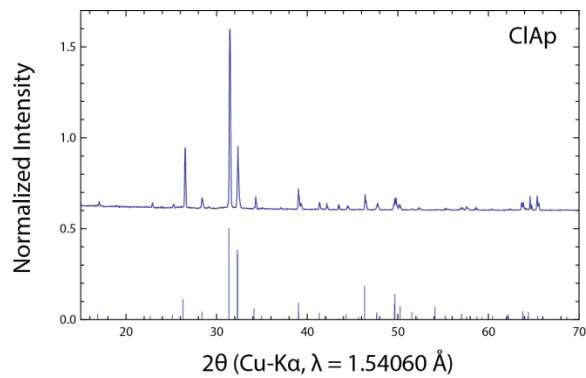


Figure 6.4: Chlorapatite XRD

Chlorapatite powder X-ray diffraction (top) and simulated reflections based on published crystal structures (bottom)⁷². Spectra are offset for clarity.

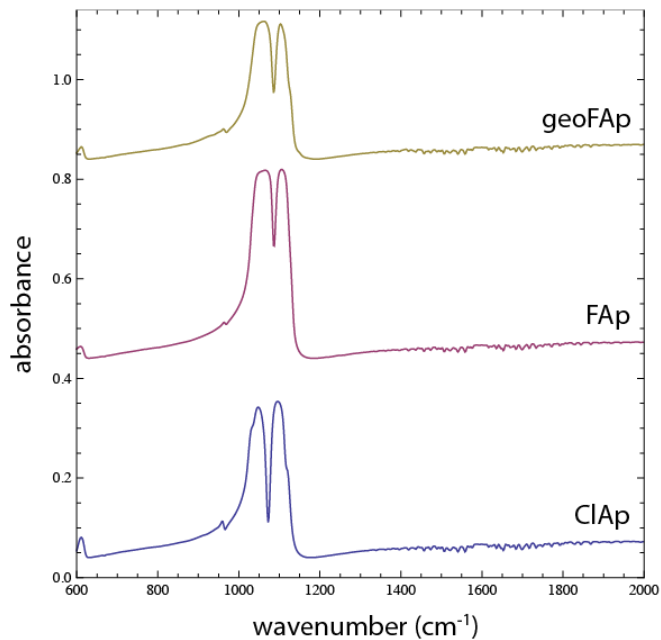


Figure 6.5: Reflectance FT-IR

Absorbance spectra from FAp, ClAp and geoFAp surfaces. Spectra are consistent with literature spectra¹⁷³. Spectra are offset vertically for clarity.

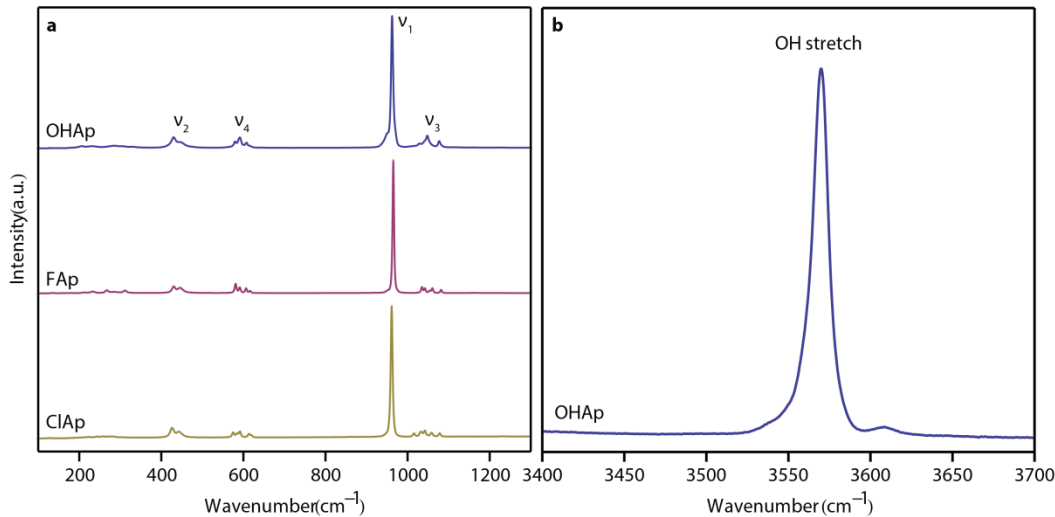


Figure 6.6: Raman Spectroscopy

a, Spectra from (100) face of faceted OHAp single crystal and randomly oriented polished FAp and ClAp surfaces. Spectra are offset for clarity and the PO_4 v_1 , v_2 , v_3 , and v_4 vibrational modes are labeled on the representative OHAp spectra. **b**, OH^- stretch region in OHAp spectra (this mode is absent in the FAp and ClAp spectra). The magnitude of OH^- stretch is $\sim 1/10$ the magnitude of the main phosphate v_1 vibrational mode in OHAp. The OH^- stretch was absent from both the FAp and ClAp spectra, confirming the absence of hydroxyl ions in these compounds.

6.2.2 Atom-probe Tomography Experimental Parameters

The primary difficulties encountered in APT of low conductive, composite materials are a) developing appropriate sample preparation protocols and b) finding APT operational parameters that minimize sample failure while optimizing the quality of spectra and reconstructions. APT samples were prepared by focused ion beam (FIB) milling. We identified operational parameters (laser pulse energy $P_e = 150 \text{ pJ}$, laser pulse frequency $P_f = 200 \text{ kHz}$) for APT of synthetic OHAp in a systematic study of the influence of laser pulse energy and laser pulse frequency on background level, spectral resolution, and the accuracy of the measured compositions as indicators of data quality (Figure 6.7). Apatite mass spectra indicate the formation Ca^{2+} , $\text{O}_2^{2+}/\text{O}_2^+$, and P_xO_y^+ cluster ions during field evaporation (Table 6.1, Figure 6.9, Figure

6.10). In addition, the channel ions give rise to characteristic spectral features. Elements that typically substitute in bone apatite, including Mg^{2+} , Na^+ , and Sr^{2+} , and trace amounts of $^{69}Ga^+$ implanted during FIB-based sample preparation, were also detected.

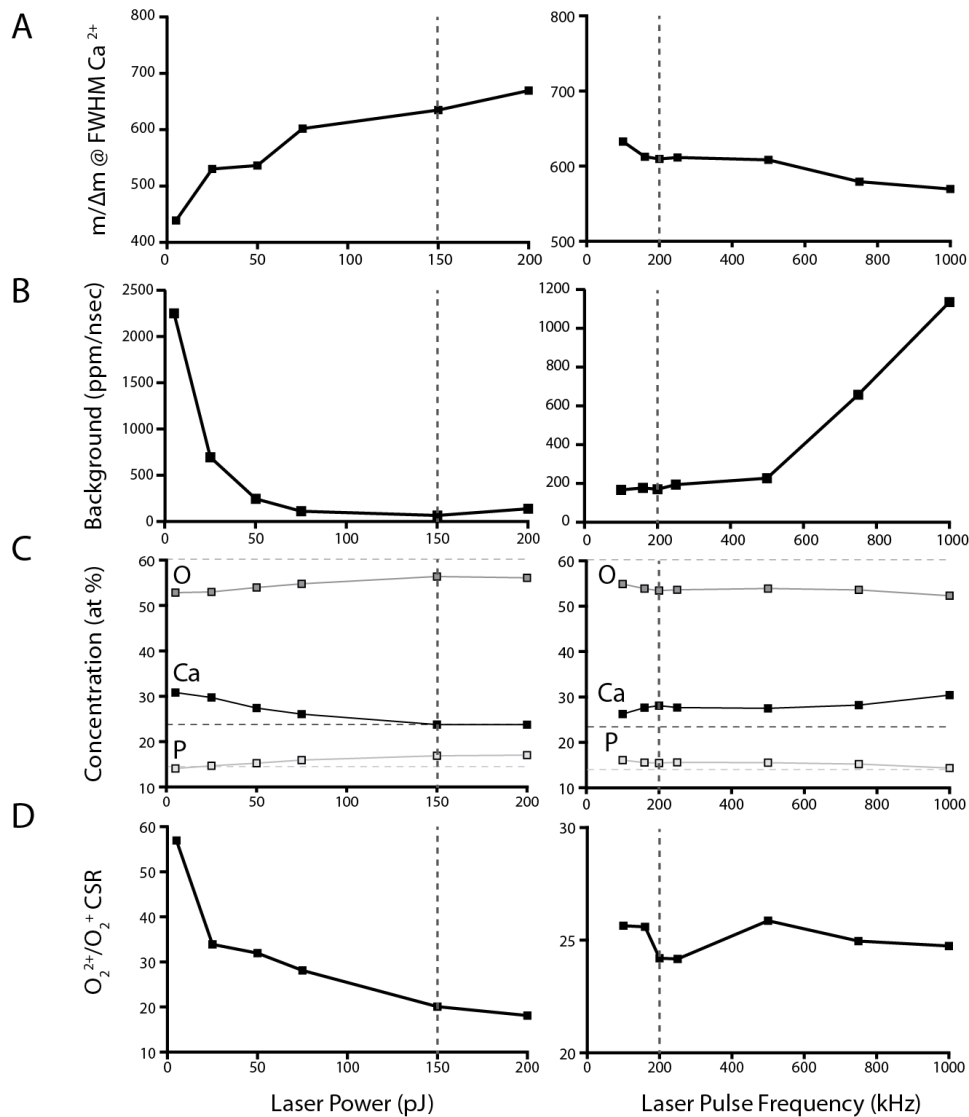


Figure 6.7: The influence of APT experimental run-time parameters on data quality

Samples prepared from single crystalline OHAp were field evaporated at fixed laser pulse frequency ($f_l=200$ kHz) or at fixed laser pulse-energy ($P_l=60$ pJ). $5 \cdot 10^5 - 10^6$ ions were collected at each condition and the mass resolving power (A), background (B), compositional accuracy (C), and charge stat ratio determined (D). The base temperature was 40 K and the tip voltage was dynamically adjusted to maintain an evaporation rate of 0.005 ions per laser pulse

(0.5%). The dashed lines indicated the experimental conditions chosen for subsequent analyses ($P_l = 150$ pJ, $f_l = 200$ kHz).

Little is known about the influence of operational parameters on APT data quality for insulating and/or ceramics with predominantly ionic bonding. We use three factors as a measure of data quality: background level, spectral resolution, and the accuracy of the measured compositions. The background level in time-of-flight (TOF) spectra is defined as the average number of background counts per bin. The mass resolving power (MRP, $m/\Delta m$) at the full-width half-maximum of the Ca^{2+} -peak was used as a measure for spectral resolution. Finally, we compared oxygen, calcium and phosphorus concentrations derived by integration over the corresponding peaks to the theoretical stoichiometry of hydroxylapatite.

In the sample prepared from flux grown single crystals of hydroxylapatite, we found a strong influence of laser energy per pulse (P_l) and laser pulse frequency (f_l) on data quality (Figure 6.7). Increasing laser energy per pulse reduces background levels and improves spectral resolution. Laser pulses with higher power deliver more energy to the tip, increasing the temperature rise and reducing the strength of the electric field required for evaporation (evaporation field). As a result, the rate of steady-state field evaporation between laser pulses decreases, reducing the background level¹⁷⁵. Analyzing specimens at lower electric field further minimizes field-induced mechanical strain and the probability of dielectric breakdown. With decreasing likelihood of catastrophic sample failure, yield increases¹⁷⁵. At high P_l , laser-induced steady-state tip heating can result in an increase in background level, excessive peak broadening (thermal tails) due to long tip cooling times and consequent delayed thermal evaporation. We did not observe such effects at a laser pulse power $P_l \leq 200$ pJ ($f_l = 200$ kHz). In contrast, increasing laser pulse frequency ($P_l = 60$ pJ) reduces the spectral resolution and increases the background level, especially for $f_l \geq 500$ kHz. This is likely a result of steady-state heating of the specimen due to the limited thermal diffusivity of hydroxylapatite.

Although spectral resolution and background levels steadily improve with increasing laser power and decreasing laser frequency, compositional measurements begin to deviate from the theoretical stoichiometry. The compositional deviation at higher laser power results from increased tip heating causing an increase in the number of ions evaporated between laser pulses (uncorrelated evaporation) and possibly the evaporation of neutral species. We find $f_l = 200$ kHz, $P_l = 150$ pJ, and an evaporation rate of 0.005 ions/pulse a suitable compromise between data quality, sample yield, acquisition rate and accuracy of the determined stoichiometry.

During the course of a run, the fraction of laser power absorbed in the tip changes as the tip blunts, and it is useful to have a quick readout of the conditions at the tip surface. The charge-state ratio (CSR), i.e. the ratio of the number of hits of two identical ions with different charge states, is commonly used for this purpose¹⁷⁶. In the case of the apatites, there are very few ions that occur both singly and doubly charged, the most abundant is O₂. The O₂ CSR (O₂⁺/O₂²⁺) was found to vary between 20 and 60 and was particularly sensitive to laser power (Figure 6.7d) this ratio could be used to continuously monitor evaporation conditions during a run and the laser power could then be adjusted in real time to maintain optimum experimental conditions.

6.2.3 Atom-probe Mass to Charge State Ratio Spectra and Molecular Ions

In atom probe spectra of metals and elemental semiconductors samples, monoatomic ions predominate. Spectra of compound semiconductors and dielectrics include numerous molecular ions. However, the process of field evaporation and molecular ion formation in dielectric materials remains poorly understood. Inspection of apatite spectra (Figure 6.8) reveals that calcium, which forms primarily ionic bonds, has a markedly different propensity to form molecular ions (Table 6.1) than the covalently bound phosphorus. In addition, differences in the chemical nature of the channel ion lead to characteristic spectral fingerprints of the structurally nearly identical apatite end members.

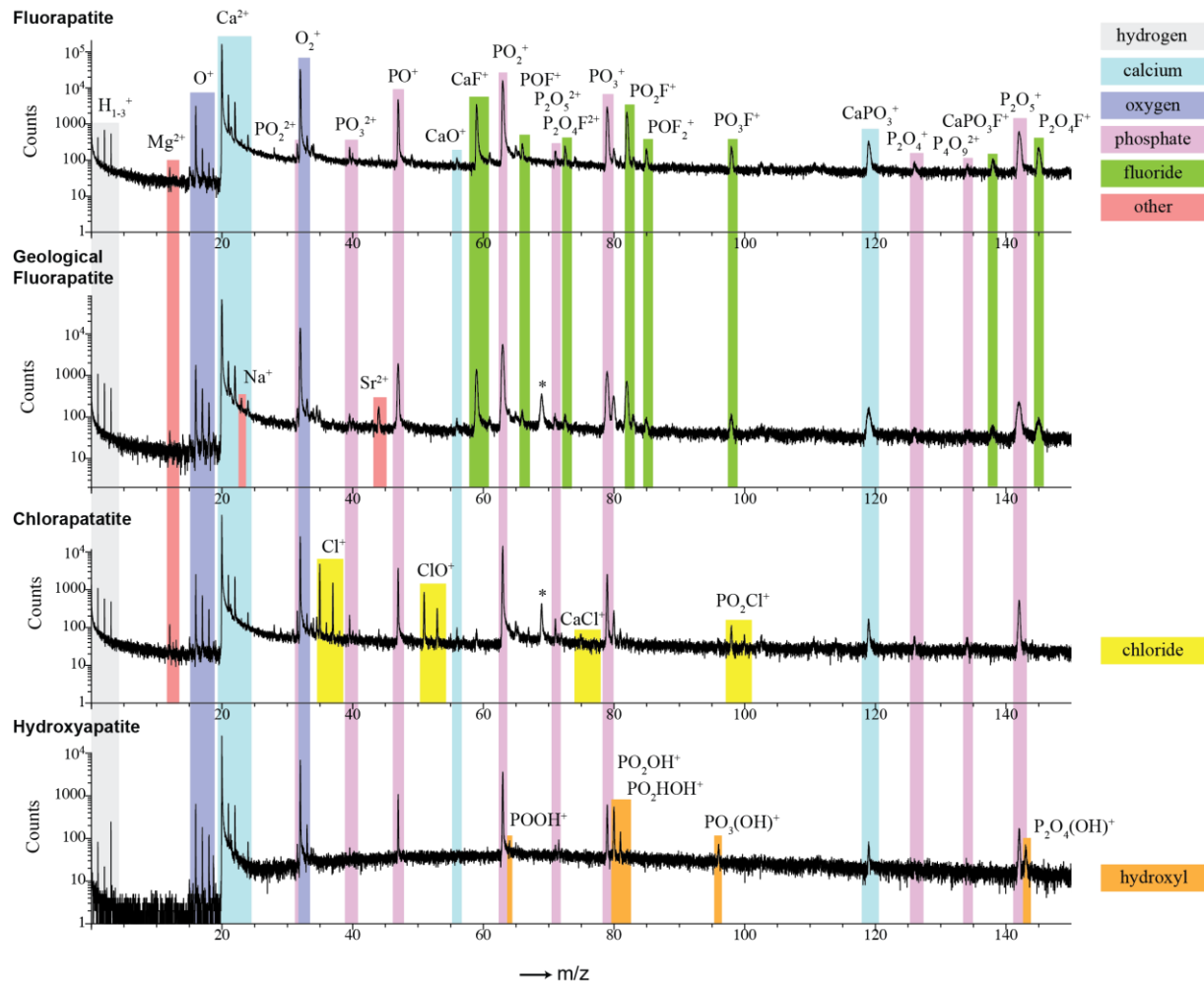


Figure 6.8: APT spectra of synthetic and geological apatites

Ions common to all apatites include Ca^{2+} and CaPO_3^+ (light blue), $\text{O}^+/\text{O}_2^{2+}$ and O_2^+ (purple), a variety of $\text{P}_x\text{O}_y^{n+}$ clusters (pink) and H_x^+ species (light gray). End members give rise to characteristic ions such as CaF^+ and $\text{P}_x\text{O}_y\text{F}_n^+$ in FAp (green), Cl^+ , ClO^+ , and PO_2Cl^+ in ClAp (yellow), and $\text{P}_x\text{O}_y(\text{OH})^+$ in OHAp (orange). FIB-implanted Ga (*) and other low-level inorganic substituents (red) are also detected. For a comprehensive list of ions formed, including those with mass-to-charge ratios > 150 , please see Table 6.1.

Table 6.1: Ions identified in Apatite Spectra

	Ion m/z												
Oxygen	O ⁺ /O ₂ ²⁺ 16	O ₂ ⁺ 32											
Calcium	Ca ²⁺ 20/21/21.5/22/24	CaPO ₃ ⁺ 99											
Phosphate	PO ⁺ 47	PO ₂ ⁺ 63	PO ₃ ⁺ 79	P ₂ O ₄ ⁺ 126	P ₅ O ₉ ²⁺ 134	P ₂ O ₅ ⁺ 142	P ₂ O ₆ ⁺ 156	P ₃ O ₇ ⁺ 205	P ₃ O ₈ ⁺ 221	P ₄ O ₁₀ ⁺ 284			
Chloride	Cl ⁺ 35/37	ClO ⁺ 51/53	PO ₂ Cl ⁺ 98/100										
Fluoride	CaF ⁺ , 59	POF ⁺ 66	PO ₂ F ⁺ 82	POF ₂ ⁺ 85	PO ₃ F ⁺ 98	CaPO ₃ F ⁺ 138	P ₂ O ₅ F ⁺ 161	P ₃ O ₇ F ⁺ 224					
Hydroxyl	PO(OH) ⁺ 64	PO ₂ (OH) ⁺ 80	PO ₃ (OH) ⁺ 86	P ₂ O ₄ (OH) ⁺ 143									
Substituents	Mg ²⁺ 12/12.5/13	Na ⁺ 23	Sr ²⁺ 44										

The stoichiometry of the apatite samples (Table 6.2) agrees reasonably well with predictions for OHAp and ClAp. However, the amount of oxygen is lower and the amount of phosphorus is higher than predicted. This error is relatively small for OHAp and ClAp, but more pronounced in FAp. As the Ca/P ratio is sensitive to instrumental parameters, run time parameters for FAp could likely be optimized. At this time, it is not clear why the stoichiometry of FAp as determined by APT deviates significantly from that of the other apatites.

Table 6.2: APT Compositional Measurements of Apatites

Sample	mole fraction (atomic %)					
	Ca	P	Ca/P	O/P	O	X
Calc. (OHAp)	22.7	13.6	1.66	4.13	59.1	4.55 (X=H)
Calc. (FAp/ClAp)	23.8	14.3	1.66	3.99	57.1	4.8 (X=F/Cl)
OHAp	23.8	16.9	1.41	3.33	56.4	2.9 (X=H)
FAp	30.7	15.6	1.97	3.20	49.9	3.6 (X=F)
geoFAp	31.5	14.3	2.20	3.47	49.6	3.1 (X=F)
ClAp	24.7	16.3	1.52	3.36	54.7	2.9 (X=Cl)

In apatite spectra, phosphorus occurs in molecular ions ranging in size from PO⁺ to P₄O₁₀⁺ (Figure 6.8). The relative abundance of the fragments increases from PO⁺ (13-16%) to PO₂⁺ (63-64%) and then decays

to PO_3^{+} (13-16%). No monoatomic $\text{P}^{+/2+}$ was detected. These relative abundances are in contrast to spectra of metal oxides, for example magnetite (Fe_3O_4), where the monoatomic metal ion (Fe^{2+}) is the most abundant (67.4%), and the relative abundance of ion type decreases with the number of oxygen atoms in the cluster (Figure 6.9). The phosphate P-O bond is clearly more robust under atom probe conditions than typical M-O bonds in transition metal oxides. This may be rationalized by considering the stabilization of the P-O bond by resonance (mesomerism) and its greater covalent nature (P-O: 61% vs. Fe-O: 49%) based on Pauling electronegativity values¹⁷⁷.

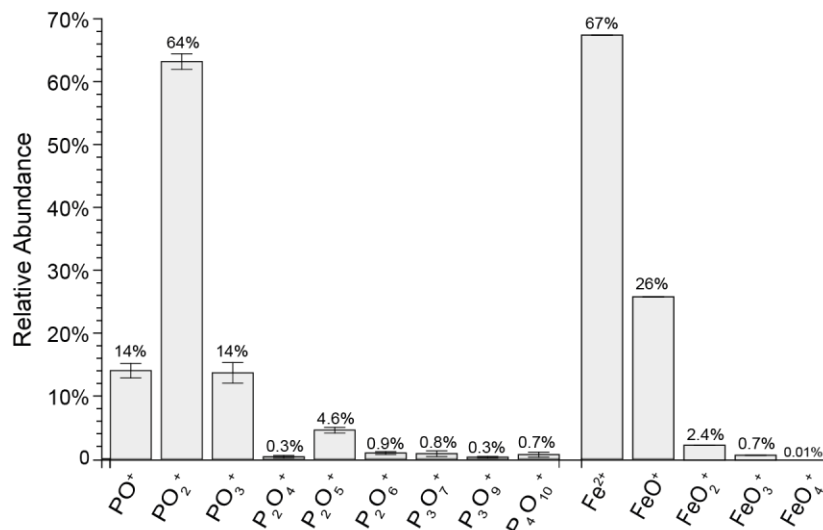


Figure 6.9: P_xO_y^+ and FeO_x^+ relative abundances

The relative abundance of P_xO_y^+ ions in apatite spectra differs from that of $\text{Fe}^{2+}/\text{FeO}_x^+$ ions in magnetite¹⁰. The error bars indicate the standard deviation of the data across four synthetic and geologic apatites (OHAp, ClAp, FAp, geoFAp). The magnetite data are from a single dataset obtained from a geologic single crystal¹⁰.

The Ca-O bond, on the other hand, is much less robust. Nearly all calcium was detected as Ca^{2+} with only a trace amount of CaO^+ apparent in spectra and less than 1% CaPO_3^+ (Figure 6.10), where oxygen likely bridges between Ca and P. Clearly, when phosphorus and calcium compete for oxygen, phosphorus wins

in the vast majority of cases. This may be a consequence of the lesser covalent nature of the Ca-O bond (21%) and the reduced ability of calcium to engage in *d*-orbital-mediated, ligand-to-metal charge-transfer.

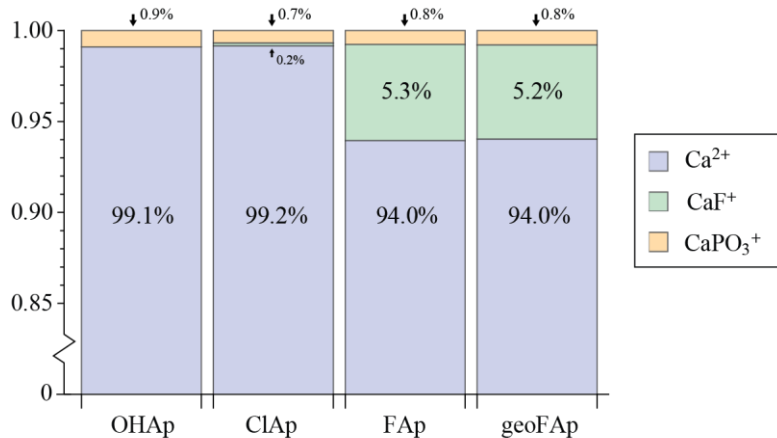


Figure 6.10: Relative abundance of Ca^+ containing ions

Relative abundance of calcium containing ions in the measured apatite samples, excluding the trace CaO and CaCl .

While the channel ions share a similar environment, they give rise to characteristic sets of spectral features (Figure 6.8, Ions identified in Apatite Spectra). Fluoride in FAp occurs as CaF^+ (47%), PO_2F^+ (36%) and a number of $\text{P}_x\text{O}_y\text{F}_z^+$ ions with lower abundance (total: 17%). ClAp spectra indicate that chloride, unlike fluoride, readily forms a monoatomic ion (Cl^+ , 76%) and ClO^+ (21%). The propensity of chloride to form molecular ions with phosphorus is significantly smaller (PO_2Cl^+ , <3%). The fingerprint of OHAp consists of a series of ions of the general form $\text{P}_x\text{O}_y(\text{OH})_z^+$, primarily $\text{PO}_2(\text{OH})^+$, which accounts for 63% of all detected hydroxyl groups. While these ions could in principle form by recombination of phosphorus and oxygen-containing ions with residual hydrogen atoms from the residual gas in the vacuum chamber, their absence in ClAp and FAp spectra indicates that they indeed form from the channel ion. However, the fingerprint peaks represent only 48% of the predicted number of hydroxyl ions. It is likely that the

remaining hydroxyl groups evaporate as H_x^+ and O_xH_y^+ ions or potentially neutral atomic or molecular hydrogen, which go undetected.

The Ca-F bond, despite its weakly covalent character (9%), is surprisingly robust and accounts for ~5% of the Ca ions and ~47% of the fluoride in FAp. In comparison, only trace amounts of CaCl^+ ions were formed from ClAp and CaOH^+ was not observed in OHAp. This is likely a consequence of the high electron affinity and first ionization potential of fluorine that also limits formation of F^+ and FO^+ species. Chloride, on the other hand, is readily oxidized to Cl^+ and ClO^+ ; oxyanions and hydroxyl groups give rise to O^+ or pick up a proton and evaporate as OH^+ . The abundance of $\text{P}_x\text{O}_y\text{X}_z^+$ clusters follows the same trend as the P-X bond strength, i.e. $\text{P-O} > \text{P-F} > \text{P-Cl}$. The tendency of chloride to oxidize further reduces the likelihood for the formation of such clusters.

Larger molecular ions of the formula, $\text{P}_x\text{O}_y\text{X}_z^+$ do not represent discrete fragments of the apatite crystal lattice, as the phosphate tetrahedra are not vertex or edge linked and they do not lie within bonding distance of the channel ion. The formation of these ions implies that atoms/ions have some mobility and can react to form larger ions (for an example of surface diffusion during APT of metals see Ref.¹⁷⁸). Chemical intuition predicts that a reaction would occur by nucleophilic attack of an “X” species (e.g. F^-) on an electrophilic phosphorus atom. If X^- has a limited lifetime because of competing processes (e.g. oxidation to form X^+), this attack is less likely to occur. Whether the reaction occurs via nucleophilic attack is what is actually happens under the extremely high electric field at the tip of the sample is not known. Regardless, a fluoride atom has to move at least 0.17 nm off its lattice position to reach bonding distance of an oxygen ion, and the formation of an O-bridged P_2O_x cluster also requires that a distance of 0.17 nm be closed. While surface diffusion and the formation of clusters reduces the resolution of the compound’s reconstruction by a small amount¹⁷⁹, these molecular ions account for only ~2-3% of the total ions, and they are homogeneously distributed within the reconstruction. It is thus unlikely that large molecular ions lead to artifacts that could affect interpretation of the data.

6.2.4 Apatite Biominerals: Bone and Dentin

Bone and dentin are hierarchically structured materials with three major components, apatite (~72 wt % of dry, de-fatted material), organics (~20 wt %), and water^{58,180}. The mineral phase best resembles OH-deficient OHAp substituted with significant carbonate (5-8 wt %) and smaller levels of Na⁺ and Mg²⁺ (0.5-1.0 wt %)⁵⁶⁻⁵⁹. Approximately 1 wt % of the composite is citrate ($C_6H_5O_7^{3-}$) that may be associated with the mineral surface and/or the collagen fibrils that constitute the majority of the organic fraction.^{60,61} The poorly crystalline mineral is thought to be present in irregular platelets approximately 50 long, 25 nm wide and 2-5 nm thick^{62,63}. In forming bone and mineralizing tendon, these platelets are roughly aligned with their crystallographic c-axis parallel to collagen fibrils.⁶⁴ Within a fibril, platelets are generally parallel to each other. However, with increasing age, as the amount of intrafibrillar and interfibrillar mineral increases and platelets grow, the orientation of platelets with respect to each other becomes less homogeneous^{8,65,66}.

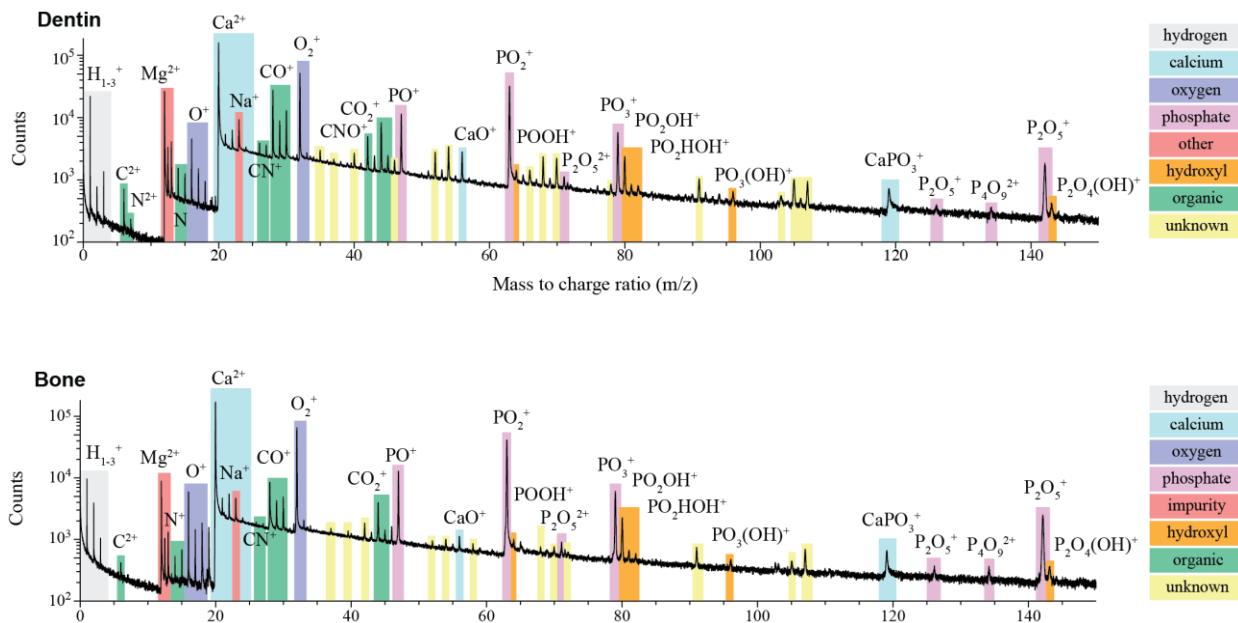


Figure 6.11: Dentin and Bone APT Spectra

Spectrum of elephant tusk dentin and rat bone (femur) highlighting the hydrogen, calcium, oxygen, phosphate, other inorganic ions, identified fragments of organic molecules, the spectral signature of OHAp and a number of unidentified molecular ions that likely derive from organic molecules.

To establish whether APT of bone-type materials is feasible, we analyzed samples prepared from rat femur cortical bone and elephant tusk dentin (ivory). As mechanically weak interfaces and the presence of organics can lead to sample failure during APT, we used FIB milling to lift out samples such that the collagen fibril direction was aligned with the long axis of the tip. Consistent with expectations, the resulting spectra (Figure 6.11) are similar to those of synthetic OHAp (Figure 6.8), with Mg²⁺ (0.5-1.7 at %) and Na⁺ (0.25-0.6 at %) as substituents. Additional features include peaks corresponding to C⁺²⁺, N⁺²⁺, molecular ions of the general formula C₁₋₄N₀₋₁O₁₋₂H₀₋₂⁺, and presumably organic ions that we have not identified (Table 6.3). While we cannot distinguish which “CHO”-containing ions arise from carbonate, citrate, or collagen, the origin of nitrogen and of larger molecular ions must be organic macromolecules^{10,168,181}.

Given the small sample size and the heterogeneous nature of bone and dentin, the match between the expected and the experimentally determined stoichiometry is reasonable.

Table 6.3: Identified organic ions and unknown ions in bone and dentin APT spectra

m/z (AMU)	Chemical Identity	m/z (AMU)	Chemical Identity
6	C ²⁺	45	CO ₂ H ⁺
7	N ²⁺	46	<i>unidentified</i>
12	C ⁺	52	<i>unidentified</i>
13	CH ⁺	54	<i>unidentified</i>
14	N ⁺	58	<i>unidentified</i>
15	NH ⁺	66	<i>unidentified</i>
26	CN ⁺	68	<i>unidentified</i>
27	CNH ⁺	70	<i>unidentified</i>
28	CO ⁺	71	<i>unidentified</i>
29	COH ⁺	78	<i>unidentified</i>
30	NO ⁺	91	<i>unidentified</i>
35	<i>unidentified</i>	96	<i>unidentified</i>
37	<i>unidentified</i>	103	<i>unidentified</i>
40	<i>unidentified</i>	105	<i>unidentified</i>
42	CNO ⁺	106	<i>unidentified</i>
43	CNOH ⁺	107	<i>unidentified</i>
44	CO ₂ ⁺		

Strikingly, in a reconstruction of an elephant tusk dentin sample, there are “CHNO”-rich fibers that run approximately parallel to the analytical *z*-direction (Figure 6.12), which corresponds to the long axis of the elephant tusk, and is the direction in which the collagen fibrils are oriented^{65,182}. The smallest organic features that can be distinguished in APT reconstructions have cross sections corresponding to collagen microfibrils consisting of 5 collagen triple helices ($2.7 \cdot 4 \text{ nm}^2$)¹⁸³. Larger assemblies are also apparent. We have not yet been able to identify features with the typical periodicity of hole and gaps zones of collagen.

Some, but not all, organic fibers co-localize with high sodium concentrations (Figure 6.12e). These fibers do not co-localize with magnesium ions, indicating that the binding is specific. We did not observe fibers that show selective binding of Mg²⁺ (Figure 6.12f). Cations are most likely bound by acidic amino acids or proteoglycans in the collagenous organic matrix. Specificity in binding implies that there are subtle

differences in the organic fibers. For example, some fibers could contain a protein or proteoglycan that binds Na^+ specifically. This could influence the charge density of such fibers, their self-assembly behavior, nucleation and growth of OHAp during mineralization, or the amount of water bound by the fiber, and thus its mechanical and self-healing properties. We first reported specific ion binding by fibers in the organic matrix of the chiton tooth.¹⁰ Having observed such specificity in invertebrate mollusks and mammals, it is intriguing to think that a chemical level of hierarchy may be a general feature that controls self-assembly and/or functional properties of biomineralized tissues. Atom probe is currently the only technique that is able to detect chemical heterogeneity in biomaterials at this length scale.

While hetero-phase interfaces between organic fibers and the mineral can be readily identified in 3D maps of the organic fragment ion distribution, there are no features in reconstructions that correspond to homo-phase interfaces, i.e. grain boundaries between crystallites. Furthermore, we see no evidence of segregation of Na^+ or Mg^{2+} to either grain boundaries or organic-inorganic interfaces. Instead, Na^+ and Mg^{2+} are nearly homogenously distributed throughout the mineral phase. This is in apparent contradiction to the current model of bone^{8,56} and dentin^{66,184}, including elephant dentin^{65,67,68} that posits that apatite crystallites have irregular platelet habit and that organic and inorganic species, particularly citrate and magnesium, segregate to platelet surfaces where they influence the biological properties of the material. There are three alternative explanations for this conundrum:

1. OHAp occurs in irregular shapes that correspond to the spaces between the organic fibrils (Figure 6.12b-d). The appearance of platelet shaped crystallites in TEM is an artifact.
2. Na^+ and Mg^{2+} do no segregate. There are platelets, but they cannot be recognized in APT reconstructions based on the Na or Mg distribution.
3. There are platelets, and Na^+ and Mg^{2+} do segregate, but interfaces cannot be resolved due to limitations of APT.

We have observed segregation of Na and Mg to interfaces in dental enamel (not shown), which argues against alternative 2. Analysis of small angle X-ray scattering data do not necessarily agree with a platelet habit, arguing in favor of alternative 1⁵⁹. We believe that a substantial amount of additional information will be required to arrive at a complete understanding of crystallite habit and interfacial segregation in different bone-type composites.

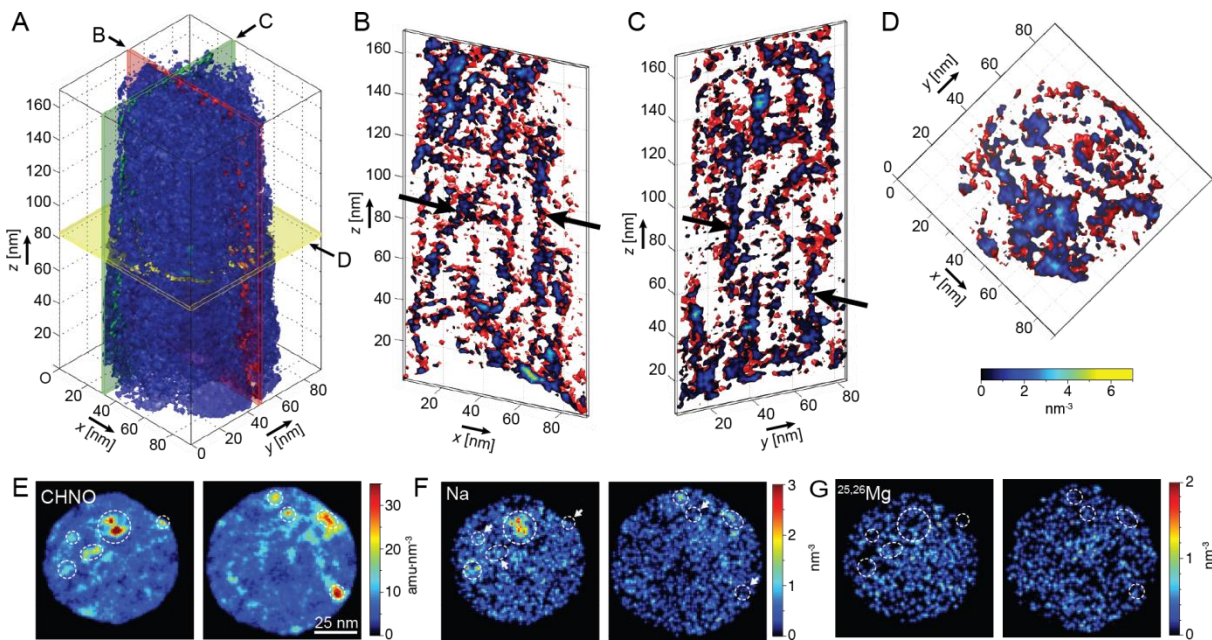


Figure 6.12: 3D reconstruction of a sample of elephant tusk dentin

A. Isosurface (blue) of the number density of organic fragment ions (1.4 nm^{-3} , ions listed in Table 6.3). B-D. Slices through the reconstructed volume parallel to the XZ plane (B), YZ plane (C) and XY plane (D). Isosurfaces (1.4 nm^{-3}) are rendered in red. Endcaps show the organic fragment number density. In B and C, a high density of organic fibers oriented roughly parallel to the z-axis (black arrows) is apparent. Fiber spacing is generally larger in the XZ plane than in the YZ plane. E-G. Elemental maps generated from 5 nm thick slices parallel to the XY plane (left: $z = 147\text{-}151 \text{ nm}$, right: $z = 47\text{-}51 \text{ nm}$) showing mass density of organics (E) number density of Na^+ , and number density of Mg^{2+} . Some organic fibers (dashed ellipses), but not all (white arrows), co-localize with sodium. Mg^{2+} is evenly distributed across the entire slice. Note that the Mg maps comprise only the minor isotopes (^{25}Mg , ^{26}Mg). Based on the natural abundances, we estimate that ions at $m/z=12$ comprise 34% C^+ and 66% $^{24}\text{Mg}^{2+}$ while the total of the ions at $m/z = 12.5$ and 13 consist only of 14% CH^+ (at $m/z = 13$).

6.3 CONCLUSION

APT offers unrivaled spatial resolution and unbiased chemical sensitivity in compositionally and texturally complex materials. Laser pulsing enables the analysis of low conductivity materials. We have shown herein that apatites, a class of phosphate minerals with exceptional flexibility in accommodating substituents and of broad importance for multiple disciplines, are suitable for APT investigation. APT spectra of different apatite end members, including OHAp, FAp, and ClAp, show a common set of atomic and molecular ions but a unique spectrometric fingerprint specific to the channel ion. We can rationalize the preferential formation of atomic and cluster ions using simple concepts of electronegativity and bond strength. Simulations of the field evaporation process may help develop a quantitative understanding of the process.

Using the synthetic apatites for reference, we analyzed elephant tusk dentin and rat femur cortical bone as examples of structurally and chemically complex biological nanocomposites. Atom probe spectra clearly identify ions derived from organic matrix molecules. Reconstructions reveal fibrous organic structures that likely correspond to individual collagen microfibrils and their assemblies in elephant dentin. We observed specificity in ion binding for some fibers, indicating a previously unknown level of chemical hierarchy in the structure of dentin. This is the second example for chemical heterogeneity at the single-fiber level after our discovery in the chiton tooth, and may represent a widespread biological strategy in biomineralization. The functional significance of the observed specificity is not yet clear.

Current reconstructions do not reproduce the platelet habit of the OHAp crystallites. It is not clear whether this is a limitation of atom probe tomography¹⁸⁵, whether platelets are an artifact of electron microscopy, or whether interfaces in bone materials are far more diffuse than the description as discrete platelets implies. We are optimistic that the structural and chemical information gleaned from electron microscopy, APT, and their correlative combination will enable a much-improved characterization of bone and other biomineralized tissues. Such analytical information, which has implications for our understanding of how

organisms manipulate apatite structure and chemistry for different applications in bone, dentin and enamel will help analyze pathological changes, and provide a basis for the development of bio-inspired nanocomposites.

6.4 MATERIALS AND METHODS

6.4.1 *Consumables*

Unless otherwise specified, the following chemicals were used without further purification: Hydroxylapatite (OHAp, $\text{Ca}_5(\text{PO}_4)_3\text{OH}$, 99.995 wt%) powder, anhydrous calcium chloride (CaCl_2), beta-tricalcium phosphate ($\text{Ca}_3(\text{PO}_4)_2$), calcium fluoride (CaF_2), aluminum nitrate nonahydrate ($\text{Al}(\text{NO}_3)_3 \cdot 9\text{H}_2\text{O}$) (Sigma Aldrich, St. Louis, MO); potassium sulfate (K_2SO_4) (EMD, Darmstadt, Germany); glutaraldehyde, sodium cacodylate (Electron Microscopy Sciences, Hatfield, PA); 5 mL alumina combustion boat, 25 mL alumina crucible, alumina crucible cover (Coors Tek, Golden, CO); 1 mL tungsten evaporation boat (R. D. Mathis, Long Beach, CA); Epo-Fix resin (Struers, Cleveland, OH); LR White resin (London Resin Company, Aldermaston, Reading, Berkshire, UK); CarbiMet II SiC grinding paper, Metadi supreme polycrystalline aqueous diamond polishing suspension, Microcloth polishing cloths (Buehler, Lake Bluff, IL); Conductive Liquid Silver Paint (Ted Pella, Redding, CA). Ultrapure Water ($\rho = 18.2 \text{ M}\Omega\cdot\text{cm}$) prepared with a Barnstead Nanopure UF+UV ultrapure water purification system (Thermo-Fisher Scientific, Waltham, MA); Geological fluorapatite single crystals (Amongems, Bangkok, Thailand).

K_2SO_4 was purified twice by recrystallization. Specifically, 25 g of K_2SO_4 was dissolved in 200 mL of boiling water while stirring. The K_2SO_4 solution was vacuum filtered and the filtrate was transferred to an ice bath to precipitate the K_2SO_4 . The precipitated K_2SO_4 was washed with acetone and dried in air at 120 °C.

6.4.2 Single Crystal Synthesis

OHAp single crystals were synthesized using a potassium sulfate flux.¹⁸⁶ Briefly, 2 g of high-purity OHAp powder was ground with a porcelain mortar and pestle and placed into a 5 mL alumina combustion boat. The sample was heated to 1000 °C (8.33 °C/min) and held at this temperature for 6 h in air to remove water and trace organic material. The powder was left to cool to room temperature in the furnace before it was mixed with K₂SO₄ at a K₂SO₄/OHAp weight ratio of 1.6:1 (1538 mg K₂SO₄ : 960 mg OHAp) with a porcelain mortar and pestle. The mixture was placed into a 5 mL alumina combustion boat, heated to 1150 °C (9.2 °C/min), and held at this temperature for 3 h in air. The sample was then cooled to room temperature in the furnace. OHAp single crystals were separated from the solidified flux by mechanically breaking up large clumps and washing with hot (90 °C) water, followed by rinsing with methanol and acetone.

Chlorapatite (ClAp) and fluorapatite (FAp) single crystals were synthesized using a calcium chloride/fluoride flux¹⁸⁷. For ClAp, CaCl₂ and Ca₃(PO₄)₂ powders were mixed with a porcelain mortar and pestle in a molar ratio of 3.33:1 (5.5 g of CaCl₂ and 4.65 g of Ca₃(PO₄)₂), placed in a 25 mL alumina crucible, and covered loosely with an alumina cover. The mixture was heated to 1375 °C (5.7 °C/min), and held at this temperature for 15 h in air. The sample was cooled slowly to 1220 °C (3 °C/h), and then cooled to room temperature in the furnace.

For FAp single crystal synthesis, CaF₂ and Ca₃(PO₄)₂ were mixed together at a molar ratio of 3.33:1 with a porcelain mortar and pestle (230 mg of CaF₂ and 280 mg of Ca₃(PO₄)₂), and placed in a 1 mL tungsten evaporation boat. The mixture was heated to 1375 °C (5.7 °C/min) and held at this temperature for 15 h under a constant flow of nitrogen gas. It was cooled slowly to 1220 °C (3 °C/h), and then cooled to room temperature in the furnace. Excess calcium fluoride flux was removed by boiling in an aqueous solution of aluminum nitrate (10 wt% Al(NO₃)₃•9H₂O). The recovered sample was washed with water repeatedly

by vacuum filtration. The crystallinity and phase purity of all synthesized apatites were verified by X-ray diffraction, Raman spectroscopy and Fourier transform infrared spectroscopy.

6.4.3 X-Ray Powder and Single Crystal Diffraction

Synthetic OHAp and ClAp and geological fluorapatite (geoFAp) single crystals were ground to a fine powder with an agate mortar and pestle. Powders were loaded into a clean quartz sample holder with a 0.2 mm deep cavity, flattened with a glass microscope slide, and fixed in place with a mixture of hairspray and isopropanol. Powder diffraction patterns were recorded using Cu-K α radiation in a D-Max X-ray diffractometer (Rigaku, The Woodlands, TX). The 2 θ angle was scanned from 15° and 70° with a step size of 0.04° and a dwell time of 2 sec. Diffraction patterns (Figure 6.2 - Figure 6.4) are consistent with patterns simulated using CrystalDiffract (CrystalMaker Software Limited, Begbroke, Oxfordshire, UK) based on published crystal structures⁷².

Unit cell parameters of a synthetic FAp crystal were determined by single-crystal X-ray diffraction at the Northwestern Integrated Molecular Structure Education and Research Center (IMSERC) using a Platform APEX II (Bruker, Madison, WI) equipped with a Mo X-ray source. Experimental values ($a = b = 9.3886 \pm 0.0202 \text{ \AA}$, $c = 6.9060 \pm 0.0148 \text{ \AA}$, $\alpha = \beta = 90^\circ$ and $\gamma = 120^\circ$) are consistent with the literature values for fluorapatite ($a = b = 9.3973$, $c = 6.8782$, $\alpha = \beta = 90^\circ$ and $\gamma = 120^\circ$)⁷².

6.4.4 Reflectance Fourier Transform Infrared Spectroscopy

Samples were analyzed using a Tensor 37 FT-IR (NIR/mid-IR, Bruker, Billerica MA) bench coupled with a HYPERION microscope equipped with MCD detector and a 15X objective. Measurements were made in reflectance mode. Spectra were collected with 4 cm $^{-1}$ spectral resolution from 7000 cm $^{-1}$ to 400 cm $^{-1}$ (Figure 6.5). Phase purity was confirmed by FTIR and spectra are consistent with literature spectra.¹⁷³

6.4.5 Raman Spectroscopy

Raman spectra were recorded in backscattering geometry using 532 nm excitation in a WITec alpha300R confocal Raman microscope (WITec Instruments Corp. Maryville, TN) with a spatial resolution of 0.7 - 1.6 μm and spectral resolution of 0.9 cm^{-1} . The laser power was set to 10-45 μW to minimize local heating of the sample. Integration times were 30-60 sec. Spectra were calibrated against a silicon standard (Figure 6.6). Observed PO_4 ν_1 , ν_2 , ν_3 , and ν_4 vibrational modes, lattice modes and the OH^- stretch were consistent with literature spectra.¹⁸⁸

6.4.6 Dissection, Fixation, Dehydration and Embedding

Central 5 mm long section of hind-left femur was removed with a bone saw and fixed in 2.5% gluteraldehyde in cacodylate buffer (100 mM, pH 7.4) overnight at 4 °C, dehydrated in a graded ethanol series (50, 75, 90, 100%) and de-fatted in chloroform. The dehydrated sample was infiltrated with LR white resin containing a benzoyl peroxide catalyst, and was subsequently polymerized overnight within a sealed gelatin capsule at 60 °C.

ClAp and FAp crystals were embedded in Epo-Fix resin and polymerized overnight at 25 °C.

6.4.7 Grinding and Polishing

The embedded femur sample was cut transversely with a low speed diamond saw (Buehler Isomet, Lake Bluff, IL). All embedded samples were ground using progressively finer grits of SiC grinding paper (400, 600, 800 and 1200 grit) and polished using polycrystalline aqueous diamond polishing suspensions (6, 3, 1, and 0.1 μm) on Microcloth polishing cloths.

The elephant tusk dentin sample was received as a polished geological thin section mounted on a glass slide. The age at death was estimated at 53 ± 5 years based on the wear pattern of last lower molar.

Polished samples were secured to an aluminum stub with cyanoacrylate adhesive, coated with ~25nm of Pt with an Ion Beam Sputter Deposition and Etching System (IBS/e, South Bay Technologies, San

Clemente, CA) operating at a base pressure of $< 10^{-4}$ Pa, a working pressure of 10^{-2} Pa argon, with two ion guns operating at 8 kV at 3 mA per gun. The coating was grounded to the stub with conductive liquid silver paint.

6.4.8 APT Sample Preparation

Samples for APT were prepared using the SEM/FIB instrument (Helios Nanolab, FEI, Hillsboro, Oregon) using established protocols.^{100,101} A rectangle of platinum (FIB-Pt) was deposited on the polished cross-section using the ion beam (30kV, 93pA) to decompose methyl cyclopentadienyl trimethyl platinum ($[C_5H_5Pt(CH_3)_3]$) gas, over a region of interest (2 x 25 μm) on the polished cross-sections or directly on faceted crystals. A wedge of material below the Pt rectangle was cut out on three sides using the FIB (30 kV, 6.5 nA). The wedge was attached to an in situ nano-manipulator (Omniprobe, Dallas, TX) using FIB-deposited Pt before cutting the final edge free. 1-2 μm wide segments were cut from the wedge and sequentially affixed to the tops of Si posts in an array (Cameca Scientific Instruments, Madison, WI) with FIB-Pt. Each tip was shaped and sharpened using annular milling patterns of increasingly smaller inner and outer diameters. The majority of the amorphized surface region and implanted gallium ions in the tip surface was removed by a final ion-milling step at 2 kV, 0.4 nA.

6.4.9 APT Methods

Atom probe tomographic analyses were conducted in a Cameca local-electrode atom-probe (LEAP 4000XS_i, Cameca, Madison, WI) tomograph using a pulsed frequency-tripled Nd:YAG laser ($\lambda = 355$ nm). Run time parameters (200 kHz, 150 pJ per pulse) were optimized for OHAp as described in Figure 6.7. The DC potential on a microtip during APT was controlled to maintain an evaporation rate of either of 0.005 or 0.0025 ions per laser pulse. The base temperature of the microtip was maintained at 40 K and the ambient vacuum pressure was $< 10^{-8}$ Pa. Peak ranges were defined as the entire visible peak and background subtraction was done using side-band subtraction.¹⁸⁹

Three-dimensional reconstruction of APT data was performed using the Cameca integrated visualization and analysis software (IVAS) based on published algorithms, assuming a hemispherical tip shape.^{83,105} Standard reconstruction parameters were used with an electric field dependent tip radius (r). The average evaporation field (F_e , 14 V·nm⁻¹) used for reconstruction of the data was determined from radius measurements on SEM or TEM images of microtips after APT analysis. The average ionic volume used for the reconstruction was calculated based on the average atomic volume (0.0129 nm³), specifically, the volume of the OHAp unit cell (0.5279 nm³) divided by the number of atoms in the OHAp unit cell (41, excluding hydrogen) based on a published crystal structure.⁷² The ionic volume (0.0258 nm³) was calculated as twice the atomic volume as a result of the formation of molecular ions (average: 2 atoms/ion). The detector efficiency parameter used in the reconstruction was adjusted to account for the large number of un-ranged hits (75%) in the data due to the large thermal tails.

7 AMORPHOUS INTERGRANULAR PHASES CONTROL THE PROPERTIES OF TOOTH ENAMEL

This chapter discusses the structure and distinct chemistry of amorphous intergranular phases in rodent tooth enamel and their controlling influence on the physiochemical properties of the tissue. Michael Cohen, Northwestern University, Dr. Qing Ma, Dr. David Vine, Argonne National Lab and Dr. Tom Regier, Canadian Light Source, assisted with X-ray spectroscopy measurements. Prof. Rebecca Metzler assisted with the X-ray photoemission electron microscopy. Dr. Keith MacRenaris at the Center for Advanced Molecular Imaging, Northwestern University performed the inductively coupled plasma mass spectroscopy to measure enamel etching rates and the composition of reference materials. Professor Jill D. Pasteris, Department of Earth and Planetary Sciences, Washington University in St. Louis performed the Raman spectroscopy of enamel and reference compounds. Dr. Charudatta Phatak, Argonne National Lab, performed the correlative TEM imaging of atom probe sample tips.

Parts of the work have been published in the following conference proceeding and are in preparation for submission in the following article:

Gordon, L., Cohen, M. & Joester, D. Correlative Microscopy and Spectroscopy of Buried Interfaces in Tooth Enamel. *Microscopy and Microanalysis* **19**, 1634-1635 (2013).

Gordon, L. M., Cohen, M. J., MacRenaris, K. Pasteris, J. D., Vine, D. J., Phatak, C., & Joester, D. Amorphous intergranular phases control the properties of tooth enamel. *in preparation*.

7.1 INTRODUCTION

Tooth enamel is the hardest, most highly mineralized tissue in vertebrates. Optimized to withstand the forces of mastication it is composed of hydroxylapatite (OHAp) nanowires, tens of thousands of which are bundled into rods that are organized in a three-dimensional weave¹⁹⁰. The outstanding fracture re-

sistance of enamel and its long fatigue life are the consequence of this hierarchical architecture. Tooth enamel is also the target of the most prevalent infectious disease in humans, dental caries (tooth decay)^{191,192}. Caries, simply put, is the destruction of tooth biominerals by chemical dissolution and commonly begins with the demineralization of enamel by acids produced in plaque biofilms⁷⁸. It has long been known that the susceptibility of OHAp to acid dissolution is greatly dependent on the presence of magnesium, carbonate, and fluoride ions. However, imaging the distribution of these impurities in enamel at the ultrastructural level has remained a great challenge, hampering our understanding of caries etiology at the mechanistic level. Here we show by a combination of atom probe tomography and X-ray absorption spectroscopy that the majority of Mg in enamel is present as an inter-crystalline (grain boundary) precipitate of Mg-substituted amorphous calcium phosphate (Mg-ACP). We find evidence that these metastable, highly soluble precipitates are responsible for the rapid and highly anisotropic acid etching of enamel and provide short circuit pathways for fluoride diffusion. The very architecture that makes enamel mechanically robust may thus be its Achilles heel. Remarkably, inspiration on how to overcome this weakness comes from pigmented rodent enamel (Figure 7.2), where Mg-ACP has been completely replaced by a mixture of metastable ferrihydrite and amorphous iron phosphate. This substitution not only renders pigmented enamel mechanically harder than regular enamel, but also hardens it to acid attack to a greater extent than topical fluoride treatment. The implications of these discoveries are two-fold. For one thing, we envision APT will emerge as an integral tool for unraveling the etiology of caries at the nanoscale and develop approaches to early detection and therapy. For another, bio-inspired engineering of enamel grain boundaries may be a pathway to developing next generation, “post fluoride” dental care products.

Dental caries, also known as tooth decay, is the most prevalent disease in humans and affects the quality of life of billions of people worldwide¹⁹³. In dental caries, a bacterial biofilm produces a highly acidic environment causing the dissolution of the underlying mineralized tissue. Enamel, the outermost covering of the tooth is the most susceptible to caries^{78,157}. Unlike other mineralized tissues such as bone and den-

tin, enamel is acellular and does not have the capacity to self-regenerate. Current treatments involve replacing damaged tissue with polymeric resins or metal alloys¹⁹⁴. This approach is far from ideal, as the synthetic materials can fail and cause complications such as infection, loosening, lack of tissue integration, wear, and damage to surrounding healthy tissue. Moreover, the treatments used today are similar to those used nearly a century ago¹⁹³; there is a need for rational design of restorative materials and prophylactic measures. However the nanoscale structure and chemistry of the tissue and its response to acidic environments are not completely understood^{195,196}.

Tooth enamel is the hardest and most highly mineralized tissue in the vertebrate body and is composed predominantly of carbonated hydroxylapatite (cHAp, $\text{Ca}_{10}(\text{PO}_4)_6(\text{OH})_2$) with trace amounts of inorganic impurities, organic molecules, and water¹⁹⁵. Enamel is organized into a remarkable hierarchical structure that provides superior toughness and wear resistance, far exceeding those of synthetic apatite, which would shatter under the typical forces seen during mastication. The tissue is composed of three to five micron diameter bundles, called rods, which are woven together in a complex pattern that is easily revealed by acid etching (Figure 7.1a). The organization of rods within the tissue varies between species, but the fundamental structure is conserved. Each rod is composed of hundreds of thousands of crystallographically oriented, high aspect-ratio cHAp nanocrystals (Figure 1b,c). Between the rods are regions composed of poorly aligned crystallites enriched with proteinaceous material (inter-rod). The structure of enamel has been well documented, however understanding the structure and chemistry of the tissue at the nanoscale is essential to elucidate the process of enamel dissolution and subsequently develop novel treatments and prophylactics for dental caries.

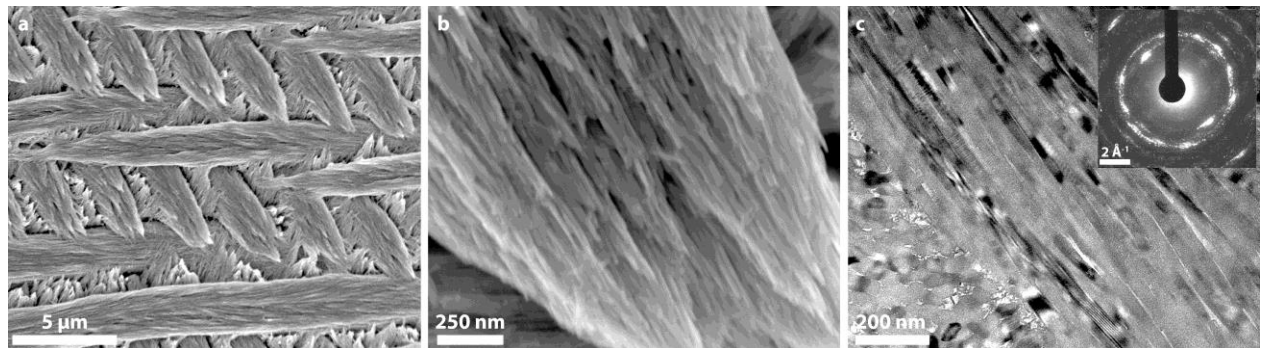


Figure 7.1: Hierarchical structure of rodent enamel

a low-magnification scanning electron micrograph (SEM) of acid etched mouse enamel surface revealing the woven layers of 3 to 5 μm rods (scale bar 20 μm). **b** higher magnification SEM image showing that each rod is in turn composed of thousands of high-aspect ratio carbonated hydroxyapatite nanocrystals (scale bar 250 nm), **c**, bright-field transmission electron micrograph through a singly rod showing the high-aspect ratio nanocrystals (scale bar 200 nm), the inset selected area electron diffraction patterns reveals the crystals are co-oriented along their crystallographic c-axis (scale bar 2 \AA^{-1}).



Figure 7.2: Rat mandible

Left side of rat mandible, red-brown iron-rich pigmented enamel layer is clearly visible on the continuously growing mandibular front incisor. Molar teeth do not exhibit the pigmented enamel layer.

7.2 RESULTS AND DISCUSSION

7.2.1 *Etching*

The susceptibility of enamel to dissolution in acidic environments was evaluated by acid etching, a technique commonly used to reveal micro- and nano-structure of mineralized tissues¹⁹⁷. Under controlled etching conditions designed to roughly approximate intra-oral conditions during carious attack, we observed that etching occurred most rapidly between the thousands of nanocrystals that make up each rod (intra-rod, Figure 7.3a). Surprisingly, we observed dramatic differences in morphology following etching when comparing inner enamel (Figure 2a) and the outer iron-rich pigmented enamel (Figure 7.3b) and synthetic high-purity sintered hydroxylapatite (Figure 7.4). Low magnification observation (Figure 7.5) of the surface prior to etching reveals limited porosity and no space between the grains, confirming dissolution was occurring during etching. Unlike the bulk inner enamel where etching was concentrated between individual crystals, the etching pattern in the pigmented outer enamel was completely reversed: the inter-crystalline material resisted etching and only slight dissolution of the bulk crystallites was observed. Quantitative measurement of etching rate, using inductively coupled plasma mass spectroscopy, (Figure 2d) corroborated these observations, non-pigmented enamel exhibited the fastest etching rate and pigmented enamel exhibited the slowest etching rate. Furthermore, removal of the pigmented layer by mechanical grinding increased the etching rate up to that of the naturally non-pigmented enamel.

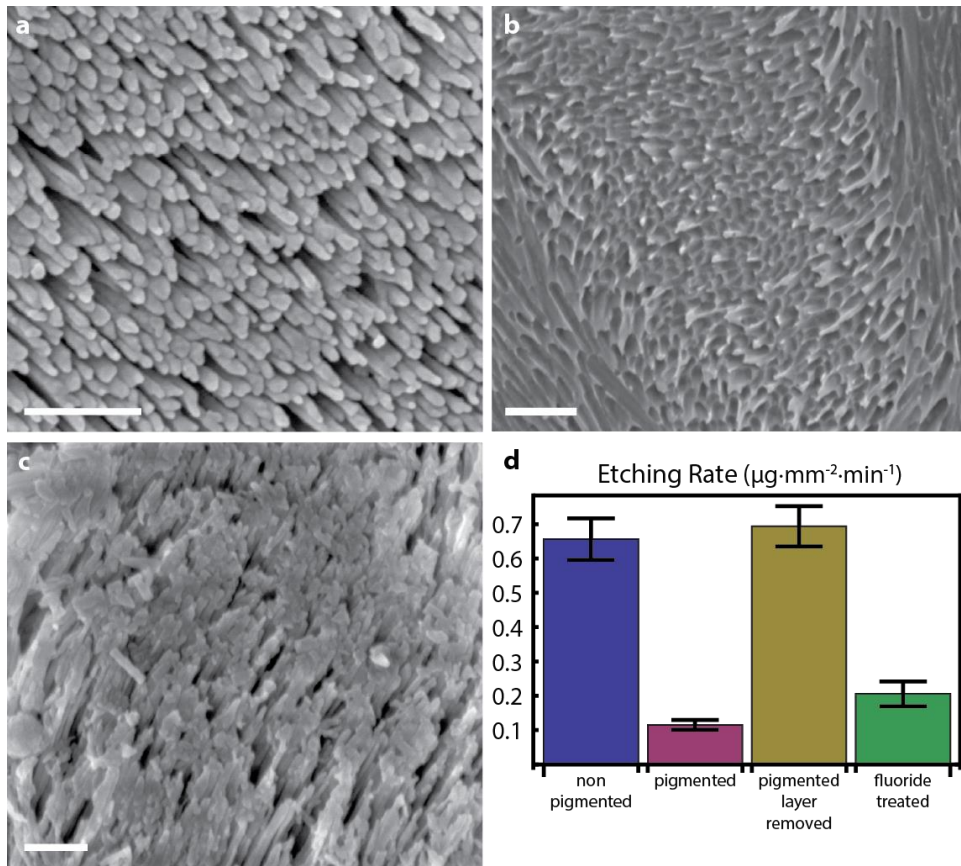


Figure 7.3: Controlled lactic acid etching of enamel

a non-pigmented inner enamel (house mouse, *Mus musculus*), **b** pigmented outer enamel (brown rat, *Rattus norvegicus*), **c** fluoride mouse inner enamel, Scale bars correspond to 250 nm. **d** Quantitative comparison of etching rates of enamel: naturally non-pigmented enamel (European rabbit, *Oryctolagus cuniculus*), beaver pigmented outer enamel, beaver inner enamel where the pigmented outer layer was mechanically removed, and fluoride treated beaver inner enamel (North American beaver, *Castor canadensis*).

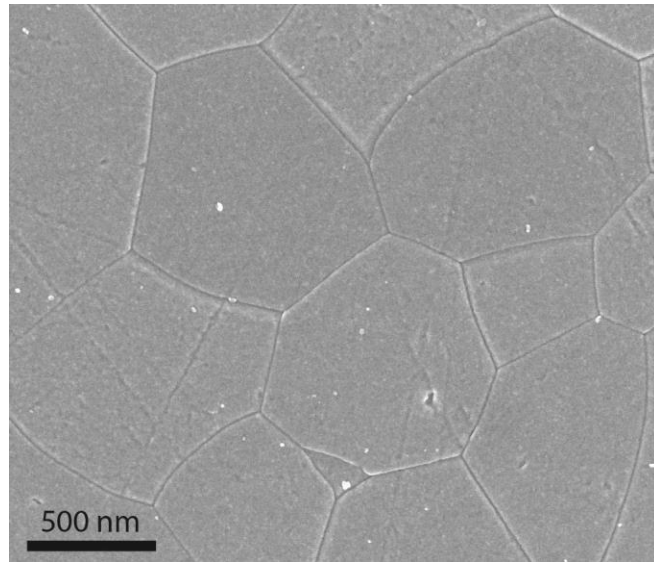


Figure 7.4: Etched sintered synthetic polycrystalline apatite.

Scanning electron micrograph of lactic acid etched surface of sintered synthetic polycrystalline apatite. Etching protocol used is identical to the enamel etching to facilitate comparison. Sample contained < 5 ppm Na and Mg impurities. Note the dramatic reduction in the magnitude of grain boundary corrosion.

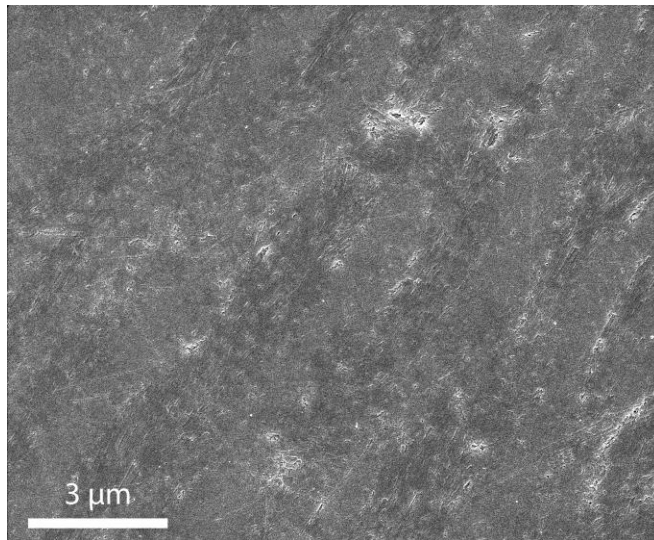


Figure 7.5: Un-etched polished enamel surface

Scanning electron micrograph of polished enamel surface before etching. Careful observation reveals faint contrast associated with the rods. Limited porosity is also visible.

Human enamel lacks the protection afforded by the insoluble pigmented coating. As such, numerous methods have been developed to reduce the susceptibility of enamel. The most widely used agent to protect enamel against dissolution and tooth decay is fluoride, which is known to reduce the solubility of enamel¹⁹³. While there is substantial empirical evidence to support its efficacy, the mechanisms responsible for protecting enamel and the role of fluoride in dental and skeletal fluorosis remain poorly understood¹⁹⁸⁻²⁰⁰. We sought to further understand the role of fluoride by topically administering soluble fluoride to enamel and performing etching experiments. Compared to the untreated inner enamel, the fluoride-treated tissue showed visually reduced dissolution (Figure 7.3c) and acid dissolution rates were reduced to values similar to that of the pigmented enamel layer. The dramatic differences in etching behavior between inner enamel, outer iron-rich pigmented enamel and fluoride treated enamel suggest that the chemistry of the tissue plays a significant role in controlling the susceptibility to acid dissolution.

7.2.2 *Mechanical Properties*

Although it is unlikely that the corrosion resistance of the pigmented enamel benefits the rodent as these teeth constantly grow. It has been suggested that the iron-rich material provides mechanical advantages, specifically; it hardens the surface of the tooth to reduce wear. Using nanoindentation we determined that the outer iron-rich pigmented layer is approximately 50% harder (up to 6 GPa) than the underlying inner enamel (3.5-4 GPa) (Figure 7.6). This is a result of changes associated with the presence of the harder iron-rich phase at the surface as non-pigmented surface regions at the edges of the tooth did not exhibit increased hardness.

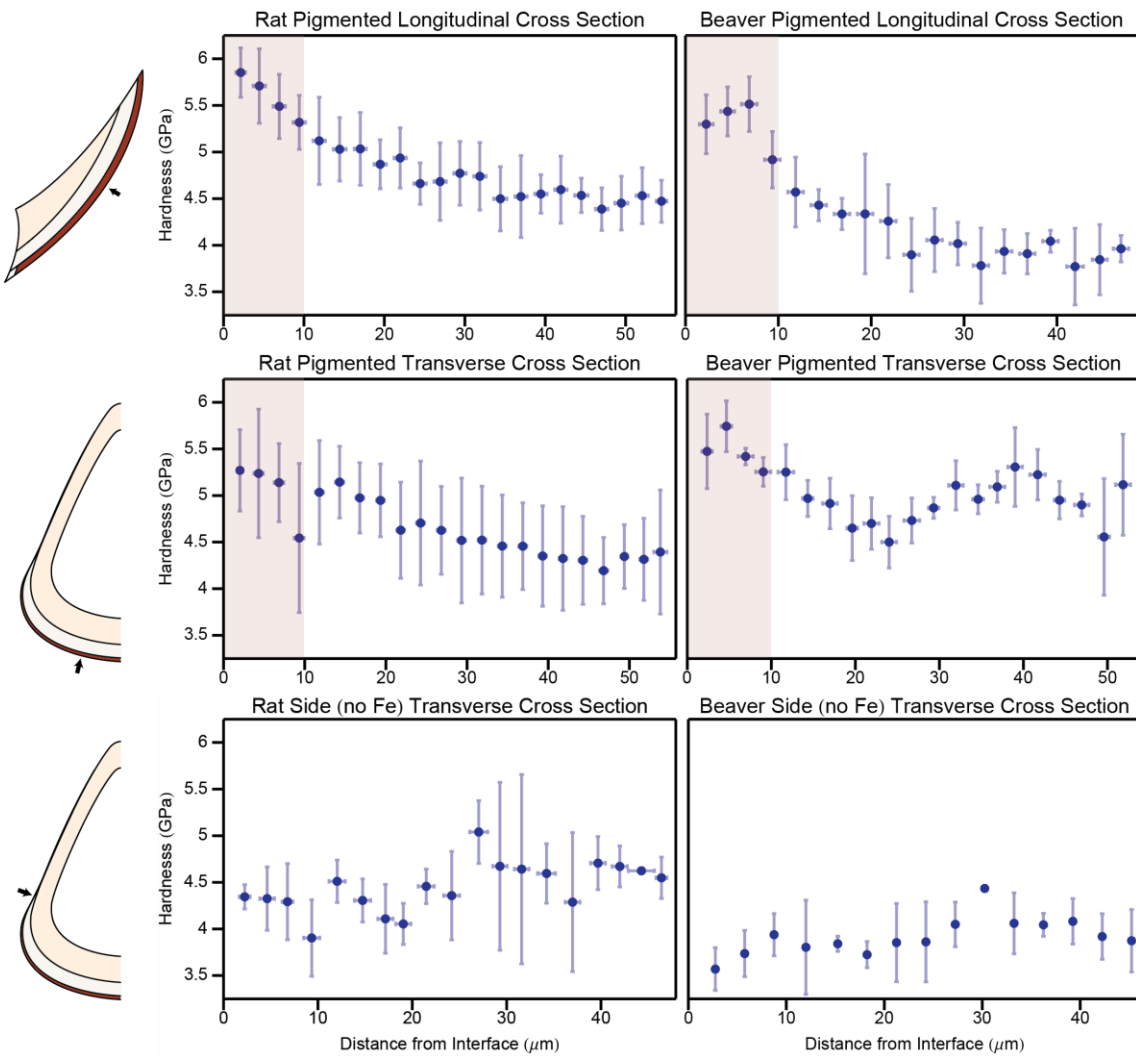


Figure 7.6: Enamel nanoindentation

Nanoindentation hardness measurements a function of the distance from the surface of rat and beaver pigmented and non-pigmented (no Fe) incisor enamel in transverse (left column) and longitudinal cross sections (right column). Black arrows on schematics of transverse and longitudinal incisor cross-sections indicate the approximate area where nanoindentations were performed. The approximate dimensions pigmented area is shaded brown in the schematics and on the plots. Areas at the side of the tooth where pigmentation (no Fe) is absent were used as a control.

7.2.3 Atom-probe tomography

Enamel is a chemically and structurally heterogeneous tissue, with trace chemical impurities that are difficult to detect with most microscopy and spectroscopy tools. Despite these challenges, these dilute impu-

rities (e.g. Na^+ , Mg^{2+} , Fe^{3+} , CO_3^{2-} , Cl^- , F) have a significant impact on enamel solubility and dictate the tissue's ability to withstand carious attack. We utilized atom-probe tomography (APT), a microscopy technique that is uniquely capable of elucidating the nanoscale structural and chemical complexity of biological minerals, including bone and dentin, which share a compositionally similar mineral phase to tooth enamel^{10,96}. APT mass to charge ratio spectra (Figure 7.7) obtained from inner, pigmented and fluoride treated enamel samples consisted primarily of Ca, P and O containing atomic and molecular ions, consistent with synthetic hydroxylapatite⁹⁶. In addition, Mg, Na, Fe, Cl, F, C and N containing ions were identified. Three-dimensional reconstruction of the sample volume containing Mg, Fe or F containing ions showed a chemically distinct intergranular phase rich in these impurities, which was particularly apparent at multiple crystal junctions (Figure 7.9). The bulk of the enamel crystals remained nearly free of most substituent elements and were clearly delineated by the Mg, Fe, or F impurities. Furthermore, correlative TEM imaging (Figure 7.8) of enamel APT sample ‘tips’ confirmed localization of impurities to crystal boundaries, and corroborates earlier observations of crystal boundaries in human enamel²⁰¹. These measurements put a new solubility limit on the order of a few hundred to a thousand ppm for Mg in biological apatite data, similar to the analyzed geological fluorapatite (Durango, 200 ppm).

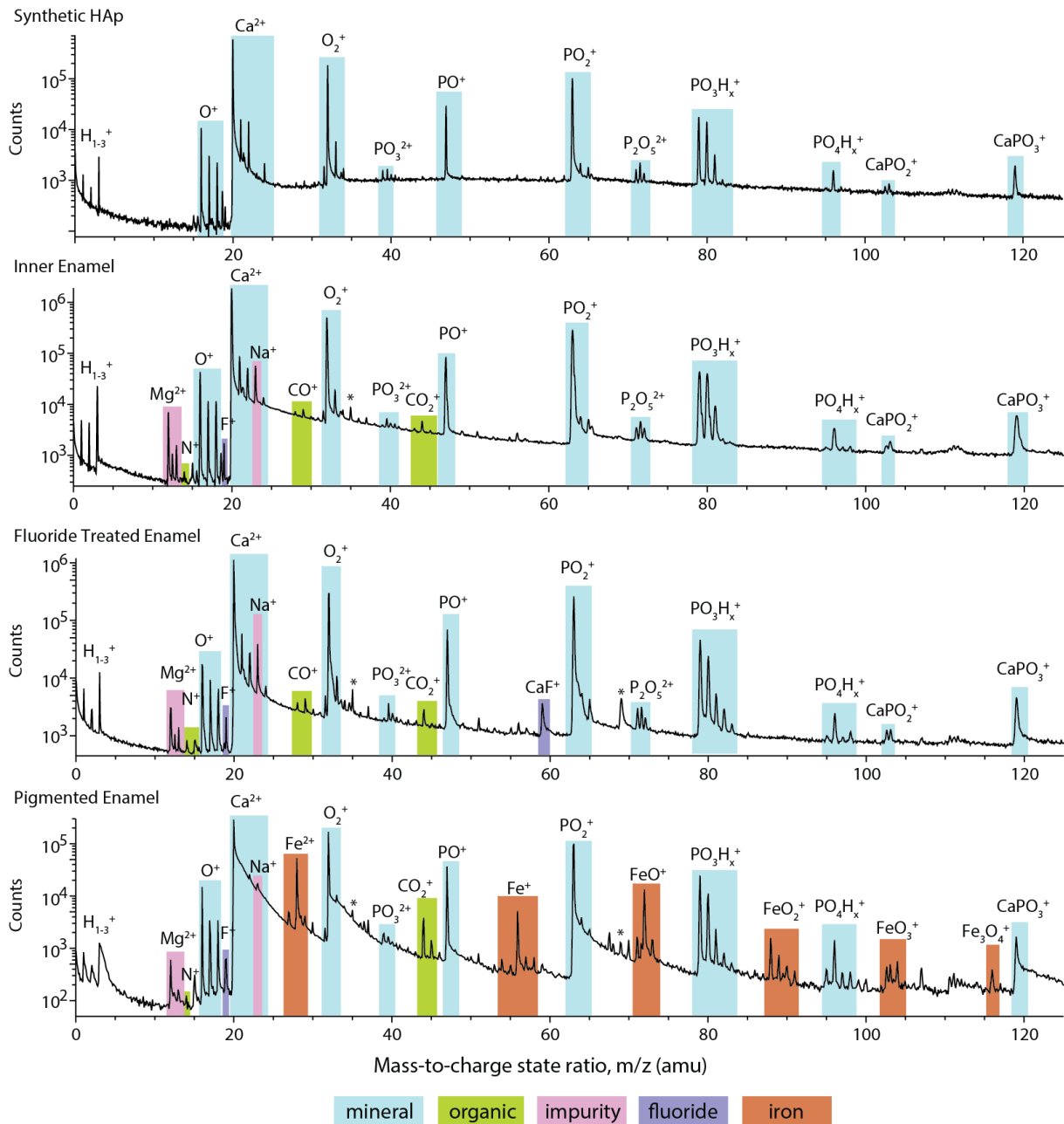


Figure 7.7: APT mass to charge ratio spectra

Mass to charge ratio spectra from APT analysis of a synthetic hydroxylapatite single crystal, mouse inner enamel, fluoride treated mouse inner enamel and rat pigmented enamel. Atomic and molecular fragments corresponding to calcium phosphates (mineral), organic molecular fragments, inorganic impurities, fluoride containing ions and iron oxides/oxyhydroxides are highlighted. * indicates focused ion beam implanted gallium.

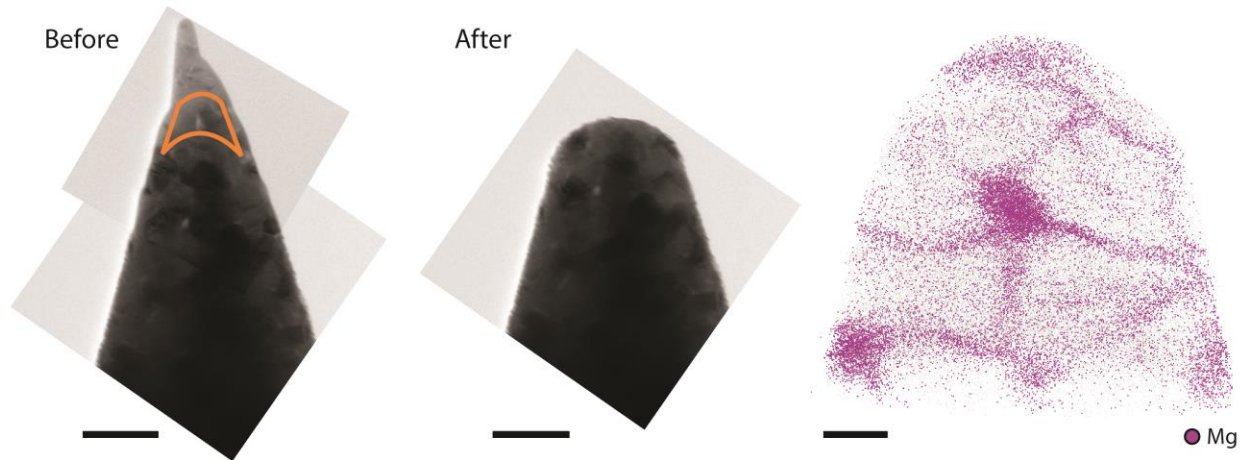


Figure 7.8: Correlative TEM imaging of enamel APT sample

Transmission electron micrographs before and after APT and corresponding 3D reconstruction of Mg ions in APT dataset. Approximate APT reconstruction volume is overlaid on the TEM image. Scale bars correspond to 100 and 10 nm for TEM and APT images, respectively.

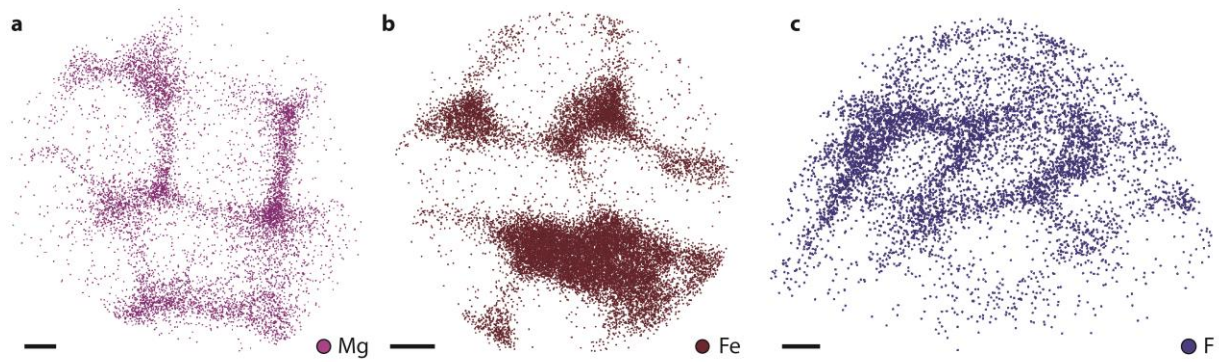


Figure 7.9: Atom-probe tomography 3D reconstructions

a Mg ($^{24}\text{Mg}^{2+}$) ion positions in mouse inner enamel, b Fe ($^{56}\text{Fe}^{2+}$) ions in pigmented rat outer enamel, c F ($^{40}\text{Ca}^{19}\text{F}^+$) ion positions in fluoride treated mouse inner enamel. For clarity ions are only rendered where local density exceeds background noise levels in the mass spectra. Scale bars correspond to 10 nm.

Intergranular phases were identified in inner enamel (Figure 7.9a), pigmented enamel (Figure 7.9b) and fluoride-treated enamel (Figure 3c), each was found to be chemically distinct both among enamel types

and unique from the bulk hydroxylapatite crystallites. The intergranular phase of inner enamel contained Na^+ , Mg^{2+} , and CO_3^{2-} , of which Mg was the most highly enriched, with concentrations of nearly one hundred times that of the bulk crystals (Table 7.1). Additionally, the majority of the remnant protein fragments, (identified by the detection of nitrogen originating from amino acids) were also found to be localized within the intergranular phase. Unlike calcitic and iron oxide biominerals the enamel apatite crystals do not appear to occlude organic material^{10,202}. In contrast to the inner enamel, the outer pigmented enamel contained an intergranular phase of dramatically different composition, highly enriched with Fe and nearly devoid of both Mg and nitrogen, indicating a lack of proteinaceous fragments. Observation of fluoride enrichment within the intergranular phase of fluoride inner enamel suggests that the intergranular phase provides a pathway for rapid diffusion into the tissue.

Table 7.1: Enamel composition

APT determined composition of synthetic OHAp single crystal, mouse inner enamel, pigmented rat enamel, and fluoride treated mouse inner enamel for both the bulk crystals and the grain boundary (G.B.) phase. The Mg-rich intergranular phase was isolated in the reconstruction with an 0.5 at% Mg isoconcentration surface, the Fe-rich intergranular phase was isolated in the reconstructions with a 5 at% Fe isoconcentration surface. C_{tot} is total carbon and C_{org} is the organic carbon estimated as 3.6 times the nitrogen concentration based on an average protein composition. Values are in at %. Bolded values highlight elements enriched in the grain. Dash indicates none detected.

	OHAp ⁹⁶		Inner Enamel		Pigmented Enamel		Fluoride Treated	
	Calc'd	Measured	Bulk	G.B.	Bulk	G.B.	Bulk	G.B.
Ca	22.7	23.8	28.4	28.0	27.7	18.4	25.7	27.8
P	13.6	16.9	14.4	14.5	17.1	13.1	15.8	14.4
O	59.1	56.4	51.5	51.2	52.7	54.2	54.2	51.1
H	4.55	2.9	4.6	3.4	1.65	3.2	2.3	2.2
Na	-	-	0.60	1.0	0.17	0.42	0.90	1.5
Mg	-	-	0.07	1.3	0.01	0.02	0.09	1.2
Fe	-	-	-	-	0.35	9.9	-	-
F	-	-	0.10	0.04	0.04	0.08	0.40	1.1
Cl	-	-	0.10	0.07	0.09	0.05	0.09	0.08
C_{tot}	-	-	0.12	0.40	0.09	0.51	0.13	0.36
C_{org}	-	-	0.03	0.14	0.09	0.40	0.06	0.18
N	-	-	0.01	0.04	0.04	0.11	0.02	0.05

To date, researchers have a limited understanding of how impurities are incorporated into enamel. There are three main paradigms that have been hypothesized:

- a) the impurities may be incorporated into the hydroxylapatite lattice
- b) they may occur in structurally distinct phases from the bulk
- c) or they may be associated with the organic fraction of enamel^{79,203}.

Our APT results eliminate the possibility of lattice incorporation, as the impurities are located between the grains of hydroxylapatite. This confirms earlier *in vitro* experiments, where researchers show that high-levels of impurities, in particular Mg, are not readily incorporated into the apatite crystal lattice^{79,204}. Furthermore, our data show that the impurity concentration exceeds the total carbon concentration, excluding the hypothesis where the impurities are all bound by organic molecules (Table 7.1). Excluding lattice accommodation and binding by organic molecules, only a single possibility remains: the impurities are present in an inorganic second phase. Thus far, possible Mg-containing phases in enamel have been proposed based largely on compositional similarities, specifically, huntite $[Mg_3Ca(CO_3)_4]$, dolomite $[CaMg(CO_3)_2]$ and whitlockite $[Mg(PO_4)_6PO_3OH]$. However these phases have not been observed experimentally⁷⁹. The Fe-rich phase is suggested to resemble ferrihydrite (a recently proposed composition is $Fe_{8.2}O_{8.5}(OH)_{7.4}\cdot 3H_2O$, see Ref.⁵³) based on Mossbauer spectroscopy²⁰⁵. Although no characteristic diffraction patterns were observed (Figure 7.14) ferrihydrite typically occurs in small nanoparticles leading to broad reflections which are difficult to detect. Enamel exposed to fluoride has been suggested to form crystalline fluorine-rich phases, such as fluorapatite $[Ca_5(PO_4)_3F]$ or fluorite (CaF_2) ²⁰⁶.

7.2.4 X-ray absorption spectroscopy

APT data indicate the interphase is an inorganic phase compositionally distinct from the bulk. While APT provided both spatial and chemical information, the technique is limited in its ability to directly resolve the atomic structure and the nature of the field evaporation process precludes straightforward interpreta-

tion of the local chemical and bonding environment of ions within the material⁹⁶. To probe the structure of Mg and Fe interphases, we utilized X-ray absorption spectroscopy (XAS), specifically X-ray absorption near edge structure (XANES) spectroscopy and extended X-ray absorption fine structure (EXAFS) spectroscopy, which provide complementary information about the short range order surrounding the absorbing atom. Mg *K*-edge XAS has been previously used to study the incorporation of Mg in biological amorphous and crystalline calcium carbonates^{109,207} and Fe *K*-edge XAS has used to probe the mineralization of iron oxides in the chiton radula where an organic complex was found to template ferrihydrite formation which subsequently transforms to magnetite (Chapter 5).

Mg XANES spectra (Figure 7.10) from crystalline reference compounds exhibit numerous peaks in the near-edge region compared to the relatively featureless enamel and ACP. The main Mg XANES feature is attributed to electronic transitions within the first-coordination sphere, while the nearby peaks evident in the crystalline samples result from multiple scattering from higher shells²⁰⁸⁻²¹⁰. The multiple scattering features are much weaker or completely absent in enamel and ACP spectra compared to the crystalline standards, suggesting that these spectra are dominated by interactions from the first coordination shell and that beyond the first shell the environment is poorly defined. The enamel XANES spectrum appears to closely match ACP and exhibits similarities with Mg substituted fluorapatite (FAp), but is otherwise distinct from the other reference samples. Compared to FAp, the spectral features in enamel are broader, indicating that Mg occupies a more disordered site. Furthermore, the edge shift to lower energies of the enamel and ACP spectra compared to whitlockite is indicative of a lower Mg-O coordination number and shorter Mg-O bond distance, consistent with an amorphous phase²⁰⁸.

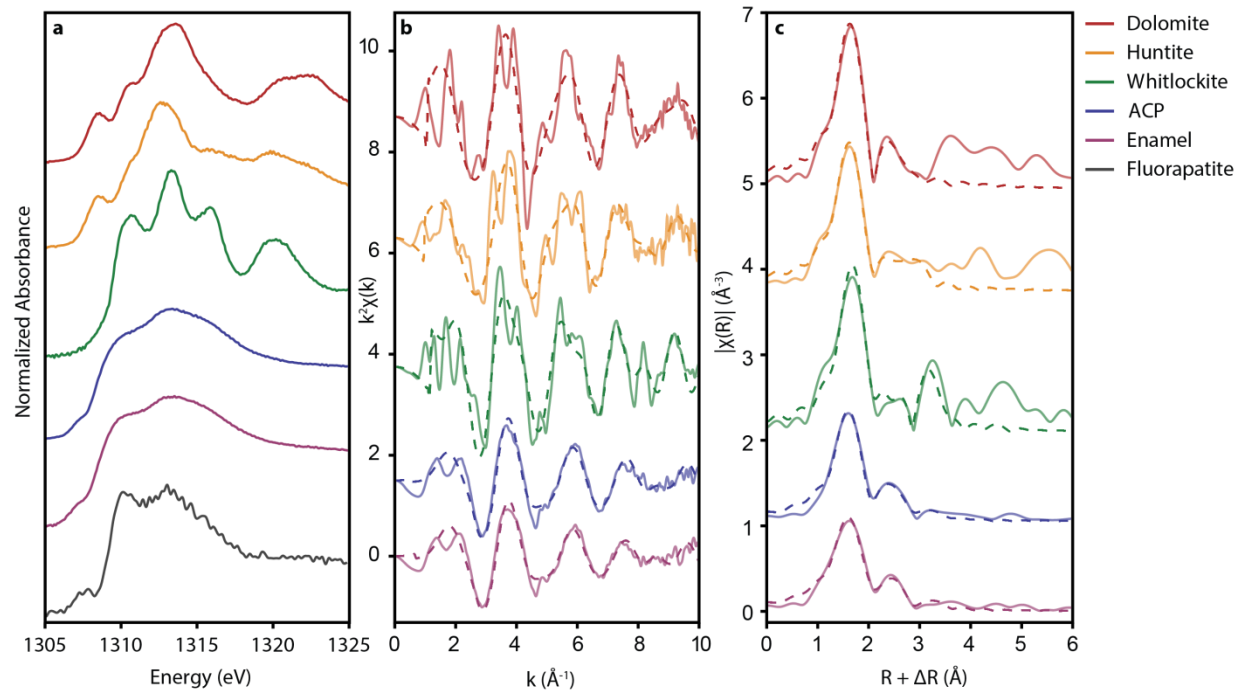


Figure 7.10: Mg K-edge X-ray absorption spectroscopy

X-ray absorption spectra of dolomite, huntite, whitlockite, Mg-substituted ACP, mouse enamel and Mg-substituted geological fluorapatite (Durango, Mexico). **a** XANES, **b** k -space (k^2 weighted) EXAFS, **c** real space EXAFS. Fits (dashed lines) are overlaid on measured EXAFS data (solid lines). Fitted EXAFS parameters are summarized in Table 7.2. EXAFS analysis could not be performed on the FAp sample due to low signal to noise arising from trace Mg concentration (200 ppm), high Na X-ray fluorescence background and overlapping absorption edges.

Confirming the qualitative assessment based on the XANES, the EXAFS spectra from enamel matches the ACP reference spectra and the dramatic reduction in higher frequency components in the enamel and ACP spectra compared to crystalline reference materials confirms the disordered environment around the Mg atoms (Figure 7.10). A quantitative analysis of the local environment around Mg was performed by fitting EXAFS spectra with theoretical scattering paths (Table 7.2). The measured Mg-O bond length in enamel (2.03 \AA) is notably shorter than the nearest neighbor Ca-O bond lengths in both HAp (2.40 \AA) and ACP (2.36 \AA)²¹¹⁻²¹³. It is likely that the compact structure around the Mg distorts the lattice and stabilizes the amorphous phase, a similar effect has been observed in biogenic Mg-substituted amorphous calcium

carbonate (ACC)²¹⁴. Not only is the Mg-O bond shorter than the Ca-O bond but the Mg-O bond length in enamel and ACP is also shorter than the Mg-O bond length in comparable crystalline reference materials, this shortening is coupled with the reduced Mg-O coordination number is indicative of an amorphous material²⁰⁸. Reduced bond distances are also associated with water in the first coordination sphere (hydrated Mg compounds have a shorter bond distance)¹⁰⁹. The Mg-rich interphase in enamel is amorphous exhibiting only short to medium range order out to approximately 3.5 Å, similar to ACP, based on Ca *K*-edge EXAFS and X-ray pair distribution function analysis^{214,25}.

There is an alternative hypothesis proposed based on Ca *K*-edge EXAFS and ²⁵Mg NMR of synthetic Mg-substituted ACP that Mg occupies disordered Ca[II] sites within the apatite crystal structure²¹⁵. We cannot exclude this possibility based on the spectroscopy data alone. However, the APT data shows a clearly distinct Mg-rich phase between the apatite crystals indicating that incorporation of the majority of the Mg within the bulk crystal lattice in enamel is unlikely.

Qualitative comparison of pigmented enamel Fe *K*-edge XANES spectra to reference standards suggests a structure similar to ferrihydrite (Figure 7.11), consistent with earlier Mossbauer results²⁰⁵, however, Fe *K*-edge XANES is not very sensitive to small changes in local structure. Comparison of the EXAFS reveals the higher frequency components are reduced, visible as a diminished beat pattern at 5 and 7.5 Å⁻¹ in *k*-space, corresponding reduced order beyond the first Fe-O coordination shell. Quantitative analysis of the EXAFS was again performed by fitting spectra with theoretical scattering paths (Table 7.2). Fe-O and Fe-Fe distances were nearly identical between pigmented enamel and synthetic ferrihydrite. The reduction in mean-square disorder (σ^2) of the first Fe-O bond, Fe-Fe coordination numbers and pre-edge intensity are all consistent with poorly crystalline ferrihydrite²¹⁶. Similar to the Mg-rich interphase the Fe-rich phase is also amorphous, exhibiting only short-medium range order up to about 4 Å and lacking any long-range order.

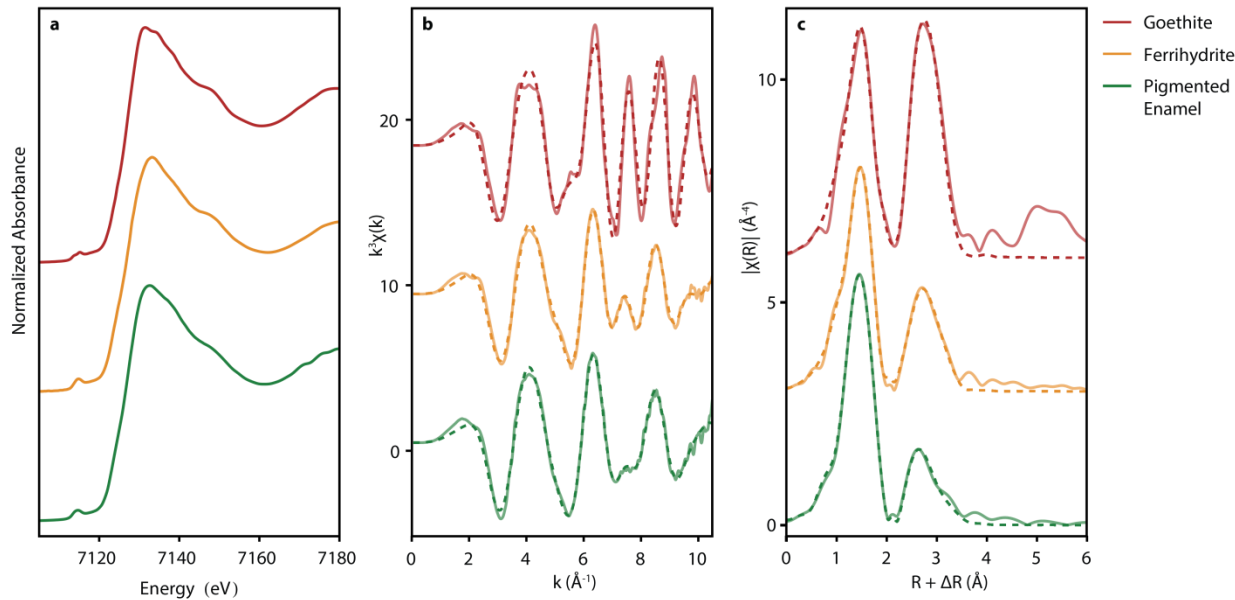


Figure 7.11: Fe K -edge X-ray absorption spectroscopy

X-ray absorption spectra of goethite, ferrihydrite and pigmented beaver enamel **a** XANES, **b** k -space (k^3 weighted) EXAFS, **c** real space EXAFS. Fits (dashed lined) are overlaid on measured EXAFS data (solid lines). Fitted EXAFS parameters are summarized in Table 7.2.

Table 7.2: EXAFS shell-by-shell fitting results

Radius, coordination number and σ^2 given for each fitted path. ΔE was fixed for individual paths but allowed to vary between samples. *R*-factors tabulated for Fe-O path, Fe-Fe paths and for all paths combined. Amplitude reduction factor (0.95 for Fe and 0.8 for Mg) was fixed based on the fit to goethite (Fe) and a simultaneous fit to Whitlockite, Huntite and Dolomite (Mg). Bolded values are held constant in the fit and asterisks indicates values fixed based on crystal structure. Multiple scattering paths are described in the methods. Uncertainty in the last digits are given in parenthesis.

Sample	Path	R (Å)	CN	σ^2	ΔE (eV)	R-factor
Dolomite	Mg-O ₁	2.07(1)	6*	0.0038(9)	4.4	0.7%
	Mg-C	2.99(3)	6*	0.001(3)		
	Mg-O-C	3.14(6)	12*	0.005		
	Mg-O ₂	3.48(4)	6*	0.010(8)		
Huntite	Mg-O ₁	2.06(1)	6*	0.006(1)	3.5	1.2%
	Mg-C	3.08(8)	6*	0.01(2)		
	Mg-O-C	3.4(2)	12*	0.02		
	Mg-O ₂	3.38(4)	6*	0.01(1)		
Whitlockite	Mg-O	2.08(2)	6*	0.006(2)	5.3	5.5%
	Mg-P	3.37(6)	6*	0.006(7)		
	Mg-Ca	3.50(4)	6*	0.004(4)		
ACP	Mg-O	2.02(2)	3.8(8)	0.005(3)	1.8	1.3%
	Mg-P ₁	3.17(6)	3(3)	0.005(9)		
	Mg-P ₂	3.39(8)	3(3)	0.005(9)		
Enamel	Mg-O	2.03(2)	4(1)	0.00899	0.9	1.0%
	Mg-P ₁	3.18(6)	3(3)	0.003(9)		
	Mg-P ₂	3.40(9)	3(3)	0.003(9)		
Goethite	Fe-O ₁	1.95(2)	3*	0.009(2)	-4.8	0.9%
	Fe-O ₂	2.06(3)	3*	0.012(4)		
	Fe-Fe ₁	3.01(1)	2*	0.005(1)		
	Fe-Fe ₂	3.23(4)	2*	0.012(7)		
	Fe-Fe ₃	3.39(1)	4*	0.009(2)		
	Fe-O-O	3.47	12*	0.009		
	Fe-O-O	3.54	12*	0.012		
Ferrihydrite	Fe-O	1.96(1)	4.6(6)	0.011(1)	-5.2	0.2%
	Fe-Fe ₁	3.04(2)	1.9(4)	0.013		
	Fe-Fe ₂	3.44(2)	1.7(4)	0.011		
	Fe-O-O	3.45	18.6	0.011		
Pigmented Enamel	Fe-O	1.95(1)	4.4(5)	0.008(1)	-5.5	0.1%
	Fe-Fe ₁	3.02(2)	1.5(4)	0.013		
	Fe-Fe ₂	3.44(3)	1.0(4)	0.011		
	Fe-O-O	3.40	17.7	0.008		

7.2.5 Amorphous iron phosphate

APT measurements indicated phosphates (13 at%) are present within the Fe-rich intergranular phase. Phosphates are known to dramatically affect the growth of iron oxyhydroxides. As an alternative to an amorphous ferrihydrite-like structure the EXAFS spectra can be interpreted as a mixture of ferrihydrite and amorphous iron phosphate, i.e. a fraction of the Fe is coordinated by phosphate (Figure 7.12)²¹⁷. This could also explain the differences in the Fe-O σ^2 fit and the pre-edge intensity (Figure 7.13). The iron-rich pigmented enamel also exhibited much greater thermal stability (Figure 7.14) compared to ferrihydrite⁵³, consistent with the presence of phosphate ligands preventing crystallization. Despite the indications for iron phosphate we did not find evidence of Fe-O-P coordination by Raman (Figure 7.15) or P K-edge XANES spectroscopy (Figure 7.16). It is likely that high levels of non-iron coordinated phosphates in the surrounding apatite masked the signal. The corrosion resistance of iron phosphates could be playing an important role in the resistance to acid dissolution exhibited by these materials²¹⁸. The P K-edge XANES spectra from the pigmented enamel spectra was broader than the corresponding spectra from synthetic OHAp. Although this could be a result of increased disorder in the biogenic apatite it is possible that it is due to the presence of a highly-disordered iron phosphate component in the pigmented enamel. Spatially resolved measurements of P K-edge XANES spectra at multiple positions from the surface on a polished incisor cross-section by X-ray photoemission electron microscopy (X-PEEM) indicated that the spectral broadening is confined to the iron-rich pigmented enamel layer and provides further evidence for the existence of amorphous iron phosphates (Figure 7.17). The presence of phosphates suggests a mineral similar to bacterioferritin cores or the amorphous iron phosphate present in certain species of chiton teeth¹. The presence of phosphates also helps explain the formation of ferrihydrite a thermodynamically unstable polymorph, where the absence of ligands which interfere with crystallization would have led to the formation of crystalline iron oxyhydroxides.

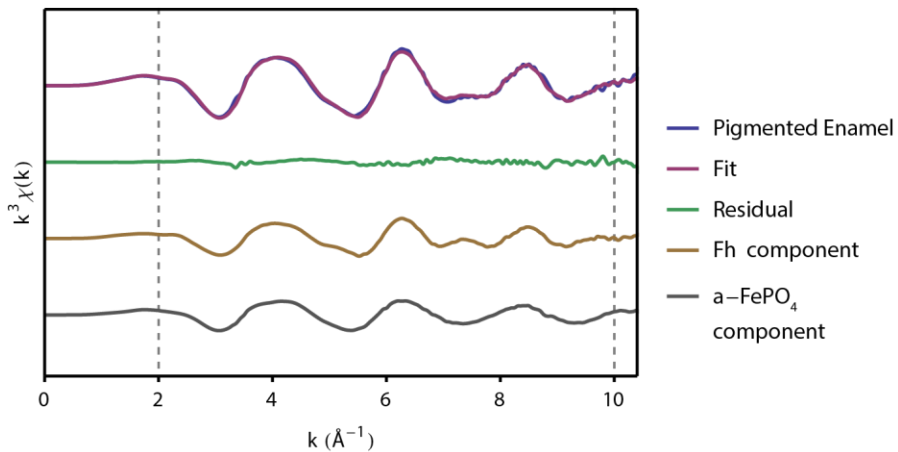


Figure 7.12: Linear combination fitting

Fitting of k^3 weighted EXAFS of beaver pigmented enamel as a linear combination of reference ferrihydrite (Fh, 58%) and amorphous iron(III) phosphate spectra ($\text{a}-\text{FePO}_4$, 42%). Spectra are offset for clarity. Uncertainty in fits is $\pm 3\%$.

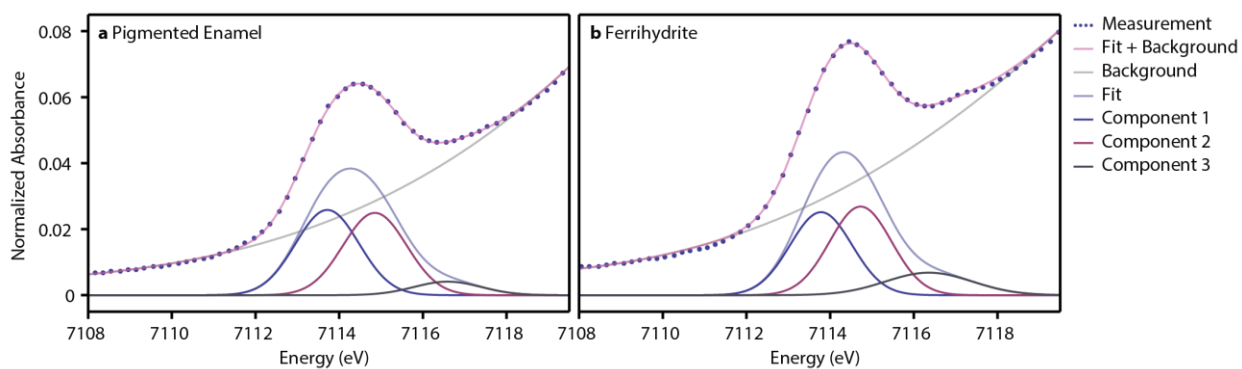


Figure 7.13: Fe K-edge XAS Pre-edge comparison

Pre-edge spectra and background subtracted Gaussian multi-component fitting of beaver pigmented enamel (a) and reference “2-line” ferrihydrite (b).

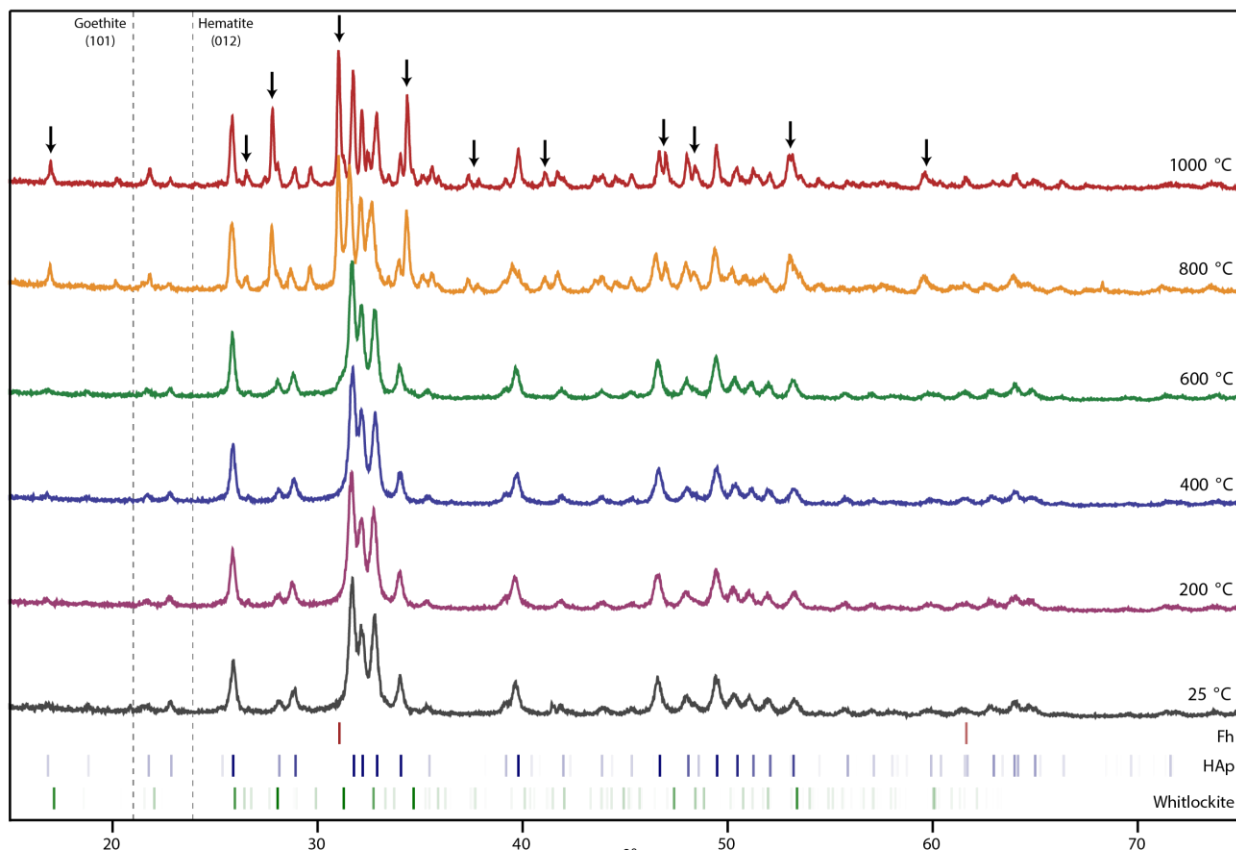


Figure 7.14: Thermal stability of pigmented enamel

Powder X-ray diffraction spectra of heated beaver pigmented enamel samples. Phase transformation, identified by the appearance of new diffraction peaks (indicated with black arrows) corresponding to whitlockite $[(\text{MgFe})(\text{PO}_4)_6\text{PO}_3\text{OH}]$ when heated to 800 °C. In comparison pure ferrihydrite will transform to more thermodynamically stable iron oxides and oxyhydroxides at temperatures as low as 200°C⁵³. Reflections for, “2-line” ferrihydrite (Fh, red), hydroxyapatite (HAp, blue) and whitlockite (green) are indicated, dashed lines correspond to strong goethite (101) and hematite (012) reflections free of overlaps which are absent in the measured spectra, yet would be expected as transformation products of ferrihydrite. Spectra are offset vertically for clarity.

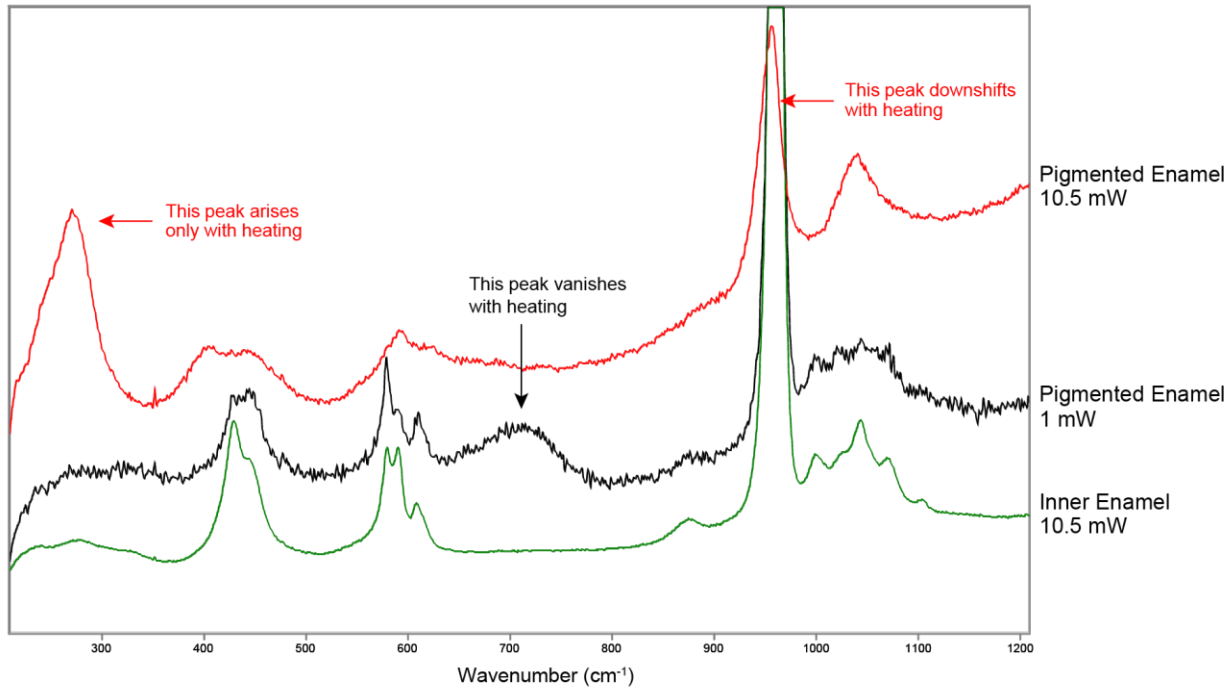


Figure 7.15: Raman spectroscopy of enamel.

Raman spectra of pigmented enamel measured at low laser power (1 mW, black) and a spectra measured under high laser power (10.5 mW, red) subject to laser heating artifacts (indicated with red arrows) compared to a reference spectra from non-pigmented inner enamel (green). The broad feature present in the spectra measured at low laser power (unheated) centered at $\sim 700\text{ cm}^{-1}$, indicated with a black arrow, which disappears upon heating is consistent with ferrihydrite²¹⁹. Spectra are offset for clarity.

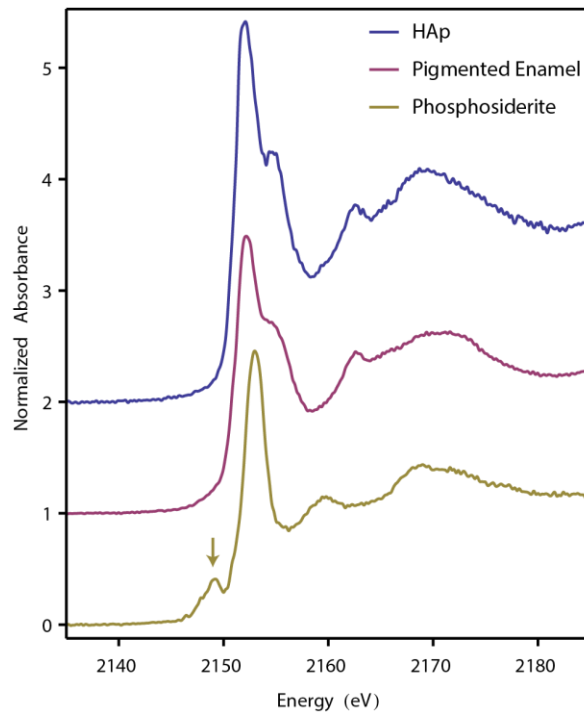


Figure 7.16: P K-edge XANES

Phosphorus K-edge XANES spectra of beaver pigmented enamel compared to hydroxylapatite (HAp) and phosphosiderite ($\text{Fe}^{3+}\text{PO}_4 \cdot 2\text{H}_2\text{O}$). Note the pre-edge feature (indicated with a yellow arrow) in the phosphosiderite spectra which results from phosphate coordinated by a 3d transition metal²²⁰, which is absent in the pigmented enamel and hydroxylapatite spectra. Spectra are offset for clarity.

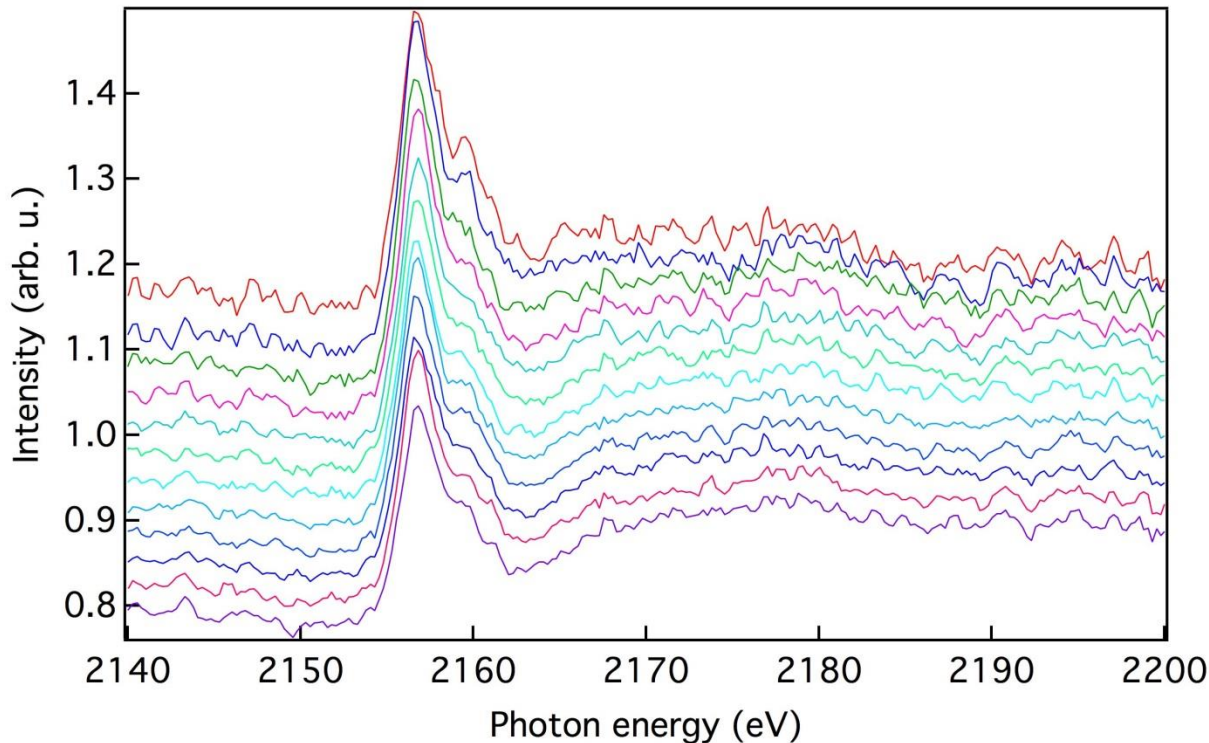


Figure 7.17: P-K edge Photoelectron Emission Microscopy

Spatially resolved XANES spectra reveal increased broadening on the P-K edge towards the pigmented enamel surface (lower spectra) from the bulk (upper spectra). This is indicative of an increasingly disordered local environment around the phosphorus in the pigmented enamel consistent with the presence of amorphous iron phosphates. However, the pre-edge which would provide definitive evidence of iron-phosphate coordination is still not resolved.

7.3 CONCLUSION

These results provide an answer to the long standing question of localization of impurities in tooth enamel. In particular, Mg, where concentrations have been suggested to exceed empirically measured solubility limits. The chemically distinct intergranular phases found in enamel were found to dramatically influence the physiochemical properties. It appears that the multitude of interfaces that contribute mechanical toughness to the tissue might result in the observed rapid anisotropic acid etching. The pigmented layer at

the surface of rodent enamel, where the soluble Mg-ACP phase is replaced by much less soluble Fe-rich phases provides potential inspiration for enamel grain boundary engineering for caries prevention.

This work addresses the influence of compositionally and structurally distinct intergranular phases on the physiochemical properties of tooth enamel. However, further study is needed to understand the complexities of the combined demineralization-remineralization occurring *in vivo*. New understanding of nanoscale chemical heterogeneity responsible for controlling tooth decay processes, possible insight into developing new prophylactics and treatments for dental caries.

7.4 MATERIALS AND METHODS

7.4.1 *Consumables*

Unless otherwise specified, the following chemicals were used without further purification: potassium hydroxide (KOH), sodium hydroxide (NaOH), acetone [(CH₃)₂CO] (VWR, West Chester, PA); bromoform (CHBr₃), Fe(III) nitrate nonahydrate [Fe(NO₃)₃·9H₂O], Fe(III) phosphate dehydrate (FePO₄·2H₂O), sodium fluoride (NaF), calcium nitrate tetrahydrate [Ca(NO₃)₂·4H₂O], magnesium nitrate hexahydrate [Mg(NO₃)₂·6H₂O], ammonium phosphate dibasic [(NH₄)₂HPO₄], sodium phosphate (Na₃PO₄), lactic acid (C₃H₆O₃), magnesium oxide (MgO) (Sigma-Aldrich, St. Louis, MO); Epo-Tek 301 epoxy (Epoxy Technology, Billerica, MA); CarbiMet II SiC grinding paper, Microcut SiC grinding paper, Metadi supreme polycrystalline aqueous diamond polishing suspension, Masterprep Alumina suspension, Trident polishing cloth, Chemomet polishing cloth (Buehler, Lake Bluff, IL); Conductive Liquid Silver Paint (Ted Pella, Redding, CA). Super Glue Cyanoacrylate Adhesive (3M, St. Paul, MN); Ultrapure Water ($\rho = 18.2\text{ M}\Omega\cdot\text{cm}$) was prepared with a Barnstead Nanopure UF+UV ultrapure water purification system (Thermo-Fisher Scientific, Waltham, MA).

7.4.2 *Embedding, Grinding and Polishing*

Lower (mandibular) incisors were dried in air following extraction and embedded in Epo-Tek 301 epoxy and polymerized overnight at 25 °C. The embedded samples were ground using progressively finer grits of Buehler SiC grinding paper (400, 600, 800 & 1200 grit), polished using 3 and 1.0 µm polycrystalline aqueous diamond polishing suspensions on a Buehler Trident polishing cloth followed by 0.05 µm Al₂O₃ suspension on a Buehler Chemomet polishing cloth. Samples were rinsed with water and dried under flowing argon gas.

7.4.3 *Fluoride Exposure*

Freshly ground and polished mouse incisor cross-sections were submerged in 0.25 M NaF solution and maintained at 37 °C for 24 hr on a rotator. Following fluoride exposure samples were rinsed with water and dried under flowing nitrogen gas.

7.4.4 *Mounting and Coating*

Samples were secured to an aluminum stub with cyanoacrylate adhesive, coated with ~5 nm of Pt with an Ion Beam Sputter Deposition and Etching System (IBS/e, South Bay Technologies, San Clemente, CA) operating at a base pressure of <10⁻⁴ Pa, a working pressure of 10⁻² Pa argon, with two ion guns operating at 8 kV at 3 mA per gun. The coating was grounded to the stub with conductive liquid silver paint.

7.4.5 *Scanning Electron Microscopy*

SEM was performed with an FEI Helios Nanolab (Hillsboro, OR) operating at 5 keV with 0.1 nA probe current.

7.4.6 *Transmission Electron Microscopy Sample Preparation*

Transmission electron microscopy (TEM) lamella were prepared from a polished mouse incisor cross section following established procedures with a DualBeam scanning electron microscope (SEM) and focused ion beam (FIB) instrument (Helios NanoLab, FEI, Hillsboro, OR)¹²⁶. First a strap of platinum (FIB-Pt)

was deposited over a region of interest on the polished cross-section using the ion beam (30kV, 93pA) to locally decompose an organometallic precursor gas (methyl cyclopentadienyl trimethyl platinum [$C_5H_5Pt(CH_3)_3$]). Two trenches were then milled out (30kV, 6.5nA) on either side of a 2 μm thick slice of material. The slice of material was cut free (30kV, 2.8nA) from the substrate on three sides leaving only small connecting bridge. An *in situ* tungsten nanomanipulator probe (Omniprobe) was attached to the free side of the substrate using FIB-Pt (30kV, 93pA). The remaining connection to the substrate was milled away (30kV, 93pA) and the probe was retracted with the sample. The sample was then welded to a copper TEM half-grid (Omniprobe) using FIB-Pt and the connection to the probe was milled away (30kV, 93pA). The lamella was successively thinned to ~100nm at 30 kV (93pA) at a 1-2° angle grazing incidence milling condition. The majority of the surface amorphization and gallium implantation was removed by low angle milling (~7°) at 5 and 2 kV (28pA) to thin the sample to approximately 60-80nm.

7.4.7 *Transmission Electron Microscopy*

TEM was performed with a Hitachi H-7700 (Hitachi High-Technologies Science America, Northridge, CA) operating at 120 kV.

7.4.8 *Atom Probe Tomography Sample Preparation*

Samples for APT were prepared using the dual-beam SEM/FIB instrument (Helios Nanolab, FEI, Hillsboro, Oregon) using established protocols^{100-102,221}. First a rectangle of platinum (FIB-Pt) was deposited over a region of interest on the polished cross-section using the ion beam (30kV, 93pA) to locally decompose an organometallic precursor gas, methyl cyclopentadienyl trimethyl platinum [$C_5H_5Pt(CH_3)_3$], over a region of interest (2 x 25 μm) on the polished cross-sections or directly on faceted crystals. A wedge of material below the Pt strap was cut out on three sides. The wedge was attached to an in-situ nanomanipulator (Omniprobe, Dallas, TX) using FIB deposited Pt before cutting the final edge free. 1-2 μm wide segments were cut from the wedge and sequentially affixed to the tops of Si posts in an array (Cameca Scientific Instruments, Madison, WI) with FIB-Pt. Each tip was shaped and sharpened using

annular milling patterns of increasingly smaller inner and outer diameters. The majority of the amorphized surface region and implanted gallium in the tip surface was removed by milling at 2 kV, 0.4 nA.

7.4.9 Atom Probe Tomography

Atom probe tomographic analyses were conducted in a Cameca local-electrode atom-probe tomograph (LEAP 4000XS_i, Cameca, Madison, WI) using a pulsed laser ($\lambda = 355$ nm, 200-250 kHz, 50-150 pJ per pulse). The DC potential on a microtip during APT was controlled to maintain an evaporation rate between of either 0.0025 or 0.005 ions per laser pulse. The base temperature of the microtip was maintained at 40 K and the ambient vacuum pressure was below 10^{-8} Pa. Peak ranges were defined as the entire visible peak and background subtraction was done using side-band subtraction¹⁸⁹.

Three-dimensional reconstruction of APT data was performed using the Cameca integrated visualization and analysis software (IVAS) based on published algorithms, assuming a hemispherical tip shape^{83,105}. Standard reconstruction parameters were used with an electric field dependent tip radius (r). The average evaporation field (F_e) of the enamel apatite ($14 \text{ V}\cdot\text{nm}^{-1}$) was measured by acquiring either SEM or TEM images of microtips after APT analysis. Atomic volumes for the reconstruction were calculated based on the hydroxyapatite crystal structure²¹³.

7.4.10 Reference Materials

Mg substituted ACP was prepared by rapidly mixing a solution 100 mL of 0.20 M Na₃PO₄ with 100 mL of 0.29 M Ca(NO₃)₂ + 0.12 M Mg(NO₃)₂ at 25°C. The resulting precipitate was immediately vacuum filtered and washed with water and dried under vacuum.

Whitlockite was prepared based on Fadeev et. al²²². Briefly, a solution of 100 mL 1 M Ca(NO₃)₂ + 1.11 M Mg(NO₃)₂ was stirred while 100 mL of 0.67 M (NH₄)₂HPO₄ was added dropwise. This solution was stirred for 4 hours and the resulting mixture was vacuum filtered, washed with water, and dried overnight at 100 °C in air. The dried powder was subsequently heated to 700 °C for 3 hours in air.

“2-line” ferrihydrite was synthesized based on a modification of the protocol given by Cornell and Schwertman¹³¹. An aqueous solution of Fe(NO₃)₃ (100 mL, 0.2 M) was rapidly titrated to pH 7 with an aqueous solution of KOH (1 M). The resulting precipitate was washed extensively with water by vacuum filtration, frozen in liquid nitrogen, and lyophilized. The lyophilized powder was ground with an agate mortar and pestle.

Goethite was synthesized based on the protocol given by Cornell and Schwertman¹³¹. Briefly, aqueous KOH (5 M, 68 mL) was rapidly added to a stirred solution of Fe(NO₃)₃ (1 M, 38 mL) in a polyethylene container, the mixture was diluted to 750 mL with water, sealed, and heated to 70 °C for 5 days. The resulting precipitate was washed extensively with water by vacuum filtration and dried under vacuum. Dried powder was ground in an agate mortar and pestle.

Geological reference minerals originated from the following localities: York, PA (Dolomite); Durango, Mexico (Fluorapatite), Tea Tree Gully, Australia (Huntite); and Andes Mountains, Peru (Phosphosiderite).

Phase purity of reference materials was verified by powder X-ray diffraction (XRD) and inductively coupled plasma mass-spectroscopy (ICP-MS).

7.4.11 Powder X-ray diffraction

Powdered samples were suspended in acetone and dispersed on the surface of an off-axis cut quartz single crystal plate (MTI Technologies, Richmond, CA). Remaining acetone was allowed to evaporate. Samples were analyzed with a Scintag diffractometer with a Cu-K α X-ray source operating at 40 kV and 20 mA. Diffracted intensity was recorded between $2\theta = 5^\circ$ - 90° with a step size of 0.05° and a dwell time of 2 seconds per step. An energy dispersive X-ray detector was used to count only diffracted Cu-K α X-rays and exclude X-ray fluorescence.

7.4.12 *Sintered Hydroxylapatite*

Synthetic apatite powder (Sigma-Aldrich) was pressed into a pellet in a steel die using a hydraulic press.

Pellet was subsequently heated to 800 °C for 3 hr in air supported in an alumina crucible.

7.4.13 *Acid etching*

For scanning electron microscopy freshly polished epoxy embedded enamel cross-section samples were etched for 15 seconds (Figure 2) or 1 minute (Figure 1) at 25 °C in 0.25 M lactic acid adjusted to pH 4.0 with NaOH.

For quantitative etching measurements incisors were cut into ~5 mm sections with a slow speed diamond saw (Buehler Isomet). Dentin surfaces were masked from etching using nail varnish (Sally Hansen, COTY Inc., New York, NY). A nail-varnish coated silicon wafer was used as a control. Sample surface areas were measured with a calibrated stereo-microscope. Samples were etched in individual 2 mL tubes each containing 1.5 mL 0.25 M lactic acid adjusted to pH 4.0 with NaOH and etched on a rotator at 37 °C. After 1, 10 and 100 min time-points, 200 µL aliquots were removed from the etchant solution for analysis by ICP-MS. Mass loss during etching was determined by calculating the total mass of Ca, P, Fe and Sr in solution and accounting for oxygen by stoichiometry. Trace levels of organics, other metals, water and carbonate were not accounted for. Etching rate was determined by fitting a linear model to the cumulative mass loss over time.

7.4.14 *Microwave Digestion*

Mineral powders were weighed out (~10 mg) using a Toledo XS205 DeltaRange analytical balance (Mettler-Toledo, Columbus, OH, USA). Powdered samples were added to pre-weighed 10 mL Nalgene™ Oak Ridge high-speed Teflon™ FEP centrifuge tubes (Thermo Fisher Scientific, Waltham, MA, USA). 200 µL of TraceSelect® nitric acid (\geq 69%, Sigma-Aldrich Chemical Co., St. Louis, MO, USA) was then added to the Teflon™ FEP centrifuge tubes and capped. Samples were then placed into Teflon™ Microwave

digestion vessels and assembled into the high pressure rotor (HPR 1000/10) of a Milestone EthosEZ closed microwave digestion system (Milestone, Sorisole, Italy). Samples were microwaved using the following parameters: ramp to 120 °C for 20 minutes at 600 W, 120 °C hold for 1 hour at 400 W, exhaust for 30 minutes. Following digestion, samples were weighed out to account for sample loss and prepared for ICP-MS analysis.

7.4.15 ICP-MS

10-100 µL aliquots of the microwave-digested mineral samples or lactic acid etching solution were placed in metal-free 1.5 mL tubes and diluted up to 10-fold with ultrapure de-ionized water (samples were diluted in order to obtain accurate ppb levels of selected elements). ICP-MS samples were then prepared by adding pre-determined amounts of diluted sample followed by addition of TraceSelect® nitric acid (final concentration of 3% v/v), 5 ng/g of a multi-element internal standard (CLISS-1 standard containing Bi, Ho, In, Li⁶, Sc, Tb, and Y from Spex CertiPrep, Metuchen, NJ, USA), and ultrapure de-ionized water to obtain a final ICP-MS sample volume of 5 mL. Fully quantitative standards for Na, Mg, P, Ca and Fe (Inorganic Ventures, Christiansburg, VA, USA) were prepared at 1000, 500, 250, 125, 62.5, 31.25, 15.625, 7.8125 and 3.90625 ng/g containing 5 ng/g multi-element internal standard and 3.0% (v/v) TraceSelect® nitric acid.

ICP-MS analysis was performed on a computer-controlled Thermo X series II ICP-MS (Thermo Fisher Scientific, Waltham, MA, USA) equipped with a CETAC 260 autosampler (Teledyne CETAC Technologies, Omaha, NE, USA). Each sample was acquired using 1 survey run (10 sweeps) and 3 main peak jumping runs (100 sweeps per run). The isotopes selected for analysis were ²³Na (LOD = 1 ppb) , ^{24,25,26}Mg (LOD = 0.1 ppb), ³¹P (LOD = 20 ppb), ⁴⁴Ca (LOD = 50 ppb), and ⁵⁷Fe (LOD = 5 ppb) using ⁴⁵Sc, ⁸⁹Y, and ¹¹⁵In for internal standardization. Instrument performance was optimized using custom autotune sequence and TuneA solution (Thermo Fisher Scientific, Waltham, MA, USA), followed by a custom performance report.

7.4.16 Enamel Separation for Mg-XAS

Mice incisors were ground in an agate mortar and pestle. Enamel was isolated by centrifugation in a bromoform-acetone mixture with specific gravity of 2.7 (8 vol % acetone). The sinking enamel fraction was separated from the floating fraction (dentin, bone and cementum) by freezing the centrifuge tube containing the bromoform-acetone solution in an acetone-dry ice mixture and subsequently sawing the frozen tube in half between the two fractions. The sinking and floating halves were removed from the sawn tube halves, allowed to thaw in separate new tubes, and washed extensively with acetone and dried under vacuum.

7.4.17 Mg K-edge XAS

XAS measurements were performed at the Spherical Grating Monochromator (SGM, 11ID-1) beamline of the Canadian Light Source in Saskatoon, SK. Dry samples were prepared by spreading a small amount of powder on graphite tape (Ted Pella). Samples were scanned relative to the edge Mg *K*-edge (1303 eV) from -60 to -12 eV in steps of 2 eV, -12 to -8 eV in steps of 0.5 eV, -8 to 30 eV in steps of 0.1 eV, 30 to 190 eV in steps of 0.2 eV, 190 to 300 eV in steps of 0.3 eV and 300 to 400 eV in steps of 0.5 eV with a constant dwell time of 2 seconds/step. Monochromator energy calibration was performed by setting the first absorbance maxima of the MgO reference sample spectra to 1309.5 eV. X-ray fluorescence intensity was measured simultaneously with four solid state silicon drift energy dispersive X-ray detectors (Amptek, Bedford, MA). Incident flux was measured by recording the current from a gold mesh upstream. The Mg X-ray fluorescence intensity was isolated from the total fluorescence intensity containing contributions from X-ray fluorescence from other elements and the scattered incident beam using custom written code in Mathematica (Wolfram Research, Champaign, IL). The exit slit was adjusted and the undulated detuned to reduce flux to prevent saturation of X-ray fluorescence detectors when measuring concentrated samples. Between 1 and 7 scans were collected for each sample and averaged. No beam-induced changes were observed when comparing sequential spectra.

7.4.18 Mg EXAFS

The absorption data were normalized, background subtracted using AUTOBK, and converted to k-space using Athena¹⁴⁹. Edge energy (E_0) was set to the maximum of the first derivative of the absorption spectra. $\chi(k)$ data were weighted by k^2 and Fourier transformed over the k range 2-9.5 Å⁻¹ applying a Hanning window with a sill width of 1 Å⁻¹. Theoretical photoelectron scattering amplitudes and phase shifts based on the crystal structures of dolomite²²³, huntite²²⁴, whitlockite²²⁵, and hydroxylapatite²¹³ were calculated using FEFF6¹⁵¹. Shell-by-shell fitting of the EXAFS data was performed in R -space using Artemis¹⁴⁹. An energy shift parameter (E_0) was maintained constant for the scattering paths but allowed to vary between samples. The amplitude reduction factor ($S_0^2 = 0.8$) was determined based on a fit to the dolomite, huntite and whitlockite spectra with coordination numbers constrained based on their respective crystal structures. Multiple scattering in the carbonate reference samples was accounted for following Reeder et al²²⁶. Enamel and ACP EXAFS were fit using a model based on the Ca[II] site of hydroxylapatite, consisting of a single Mg-O and two Mg-P scattering paths^{211,212}.

7.4.19 Fe K-edge XAS

Powdered samples that adhered well to Kapton tape (3M 7419, St. Paul MN), were spread uniformly and multiple layers of tape were stacked to optimize X-ray absorption. Poorly adhering powders were diluted with microcrystalline cellulose (Sigma-Aldrich 310697) and pressed into a pellet with a diameter of 13 mm and a thickness of ~200 µm. EXAFS measurements were conducted at beam line 5-BM-D part of the Dupont-Northwestern-Dow collaborative access team at the Advanced Photon Source at Argonne National Laboratory. The energy of the Si(111) two-crystal monochromator was calibrated by assigning an energy of 7112 eV to the first zero-crossing of the second derivative (inflection point) of the absorption edge of an iron foil measured in transmission. The monochromator was detuned to eliminate harmonics. Absorption spectra of reference standards were recorded at the Fe- K edge in transmission by simultaneously measuring the incident and transmitted flux with two ion chambers (FMB-Oxford IC Spec). An iron

foil was placed behind the second ion chamber before the third ion chamber and measured simultaneously with each sample for energy calibration. Due to reduced concentration and sample volume, absorption spectra from pigmented enamel, samples were recorded by measuring the total Fe-*K*_a fluorescence yield with two Vortex ME-4 four element silicon drift detectors (Hitachi High-Technologies Science America, Northridge, CA) placed close to the sample. Al foil was placed over the detectors to absorb Ca-*K* fluorescence. Background was collected from -150 eV to -20 eV (relative to the edge) with steps of 5 eV, XANES was collected from -20 eV to +35 eV ($k = 3 \text{ \AA}^{-1}$) with steps of 0.1 eV. EXAFS data were collected from +35 eV to +750 eV ($k = 3 \text{ \AA}^{-1} - 14 \text{ \AA}^{-1}$) with a $k^{1.5}$ weighted count time and a k -increment of .05 \AA^{-1} . A base count time of 1 second and a final count time of 10 seconds were used. Absorption data were normalized using Athena¹⁴⁹. Between 2 and 16 scans were collected for each sample and averaged. No beam-induced changes were observed when comparing sequential spectra.

7.4.20 Fe EXAFS

The absorption data were normalized, background subtracted using AUTOBK, and converted to k-space using Athena¹⁴⁹. A constant edge energy (E_0) of 7128 eV was used. $\chi(k)$ data were weighted by k^3 and Fourier transformed over the k range 3-12 \AA^{-1} applying a Hanning window with a sill width of 3 \AA^{-1} . Due to reduced signal to noise ratios in the spectra from pigmented enamel, a reduced k range of 3-9.5 \AA^{-1} was used. Theoretical photoelectron scattering amplitudes and phase shifts based on the crystal structure of goethite¹⁵⁰ were calculated using FEFF6¹⁵¹. The amplitude reduction factor ($S_0^2 = 0.95$) was determined based on a fit to the reference goethite spectra with coordination numbers constrained based on the crystal structure¹⁵⁰. Shell-by-shell fitting of the EXAFS data was performed in *R*-space using Artemis¹⁴⁹. Four paths were fit for each sample, Fe-O, two Fe-Fe paths and an Fe-O-O multiple scattering path. An energy shift parameter (E_0) was maintained constant for the scattering paths but allowed to vary between samples. Triangular Fe-O-O multiple scattering paths within the FeO₆ octahedra were included following Mikutta¹⁵²

with radius, coordination number, and σ^2 constrained based on the Fe-O paths, specifically: $R_{\text{Fe}-\text{O}-\text{O}} = R_{\text{Fe}-\text{o}}(1 + \sqrt{2}/2)$; $CN_{\text{Fe}-\text{O}-\text{O}} = 4CN_{\text{Fe}-\text{O}}$; $\sigma^2_{\text{Fe}-\text{O}-\text{O}} = \sigma^2_{\text{Fe}-\text{O}}$.

7.4.21 Fe EXAFS linear combination fitting

Least squares linear combination fitting¹⁵³ was performed with Athena¹⁴⁹ using k^3 -weighted spectra over a k -range of 2-9.5 Å⁻¹ were used.

7.4.22 P K-edge XAS

Powdered samples were spread uniformly on Kapton tape. Measurements were conducted at beam line 2-ID-B at the Advanced Photon Source at Argonne National Laboratory. An in-line X-ray beam energy monitor containing a sample of hydroxylapatite (NIST standard reference material SRM 2910) was used to calibrate the monochromator²²⁷. Energy was scanned from 2123 eV to 2203 eV in steps of 0.1 eV. P-K_a X-ray fluorescence intensity was monitored with an energy dispersive silicon drift detector (Hitachi High-Technologies Science America, Northridge, CA). Absorption data were normalized using Athena¹⁴⁹.

7.4.23 X-PEEM

X-ray photoelectron emission microscopy was performed at beamline 4-ID-D at the Advanced Photon Source using an Elmitec PEEM III (Clausthal-Zellerfeld, Germany). Incident X-ray energy was scanned from 2123 eV to 2203 eV in steps of 0.1 eV. Photoelectrons were amplified by a micro-channel plate and converted to photons with a phosphor screen; the phosphor screen was recorded with a Photometrics Roper CoolSNAP HQ Monochrom CCD camera (Tucson, AZ).

7.4.24 Nanoindentation

Nanoindentation was performed with TI 900 Triboindenter (Hysitron, Minneapolis, MN) equipped with a diamond Berkovitch tip. A peak load 1500 μN was used with a dwell of 2 seconds at maximum load. Indent surface area was determined based on tip displacement and tip-area calibration. Hardness was determined based on maximum load and indent surface area.

8 ATOM PROBE TOMOGRAPHY OF FERRITIN

This chapter discusses the application atom probe tomography to analyze ferritin, a core-shell protein-iron oxide nanoparticle, and a model system for APT for the past three decades²²⁸⁻²³⁰.

Parts of the work have been published in the following conference proceeding:

Gordon, L., Cohen, M. & Joester, D. Towards Atom Probe Tomography of Hybrid Organic-Inorganic Nanoparticles. *Microscopy and Microanalysis* **19**, 952-953 (2013).

8.1 INTRODUCTION

Surface functionalization of inorganic nanoparticles is widely used to modify material properties for a variety of applications including medical therapies and diagnostics. While inorganic nanoparticles may be characterized via electron microscopy and X-ray scattering, further study of the organic components and the buried organic-inorganic interfaces is very challenging. Here we discuss advances in the use of atom probe tomography (APT) to image organic-inorganic interfaces within nanoparticles. Using ferritin as a model nanoparticle system, we successfully imaged the protein-mineral interface.

Ferritin is a structurally well-characterized protein, critical in biology to store and transport iron as mineralized Fe (III)²³¹. This 24-subunit 12 nm protein has a spherical 8 nm core into which Fe (II) enters and is subsequently oxidized. It has been identified in the chiton tooth system as the main source of iron for biomineralization²³². Iron is stored within the protein shell of ferritin as a hydrated ferric oxide nanoparticle with a structure similar to the mineral ferrihydrite^{46,233}. Protein crystallography has revealed the complete structure of the protein (Figure 8.1)²³⁴ while the structure of the ferrihydrite core (Figure 8.2) is still under debate²³⁵⁻²³⁹, however, the nature of the interface between the inorganic core and the organic protein shell is not well characterized. The majority of the core is located in close proximity to the interface with the protein shell, therefore to understand the protein-mineral interaction it is necessary to characterize the or-

ganic-inorganic interface. For example, phosphate, known to be important in stabilizing the ferrihydrite core, may be segregated at the protein-mineral interface, currently the location is unknown⁴⁶.

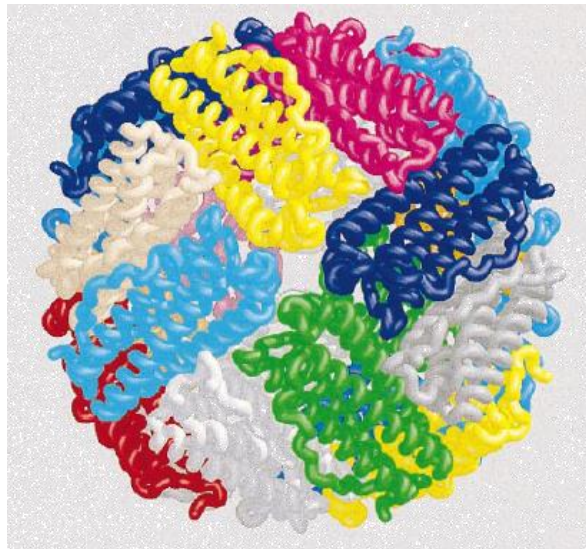


Figure 8.1: X-ray crystal structure of ferritin

Graphic representations of the α -helical structure of human ferritin protein: 24 subunits viewed down a fourfold axis. Adapted from⁴⁶.

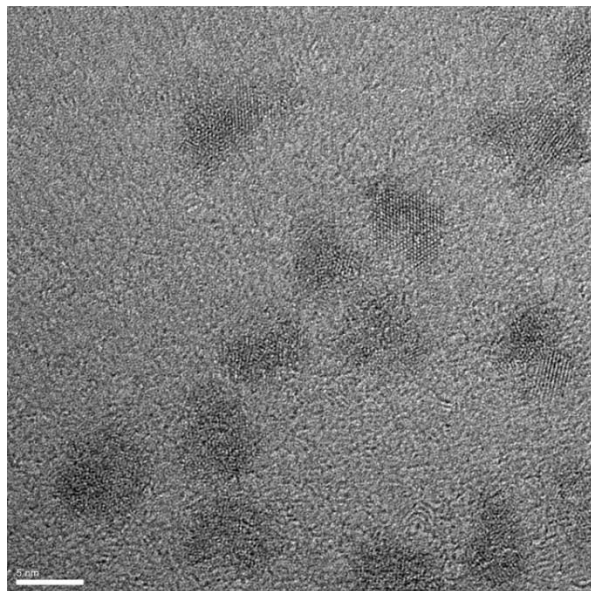


Figure 8.2: High-resolution TEM of ferritin

Crystallographic lattice of the mineralized cores is visible.

APT is uniquely capable of providing the necessary chemical and structural insight at the atomic scale by directly probing the location and chemical identity of the atoms within a small sample of material. APT consists of a field-ion microscope coupled to a time-of-flight mass spectrometer, providing chemical and three-dimensional positional information of ions successively field evaporated from a sharp sample. The advent of ultraviolet laser pulsing has widely enlarged the scope of APT to include a range of insulating materials, including hybrid organic-inorganic materials¹⁶⁸. APT is specifically adept at characterizing nanomaterials with numerous internal organic-inorganic interfaces, due to its elemental sensitivity and spatial accuracy. We recently demonstrated this capability in biological minerals in the magnetite cusp of the chiton tooth and vertebrate bone and dentin^{10,96}.

We report here on the characterization of native equine spleen ferritin using APT. Greene *et al.* recently used APT to analyse ferritin as a model for characterizing biological materials using APT. In this work, researchers used a solidified organic/salt matrix, which contained many ferritin complexes⁹². These APT tips of dense deposits were able to undergo APT, providing a proof of concept through mass spectrometry results. However, they were unable to characterize individual proteins and their experiments suffered from drastic tip bending, preventing meaningful reconstructions⁹².

8.2 RESULTS AND DISCUSSION

To image individual ferritin protein complexes, a dilute solution of purified equine spleen ferritin was deposited onto an Au-Pd coated silicon post (Figure 8.3). The adsorbed molecules were then encapsulated in an additional layer of Au-Pd and then sharpened into APT sample tips using focused ion beam milling. Similar metal encapsulation processes have been used to analyse other nanoparticles, including pre-solar diamond nanoparticles extracted from meteorites²⁴⁰. Based on previous analysis of buried organic-inorganic interfaces in the magnetite cusp of the chiton tooth and elephant tusk dentin atom probe tomography could provide unique insight into the nanoscale structure and chemistry of ferritin. In particular

APT analysis of the organic-inorganic could provide new insight into the processes responsible for controlling mineralization and stabilizing the ferrihydrite nanoparticle core.

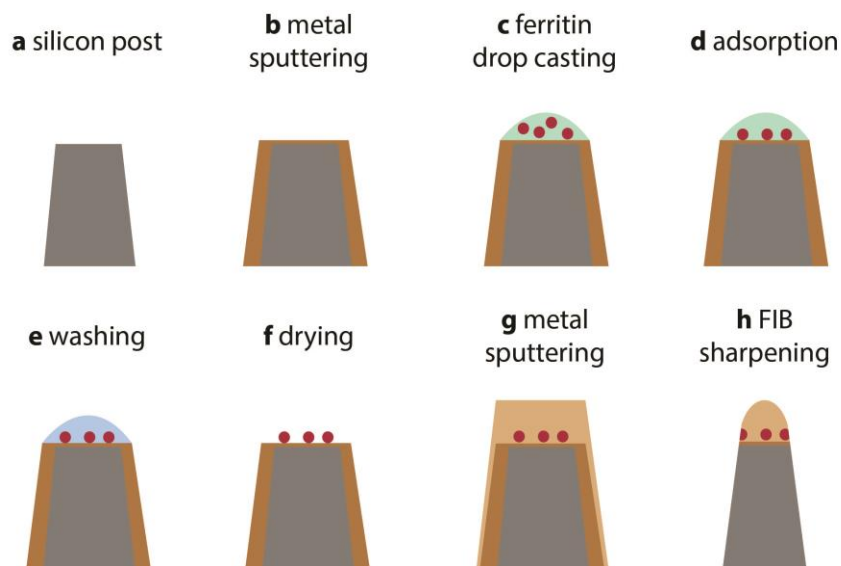


Figure 8.3: Method for fabricating ferritin atom probe tomography sample tips.

Starting with a pre-fabrication silicon post (a), metal (Au-Pd) is sputter coated onto the post (b), onto which a dilute ferritin solution is deposited (c), ferritin adsorbs to the post (d) and excess buffer salts are subsequently washed away with water (e) and the sample is dried in air (f). Au-Pd is then coated onto the sample (g) to protect the ferritin from focused ion beam (FIB) damage and to create a conductive matrix for the APT tip. FIB protocols are used to shape and sharpen the APT sample tip containing the encapsulated ferritin (h).

Expectations vs observations

APT mass to charge ratio spectra (Figure 8.4) from the ferritin complexes were consistent with expectations. The overall spectrum was dominated by Au and Pd monoatomic ions originating from the metal matrix. Au and Pd ions are relatively heavy and exhibited only low charge stages ($1+/2+$) in the spectrum resulting in minimal interference with other important ions in the spectra. Small numbers of Al and Ar ions were detected which occur as impurities in the sputtered film. Atomic Fe and molecular Fe-O con-

taining ions were also observed, consistent with expectations for the iron oxide ferritin core based on spectra from biogenic and geological magnetite¹⁰. In addition low levels of Na were observed, likely residual salt from the buffer. A range of small C- and N- containing ions were observed, predominately C⁺, similar to the small fragments observed from the organic fibers occluded in the chiton tooth, metal encapsulated chitin thin films and collagen fibrils in bone and dentin⁹⁶. Similar to the chiton tooth, which has a similar combination of iron oxides and organics, spectra spectral overlaps were observed between ⁵⁶Fe²⁺ and CO⁺ at m/z = 28 and ⁵⁶FeO₂²⁺ and CO₂⁺ at m/z = 44. Mass spectra from chitin thin films indicate that a large fraction of the organic material evaporates might be evaporating as CO⁺ and CO₂⁺ molecular ions which cannot be separated from the overlapping Fe-containing ions, in particular the highly abundant Fe²⁺. Isotopic labeling, specifically replacement of the natural iron with enriched ⁵⁷Fe or ⁵⁸Fe, provides a possible mechanism to resolve the spectral overlaps. There was no evidence of phosphates in the spectra, however, phosphate is present in low concentrations in mammalian ferritin unlike bacterial ferritin cores which contain much higher levels of phosphates⁴⁶.

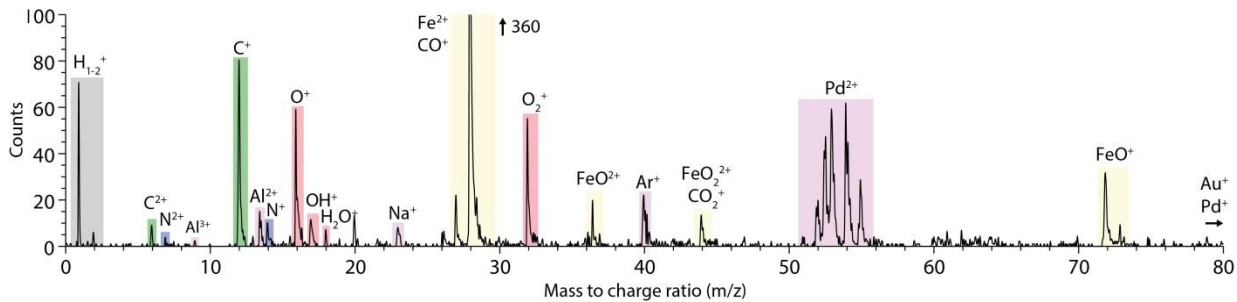


Figure 8.4: APT spectra of ferritin

Atom-probe tomography ion mass to charge ratio spectra of ferritin clusters in Au-Pd matrix (Al and Ar are impurities in the sputtered metal film). Spectral overlaps between certain Fe- and CO- containing ions were observed. Na likely originates from the NaCl buffer the ferritin was deposited from.

Using an isoconcentration surface of 5 Fe ions/nm^3 we can identify the $\sim 5 \text{ nm}$ diameter iron-rich ferritin cores (Figure 8.5). A proximity histogram composition profile reveals the clear iron-rich core of ferritin, while the carbon concentration peaks just beyond core, corresponding with the organic protein shell. While APT does not enable designation between Fe (II) and Fe (III), which could help resolve catalytic iron oxidation site on the protein, we can see the accumulation and storage of iron and the associated oxygen in the core of the protein surrounded by a carbon rich sphere. It is likely that there are local magnification effects and trajectory aberrations which distort the geometry and density of the reconstruction since Au-Pd and the ferritin molecule likely have different evaporation fields.

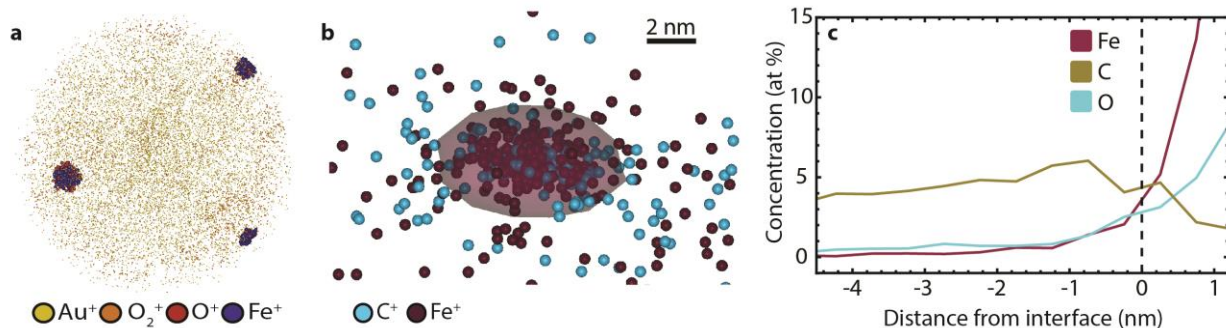


Figure 8.5: Ferritin APT reconstruction and proxigrams

a, APT reconstruction of tip containing three gold-palladium encapsulated ferritin proteins. **b**, single ferritin molecules including a 5 Fe ions/nm^3 isoconcentration surface. **c**, proximity histogram, which plots the radial ionic concentration from the isoconcentration surface, showing atomic concentration of iron, carbon and oxygen relative to the interface between then core within the ferritin and the protein (defined by isoconcentration surface five Fe ions/nm^3).

Proxigrams show an increase in carbon concentration surrounding the iron-rich ferritin core; however, this was not clearly visible in the 3D reconstructions due to carbon contamination on the lower Au-Pd surface, just below the plane where the ferritin complexes were observed. The carbon contamination is

evident in 1D concentration profile down the tip axis (Figure 8.6) where it appears just below the ferritin cores, associated with elevated O_2^+ levels of unknown origin, potentially adsorbed water.

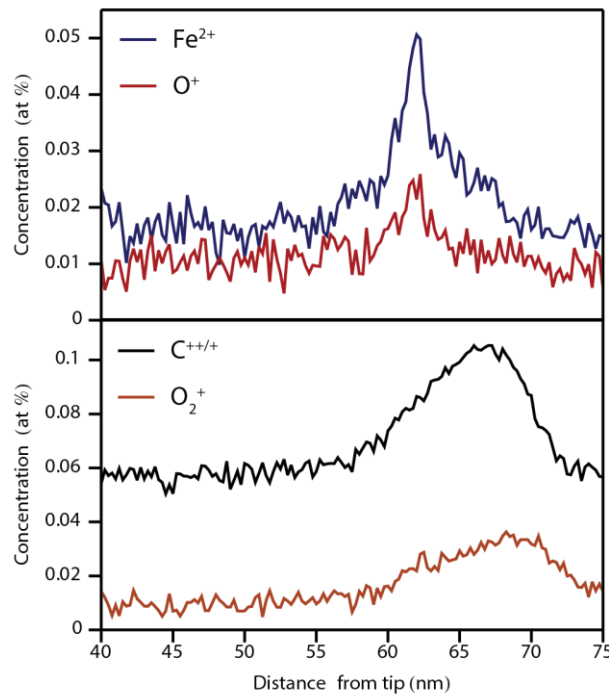


Figure 8.6: 1D concentration profile along tip z-axis

Fe/O enrichment due to ferritin cores is evident, however, carbon concentration appears to peak just below the ferritin cores, suggesting a possible layer of contamination on the surface.

8.3 CONCLUSION

This work demonstrates the ability of APT to characterize ferritin and also demonstrates the first steps towards developing a successful paradigm to use for APT characterization of protein complexes and nanoparticles in order to gain new insight to facilitate clinical and scientific advances. Further work is necessary to resolve spectral interferences and carbon contamination to better study ferritin with APT.

8.4 MATERIALS AND METHODS

8.4.1 Sample Preparation

Commercially available silicon microtip arrays were coated with ~50nm of Au-Pd with an Ion Beam Sputter Deposition and Etching System (IBS/e, South Bay Technologies, San Clemente, CA) operating at a base pressure of $< 10^{-4}$ Pa, a working pressure of 10^{-2} Pa argon, with two ion guns operating at 8 kV at 3 mA per gun. A 5 nm Cr layer was deposited prior to the Au-Pd layer directly on the Si to improve adhesion.

Purified equine spleen ferritin (Sigma-Aldrich) was diluted to 0.1 mg/mL in 0.15 M NaCl and pipetted onto the coated substrate. After 10 min the excess liquid was wicked away with filter paper and the substrate was washed twice with water. The ferritin layer was subsequently capped ~50nm of Au-Pd and ~100 nm of Ni.

Samples for APT were prepared. Each tip was shaped and sharpened using the SEM/FIB instrument (Helios Nanolab, FEI, Hillsboro, Oregon) following established protocols^{100,101} using annular milling patterns of increasingly smaller inner and outer diameters. The majority of the amorphized surface region and implanted gallium ions in the tip surface was removed by a final ion-milling step at 2 kV, 0.4 nA.

8.4.2 APT Methods

Atom probe tomographic analyses were conducted in a Cameca local-electrode atom-probe (LEAP 4000XS, Cameca, Madison, WI) tomograph using a pulsed frequency-tripled Nd:YAG laser ($\lambda = 355$ nm). Run time parameters were 160 - 500 kHz and 40-75 pJ per pulse. The DC potential on a microtip during APT was controlled to maintain an evaporation rate of either 0.005 or 0.0025 ions per laser pulse. The base temperature of the microtip was maintained at 40 or 60 K and the ambient vacuum pressure was $< 10^{-8}$ Pa. Peak ranges were defined as the entire visible peak. Three-dimensional reconstruction of APT data was performed using the Cameca integrated visualization and analysis software (IVAS)

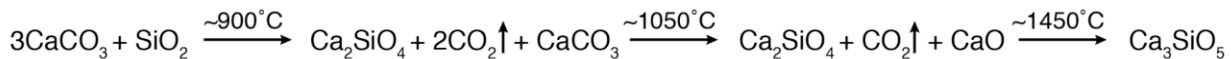
based on published algorithms, assuming a hemispherical tip shape.^{83,105} Standard reconstruction parameters were used with an electric field dependent tip radius (r).

9 EARLY HYDRATION OF TRICALCIUM SILICATE

This chapter discusses the application of atom probe tomography to study the early stage hydration of tricalcium silicate to resolve long standing questions in the field of cement chemistry. The work was conducted in collaboration with Dr. Thomas Sowoidnich and Dr. Frank Bellmann at the Bauhaus-Universität Weimar in Weimar, Germany.

9.1 INTRODUCTION

Concrete, composed of coarse granular material (aggregate) suspended in a matrix of hardened cement, is the most widely used material on earth. Production of cement for the concrete industry is responsible for a significant fraction of worldwide CO₂ emissions (5-8 %, 660 kg CO₂ per metric ton of cementitious product) and simultaneously consumes large amounts of water and energy²⁴¹⁻²⁴³. Cement production exceeded 10¹⁵ g (1 billion tons) in 2011 worldwide according to United States Geological Survey²⁴⁴. Rapid industrialization in Asia and the associated increasing concrete usage in construction, particularly China (~60 % of world consumption) is expected to more than double cement demand over the next two decades. The majority (60 %, 2 equivalents of CO₂ per dicalcium silicate and 3 equivalents per tricalcium silicate) of the CO₂ emissions result from CO₂ produced during the chemical transformations occurring during clinker formation in cement kilns (Scheme 9.1). The remaining 40% are from burning of fuels to generate the necessary process heat.



Scheme 9.1: Simplified Portland Cement Clinker Formation

Starting from limestone (CaCO₃) and sources of silica, dicalcium silicate (C₂S) forms with release of two equivalents of CO₂. Further heating generates a third equivalent of CO₂ and calcium oxide (CaO). In a third step, CaO reacts with C₂S to give tricalcium silicate (C₃S). During sintering, impurities such as Al, Mg, and Fe form solid solutions in C₃S and C₂S. The resulting clinker contains both alite (C₃S) and belite (C₂S).

Portland cement clinker is produced from limestone (CaCO_3) and clay, shale, or sand²⁴⁵. During calcination (Scheme 9.1), CO_2 is released as CaO is formed. This endothermic process consumes 65 % of the process heat. In the cement kiln, the resulting CaO and silica sources are fired to 1450°C to give tricalcium silicate and dicalcium silicate in addition to other minor phases. Intergrinding the clinker and additives produces the final cement powder. General-purpose cements contain alite (C_3S) and belite (C_2S) at a ratio of approximately 2.9:1.

Reducing CO_2 emissions associated with cement production has traditionally focused on increasing overall process energy efficiency, substituting fossil fuels with carbon-neutral biofuels, reducing the amount of carbonate raw materials in clinker production and limiting clinker content in the final cementitious product by admixing fly ash, granulated blast furnace slags, or pozzolanas. Reducing clinker content in concrete or introducing new lower carbonate clinkers are possible approaches to reducing emissions from calcination and fuel use substantially. However, these concretes develop strength too slowly for the majority of applications. Slow strength development is directly linked to the hydration kinetics of the two primary components of ordinary Portland cement (OPC), tricalcium silicate (Ca_3SiO_5 , C_3S , alite) and dicalcium silicate (Ca_2SiO_4 , C_2S , belite). Specifically, the strength development is controlled by an induction period of slow hydration following the initial rapid reaction^{245,246}. Low solubility Calcium-Silicate-Hydrate (C-S-H) intermediate phases have been suggested to passivate the surface of the reactive alite particles during the induction period.

Substitution of the traditional alite-belite mixture in Portland cement with an all-belite cement could dramatically reduce CO_2 emissions (up to 30 %). However, belite clinkers exhibit dramatically decelerated strength development that prevents use in the majority of applications. This leads to one of the longest standing problems in cement chemistry, the mechanism by which C_3S and C_2S are converted to C-S-H,

the phase responsible for strength development in concrete²⁴⁵⁻²⁴⁸. Hydration starts rapidly, with a burst of heat released during the first 15 minutes. However, the rate then drops precipitously, and an induction period of low activity and low heat release follows (Figure 9.1). After about 2.5h, the rate starts increasing again, this is recognizable by loss of workability and increasing strength of concrete²⁴⁵. Control over the timing of the induction period and strength development is of critical importance in construction. Accelerated strength development is a necessary prerequisite to realizing the potential for CO₂ reduction of highly substituted and low carbonate clinkers.

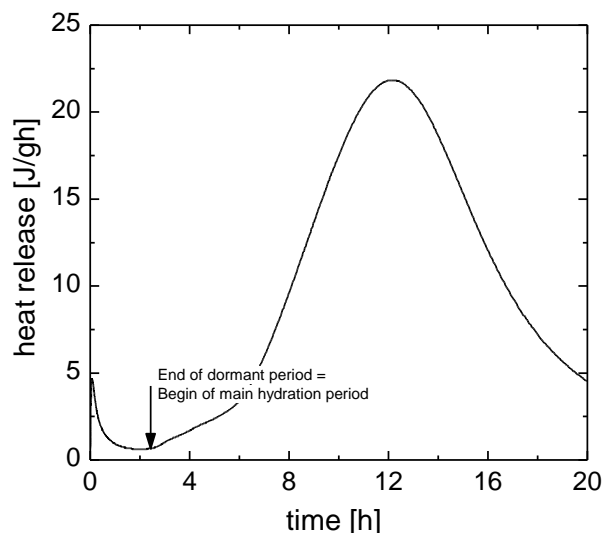


Figure 9.1: Cement Hydration

Isothermal heat conduction calorimetry indicates the rate of heat release during the hydration of C3S. A rapid initial process is followed by slow hydration during the induction period

The mechanism responsible for the induction period, specifically, the reduction in hydration rate after the initial burst is not understood. It has been suggested that initial hydration forms an intermediate low solubility C-S-H phase that passivates the surface of C3S. However, the structure and composition of this proposed phase are unknown. Rational strategies to control the kinetics of the reaction process and the

induction period of alite and belite require a thorough understanding of this passivation layer and how its structure and reactivity can be tuned by specific cement additives.

9.2 RESULTS AND DISCUSSION

Atom probe tomography was performed on anhydrous bulk C3S and the surface of a hydrated specimen to investigate the nanoscale structural and chemical changes associated with the hydration reaction. The resulting APT from anhydrous bulk C3S spectra are dominated by the major ions, Ca^{2+} , SiO_x^+ , $\text{O}^+/\text{O}_2^{2+}$ and O_2^+ with smaller levels of metallic impurities Mg^{2+} , Al^{2+} and FeO_x^+ . Application of APT to characterize hydrated C3S surfaces would be complicated by the high levels of atomic and molecular hydrogen (H_x^+) ions along with protonated oxygen species (OH_x^+) detected in the anhydrous spectra due to residual gas in the vacuum system and possible trace hydrogen/water within the sample itself. The number of H_2^+ ions ($m/z = 2$) detected was over an order of magnitude lower than the number of H^+ ions ($m/z = 1$) in the anhydrous C3S. To improve the sensitivity for detecting hydrated species, C3S samples for APT were hydrated with isotopically labelled deuterium oxide (heavy water, D_2O), where the D^+ signal should be more easily detected at $m/z = 2$ compared to the H^+ signal at $m/z = 1$. Total ion spectra of hydrated samples (Figure 9.2) indicate a ~3-fold increase in peak area at $m/z = 2$ relative to $m/z = 1$ and $m/z = 3$ compared to the anhydrous C3S. This indicates the presence of D_2O on the sample surface or in C-S-H phases.

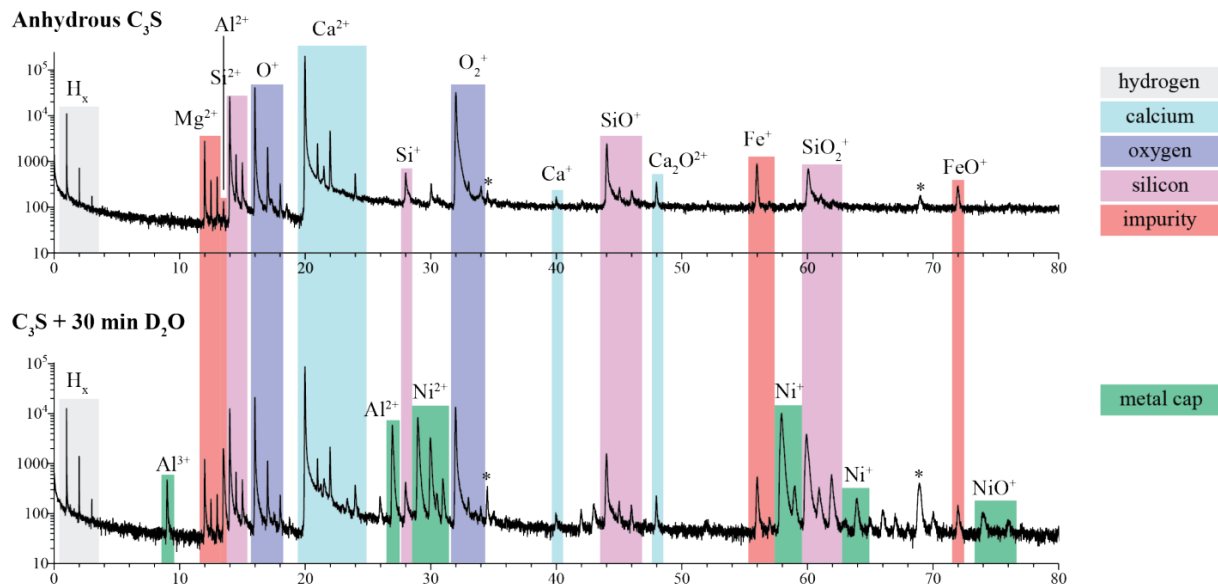


Figure 9.2: C₃S APT Spectra

Atom probe total ion spectra of anhydrous alite (C₃S) and after exposure to D₂O for 30 minutes. Peaks corresponding to Ca²⁺, SiO_x⁺, O⁺/O₂²⁺ and O₂⁺ dominate the spectra. Mg²⁺, Al²⁺ and FeO_x⁺ impurities are minor species. A small amount of residual Ga from FIB milling is also present (asterisk).

Horizontal slices and concentration profiles through a reconstruction of a hydrated C₃S sample show a narrow, slightly rough interface (Figure 9.3 and Figure 9.4). Two nanometers above the interface (-2 to 0 nm), the dominant species is Ni, from the protective metallic cap, while very little Ca or Si is detected. In the slice below (0 to 2 nm), Ni concentration has dropped sharply while Ca rises concentration rises. Hotspots in the 2H map and total hydrogen map (Σ H) are correlated with Si concentration, no correlation is observed with Ni, and Ca and Si concentrations are anti-correlated. The high-silica and low-calcium concentration areas are consistent with a calcium-poor, silica-rich C-S-H phases such as Jennite (Ca_{1.6}SiO₂(OH)_{3.33} · 0.43H₂O) or Tobermorite (Ca_{0.83}SiO₂(OH)_{1.67} · 0.5H₂O) C-S-H, which are known C₃S hydration products²⁴⁹. The interphase appears to cause some surface roughness, as apparent from hotspots in the 2H map.

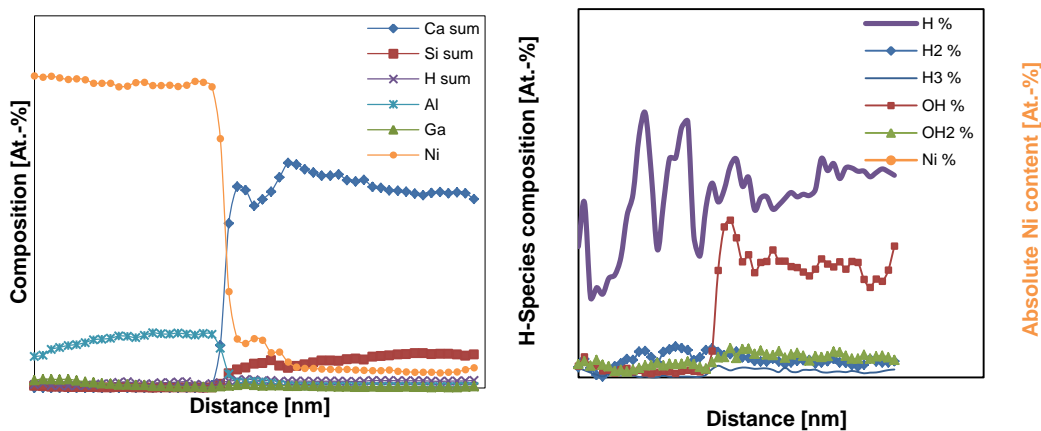


Figure 9.3: Hydrated C₃S APT Concentration Profiles

Profile of the main element distribution from the hydrated C₃S surface 30 min after contact with D₂O. Absolute H-Species composition 30 min after hydration of C₃S with D₂O. On the second ordinate Ni is shown to illustrate the sample regions.

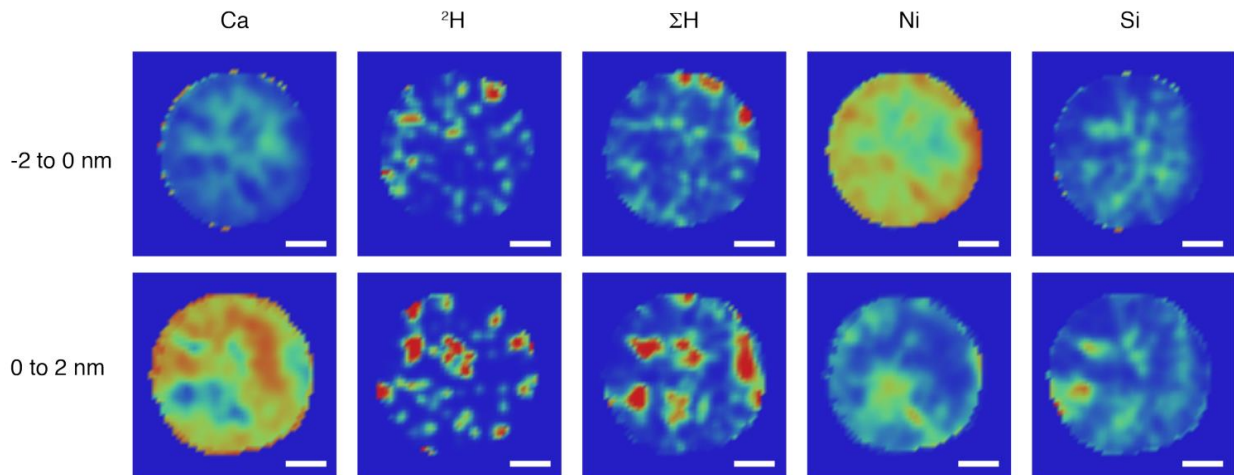


Figure 9.4: Slices through Hydrated C₃S reconstruction

Slices through reconstruction of C₃S hydrated with D₂O for 30 minutes. The top row corresponds to projected concentration in a 2 nm slice parallel to and immediately above the surface; the bottom row corresponds to the 2 nm slice immediately below. Warmer colors indicate higher concentrations. Scale bar corresponds to 10 nm.

9.3 CONCLUSION

We have shown, for the first time, that laser pulsed atom probe tomography is capable of analyzing both anhydrous bulk C₃S and hydrated C₃S surfaces at the nanometer scale. On the surface of D₂O-treated C₃S, there are clear indications for the formation of a new phase.

9.4 MATERIALS AND METHODS

9.4.1 *C₃S Synthesis*

Triclinic C₃S was produced via solid state reaction by pressing a mixture of CaCO₃ and SiO₂ at 20 MPa 4 cm diameter (0.5 cm thick) pellets and heating repeatedly at 1600 °C for 10 h.

9.4.2 *Hydration*

Hydration was started by pipetting a drop of deuterium oxide (D₂O) on the C₃S surface at 25 °C. After 30 min the hydration was stopped by washing the surface with isopropanol.

9.4.3 *Embedding, Grinding and Polishing*

C₃S was embedded in Epo-Fix resin and polymerized overnight at 25 °C. All embedded samples were ground using progressively finer grits of SiC grinding paper (400, 600, 800 and 1200 grit) lubricated with an ethylene glycol/ethanol solution. Samples were polished using polycrystalline alumina suspended in and ethylene glycol/ethanol solution on Microcloth polishing cloths.

Polished samples were secured to an aluminum stub with cyanoacrylate adhesive, coated with ~100nm of Ni with an Ion Beam Sputter Deposition and Etching System (IBS/e, South Bay Technologies, San Clemente, CA) operating at a base pressure of < 10⁻⁴ Pa, a working pressure of 10⁻² Pa argon, with two ion guns operating at 8 kV at 3 mA per gun. The coating was grounded to the stub with conductive liquid silver paint.

9.4.4 APT Sample Preparation

Samples for APT were prepared using the SEM/FIB instrument (Helios Nanolab, FEI, Hillsboro, Oregon) using established protocols.^{100,101} A rectangle of platinum (FIB-Pt) was deposited on the polished cross-section using the ion beam (30kV, 93pA) to decompose methyl cyclopentadienyl trimethyl platinum ($[C_5H_5Pt(CH_3)_3]$) gas, over a region of interest (2 x 25 μm) on the polished cross-sections or directly on faceted crystals. A wedge of material below the Pt rectangle was cut out on three sides using the FIB (30 kV, 6.5 nA). The wedge was attached to an in situ nano-manipulator (Omniprobe, Dallas, TX) using FIB-deposited Pt before cutting the final edge free. 1-2 μm wide segments were cut from the wedge and sequentially affixed to the tops of Si posts in an array (Cameca Scientific Instruments, Madison, WI) with FIB-Pt. Each tip was shaped and sharpened using annular milling patterns of increasingly smaller inner and outer diameters. The majority of the amorphized surface region and implanted gallium ions in the tip surface was removed by a final ion-milling step at 2 kV, 0.4 nA. To protect the hydrated surface layer the entire protective nickel cap was not removed during final ion milling.

9.4.5 APT Methods

Atom probe tomographic analyses were conducted in a Cameca local-electrode atom-probe (LEAP 4000XS_i, Cameca, Madison, WI) tomograph using a pulsed frequency-tripled Nd:YAG laser ($\lambda = 355$ nm). Run time parameters were 160 - 500 kHz and 40-75 pJ per pulse. The DC potential on a microtip during APT was controlled to maintain an evaporation rate of either 0.005 or 0.0025 ions per laser pulse. The base temperature of the microtip was maintained at 40 or 60 K and the ambient vacuum pressure was $< 10^{-8}$ Pa. Peak ranges were defined as the entire visible peak. Three-dimensional reconstruction of APT data was performed using the Cameca integrated visualization and analysis software (IVAS) based on published algorithms, assuming a hemispherical tip shape.^{83,105} Standard reconstruction parameters were used with an electric field dependent tip radius (r).

9.4.6 *Thin Films*

C3S thin films were prepared using pulsed laser deposition. Briefly, a physical vapor is created within the deposition chamber by targeting a pulsed laser at a bulk sample target. The chamber was evacuated and backfilled to a working pressure of 10^{-5} Pa O₂. The glass substrate was heated to 400 °C while the target was ablated for 15 min. Thin films were characterized using grazing incidence X-ray diffraction. The sample was oriented with a 0.4° grazing angle and the detector was swept from 10° to 70° with a step of 0.05°.

10 CONSTRAINING ATOM PROBE TOMOGRAPHY RECONSTRUCTIONS OF CRYSTALLINE OXIDES

This chapter describes our efforts to validate reconstruction parameters for atom probe tomography of crystalline oxides. The work was conducted in collaboration with Dr. Santosh Suram, Dr. Kaustaubh Kaluskar and Professor Krishna Rajan at Iowa State University. Dr. Santosh Suram developed the SDM alignment algorithm and identified the first pole and corresponding lattice planes in the chiton tooth magnetite atom-probe reconstruction. Professor John Valley at the University of Wisconsin, Madison, graciously provided the unique geological magnetite crystals with precipitates (LP-204-1 from the Weston Mine, Adirondack Mountains, New York). Dr. Dan Schreiber at Pacific Northwest National Laboratory collaborated on the analysis and provided atom probe samples of synthetic trevorite.

Parts of the work have been published in the following conference proceedings:

Cohen, M. *et al.* Constraining Atom Probe Tomography Reconstructions of Crystalline Oxides. *Microscopy and Microanalysis* **19**, 1010-1011 (2013).

Gordon, L., Joester, D., Suram, S., Kaluskar, K. & Rajan, K. Atom Probe Tomography of Organic/Inorganic Interfaces in Biominerals. *Microscopy and Microanalysis* **18**, 1608-1609 (2012).

10.1 INTRODUCTION

Atom-probe tomography (APT) is uniquely capable of directly probing the location and chemical identity of the atoms within a sample of material with sub-nanometer spatial resolution and parts-per-million chemical sensitivity. APT consists of a field-ion microscope coupled to a time-of-flight mass spectrometer, providing chemical and three-dimensional positional information of ions successively field evaporated from a sharp sample. While early application of APT was limited to electrically conductive metals

and heavily doped semiconductors recent advancements in ultraviolet laser pulsing has enabled the analysis of a range of dielectric materials²⁵⁰.

While APT provides a detailed picture of the distribution of elements in three-dimensions there are a number of parameters that control how the impact position and sequence of ions are translated into the final 3D reconstruction. In pure metals and elemental semiconductors field evaporation processes result in multiple low-density regions in the detector histogram corresponding to low-index crystallographic poles. These regions are also often accompanied by lattice-plane resolution in the dataset. The presence of multiple poles and lattice plane resolution provides key information to constrain the reconstruction algorithm²⁵¹. In complex multi-component materials, fewer crystallographic poles and lattice planes are observed in reconstructions, with only a few examples in the literature to date²⁵². We report here on the combination of sample orientation, X-ray and electron diffraction and advanced data analysis to identify lattice planes, crystallographic orientation and calibrate reconstruction parameters in single- and nanocrystalline oxide materials, including geological and biogenic magnetite (Fe_3O_4 , Figure 10.1)¹⁰.

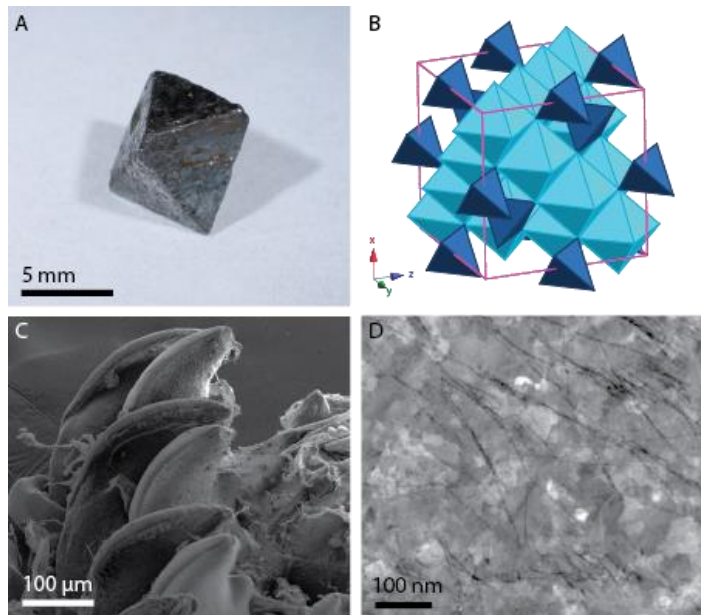


Figure 10.1: Overview of geological and biological magnetic

a geological magnetite single crystal displaying the crystallographic (111) facets. **b** magnetite crystal structure, illustrating the tetrahedrally and octahedrally coordinated iron atoms. **c** scanning electron micrograph of the teeth of the chiton *Chaetopleura apiculata*. **d** high-angle annular dark field scanning transmission electron micrograph of the nanocrystalline magnetite within the chiton tooth cusp, weakly scattering 5-10nm diameter organic fibers are seen throughout the mineral¹⁰.

10.2 RESULTS AND DISCUSSION

Selection of appropriate parameters is very important for accurate three-dimensional reconstructions of APT data. Many of these parameters are dependent on sample geometry, chemistry and analysis conditions. Since APT is a destructive technique, it is not always possible measure sample geometry once the experiment is complete. Crystal structure information contained in APT reconstruction is a proven method to refine input parameters²⁵³. In the present work, we used single crystal geological magnetite samples of known crystallographic orientation to constrain reconstruction parameters. This information was then used to estimate reconstruction parameters for polycrystalline biogenic magnetite.

Atom probe data sets contain information about the identity and arrangement of 10^5 - 10^8 atoms. A common way to ensure accurate reconstruction of atomic positions is to

- I) Identify regions where crystallographic order is present in the reconstruction.
- II) Determine the associated zone axis.
- III) Adjust reconstruction parameters until the observed planar spacing matches a known or independently determined value
- IV) If multiple crystallographic axis are observed adjust reconstruction parameters until the observed angle separating the poles matches the known crystallographic angle.

10.2.1 Crystallographic Poles

For reasons related to the physics of field evaporation and the reconstruction process, crystalline order in atom probe reconstructions is best reproduced around crystallographic poles^{185,254-256}. A pole is equivalent to a crystallographic pole in a stereographic projection of a crystal structure. Poles in APT data can be recognized in the detector event histogram by their low density (Figure 10.4)²⁵⁷. Generally, only low index poles are visible. Under ideal conditions, multiple poles are seen and pole axes can be mapped to poles by superposition of the stereographic projection with the detector event histogram^{99,258,259}. In a sample of biogenic nanocrystalline magnetite, we have observed at most only a single pole (Figure 10.2). This is typical also for highly alloyed metals, semiconductors, and dielectrics where few poles are observed. In the absence of multiple poles or clear symmetry in the detector histogram, identification of the pole and accurate reconstruction remains a significant challenge²⁶⁰. Pole identification based on measured lattice spacing is difficult as the interplanar spacing is very sensitive to the reconstruction parameters. To determine the possible orientation of the observed pole in biogenic magnetite we analyzed a series of geological magnetite single crystals crystallographically oriented with low index zone axes roughly parallel to the analytical z-axis of the atom probe sample.

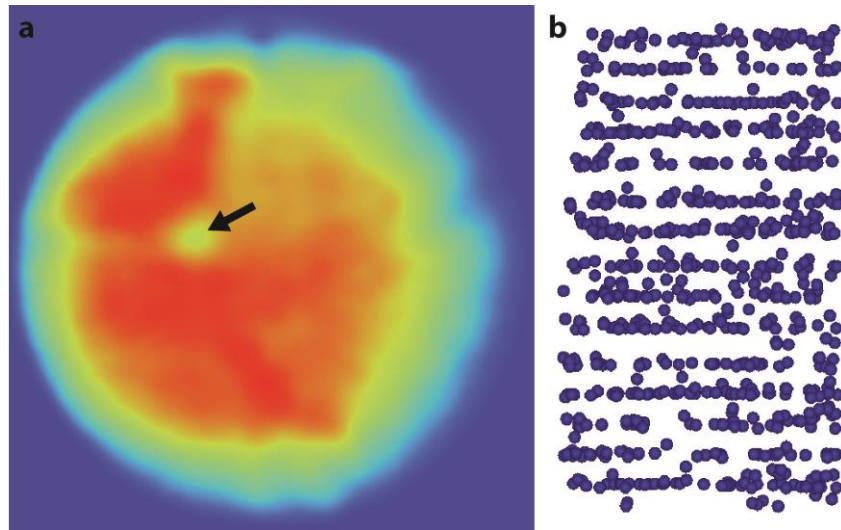


Figure 10.2: Detector histogram of biogenic chiton tooth magnetite sample

A single low density area corresponding to a crystallographic pole (black arrow) was observed in the detector event histogram (a) of an APT sample tip prepared from nanocrystalline (grain size 30-50 nm) biogenic magnetite from the chiton tooth. Lattice planes (b) were observed in the associated region within the three dimensional reconstruction.

Geological magnetite single crystals were oriented with faces parallel to the (100), (110) and (111) planes using Laue backscatter X-ray diffraction (Figure 10.4) and electron backscatter diffraction. Oriented crystals were cut with a slow speed diamond saw and polished with successively finer grits of silicon carbide abrasive discs and diamond suspension. Standard focused ion beam lift out and tip sharpening protocols were then used to prepare tips from the polished oriented surfaces.

For geological magnetite, we tested sample of $\langle 111 \rangle$, $\langle 110 \rangle$, and $\langle 100 \rangle$ orientation. In the case of the $\langle 111 \rangle$ oriented specimen, a low density region, with corresponding lattice planes (Figure 10.3) was observed at the center of the detector event histogram consistent with the $\langle 111 \rangle$ pole. Presence of a $\langle 111 \rangle$ is consistent with earlier field ion microscopy (FIM) images¹⁶⁹. No other low density regions were observed in the

$\langle 111 \rangle$ oriented sample. No low density regions were observed in the $\langle 100 \rangle$ oriented sample. In the $\langle 110 \rangle$ oriented samples, no low density region was observed at, or around, the center where the $\langle 110 \rangle$ pole would be expected. However, two low density regions were observed at opposite points near the edge of the detector event histogram potentially corresponding to either the $\langle 111 \rangle$ or $\langle 100 \rangle$ poles (Figure 10.3). Since no low density regions were observed in the $\langle 100 \rangle$ oriented sample but a low density region was observed in $\langle 111 \rangle$ oriented sample, it is more probable that low density region corresponded to $\langle 111 \rangle$ direction. Furthermore, the observation of two opposite $\langle 100 \rangle$ family poles would imply an unrealistic 90° field of view, while two opposite $\langle 111 \rangle$ family poles indicates a more reasonable, although still large, 70° field of view.

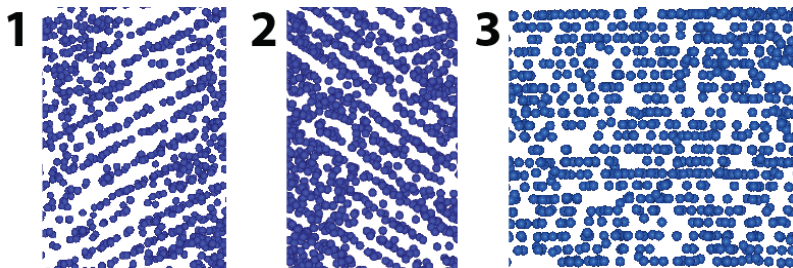


Figure 10.3: Lattice reconstructions

3D APT reconstructions corresponding to numbered $\langle 111 \rangle$ poles in Figure 10.4 with (111) lattice planes visible in the regions surrounding the poles. 1 and 2 are from the $\langle 110 \rangle$ oriented tip and 3 is from the $\langle 111 \rangle$ oriented tip.

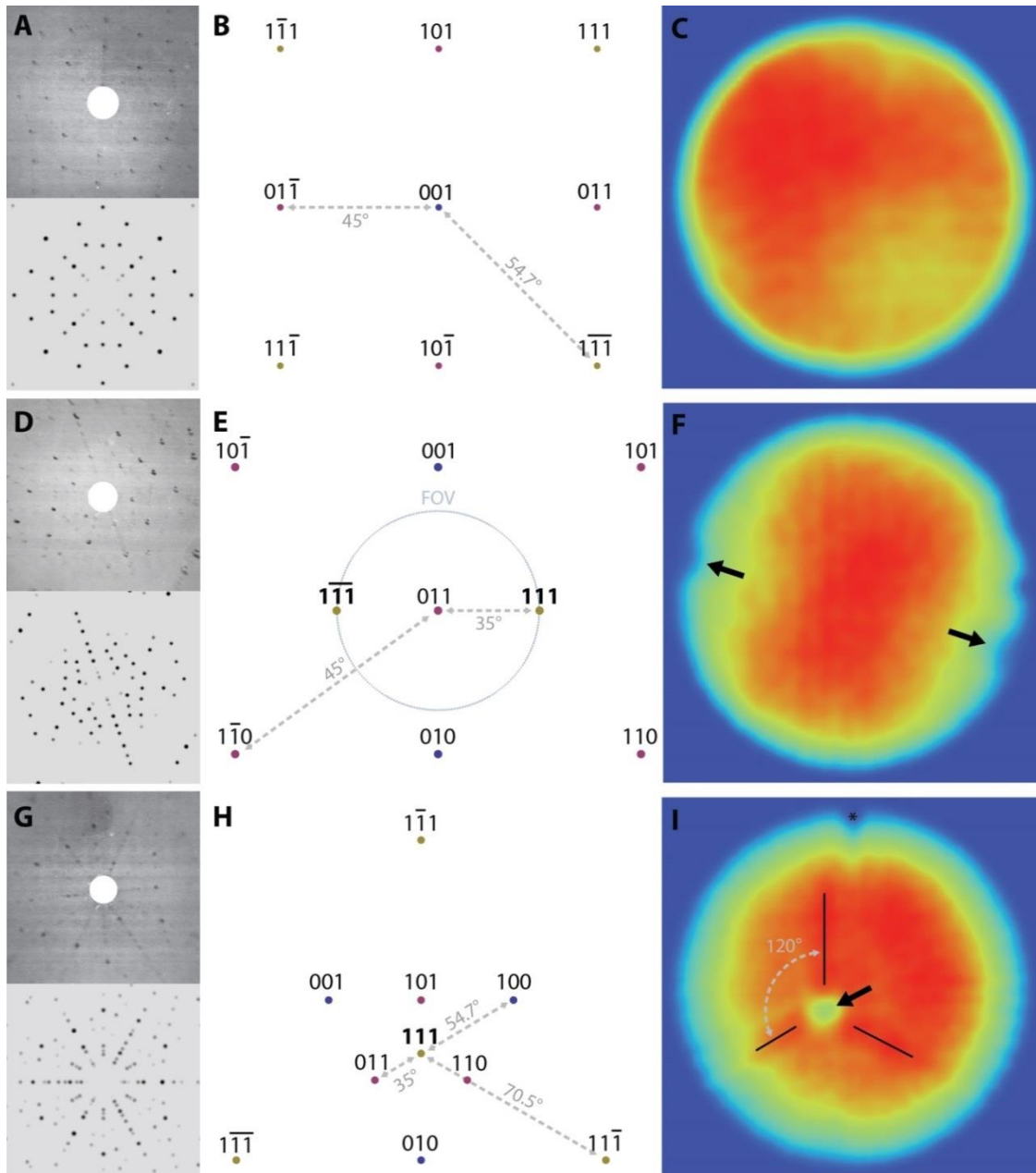


Figure 10.4: Laue backscatter X-ray diffraction, radial pole projections and APT detector histograms

(a, d, g). Laue backscatter X-ray diffraction of magnetite single crystals and corresponding simulated diffraction patterns. (b, e, h) radial pole projections for $\langle 100 \rangle$, $\langle 110 \rangle$ and $\langle 111 \rangle$ orientations, 70° field of view and angular separation between poles are indicated. (c, f, i) 2D ion density maps of APT reconstructions for the $\langle 100 \rangle$, $\langle 110 \rangle$ and $\langle 111 \rangle$ oriented magnetite crystals, only $\langle 111 \rangle$ poles are visible as low-density regions (black arrows). Three-fold symmetry is observed in the $\langle 111 \rangle$ oriented sample (indicated with black lines and 120° angle labeled), * indicates a low density artifact resulting from a detector defect not a crystallographic pole.

10.2.2 Spatial Distribution Maps

Crystallographic information was extracted from the reconstruction by way of a spatial distribution map (SDM) following the approach introduced by Moody and coworkers²⁵³. This approach is less computationally intensive and less susceptible to noise than Fourier-transform (FT) and related autocorrelation methods²⁶¹⁻²⁶⁴.

An SDM is the cumulative 3D histogram of the vectors between each atom in a given volume and its neighbors, typically those within +/- 1 nm along x-, y-, and z-direction. Our implementation uses the Chebyshev or chessboard distance to select the ions in a +/- 1 nm box instead of the Euclidean distance to select ions in a +/- 1 nm sphere. It is frequently useful to restrict SDMs to distances between specific elements, e.g. O-O, Fe-Fe, or Fe-O. Any SDM can be collapsed into a one-dimensional SDM along an arbitrary direction. The planar spacing in this direction can then be extracted from the period of the SDM. In the oriented magnetite samples, the only poles observed correspond to the $\langle 111 \rangle$ zone axis. However, as the pole is never perfectly aligned with the sample z-axis we have to identify the direction of the pole in the sample in order to extract the planar spacing and compare it to the expected value. There are several possibilities to do so by advanced SDM or Hough transform methods^{253,265}.

We selected cylindrical regions of interest (ROI) from the reconstructed data, with the cylinder axis parallel to the analytical z-direction, centered on the pole, a radius of 5 nm, and a length corresponding to the depth of the entire data set in the z-direction. We then performed a systematic search over approximately 10^5 different orientations of this ROI ($\pm 45^\circ$). In case of multiple poles, this was done for each pole separately. For each orientation, described by the angles of rotation about two axes (Θ, ϕ), we calculated the maximum value of the one-dimensional Fe-Fe SDM in the analytical z-direction (Fe-Fe z-SDM).²⁶⁶ We used the global maximum (Figure 10.5) of the z-SDMs to identify the orientation of the pole with respect

to the analytical z-direction. This algorithm essentially captures manual alignment of a crystal structure model by rotating it until crystallographic planes are viewed edge on. Z-SDM from a $\langle 111 \rangle$ aligned tip is shown in Figure 10.6 and a zSDM from one of the $\langle 111 \rangle$ poles observed in a $\langle 110 \rangle$ oriented tip is shown in Figure 10.7.

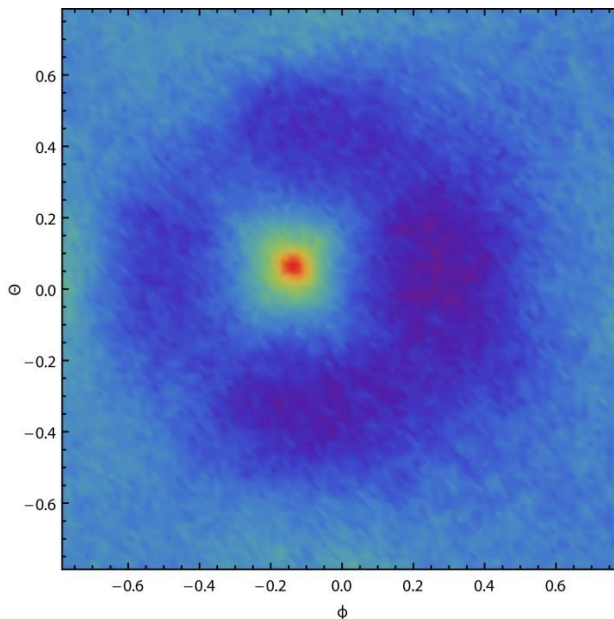


Figure 10.5: SDM Alignment Optimization

SDM alignment optimization for tip with $\langle 111 \rangle$ within 0.2 radians in Θ and ϕ of the original analytical z-axis (0,0). Color values (rainbow) represent maximum value of the SDM for the specific orientation with specific Θ and ϕ rotation angles, effectively corresponding to the number of ions lying on the same planes (± 10 pm). High values (red) represent the orientation where the $\langle 111 \rangle$ direction is now closely aligned (most ions now lie on the same planes) with the new rotated z-axis. The interplanar spacing can then be determined by computing the histogram of the new z-distances between ions after rotation of the coordinate system.

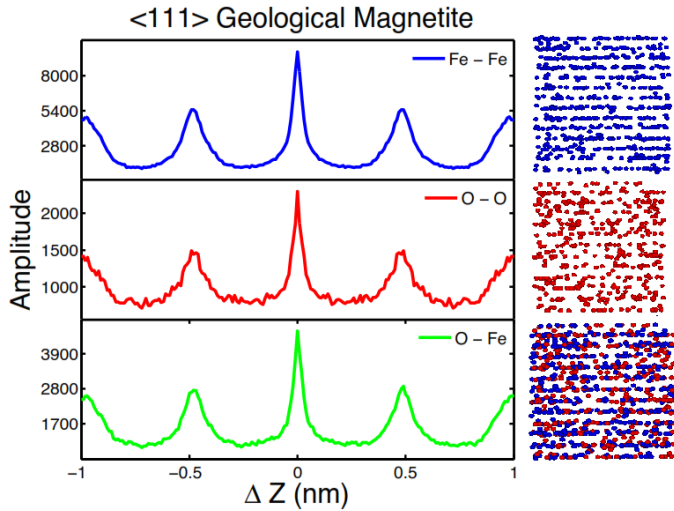


Figure 10.6: $\langle 111 \rangle$ zSDM from $\langle 111 \rangle$ oriented tip

Fe-Fe, O-O and O-Fe z-SDMs calculated for a 5 nm cylindrical region of interest centered on the $\langle 111 \rangle$ crystallographic pole in the nanoscale magnetite phase of a geological magnetite oriented along $\langle 111 \rangle$ after optimal rotation. A small region of the aligned APT dataset is plotted on the right with elements corresponding to the elements in the respective zSDM.

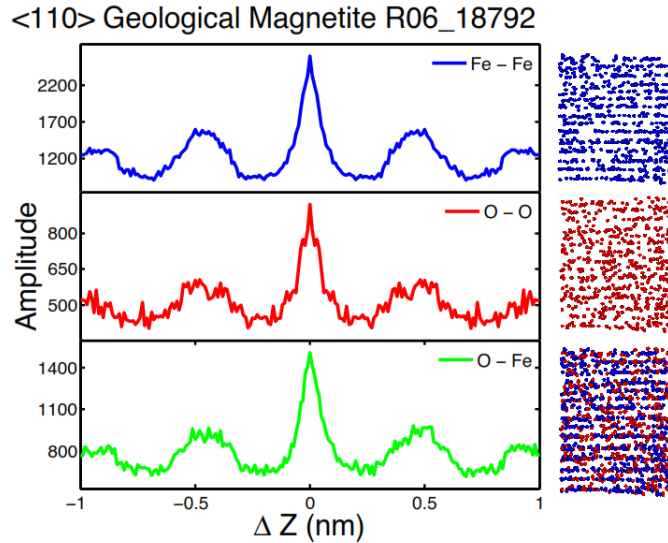


Figure 10.7: $\langle 111 \rangle$ zSDM from $\langle 110 \rangle$ oriented tip

Fe-Fe, O-O and O-Fe z-SDMs calculated for a 5 nm cylindrical region of interest centered on the $\langle 111 \rangle$ crystallographic pole in the nanoscale magnetite phase of a geological magnetite oriented along $\langle 110 \rangle$ after optimal rotation.

A small region of the rotated APT dataset is plotted on the right with elements corresponding to the elements in the respective zSDM.

For the analysis of the reconstruction of biogenic magnetite from the chiton tooth cusp, we identified and aligned the single pole using the same strategy as outlined above. While the z-SDM of the biogenic magnetite has lower signal-to-noise ratio, peaks corresponding to planes are clearly visible (Figure 10.8). Similarly, planes can be identified by eye in the reconstruction. In our experiments using oriented single crystals only $\langle 111 \rangle$ poles have been observed, therefore we suspect the pole observed in the biogenic sample is also a $\langle 111 \rangle$ pole and again we adjusted the image compression factor such that the d_{111} -spacing in the reconstructed z-SDM matches the expected value (0.48 nm). When two poles were observed the angle separating the poles on the detector histogram and within the 3D reconstruction were used to further constrain the reconstruction²⁶⁷.

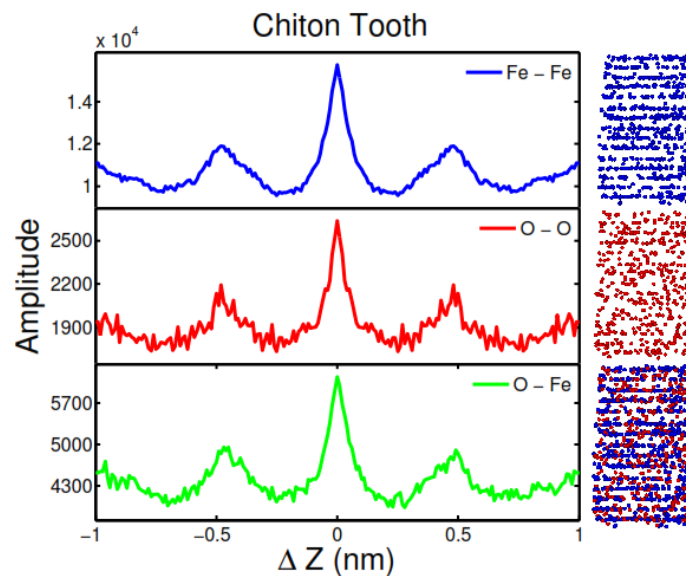


Figure 10.8: Chiton Tooth zSDM

Fe-Fe, O-O and O-Fe z-SDMs calculated for a 5 nm cylindrical region of interest centered on the crystallographic pole in the nanoscale magnetite phase of a biomineral chiton tooth dataset after optimal rotation. A small region of the rotated APT dataset is plotted on the right with elements corresponding to the elements in the respective zSDM.

Reconstruction of atom probe data requires the geometric field factor k_f , the evaporation field strength F_e , the image compression factor ξ , detector efficiency, α , and average ionic volume as input.⁹⁹ The image compression factor, ξ , is the ratio of expected angle between crystallographic zone-axis and the angle observed between low density regions on detector event histogram (poles)²⁶⁸. The product $k_f F_e$ can be estimated experimentally by analysis of the shape of the sample tip during/after atom probe measurements. When multiple poles (low density regions on detector event histogram) are observed, the corresponding zone axes can be identified by calculating the angle between low density regions and by taking its ratio with expected angle.

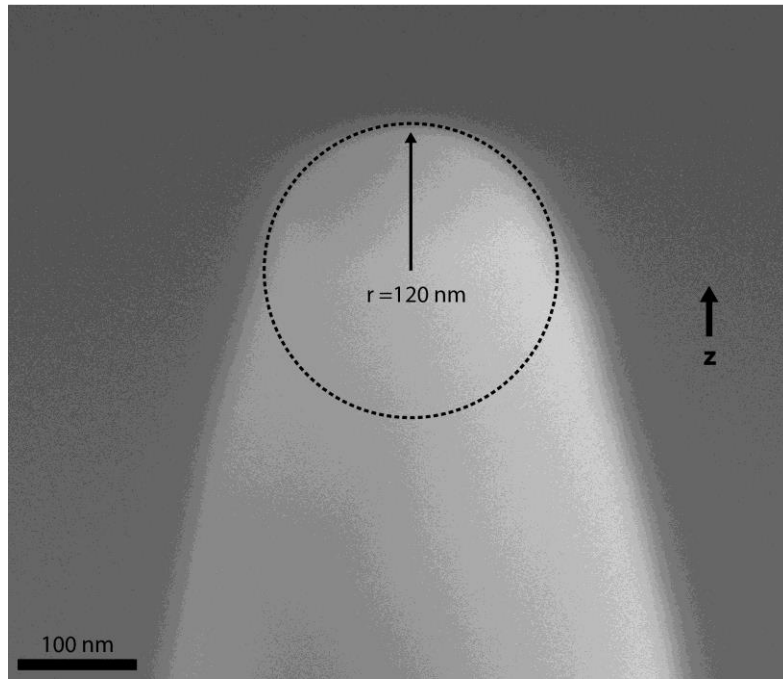


Figure 10.9: Post-LEAP SEM

Scanning electron micrograph of the geological magnetite sample tip with the <111> direction parallel to the analytical z-axis (black arrow) after analysis. Measured final tip radius (r) of 120 nm (dashed circle), final voltage (V) when run stopped of 8.2 kV, calculated evaporation field (E_f) using, $r = V/(k_f \cdot E_f)$, of 21 V/nm with $k_f = 3.3$.

With the selection of reasonable reconstruction parameters using literature and default values based on metals and semiconductors the expected Fe-Fe zSDM distance of 0.24 nm was not reproduced.. Instead a value almost double, 0.48 nm was observed. Furthermore the alternating Fe and O layers were not observed. Two possible explanations for this phenomenon are:

1. The reconstruction parameters we determined are incorrect for magnetite.
2. An evaporation artifact results in not all of the planes along the $\langle 111 \rangle$ direction being individually resolved.

Missing planes have also been observed in ordered $L1_0$ Fe-Pt alloys where extreme differences in fields required for field evaporation of the Fe and Pt elemental layers leads to evaporation artifacts in the $\langle 001 \rangle$ orientation²⁶⁹.

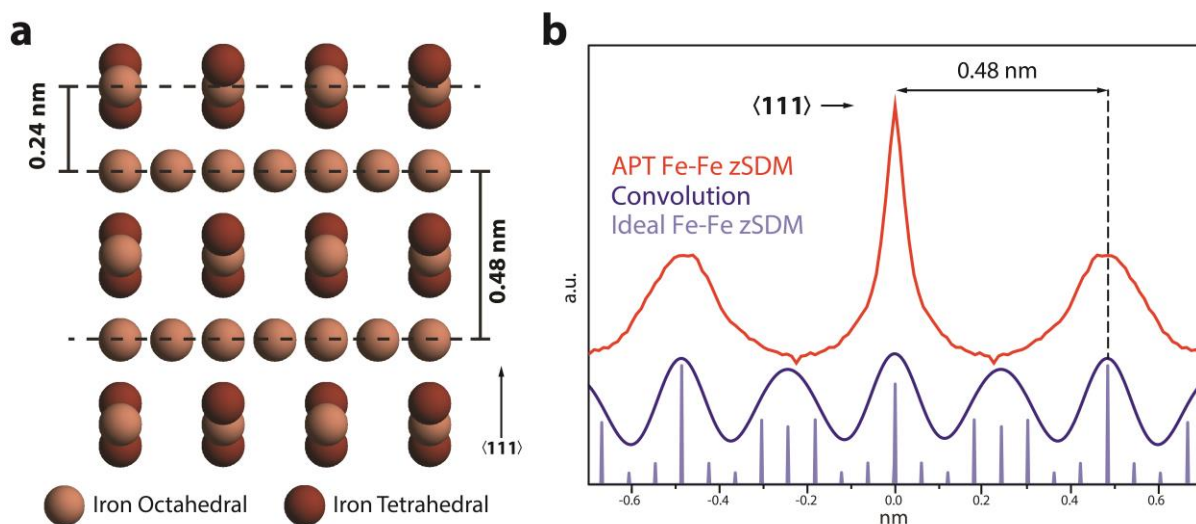


Figure 10.10: Magnetite crystal structure, theoretical and measured SDM

Magnetite crystal structure along the (111) direction, illustrating the expected 0.24nm zSDM spacing. b Representative Fe-Fe $\langle 111 \rangle$ zSDM (red), theoretical (light blue) and convolution of the theoretical SDM with a Gaussian to simulate the limited resolution of the atom probe (dark blue). Note that even following convolution the simulated SDM does not match the representative experimental SDM.

10.2.3 Reconstruction calibration with microstructural features

To eliminate the former possibility a sample with additional features to fix the free reconstruction parameters was needed. Unlike in many traditional metal systems in most oxides there are an inadequate number of crystallographic poles to completely solve for all the parameters simultaneously^{251,252}. In addition to crystallographic poles observed in the detector histogram microstructural features with a well-established geometry or relationship to the crystal lattice can also be used to calibrate reconstruction parameters. A set of geological magnetite crystals, LP-204-1, have been discovered which contain numerous platelet shaped precipitates enriched in Mn and Al (Figure 10.11)²⁷⁰. These precipitates are aligned parallel to (100) planes and are disc shaped. This material was previously analyzed by field ion microscopy and voltage pulsed atom probe tomography, however, due to frequent sample failures the precipitates were not captured¹⁶⁹.

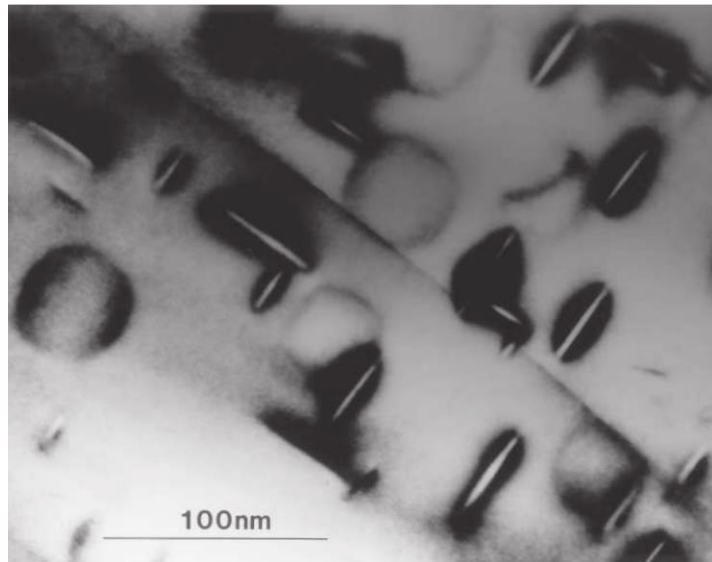


Figure 10.11 TEM micrograph down [100] of LP204-1 magnetite

The three orientations of the Mn- and Al-enriched platelets parallel to (100) family planes in magnetite are visible. Adapted from ref²⁷⁰.

Using laser pulsed atom probe tomography analysis of LP-204-1 samples was successful following the same careful crystallography orientation, sample preparation and analysis procedures used for the previous geological magnetite single crystals (Figure 10.12). Consistent with expectations lattice planes were observed along the $\langle 111 \rangle$ directions. Using the same protocols to calibrate the reconstruction used for the other samples we found the same $\langle 111 \rangle$ zSDM spacing of 0.48 nm, approximately double the expected value. Based on the aspect ratio of the platelets, determined based on the aspect ratio of the convex hull of the ion positions contained within the $1.5 \text{ Al}/\text{nm}^3$ isodensity surface, and the angles between the platelets, determined based on the angles between the eigenvector of the covariance matrix (the principle axes) perpendicular to the platelet, it was clear the reconstruction parameters were accurate. When the reconstructions parameters were adjusted to result in the expected $\langle 111 \rangle$ zSDM spacing the reconstruction is distorted (Figure 10.14). Clearly, incorrect reconstruction parameters were not the cause of the “missing planes”. Furthermore, at least for magnetite, the reconstruction parameters commonly accepted as defaults

for metals and semiconductors appear to produce reasonably accurate results and are similar to the calibrated values.

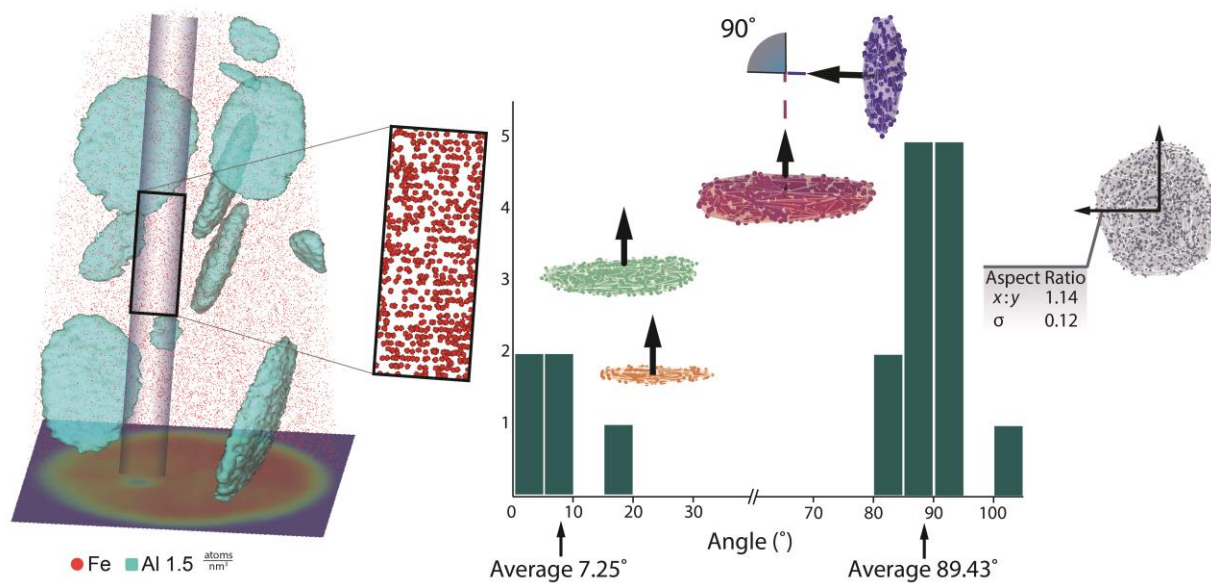


Figure 10.12: Reconstruction of LP-204-1

Three dimensional APT reconstruction of LP-204-1 geological magnetite single crystals. Platelets are apparent in reconstruction, defined by a 1.5 Al/nm³ isodensity surface. Lattice planes are clearly observed in the pole region. Angles between the platelets and the platelet aspect ratio were used to constrain the reconstruction.

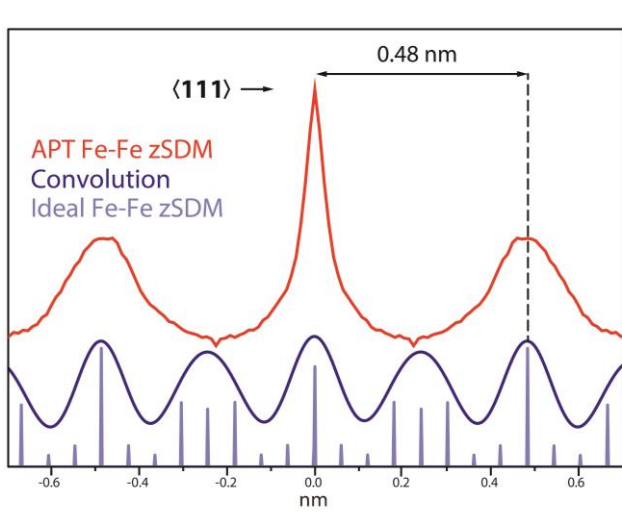


Figure 10.13: LP-204-1 SDM

Normalized LP-204-1 Fe-Fe (111) zSDM (red), theoretical (light blue) and convolution of the theoretical SDM with a Gaussian to simulate the limited resolution of the atom probe (dark blue). Note that even following convolution the simulated SDM does not match the experimental SDM.

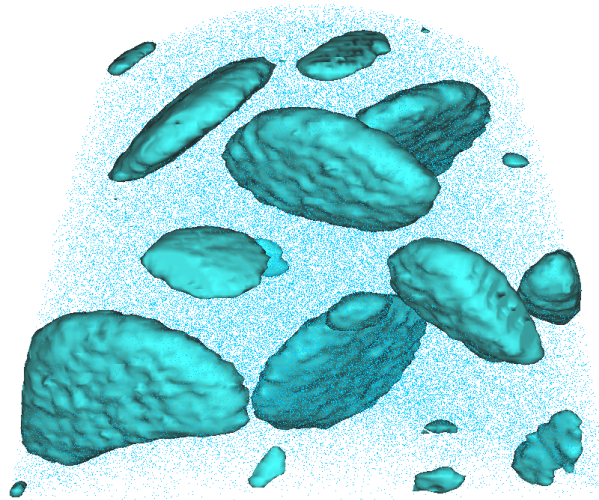


Figure 10.14: Distorted reconstruction

Distorted reconstruction of LP-204-1 magnetite where detection efficiency has been adjusted to “correct” the zSDM spacing to 0.24 nm consistent with the expected value. Note how the angles between the platelets are now not 90° and the aspect ratio of the platelets has diverged from unity. $\xi = 1.9$, $\alpha = 0.98$, $k_f = 3.3$, $F_e = 18$. Note that the detection is nonphysical as it exceeds the theoretical maximum efficiency of the micro-channel plate detector.

The confirmed microstructural relationship between the platelets and their well-defined geometry confirmed that the reconstruction was correct and that the incorrect spacing results from an evaporation artifact. Most likely, evaporation does not happen in discrete layers but multiple layers evaporate simultaneously leading to the reconstruction artifact.

10.2.4 Multilayer evaporation artifact

The inability of APT to distinguish between the Fe(II) and Fe(III) in the magnetite crystal lattice makes it difficult to distinguish if there is a layer which is “missing” or not resolved. Analysis of mixed metal oxide spinels which present compositionally distinct layers (Figure 10.15) along the $\langle 111 \rangle$ direction that can be detected provides a potential solution.

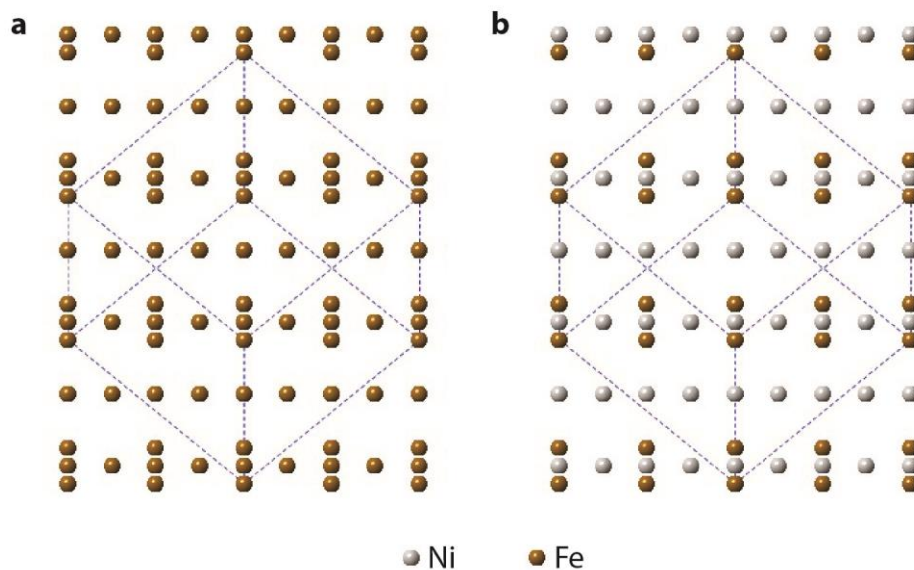


Figure 10.15: Magnetite ($\text{FeO} \cdot \text{Fe}_2\text{O}_3$) and trevorite ($\text{NiO} \cdot \text{Fe}_2\text{O}_3$) crystal structure

Comparison of the magnetite and trevorite crystal structure viewed perpendicular to the $\langle 111 \rangle$ direction. Easily distinguished alternating Ni- and Fe-rich layers are present in trevorite. Unit cell edges overlaid in dashed purple lines.

Preliminary data from an oriented trevorite ($\text{NiO} \cdot \text{Fe}_2\text{O}_3$) crystal reveals the same $\langle 111 \rangle$ zSDM spacing of 0.48 nm; however, in this case the presence of distinct cations in the layers provides a potential method to identify the evaporation issues. In trevorite Fe is present only in alternating layers and, in fact, the Fe-Fe SDM spacing should be ~0.5 nm, however, as Ni is present in both layers, the zSDM spacing should be 0.25 nm. Similar to magnetite both Ni and Fe exhibited a $\langle 111 \rangle$ zSDM spacing of 0.5 nm (Figure 10.16). Furthermore, if a specific Fe- or Ni-rich plane exhibited different evaporation behavior the measured stoichiometry in the ROI at the pole would differ from the overall stoichiometry, similar to the case of ordered intermetallic Fe-Pt alloys where depletion of Fe at the (002) pole and zone axes was observed. For the case of Trevorite there was very little stoichiometry difference between the difference between the pole ROI ($\text{Ni}/\text{Fe} = 0.61$) and the bulk of the tip ($\text{Ni}/\text{Fe} = 0.59$). There is also no evidence of alternating Fe- and Ni-rich layers in the reconstruction along the $\langle 111 \rangle$ direction (Figure 10.16).

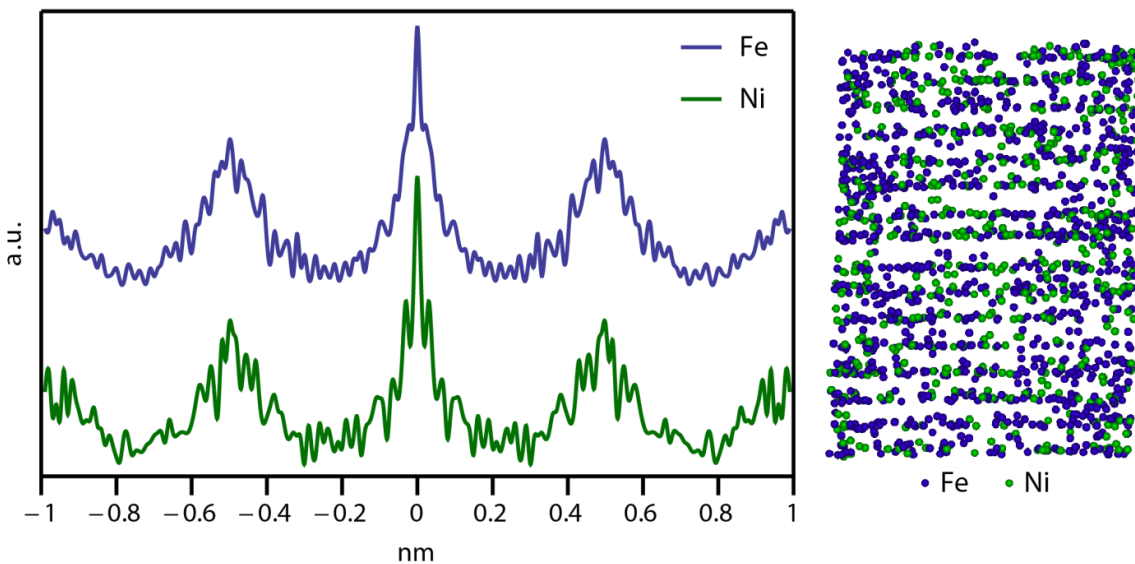


Figure 10.16: Trevorite Fe-Fe and Ni-Ni zSDM

Normalized Fe-Fe and Ni-Ni zSDM for $\langle 111 \rangle$ oriented trevorite and associated 3D APT reconstruction showing lattice planes. Note the lack of alternative Fe- and Ni- planes in the reconstruction.

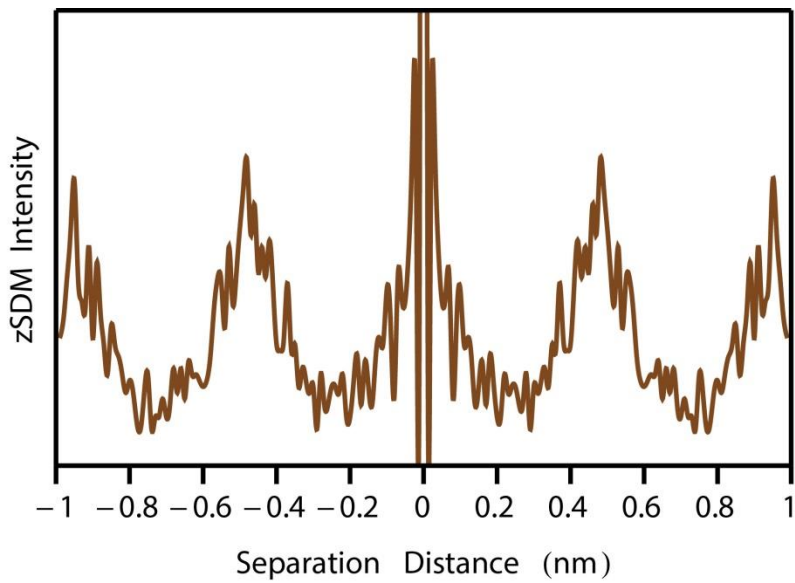


Figure 10.17: Trevorite Fe-Ni zSDM

Normalized Fe-Ni zSDM for $\langle 111 \rangle$ oriented trevorite. Note the large peak at a separation distance of 0 nm indicating that the expected alternating Fe and Ni rich layers have collapsed into a single layer.

It appears that the evaporation doesn't proceed exactly layer by layer; some ions might evaporate from a lower layer before the surface layer is completely evaporated. The standard reconstruction algorithm would then result in incorrect zSDM spacings. In addition to the lack of the expected alternating Fe- and Ni-rich layers, the oxygen sub-lattice has also collapsed and, in fact, it appears that four distinct layers, two pairs of alternating cation and anion layers of the crystal lattice appear to evaporate as a single layer.

10.3 CONCLUSION

We validated an advanced SDM approach for detection and identification of single crystallographic poles in atom probe reconstructions of single crystalline geological magnetite. Upon careful analysis of the interplanar spacing it became apparent that the observed spacing did not match the expected value. Reconstruction parameters were verified to be correct using geological single crystals containing well defined microstructural features that constrain the reconstruction parameters. However, even with properly con-

strained reconstructions the incorrect interplanar spacing remained, indicating the possibility of an evaporation artifact. Initial experiments focused on magnetite, a mixed-valence iron spinel mineral with both Fe^{2+} and Fe^{3+} , however, it is not possible to determine the valence of the iron in the lattice following field evaporation. Analysis of mixed metal oxides, where alternating planes exhibit detectable elemental differences (i.e. Ni- and Fe-rich) were used to attempt to identify the mechanisms responsible for the evaporation artifact leading to the incorrect spacing. Results suggest that multiple planes evaporate as a single layer, leading to the incorrect interplanar spacing in the reconstruction.

10.4 MATERIALS AND METHODS

10.4.1 Optimal rotation of the APT dataset

The geometric relationships between the rotated coordinates (x'', y'', z'') and the initial coordinates (x, y, z) can be obtained according to equations 1-3.

$$x'' = x \cos \theta - z \sin \theta \cos \phi + y \sin \theta \sin \phi \quad [1]$$

$$y'' = y \cos \phi + z \sin \phi \quad [2]$$

$$z'' = x \sin \theta + z \cos \theta \cos \phi - y \cos \theta \sin \phi \quad [3]$$

The global maximum obtained in the z-SDM at each rotation as a function of the rotation coordinates is plotted in figure 2. The rotation coordinates that maximize the global maximum obtained in the z-SDM represents the optimal rotation for aligning the crystallographic axis along the analytical z-direction.

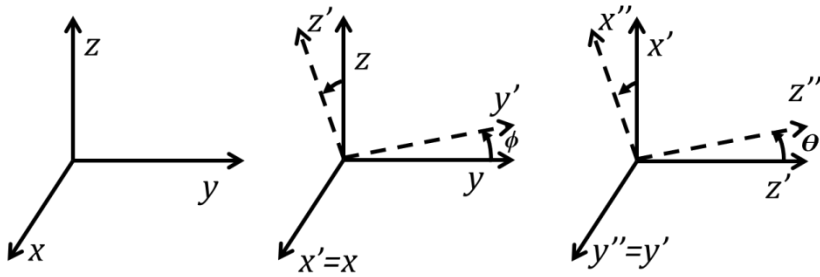


Figure 10.18: SDM alignment coordinate system

The geometry for the rotation of the coordinate system of the APT dataset is shown. (a) Initial coordinate system, (b) Rotation of the coordinates with respect to x-axis by an angle ϕ resulting in y' and z' (c) Rotation of the coordinates with respect to the new y-axis (y') by an angle θ resulting in the final coordinate system (x'' , y'' , z'').

10.4.2 SDM to limit reconstruction parameters

For geological magnetite, we tested samples of $<111>$, $<110>$, and $<100>$ orientation. In APT, low density regions in the detector event histogram are indicative of presence of a crystallographic pole. In the case of the $<111>$ oriented specimen, a low density region was observed at the center of the detector event histogram consistent with the $<111>$ pole. No other low density regions were observed. No low density regions were observed in the $<100>$ oriented sample. In the $<110>$ oriented samples, no low density region was observed at, or around, the center where the $<110>$ pole would be expected. However, two low density regions were observed at opposite points near the edge of the detector event histogram potentially corresponding to either the $<111>$ or $<100>$ poles opposite the unobserved $<110>$ pole at the center. Since no low density regions were observed in $<100>$ oriented sample but a low density region was observed in $<111>$ oriented sample, it was more probable that low density region corresponded to $<111>$ direction. Additionally, the observation of two opposite $<100>$ family poles would imply an unrealistic 90° field of view, while two opposite $<111>$ family poles indicates a much more reasonable 70° field of view.

While reconstruction parameters are a function of specimen geometry and chemistry, and therefore can change throughout the experiment, their value can be guessed reasonably accurately if we focus only on a subset of the total evaporated ions. There are 5 unknowns: the field factor, k , the evaporation field, E_f , the

image compression factor, ICF, the atomic volume, and the detection efficiency. Based on the $<110>$ oriented samples where two opposite $<111>$ family poles were observed a number of the reconstruction parameters can be fixed.

10.4.3 Quantifying k and E_f

The final radius, R , of the specimen was measured from a post field evaporation scanning electron microscopy (SEM) image. Combining the radius with the final voltage, V , from the experiment we can solve for the product $k^* E_f$ as per: $R = V/k^* E_f$. As both k and E_f are unknown yet appear in all the expressions as the product $k^* E_f$ they cannot both be solved for simultaneously. Since E_f for magnetite is not known we used default value, 3.3 for k and calculated E_f .

10.4.4 Quantifying ICF

In the $<110>$ oriented sample two low density regions were observed corresponding to two opposite $<111>$ family poles. The ICF was then calculated from formula: $ICF = \text{Expected angle} / \text{Observed Angle}$.

10.4.5 Atomic Volume

The atomic volume (0.0105 nm^3) was calculated based on number of ions per unit cell (56) divided by the total volume of the magnetite unit cell (0.5906 nm^3)¹²⁸.

10.4.6 Detection Efficiency

Detector efficiency is an instrument property. However, standard procedure to quantify detector efficiency assumes well assigned mass to charge range. But in biological samples, mass to charge histograms has very large tails and it not all detected ions are assigned to any chemical identity. This introduces artificial loss of efficiency. Also, for SDM calculations, we are focused on region in and around low density region to extract crystallographic information. This region has low density compared to rest of the reconstructed sample. By using instrumental detector efficiency in cases when many ions are not ranged or when focus is low density region, final reconstruction will not be accurate. This was the parameter which was fixed

by iterations so that d-spacing from the reconstruction correspond to 0.48 nm. Expected d-spacing was achieved for efficiency of 0.40.

11 FUTURE OUTLOOK

11.1 MECHANISMS OF BIOMINERALIZATION IN THE CHITON TOOTH

The chiton tooth cusp, which is the hardest component of the tooth, is composed primarily of magnetite with various impurities, including organic chitin and proteins as well as inorganic species such as sodium, magnesium, and manganese. Our findings from atom probe tomography revealed organic fibers within the chiton tooth selectively decorated with either sodium or magnesium ions. Further investigation with XAS and EPR revealed that iron complexes associated with organic macromolecules were present. These complexes were found to be responsible for selectively forming metastable ferrihydrite, which subsequently transforms into magnetite. However, the importance of the other cations bound to the organic matrix was not determined throughout this work and remains an open question. Implementing *in vitro* models to probe the influence of biologically relevant cations on iron-organic complexes in mineralization will provide a suitable model system to further understand the mechanisms of chiton tooth mineralization. Preliminary experiments investigating organic matrix-mediated iron-oxide biomineratization inspired by the chiton tooth implemented a model system using chitin hydrogels. We demonstrated that the chitin hydrogel alone was unable to control polymorph selectivity, suggesting that additives such as proteins or inorganic cations play a significant role in mineralization. To this end, the development of a chemically functionalized hydrogel that can selectively bind ions will provide further mechanistic insight into the role of additives on iron-oxide biomineratization. Fourier transformation infrared spectroscopy and EPR spectroscopy measurements performed *in situ* during the course of iron oxidation, complexation and mineralization within the model system will help elucidate the specific mechanisms and complexes responsible for polymorph selectivity.

In addition to synthetic model systems the native tooth organic scaffold can be used for additional experiments, specifically, *in vitro* mineralization of unmineralized chiton teeth or remineralization of the organ-

ic scaffold from demineralized chiton teeth under physiological conditions. Similar experiments have been performed with unmineralized and demineralized collagen scaffolds to understand the formation of bone and dentin²⁷¹. These experiments when combined with chelation and deproteination treatments to selectively remove bound metal ions and acidic proteins from the polysaccharide scaffold; will provide further insight into the importance of these species on the biomineralization process.

Comparison of the EPR spectra of the native chiton tooth iron-organic complexes to a uniform Fe-EDTA complex indicated that the species present within the chiton tooth exhibits variable conformations, however, the exact structure and chemistry of the complex remains unknown. Further EPR experiments, in particular, across a range of temperatures could provide further insight into the complex and even determine the exact nuclearity of the species present or prove the existence of a purely mononuclear iron-organic complex. Given that chiton teeth are the hardest and most wear resistant biominerals, understanding this material has profound implications for biologically inspired material syntheses.

11.2 STRUCTURE OF APATITES AND BONE-TYPE MINERALIZED TISSUES

Current structural models of bone^{8,56} and dentin^{66,184}, including elephant tusk ivory dentin^{65,67,68} posits that apatite crystallites have irregular platelet habit and that organic and inorganic species, particularly citrate and magnesium, segregate to platelet surfaces. Based on this model of bone, it was very surprising that our APT experiments were unable to identify segregation of Na^+ , Mg^{2+} or organic molecules to grain boundaries. Instead, Na^+ and Mg^{2+} were nearly homogeneously distributed throughout the mineral phase. This observation was surprising because enamel, another apatite-based biomineral with similar impurities as bone and dentin, showed Na^+ , Mg^{2+} and organic molecules clearly associated with grain boundaries. In particular, we expected impurities such as Mg, which is insoluble in the apatite crystal lattice, to be segregated from the bulk crystals. Therefore, we postulate three possibilities to explain our results: (1) the current model is flawed and the apatite crystals do not exhibit a platelet shape, (2) there is no segregation to platelet interfaces, or (3) platelet shaped crystals may be present with interfacial segregation, but limita-

tions of APT prevent resolution of these features. The preliminary data thus far is not adequate to satisfactorily resolve the issue of the platelet shaped crystals in bone and further investigation of bone and dentin by APT is necessary. Additionally, cryogenic APT of forming bone could provide further insight into the structure of the tissue and the mechanism of its formation.

Although current APT data is inadequate to directly resolve the exact nature of bone crystals, the unique sub-nanometer spatial resolution and parts-per-million chemical sensitivity of APT provides unique opportunities for further studying bone and bone-implant interfaces. Metallic implants are widely used in the clinic with varying degrees of success to repair broken bones and replace joints. The permanent nature of metal implants in the body can lead to corrosion of the metal implant over time²⁷². APT has a unique ability to map the distribution of numerous elements with high sensitivity, providing the means to detect and study the incorporation of implant-derived metals into the surrounding bone tissue, which could possibly be a source of toxicity. Furthermore, APT of metal-implant interfaces, while experimentally challenging, could provide extremely useful insight into nanoscale processes and morphological changes occurring during implant osseointegration²⁷³. In particular, evaluation of the nanoscale structure and chemistry of the bone-implant interface in the presence of osteogenic or bioactive coatings could probe the necessary information to rationally design implant coatings and surface treatments. Furthermore, comparison of the nanoscale structure and chemistry of healthy and diseased bone provides the possibility of providing new insight into bone disease and essential information for developing novel treatments.

Beyond the importance of apatite in biological minerals, the nanoscale structure and chemistry of apatite minerals is of wide interest in geological and industrial applications. In particular the distribution of trace elements and structure of defects influences fission track dating of apatite minerals and the development of novel phosphors and high-energy lasers.

11.3 INTERGRANULAR PHASES IN TOOTH ENAMEL

The relation between chemistry and structure of enamel that makes it susceptible to acid dissolution from dental caries is unknown. In particular, impurities such as Na^+ , Mg^{2+} , and CO_3^- are known to increase the solubility of the mineral phase while F^- decreases solubility, but a detailed understanding of how these impurities are incorporated into the tissue architecture is lacking. In our work, we examined rodent enamel with a combination of APT and XAS techniques and discovered that the majority of Mg in enamel is present as an inter-crystalline (grain boundary) precipitate of Mg-substituted amorphous calcium phosphate (Mg-ACP). These metastable and highly soluble precipitates were found to be responsible for rapid and highly anisotropic acid etching of enamel, providing short circuit pathways for fluoride diffusion. Future experiments performing both APT and XAS of human enamel are important to determine if similar trends in structure and chemistry are present. If similar trends are observed, strategies to protect enamel from carious attack may be afforded by the replacement of this phase with a more stable mineral phase. Remarkably, inspiration on how to overcome this weakness comes from experiments performed on pigmented rodent enamel that showed that the Mg-ACP had been completely replaced by a mixture of metastable ferrihydrite and amorphous iron phosphate. This substitution not only rendered pigmented enamel mechanically harder, but also more resistant to acid attack to a greater extent than topical fluoride treatment. These concepts will inspire the engineering of enamel grain boundaries and provide insight for developing next generation dental care products, including novel prophylactics and treatments for dental caries.

Our experiments demonstrated that fluoride is easily incorporated into the inter-crystalline Mg-ACP, however the effect of fluoride exposure during tooth development can result in pathologies such as dental and skeletal fluorosis. We have performed preliminary experiments to elucidate the enamel fluoridation following systemic fluoride exposure compared to our results following topical fluoride exposure.

APT experiments of rodent enamel from genetically modified mice strains²⁷⁴ were inconclusive due to challenges associated with complete removal of fluoride from the feed provided to the control group. The initial work suggested that fluoride incorporation following systemic exposure to fluoride was concentrated in the dentin within mouse incisors and not the enamel. However, further work is required to develop a suitable model for systemic enamel fluoridation to complement the successful investigation of topical fluoridation. Improved fluoride-free foods or changing to a rat model where fluoride is naturally accumulated in enamel²⁷⁵ provide potential solutions to experimental challenges.

In addition to impurities, the nature of water incorporation within enamel and its influence on ion diffusion through the tissue can provide insight into mechanisms leading to acid dissolution. Initial experiments with $^2\text{D}_2^{18}\text{O}$ isotopically labelled water were hampered by the inability to separate ^{18}O and $^1\text{H}_2\text{O}$ in the mass spectrum. Spectral signature of $^2\text{D}_2^{17}\text{O}$, or even the mildly radioactive, $^3\text{T}_2\text{O}$, might be more easily resolved in the mass spectrum. Extensive dehydration of native enamel prior to exposure to the isotopically labelled water may help further mitigate this issue. Additional easily detectable isotopes, including ^6Li and ^9Be , could provide further insight into diffusion mechanisms.

11.4 FERRITIN AND HYBRID ORGANIC-INORGANIC NANOPARTICLES

Dating back to the 1980's, when Panitz imaged ferritin nanocages using APT²²⁸⁻²³⁰, there has been great interest in performing routine analysis of APT of biomolecules and nanoparticles, particularly organic-inorganic nanoparticles. The two main challenges with performing APT of nanoparticles are the lack of sample reliability and complicated spectral interferences in the mass spectra. In an attempt to analyze nanoparticles, we have demonstrated the capability of imaging ferritin, a crucial metal ion-transport protein using APT, which has potential to unravel the chemistry at the organic-inorganic interfaces and elucidate mechanisms of metal binding and stabilization for transport.

For the successful use of APT for nanoparticle analysis, it is necessary to develop a protocol to deposit nanoparticles uniformly at a desired density on a substrate from which sample tips can be routinely and reliably fabricated for APT analysis. In many microscopy techniques, the microscopist can scan broad areas of the sample at low magnification prior to selecting a region of interest to investigate in greater detail (ex. higher magnification). This makes it possible to image samples with non-uniform nanoparticle deposition on the substrate. Unfortunately, this is not the case for atom probe because sample tips are fabricated in the FIB, where small nanoparticles and thick protective capping layers make it impossible to visualize regions containing a uniform coating of nanoparticles. Analysis of overly dense nanoparticle layers led to a very weak interface and subsequent sample failure during APT analysis. The opposite problem occurred when sample tips did not contain the nanoparticles of interest. One possible strategy to produce highly uniform nanoparticle deposits is to take advantage of the tendency of certain molecules and nanoparticles to form two dimensional crystals under specific conditions, which can then be transferred directly to the substrate^{276,277}. Based on our experiments, improvements in the cleanliness of the sample are also required to mitigate carbon contamination and improve the yield of successful samples.

In addition to sample reliability concerns, spectral interferences complicate analysis. Ferritin is a flexible molecule which can be easily demineralized and remineralized *in vitro* with other hydrated oxides such as cobalt or manganese oxides or even isotopically labeled iron to reduce spectral interferences^{46,278,279}. Certain noble metals and metal alloys can also be deposited in the ferritin core.

11.5 EARLY HYDRATION OF TRICALCIUM SILICATE

Preliminary APT analysis of C3S hydrated with D₂O provided evidence for the formation of a new phase on the cement surface. However, the APT analysis revealed the presence of surface topography on the samples, indicating that the hydration reaction may have proceeded past the initial passivation layer. Future experiments should include experimental parameters such as shortening of hydration times to reduce the confounding topographical effects and facilitate investigation of the initial passivation layer.

Another significant shortcoming of these experiments includes the complication due to spectral interferences, particularly from hydrogen ions and hydrogen-containing molecular ions. Although we used deuterium labeled heavy water for hydration experiments to reduce the spectral interference from hydrogen, residual hydrogen and water molecules in the ultra-high vacuum chamber contributed to a number of isobaric atomic and molecular species containing hydrogen. As an alternative, experiments implementing doubly isotopically-labeled water ($D_2^{17}O$ or $D_2^{18}O$) could help alleviate this problem by simultaneously labeling oxygen atoms; the spectral signatures should be much more straightforward to identify and thus localize in reconstructions. Additionally, tritiated water, (3T_2O), although slightly radioactive, if available in sufficient purity (degree of isotopic enrichment), could provide spectral signatures that are even easier to detect. Additionally, the deposition of the protective metal film is an additional source of hydrogen contamination. Therefore, reducing the hydrogen levels in the vacuum system during deposition, for example by pre-evaporating/sputtering a hydrogen getter, should help minimize these levels in the capping film.

In addition to surface topography resulting from extended reaction times with D_2O , anhydrous polishing methods used to prepare the surface of sintered polycrystalline C3S pellets for analysis did not produce a satisfactory surface finish. Minimizing roughness will further improve data quality and facilitate identification of reaction products on the surface. We are currently pursuing alternatives to polishing sintered C3S, in particular fabricating thin-films of C3S using pulsed-laser deposition (PLD) in collaboration with Dr. Bruce Buchholz, based on the e-beam evaporation processes developed by Rheinhamer and Casanova²⁸⁰. Furthermore, thin films directly deposited on flat-topped microfabricated Si micro-array posts eliminates the need for FIB lift-out procedures which introduces additional contamination. However, poor adhesion of C3S thin films could be detrimental to successful analysis by APT. Thus, as an alternative we are also pursuing growing single crystals of C3S in molten salt with faceted surfaces based on the early work of Lea and Nurse²⁸¹.

11.6 ATOM PROBE TOMOGRAPHY RECONSTRUCTIONS OF CRYSTALLINE OXIDES

Analysis of geological magnetite single crystals with specific microstructural features with a known relationship to the crystal lattice clearly revealed an artifact in the APT data, specifically, the $<111>$ zSDM interplanar spacing was incorrect. Magnetite crystals exhibit alternating layers of octahedrally coordinated Fe and mixed tetrahedrally and octahedrally coordinated Fe, separated by close packed oxygen planes; the field evaporation process during APT makes it impossible to determine which Fe atom belongs to each layer. Analysis of a mixed metal oxide, trevorite, where alternating Ni and mixed Ni-Fi layers could be detected based on composition differences indicated that it is not the phenomenon is not related to a specific layer. However, the exact nature of the artifact remains unknown.

Application of high-resolution TEM to directly image the equilibrium field evaporated tip end form after an atom probe experiment²⁸² should help elucidate the mechanism responsible for the lattice plane spacing error. Atomic resolution electron energy loss or energy dispersive X-ray spectroscopy in the TEM will make it possible to directly identify the elements at the surface of the tip in a mixed metal oxide. Advances in theoretical modeling of the field evaporation process in oxides will also help understand the process²⁸³⁻²⁸⁵.

In trevorite, the alternating Ni and mixed Ni-Fi layers are not ideal, due to the mixed composition of every other layer, an alternative compound, such as kamiokite ($\text{Fe}_2\text{Mo}_3\text{O}_8$), a rare iron-molybdenum oxide mineral with a spinel-like structure²⁸⁶, exhibits alternating layers of elementally pure Fe and Mo. APT analysis of crystallographically oriented kamiokite in combination with TEM of the post-analysis APT tips should provide further insight into the evaporation process. In addition to spinel-type oxides, lattice planes have recently been recently observed in other compounds, including iron pnictide superconductors and zinc oxide. Performing further experiments on these materials will aid in investigation of the field evaporation process leading to lattice plane resolution and help to extend the capabilities of APT²⁵².

REFERENCES

- 1 Lowenstam, H. A. & Weiner, S. *On biomineralization*. (Oxford University Press, 1989).
- 2 Mann, S. *Biominerization: principles and concepts in bioinorganic materials chemistry*. (Oxford University Press, USA, 2001).
- 3 Aizenberg, J. in *Nanomechanics of Materials and Structures* (eds T. J. Chuang, P. M. Anderson, M. K. Wu, & S. Hsieh) 99-108 (Springer Netherlands, 2006).
- 4 Currey, J. MATERIALS SCIENCE: Hierarchies in Biomimetic Structures. *Science* **309**, 253 (2005).
- 5 Fratzl, P., Gupta, H., Paschalis, E. & Roschger, P. Structure and mechanical quality of the collagen–mineral nano-composite in bone. *Journal of Materials Chemistry* **14**, 2115-2123 (2004).
- 6 Gao, H., Ji, B., Jager, I. L., Arzt, E. & Fratzl, P. Materials become insensitive to flaws at nanoscale: Lessons from nature. *Proceedings of the National Academy of Sciences* **100**, 5597-5600 (2003).
- 7 Munch, E. *et al.* Tough, Bio-Inspired Hybrid Materials. *Science* **322**, 1516-1520, doi:10.1126/science.1164865 (2008).
- 8 McNally, E. A., Schwarcz, H. P., Botton, G. A. & Arsenault, A. L. A Model for the Ultrastructure of Bone Based on Electron Microscopy of Ion-Milled Sections. *PLoS One* **7**, e29258 (2012).
- 9 Li, H. *et al.* Calcite Prisms from Mollusk Shells (*Atrina Rigida*): Swiss-cheese-like Organic–Inorganic Single-crystal Composites. *Advanced Functional Materials* **21**, 2028-2034 (2011).
- 10 Gordon, L. M. & Joester, D. Nanoscale chemical tomography of buried organic-inorganic interfaces in the chiton tooth. *Nature* **469**, 194-197 (2011).
- 11 Weiner, S. & Wagner, H. D. The material bone: structure-mechanical function relations. *Annu. Rev. Mater. Res.* **28**, 271-298 (1998).
- 12 Falini, G. & Fermani, S. Chitin mineralization. *Tissue Eng.* **10**, 1-6 (2004).
- 13 George, A. & Veis, A. Phosphorylated Proteins and Control over Apatite Nucleation, Crystal Growth, and Inhibition. *Chem. Rev.* **108**, 4670-4693, doi:10.1021/cr0782729 (2008).
- 14 Gotliv, B. *et al.* Asprich: a novel aspartic acid-rich protein family from the prismatic shell matrix of the bivalve *Atrina rigida*. *ChemBioChem* **6**, 304-314 (2005).
- 15 Evans, J. S. "Tuning in" to Mollusk Shell Nacre- and Prismatic-Associated Protein Terminal Sequences. Implications for Biomineralization and the Construction of High Performance Inorganic-Organic Composites. *Chem. Rev.* **108**, 4455-4462, doi:10.1021/cr078251e (2008).

- 16 Wang, D., Wallace, A. F., De Yoreo, J. J. & Dove, P. M. Carboxylated molecules regulate magnesium content of amorphous calcium carbonates during calcification. *Proceedings of the National Academy of Sciences of the United States of America* **106**, 21511 (2009).
- 17 Tao, J. H., Zhou, D. M., Zhang, Z. S., Xu, X. R. & Tang, R. K. Magnesium-aspartate-based crystallization switch inspired from shell molt of crustacean. *Proceedings of the National Academy of Sciences of the United States of America* **106**, 22096-22101, doi:10.1073/pnas.0909040106 (2009).
- 18 Omelon, S. J. & Grynpas, M. D. Relationships between polyphosphate chemistry, biochemistry and apatite biomineralization. *Chem. Rev* **108**, 4694-4715 (2008).
- 19 Belcher, A. *et al.* Control of crystal phase switching and orientation by soluble mollusc-shell proteins. (1996).
- 20 Falini, G., Albeck, S., Weiner, S. & Addadi, L. Control of aragonite or calcite polymorphism by mollusk shell macromolecules. *Science* **271**, 67 (1996).
- 21 Evans, L., Macey, D. & Webb, J. Matrix heterogeneity in the radular teeth of the chiton *Acanthopleura hirtosa*. *Acta zoologica(Stockholm)* **75**, 75-79 (1994).
- 22 Evans, L., Macey, D. & Webb, J. Distribution and composition of matrix protein in the radula teeth of the chiton *Acanthopleura hirtosa*. *Marine Biology* **109**, 281-286 (1991).
- 23 Evans, L. A., Macey, D. J. & Webb, J. Characterization and Structural Organization of the Organic Matrix of the Radula Teeth of the Chiton *Acanthopleura hirtosa*. *Philosophical Transactions of the Royal Society B: Biological Sciences* **329**, 87-96 (1990).
- 24 Roach, H. I. Why does bone matrix contain non-collagenous proteins? The possible roles of osteocalcin, osteonectin, osteopontin and bone sialoprotein in bone mineralisation and resorption. *Cell Biology International* **18**, 617-628 (1994).
- 25 Weiner, S. & Traub, W. Bone structure: from angstroms to microns. *The FASEB journal* **6**, 879-885 (1992).
- 26 Robinson, R. A. An electron-microscopic study of the crystalline inorganic component of bone and its relationship to the organic matrix. *The Journal of Bone and Joint Surgery* **34**, 389 (1952).
- 27 Nudelman, F. *et al.* Forming nacreous layer of the shells of the bivalves *Atrina rigida* and *Pinctada margarifera*: An environmental-and cryo-scanning electron microscopy study. *Journal of Structural Biology* **162**, 290-300 (2008).
- 28 Ehrlich, H., Koutsoukos, P., Demadis, K. & Pokrovsky, O. Principles of demineralization: Modern strategies for the isolation of organic frameworks:: Part II. Decalcification. *Micron* **40**, 169-193 (2009).
- 29 Newcomb, C. J., Moyer, T. J., Lee, S. S. & Stupp, S. I. Advances in cryogenic transmission electron microscopy for the characterization of dynamic self-assembling nanostructures. *Current opinion in colloid & interface science* (2012).

- 30 Sone, E. D., Weiner, S. & Addadi, L. Biomineralization of limpet teeth: A cryo-TEM study of the organic matrix and the onset of mineral deposition. *Journal of Structural Biology* **158**, 428-444 (2007).
- 31 Sone, E. D., Weiner, S. & Addadi, L. Morphology of Goethite Crystals in Developing Limpet Teeth: Assessing Biological Control over Mineral Formation. *Crystal Growth & Design* **5**, 2131-2138, doi:doi:10.1021/cg0501711 (2005).
- 32 Li, H., Xin, H. L., Muller, D. A. & Estroff, L. A. Visualizing the 3D Internal Structure of Calcite Single Crystals Grown in Agarose Hydrogels. *Science* **326**, 1244 (2009).
- 33 Addadi, L., Raz, S. & Weiner, S. Taking advantage of disorder: amorphous calcium carbonate and its roles in biomimetic mineralization. *Advanced Materials* **15**, 959-970 (2003).
- 34 Weiner, S. & Addadi, L. Crystallization pathways in biomimetic mineralization. *Annual Review of Materials Research* **41**, 21-40 (2011).
- 35 Tester, C. C. *et al.* Time-Resolved Evolution of Short-and Long-Range Order During the Transformation of Amorphous Calcium Carbonate to Calcite in the Sea Urchin Embryo. *Advanced Functional Materials* (2013).
- 36 Addadi, L., Raz, S. & Weiner, S. Taking advantage of disorder: amorphous calcium carbonate and its roles in *Adv Mater* (2003).
- 37 Mahamid, J., Sharir, A., Addadi, L. & Weiner, S. Amorphous calcium phosphate is a major component of the forming fin bones of zebrafish: Indications for an amorphous precursor phase. *Proc Natl Acad Sci USA* **105**, 12748-12753, doi:10.1073/pnas.0803354105 (2008).
- 38 Beniash, E., Metzler, R. A., Lam, R. S. K. & Gilbert, P. U. P. A. Transient amorphous calcium phosphate in forming enamel. *J Struct Biol* **166**, 133-143, doi:10.1016/j.jsb.2009.02.001 (2009).
- 39 Tester, C. & Joester, D. Precipitation in liposomes as a model for intracellular biomimetic mineralization. *Methods in enzymology* **532**, 257-276 (2012).
- 40 Tester, C. C. *et al.* In vitro synthesis and stabilization of amorphous calcium carbonate (ACC) nanoparticles within liposomes. *CrystEngComm* **13**, 3975-3978 (2011).
- 41 Tester, C. C., Wu, C.-H., Weigand, S. & Joester, D. Precipitation of ACC in liposomes—a model for biomimetic mineralization in confined volumes. *Faraday Discussions* **159**, 345-356 (2012).
- 42 Aizenberg, J. Crystallization in Patterns: A Bio-Inspired Approach. *Advanced Materials* **16**, 1295-1302 (2004).
- 43 Aizenberg, J., Muller, D. A., Grazul, J. L. & Hamann, D. Direct fabrication of large micropatterned single crystals. *Science* **299**, 1205-1208 (2003).
- 44 Aizenberg, J., Lambert, G., Weiner, S. & Addadi, L. Factors involved in the formation of amorphous and crystalline calcium carbonate: a study of an ascidian skeleton. *Journal of the American Chemical Society* **124**, 32-39 (2002).

- 45 Politi, Y., Mahamid, J., Goldberg, H., Weiner, S. & Addadi, L. Asprich mollusk shell protein: in vitro experiments aimed at elucidating function in CaCO₃ crystallization. *CrystEngComm* **9**, 1171-1177 (2007).
- 46 Chasteen, N. & Harrison, P. Mineralization in ferritin: an efficient means of iron storage. *Journal of Structural Biology* **126**, 182-194 (1999).
- 47 Kim, K.-S., Macey, D., Webb, J. & Mann, S. Iron mineralization in the radula teeth of the chiton Acanthopleura hirtosa. *Proceedings of the Royal Society of London. B. Biological Sciences* **237**, 335-346 (1989).
- 48 Baumgartner, J. *et al.* Magnetotactic bacteria form magnetite from a phosphate-rich ferric hydroxide via nanometric ferric (oxyhydr) oxide intermediates. *Proceedings of the National Academy of Sciences* (2013).
- 49 Schwertmann, U. & Cornell, R. M. *Iron oxides in the laboratory*. (John Wiley & Sons, 2008).
- 50 Brooker, L. R. & Shaw, J. A. The Chiton Radula: A Unique Model for Biomineralization Studies. *Seto J. Advanced Topics in Biomineralization. InTech*, 65-84 (2012).
- 51 Weaver, J. C. *et al.* Analysis of an ultra hard magnetic biomineral in chiton radular teeth. *Materials Today* **13**, 42-52 (2010).
- 52 van der Wal, P., Giesen, H. J. & Videler, J. J. Radular teeth as models for the improvement of industrial cutting devices. *Materials Science and Engineering: C* **7**, 129-142 (2000).
- 53 Michel, F. M. *et al.* Ordered ferrimagnetic form of ferrihydrite reveals links among structure, composition, and magnetism. *Proceedings of the National Academy of Sciences* **107**, 2787-2792 (2010).
- 54 Lowenstam, H. & Weiner, S. *On biomineralization*. (Oxford University Press, USA, 1989).
- 55 Jacobs, J. J., Andersson, G. B. J., Bell, J.-E., Weinstein, S. L. & Dormans, J. P. *Burden of Musculoskeletal Diseases in the United States: Prevalence, Societal and Economic Cost*. (American Academy of Orthopaedic Surgeons, 2008).
- 56 Wopenka, B. & Pasteris, J. D. A mineralogical perspective on the apatite in bone. *Mater. Sci. Eng., C* **25**, 131-143 (2005).
- 57 Nriagu, J. O. & Moore, P. B. *Phosphate minerals*. (Springer-Verlag, 1984).
- 58 Elliott, J. C. Calcium phosphate biominerals. *Rev. Mineral. Geochem.* **48**, 427-453 (2002).
- 59 Glimcher, M. J. Bone: nature of the calcium phosphate crystals and cellular, structural, and physical chemical mechanisms in their formation. *Reviews in mineralogy and geochemistry* **64**, 223-282 (2006).
- 60 Xie, B. & Nancollas, G. H. How to control the size and morphology of apatite nanocrystals in bone. *Proc. Natl. Acad. Sci. USA* **107**, 22369-22370 (2010).

- 61 Hu, Y. Y., Rawal, A. & Schmidt-Rohr, K. Strongly bound citrate stabilizes the apatite nanocrystals in bone. *Proc. Natl. Acad. Sci. USA* **107**, 22425-22429, doi:10.1073/pnas.1009219107 (2010).
- 62 Weiner, S. & Traub, W. Bone structure: from angstroms to microns. *FASEB J.* **6**, 879-885 (1992).
- 63 Landis, W. J. Mineral characterization in calcifying tissues: atomic, molecular and macromolecular perspectives. *Connect Tissue Res* **34**, 239-246 (1996).
- 64 Landis, W., Song, M., Leith, A., McEwen, L. & McEwen, B. Mineral and organic matrix interaction in normally calcifying tendon visualized in three dimensions by high-voltage electron microscopic tomography and graphic image reconstruction. *J Struct Biol* **110**, 39-54 (1993).
- 65 Jantou-Morris, V., Horton, M. A. & McComb, D. W. The nano-morphological relationships between apatite crystals and collagen fibrils in ivory dentine. *Biomaterials* **31**, 5275-5286 (2010).
- 66 Märten, A., Fratzl, P., Paris, O. & Zaslansky, P. On the mineral in collagen of human crown dentine. *Biomaterials* **31**, 5479-5490 (2010).
- 67 Jantou, V., Turmaine, M., West, G., Horton, M. & McComb, D. Focused ion beam milling and ultramicrotomy of mineralised ivory dentine for analytical transmission electron microscopy. *Micron* **40**, 495-501 (2009).
- 68 Cui, F., Wen, H., Zhang, H., Ma, C. & Li, H. Nanophase hydroxylapatite-like crystallites in natural ivory. *J. Mater. Sci. Lett.* **13**, 1042-1044 (1994).
- 69 Weiner, S. & Wagner, H. D. The material bone: structure-mechanical function relations. *Annual Review of Materials Science* **28**, 271-298 (1998).
- 70 Information, K. (2008).
- 71 Palmer, L. C., Newcomb, C. J., Kaltz, S. R., Spoerke, E. D. & Stupp, S. I. Biomimetic systems for hydroxylapatite mineralization inspired by bone and enamel. *Chemical reviews* **108**, 4754-4783 (2008).
- 72 Hughes, J. M., Cameron, M. & Crowley, K. D. Structural variations in natural F, OH, and Cl apatites. *Am. Mineral.* **74**, 870 (1989).
- 73 Isaac, S., Brudevold, F., Smith, F. A. & Gardner, D. E. Solubility rate and natural fluoride content of surface and subsurface enamel. *Journal of Dental Research* **37**, 254-263 (1958).
- 74 Hellwig, E. & Lennon, A. Systemic versus topical fluoride. *Caries research* **38**, 258-262 (2004).
- 75 Fejerskov, O., Manji, F. & Baelum, V. The nature and mechanisms of dental fluorosis in man. *Journal of Dental Research* **69**, 692 (1990).
- 76 Brudevold, F., Gardner, D. E. & Smith, F. A. The distribution of fluoride in human enamel. *Journal of Dental Research* **35**, 420-429 (1956).

- 77 Hercules, D. M. & Craig, N. L. Composition of fluoridated dental enamel studied by X-ray photoelectron spectroscopy (ESCA). *Journal of Dental Research* **55**, 829-835 (1976).
- 78 Robinson, C. *et al.* The chemistry of enamel caries. *Critical Reviews in Oral Biology & Medicine* **11**, 481 (2000).
- 79 Terpstra, R. & Driessens, F. Magnesium in tooth enamel and synthetic apatites. *Calcified tissue international* **39**, 348-354 (1986).
- 80 Kelly, T. F. & Miller, M. K. Invited Review Article: Atom probe tomography. *Review of Scientific Instruments* **78**, 031101 (2007).
- 81 Marquis, E. A. *et al.* On the current role of atom probe tomography in materials characterization and materials science. *Current Opinion in Solid State and Materials Science* **17**, 217-223 (2013).
- 82 Gault, B., Moody, M., Cairney, J. & Ringer, S. *Atom Probe Microscopy*. Vol. 160 3 (Springer New York, 2012).
- 83 Miller, M. K. *Atom Probe Tomography: Analysis at the Atomic Level*. (Plenum Pub Corp, 2000).
- 84 Seidman, D. N. & Stiller, K. An Atom-Probe Tomography Primer. *MRS Bulletin* **34** (2009).
- 85 Kelly, T. F. *et al.* Atom Probe Tomography of Electronic Materials. *Annual Review of Materials Research* **37**, 681-727 (2007).
- 86 Thompson, K., Flaitz, P., Ronsheim, P., Larson, D. & Kelly, T. Imaging of arsenic Cottrell atmospheres around silicon defects by three-dimensional atom probe tomography. *Science* **317**, 1370 (2007).
- 87 Prosa, T. *et al.* Atom Probe Tomography of Mammalian Cells: Advances in Specimen Preparation. *Microscopy and Microanalysis* **16**, 482-483 (2010).
- 88 Prosa, T. J., Keeney, S. K. & Kelly, T. F. Atom probe tomography analysis of poly (3-alkylthiophene) s. *Journal of Microscopy* **237**, 155-167 (2010).
- 89 Larson, D. J. *et al.* Analysis of Bulk Dielectrics with Atom Probe Tomography. *Microscopy and Microanalysis* **14**, 1254-1255, doi:doi:10.1017/S1431927608083657 (2008).
- 90 Chen, Y., Ohkubo, T., Kodzuka, M., Morita, K. & Hono, K. Laser-assisted atom probe analysis of zirconia/spinel nanocomposite ceramics. *Scripta Materialia* **61**, 693-696 (2009).
- 91 Heck, P. *et al.* 2112.
- 92 Greene, M., Prosa, T. J., Larson, D. J. & Kelly, T. F. Focused Ion Beam Fabrication of Solidified Ferritin into Nanoscale Volumes for Compositional Analysis Using Time-of-Flight Mass Spectrometry Methods. *Microscopy and Microanalysis* **16**, 1860-1861 (2010).
- 93 Stadermann, F. *et al.* 2134.

- 94 Mayama, N. *et al.* Characterization of carbonaceous films deposited on metal substrates by liquid-phase electrodeposition in methanol. *Diamond and Related Materials* (2010).
- 95 Kuhlman, K. R., Martens, R. L., Kelly, T. F., Evans, N. D. & Miller, M. K. Fabrication of specimens of metamorphic magnetite crystals for field ion microscopy and atom probe microanalysis. *Ultramicroscopy* **89**, 169-176 (2001).
- 96 Gordon, L. M., Tran, L. & Joester, D. Atom Probe Tomography of Apatites and Bone-Type Mineralized Tissues. *ACS nano* **6**, 10667-10675 (2012).
- 97 Müller, E. W., Panitz, J. A. & McLane, S. B. The atom-probe field ion microscope. *Review of Scientific Instruments* **39**, 83-86 (1968).
- 98 Müller, E. The atom-probe field ion microscope. *Naturwissenschaften* **57**, 222-230 (1970).
- 99 Miller, M. *Atom probe tomography: analysis at the atomic level*. . (New York: Kluwer Academic/Plenum Publishers. , 2000).
- 100 Miller, M. K., Russell, K. F. & Thompson, G. B. Strategies for fabricating atom probe specimens with a dual beam FIB. *Ultramicroscopy* **102**, 287-298 (2005).
- 101 Thompson, K. F. *et al.* In situ site-specific specimen preparation for atom probe tomography. *Ultramicroscopy* **107**, 131-139 (2007).
- 102 Miller, M. K., Russell, K. F., Thompson, K., Alvis, R. & Larson, D. J. Review of Atom Probe FIB-Based Specimen Preparation Methods. *Microscopy and Microanalysis* **13**, 428-436 (2007).
- 103 Miller, M., Russell, K. & Thompson, G. Strategies for fabricating atom probe specimens with a dual beam FIB. *Ultramicroscopy* **102**, 287-298 (2005).
- 104 Kellogg, G. & Tsong, T. Pulsed-laser atom-probe field-ion microscopy. *Journal of Applied Physics* **51**, 1184 (1980).
- 105 Bas, P., Bostel, A., Deconihout, B. & Blavette, D. A general protocol for the reconstruction of 3D atom probe data. *Applied Surface Science* **87**, 298-304 (1995).
- 106 Larson, D. J., Prosa, T. J. & Kelly, T. F. *Local Electrode Atom Probe Tomography*. (Springer, 2013).
- 107 Gault, B. *et al.* Spatial Resolution in Atom Probe Tomography. *Microscopy and Microanalysis* **16**, 99-110 (2010).
- 108 Ankudinov, A., Ravel, B., Rehr, J. & Conradson, S. Real-space multiple-scattering calculation and interpretation of x-ray-absorption near-edge structure. *Physical Review B* **58**, 7565 (1998).
- 109 Politi, Y. *et al.* Role of Magnesium Ion in the Stabilization of Biogenic Amorphous Calcium Carbonate: A Structure– Function Investigation. *Chemistry of Materials* **22**, 161-166 (2009).
- 110 Meldrum, F. C. & Colfen, H. Controlling Mineral Morphologies and Structures in Biological and Synthetic Systems. *Chem. Rev.* **108**, 4332-4432, doi:10.1021/cr8002856 (2008).

- 111 Weiner, S. Biomineralization: A structural perspective. *J. Struct. Biol.* **163**, 229-234, doi:10.1016/j.jsb.2008.02.001 (2008).
- 112 Fratzl, P. & Weinkamer, R. Nature's hierarchical materials. *Prog. Mater Sci.* **52**, 1263-1334 (2007).
- 113 Koch, N. Organic electronic devices and their functional interfaces. *ChemPhysChem* **8**, 1438-1455 (2007).
- 114 Seidman, D. N. & Stiller, K. A Renaissance in Atom-Probe Tomography. *MRS Bulletin* **10**, 717-749 (2009).
- 115 Larson, D. J. *et al.* Analysis of bulk dielectrics with atom probe tomography. *Microsc. Microanal.* **14**, 1254-1255 (2008).
- 116 Marin, F., Luquet, G., Marie, B. & Medakovic, D. Molluscan shell proteins: Primary structure, origin, and evolution. *Current Topics in Developmental Biology* **80**, 209-276, doi:10.1016/s0070-2153(07)80006-8 (2008).
- 117 Law, N., Caudle, M. & Pecoraro, V. Manganese redox enzymes and model systems: properties, structures, and reactivity. *Advances in Inorganic Chemistry* **46**, 305-440 (1998).
- 118 Evans, L. A., Macey, D. J. & Webb, J. Characterization and Structural Organization of the Organic Matrix of the Radula Teeth of the Chiton *Acanthopleura hirtosa*. *Philos. Trans. R. Soc. Lond. B Biol. Sci.* **329**, 87-96 (1990).
- 119 Lehn, J. Supramolecular chemistry. *Journal of Chemical Sciences* **106**, 915-922 (1994).
- 120 Hellman, O., Vandebroucke, J., Rüsing, J., Isheim, D. & Seidman, D. Analysis of three-dimensional atom-probe data by the proximity histogram. *Microscopy and Microanalysis* **6**, 437-444 (2002).
- 121 Addadi, L., Joester, D., Nudelman, F. & Weiner, S. Mollusk shell formation: a source of new concepts for understanding biomineralization processes. *Chemistry* **12**, 980-987 (2006).
- 122 Fantner, G. *et al.* Sacrificial bonds and hidden length dissipate energy as mineralized fibrils separate during bone fracture. *Nature materials* **4**, 612-616 (2005).
- 123 Tsai, G. J., Su, W. H., Chen, H. C. & Pan, C. L. Antimicrobial activity of shrimp chitin and chitosan from different treatments and applications of fish preservation. *Fisheries Science* **68**, 170-177 (2002).
- 124 Li, J., Revol, J. F. & Marchessault, R. H. Effect of degree of deacetylation of chitin on the properties of chitin crystallites. *Journal of Applied Polymer Science* **65**, 373-380 (1997).
- 125 Sikorski, P., Hori, R. & Wada, M. Revisit of -Chitin Crystal Structure Using High Resolution X-ray Diffraction Data. *Biomacromolecules* **10**, 1100-1105 (2009).
- 126 Giannuzzi, L. A. & Stevie, F. A. A review of focused ion beam milling techniques for TEM specimen preparation. *Micron* **30**, 197-204 (1999).

- 127 Shannon, R. Revised effective ionic radii and systematic studies of interatomic distances in halides and chalcogenides. *Acta Crystallographica Section A* **32**, 751-767, doi:doi:10.1107/S0567739476001551 (1976).
- 128 Fleet, M. The structure of magnetite. *Acta Crystallographica Section B: Structural Crystallography and Crystal Chemistry* **37**, 917-920 (1981).
- 129 Evans, L., Macey, D. & Webb, J. Distribution and composition of matrix protein in the radula teeth of the chiton *Acanthopleura hirtosa*. *Marine Biology* **109**, 281-286 (1991).
- 130 Wang, Q. *et al.* Phase Transformations and Structural Developments in the Radular Teeth of *Cryptochiton Stelleri*. *Advanced Functional Materials* (2013).
- 131 Cornell, R. M. & Schwertmann, U. *The iron oxides: structure, properties, reactions, occurrences and uses*. (Wiley-vch, 2003).
- 132 Gupta, A. K. & Gupta, M. Synthesis and surface engineering of iron oxide nanoparticles for biomedical applications. *Biomaterials* **26**, 3995-4021 (2005).
- 133 Baumgartner, J. *et al.* Nucleation and growth of magnetite from solution. *Nature materials* **12**, 310-314 (2013).
- 134 Li, D. *et al.* Direction-specific interactions control crystal growth by oriented attachment. *Science* **336**, 1014-1018 (2012).
- 135 Banfield, J. F., Welch, S. A., Zhang, H., Ebert, T. T. & Penn, R. L. Aggregation-based crystal growth and microstructure development in natural iron oxyhydroxide biominerization products. *Science* **289**, 751-754 (2000).
- 136 Rosenberg, L. P. & Chasteen, N. D. in *The Biochemistry and Physiology of Iron* (eds Paul Saltman & Jack Hegenauer) (Elsevier North Holland, Inc., 1982).
- 137 Mahamid, J., Sharir, A., Addadi, L. & Weiner, S. Amorphous calcium phosphate is a major component of the forming fin bones of zebrafish: Indications for an amorphous precursor phase. *Proceedings of the National Academy of Sciences* **105**, 12748-12753 (2008).
- 138 Nemoto, M. *et al.* Proteomic analysis from the mineralized radular teeth of the giant Pacific chiton, *Cryptochiton stelleri* (Mollusca). *Proteomics* **12**, 2890-2894 (2012).
- 139 Shaw, J. A. *et al.* Methods of sample preparation of radula epithelial tissue in chitons (Mollusca: Polyplacophora)*. *American Malacological Bulletin* **25**, 35-41 (2008).
- 140 Numako, C. & Nakai, I. XAFS studies of iron in the teeth of chiton, *Acanthopleura japonica*. *Le Journal de Physique IV* **7**, 2-2 (1997).
- 141 Westre, T. E. *et al.* A multiplet analysis of Fe K-edge 1s→ 3d pre-edge features of iron complexes. *Journal of the American Chemical Society* **119**, 6297-6314 (1997).

- 142 Wilke, M., Farges, F., Petit, P.-E., Brown, G. E. & Martin, F. Oxidation state and coordination of Fe in minerals: An Fe K-XANES spectroscopic study. *American Mineralogist* **86**, 714-730 (2001).
- 143 Mikutta, C., Frommer, J., Voegelin, A., Kaegi, R. & Kretzschmar, R. Effect of citrate on the local Fe coordination in ferrihydrite, arsenate binding, and ternary arsenate complex formation. *Geochimica et Cosmochimica Acta* **74**, 5574-5592 (2010).
- 144 Bou-Abdallah, F. & Chasteen, N. D. Spin concentration measurements of high-spin ($g' = 4.3$) rhombic iron (III) ions in biological samples: theory and application. *JBIC Journal of Biological Inorganic Chemistry* **13**, 15-24 (2008).
- 145 Weiss, B. P. *et al.* Ferromagnetic resonance and low-temperature magnetic tests for biogenic magnetite. *Earth and Planetary Science Letters* **224**, 73-89 (2004).
- 146 Krishnamurti, G. & Huang, P. Influence of citrate on the kinetics of Fe (II) oxidation and the formation of iron oxyhydroxides. *Clays and Clay Minerals* **39**, 28-34 (1991).
- 147 Navrotsky, A., Mazeina, L. & Majzlan, J. Size-driven structural and thermodynamic complexity in iron oxides. *Science* **319**, 1635-1638 (2008).
- 148 Siponen, M. I. *et al.* Structural insight into magnetochrome-mediated magnetite biomineralization. *Nature* **502**, 681-684 (2013).
- 149 Ravel, B. & Newville, M. ATHENA, ARTEMIS, HEPHAESTUS: data analysis for X-ray absorption spectroscopy using IFEFFIT. *Journal of Synchrotron Radiation* **12**, 537-541 (2005).
- 150 Yang, H., Lu, R., Downs, R. T. & Costin, G. Goethite,-FeO (OH), from single-crystal data. *Acta Crystallographica Section E: Structure Reports Online* **62**, i250-i252 (2006).
- 151 Rehr, J. J. & Albers, R. Theoretical approaches to x-ray absorption fine structure. *Reviews of Modern Physics* **72**, 621 (2000).
- 152 Mikutta, C. X-ray absorption spectroscopy study on the effect of hydroxybenzoic acids on the formation and structure of ferrihydrite. *Geochimica et Cosmochimica Acta* **75**, 5122-5139 (2011).
- 153 Huggins, F. E., Kim, D. J., Dunn, B. C., Eyring, E. M. & Huffman, G. P. An evaluation of least-squares fitting methods in XAFS spectroscopy: Iron-based SBA-15 catalyst formulations. *Spectrochimica Acta Part A: Molecular and Biomolecular Spectroscopy* **72**, 975-983 (2009).
- 154 Boskey, A. Bone mineral crystal size. *Osteoporosis Int* **14**, 16-21 (2003).
- 155 Fratzl, P., Gupta, H., Paschalis, E. & Roschger, P. Structure and mechanical quality of the collagen–mineral nano-composite in bone. *J. Mater. Chem.* **14**, 2115-2123 (2004).
- 156 Launey, M. E., Buehler, M. J. & Ritchie, R. O. On the mechanistic origins of toughness in bone. *Annu. Rev. Mater. Res.* **40**, 25-53 (2010).

- 157 Campbell, A., LoRe, M. & Nancollas, G. The influence of carbonate and magnesium ions on the growth of hydroxylapatite, carbonated apatite and human powdered enamel. *Colloids and surfaces* **54**, 25-31 (1991).
- 158 Kohn, M. J., Rakovan, J. & Hughes, J. M. in *Reviews in mineralogy and geochemistry* Vol. 48 742 (Minerological Society of America Geochemical Society, 2002).
- 159 Kreidler, E. & Hummel, F. The crystal chemistry of apatite: structure fields of fluor-and chlorapatite. *Am. Mineral* **55**, 170–184 (1970).
- 160 Jaffe, W. L. & Scott, D. F. Current Concepts Review-Total Hip Arthroplasty with Hydroxylapatite-Coated Prostheses*. *J. Bone Joint Surg.* **78**, 1918-1934 (1996).
- 161 Waychunas, G. A. Apatite luminescence. *Rev. Mineral. Geochem.* **48**, 701-742 (2002).
- 162 Bergstrom, W. H. & Wallace, W. M. Bone as a sodium and potassium reservoir. *J Clin Investig* **33**, 867 (1954).
- 163 Copp, D. H. & Shim, S. The homeostatic function of bone as a mineral reservoir. *Oral Surg. Oral Med. Oral Pathol.* **16**, 738-744 (1963).
- 164 Roelofs, A. J., Ebetino, F. H., Reszka, A. A., Russel, R. G. G. & Rogers, M. J. in *Principles of Bone Biology* (eds John P. Bilezikian, Lawrence G. Raisz, & T. John Martin) 1737-1767 (Elsevier/Academic Process, Amsterdam ; Boston, 2008).
- 165 Featherstone, J. D. B. Prevention and reversal of dental caries: role of low level fluoride. *Comm Den Or* **27**, 31-40 (1999).
- 166 Krishnamachari, K. Skeletal fluorosis in humans: a review of recent progress in the understanding of the disease. *Prog Food Nutr Sci* **10**, 279 (1986).
- 167 Andress, D. L., Maloney, N. A., Endres, D. B. & Sherrard, D. J. Aluminum-associated bone disease in chronic renal failure: High prevalence in a long-term dialysis population. *J Bone Miner Res* **1**, 391-398 (1986).
- 168 Joester, D., Hillier, A., Zhang, Y. & Prosa, T. J. Organic Materials and Organic/Inorganic Heterostructures in Atom Probe Tomography. *Microscopy Today* **20**, 26-31 (2012).
- 169 Kuhlman, K., Martens, R., Kelly, T., Evans, N. & Miller, M. Fabrication of specimens of metamorphic magnetite crystals for field ion microscopy and atom probe microanalysis. *Ultramicroscopy* **89**, 169-176 (2001).
- 170 McMurray, S., Gorman, B. & Diercks, D. TEM and Atom Probe Investigation of Calcium Carbonate Precipitation in Seawater. *Microsc. Microanal* **17**, 759 (2011).
- 171 Chen, Y., Ohkubo, T. & Hono, K. Laser assisted field evaporation of oxides in atom probe analysis. *Ultramicroscopy* (2010).

- 172 Larson, D. *et al.* Analysis of bulk dielectrics with atom probe tomography. *Microsc Microanal* **14**, 1254-1255 (2008).
- 173 Siddall, R. & Hurford, A. J. Semi-quantitative determination of apatite anion composition for fission-track analysis using infra-red microspectroscopy. *Chem. Geol.* **150**, 181-190 (1998).
- 174 Hughes, J. M. *et al.* Solid solution in the fluorapatite-chlorapatite binary system: High-precision crystal structure refinements of synthetic F-Cl apatite. *American Mineralogist* **99**, 369-376 (2014).
- 175 Bunton, J., Olson, J., Lenz, D., Larson, D. & Kelly, T. Optimized Laser Thermal Pulsing of Atom Probe Tomography: LEAP 4000X™. *Microsc Microanal* **16**, 10-11 (2010).
- 176 Marquis, E. A. & Gault, B. Determination of the tip temperature in laser assisted atom-probe tomography using charge state distributions. *J. Appl. Phys.* **104**, 084914-084914-084918 (2008).
- 177 Pauling, L. The nature of the chemical bond 1992. *J. Chem. Educ.* **69**, 519 (1992).
- 178 Kellogg, G. L. Field ion microscope studies of single-atom surface diffusion and cluster nucleation on metal surfaces. *Surf. Sci. Rep.* **21**, 1-88 (1994).
- 179 Chiba, T., Nojima, M. & Owari, M. Improvement of a method for reconstructing the three-dimensional atom probe (3DAP) data. *Surf. Interface Anal.* **38**, 1751-1755 (2006).
- 180 Weiner, S. & Wagner, H. D. The material bone: structure-mechanical function relations. *Annu. Rev. Mater. Sci.* **28**, 271-298 (1998).
- 181 Greene, M., Prosa, T., Larson, D. & Kelly, T. Focused Ion Beam Fabrication of Solidified Ferritin into Nanoscale Volumes for Compositional Analysis Using Time-of-Flight Mass Spectrometry Methods. *Microsc Microanal* **16**, 1860-1861, doi:doi:10.1017/S143192761005539X (2010).
- 182 Cui, F. Z., Li, Y. & Ge, J. Self-assembly of mineralized collagen composites. *Materials Science and Engineering: R: Reports* **57**, 1-27 (2007).
- 183 Orgel, J. P. R. O., Irving, T. C., Miller, A. & Wess, T. J. Microfibrillar structure of type I collagen in situ. *Proc. Natl. Acad. Sci. USA* **103**, 9001-9005 (2006).
- 184 Ji, B. & Gao, H. Mechanical properties of nanostructure of biological materials. *Journal of the Mechanics and Physics of Solids* **52**, 1963-1990 (2004).
- 185 Vurpillot, F., Bostel, A. & Blavette, D. Trajectory overlaps and local magnification in three-dimensional atom probe. *Appl. Phys. Lett.* **76**, 3127-3129 (2000).
- 186 Tas, A. C. Molten salt synthesis of calcium hydroxylapatite whiskers. *J. Am. Ceram. Soc.* **84**, 295-300 (2001).
- 187 Prener, J. S. The Growth and Crystallographic Properties of Calcium Fluor- and Chlorapatite Crystals. *J. Electrochem. Soc.* **114**, 77-83, doi:10.1149/1.2426512 (1967).

- 188 O'Shea, D., Bartlett, M. & Young, R. Compositional analysis of apatites with laser-Raman spectroscopy:(OH, F, Cl) Apatites. *Arch Oral Biol* **19**, 995-1006 (1974).
- 189 Oltman, E., Ulfig, R. & Larson, D. Background Removal Methods Applied to Atom Probe Data. *Microsc Microanal* **15**, 256-257 (2009).
- 190 Nanci, A. *Ten Cate's Oral Histology: Development, Structure, and Function*. 8 edn, (C.V. Mosby Co., 2012).
- 191 Caufield, P. W., Li, Y. & Dasanayake, A. Dental caries: an infectious and transmissible disease. *Compendium of continuing education in dentistry (Jamesburg, N.J. : 1995)* **26**, 10-16 (2005).
- 192 Taubman, M. A. & Nash, D. A. The scientific and public-health imperative for a vaccine against dental caries. *Nature Reviews Immunology* **6**, 555-563, doi:10.1038/nri1857 (2006).
- 193 Selwitz, R. H., Ismail, A. I. & Pitts, N. B. Dental caries. *The Lancet* **369**, 51-59 (2007).
- 194 Featherstone, J. D. B. The science and practice of caries prevention. *The Journal of the American Dental Association* **131**, 887 (2000).
- 195 Eanes, E. Enamel apatite: chemistry, structure and properties. *Journal of Dental Research* **58**, 829 (1979).
- 196 Warshawsky, H. Organization of crystals in enamel. *The Anatomical Record* **224**, 242-262 (1989).
- 197 Silverstone, L., Saxton, C., Dogon, I. & Fejerskov, O. Variation in the pattern of acid etching of human dental enamel examined by scanning electron microscopy. *Caries research* **9**, 373-387 (1975).
- 198 Murray, M. The chemical composition of teeth: The calcium, magnesium and phosphorus contents of the teeth of different animals. A brief consideration of the mechanism of calcification. *Biochemical Journal* **30**, 1567 (1936).
- 199 Ten Cate, J. In vitro studies on the effects of fluoride on de-and remineralization. *Journal of Dental Research* **69**, 614 (1990).
- 200 Hiller, C., Robinson, C. & Weatherell, J. Variations in the composition of developing rat incisor enamel. *Calcified tissue international* **18**, 1-12 (1975).
- 201 Shulin, W. Human enamel structure studied by high resolution electron microscopy. *Electron Microscopy Reviews* **2**, 1-16 (1989).
- 202 Li, H. *et al.* Calcite Prisms from Mollusk Shells (*Atrina Rigida*): Swiss-cheese-like Organic-Inorganic Single-crystal Composites. *Advanced Functional Materials* **21**, 2028-2034 (2011).
- 203 Kozawa, Y. *et al.* Electron-microscopic and microprobe analyses on the pigmented and unpigmented enamel of *Sorex* (Insectivora). *Histochemistry* **90**, 61-65 (1988).

- 204 Legfros, R., Sakae, T., Bautista, C., Retino, M. & LeGeros, J. Magnesium and carbonate in enamel and synthetic apatites. *Advances in Dental Research* **10**, 225 (1996).
- 205 Madsen, M. B., Mørup, S., Koch, C. J. & Lindemann, G. A study of the sump beaver's dental enamel. *Hyperfine Interactions* **29**, 1431-1434 (1986).
- 206 Ingram, G. Chemical events during tooth dissolution. *Journal of Dental Research* **69**, 581 (1990).
- 207 Cusack, M., Pérez-Huerta, A., Janousch, M. & Finch, A. A. Magnesium in the lattice of calcite-shelled brachiopods. *Chemical Geology* **257**, 59-64 (2008).
- 208 Dien, L., Mingsheng, P. & Murata, T. Coordination and local structure of magnesium in silicate minerals and glasses; Mg K-edge XANES study. *The Canadian Mineralogist* **37**, 199-206 (1999).
- 209 Wu, Z., Mottana, A., Marcelli, A., Natoli, C. R. & Paris, E. Theoretical analysis of X-ray absorption near-edge structure in forsterite, Mg₂SiO₄-Pbnm, and fayalite, Fe₂SiO₄-Pbnm, at room temperature and extreme conditions. *Physics and chemistry of minerals* **23**, 193-204 (1996).
- 210 Cabaret, D., Sainctavit, P., Ildefonse, P. & Flank, A.-M. Full multiple scattering calculations of the X-ray absorption near edge structure at the magnesium K-edge in pyroxene. *American Mineralogist* **83**, 300-304 (1998).
- 211 Harries, J., Hukins, D., Holt, C. & Hasnain, S. Conversion of amorphous calcium phosphate into hydroxylapatite investigated by EXAFS spectroscopy. *Journal of crystal growth* **84**, 563-570 (1987).
- 212 Holt, C. *et al.* Preparation of amorphous calcium-magnesium phosphates at pH 7 and characterization by X-ray absorption and fourier transform infrared spectroscopy. *Journal of crystal growth* **92**, 239-252 (1988).
- 213 Hughes, J. M., Cameron, M. & Crowley, K. D. Structural variations in natural F, OH, and Cl apatites. *American Mineralogist* **74**, 870-876 (1989).
- 214 Posner, A. S. & Betts, F. Synthetic amorphous calcium phosphate and its relation to bone mineral structure. *Accounts of Chemical Research* **8**, 273-281 (1975).
- 215 Laurencin, D. *et al.* Magnesium incorporation into hydroxylapatite. *Biomaterials* **32**, 1826-1837 (2011).
- 216 Zhao, J., Huggins, F. E., Feng, Z. & Huffman, G. P. Ferrihydrite: Surface structure and its effects on phase transformation. *Clays and Clay Minerals* **42**, 737-746 (1994).
- 217 Rose, J., Flank, A.-M., Masion, A., Bottero, J.-Y. & Elmerich, P. Nucleation and growth mechanisms of Fe oxyhydroxide in the presence of PO₄ ions. 2. P K-edge EXAFS study. *Langmuir* **13**, 1827-1834 (1997).
- 218 Gorecki, G. Iron phosphate coatings-composition and corrosion resistance. *Corrosion* **48**, 613-616 (1992).

- 219 Hanesch, M. Raman spectroscopy of iron oxides and (oxy) hydroxides at low laser power and possible applications in environmental magnetic studies. *Geophysical Journal International* **177**, 941-948 (2009).
- 220 Ingall, E. D. *et al.* Phosphorus K-edge XANES spectroscopy of mineral standards. *Journal of synchrotron radiation* **18**, 189-197 (2010).
- 221 Thompson, K. *et al.* In situ site-specific specimen preparation for atom probe tomography. *Ultramicroscopy* **107**, 131-139 (2007).
- 222 Fadeev, I., Shvorneva, L., Barinov, S. & Orlovskii, V. Synthesis and structure of magnesium-substituted hydroxylapatite. *Inorganic materials* **39**, 947-950 (2003).
- 223 Antao, S. M., Mulder, W. H., Hassan, I., Crichton, W. A. & Parise, J. B. Cation disorder in dolomite, CaMg (CO₃)₂, and its influence on the aragonite+ magnesite↔ dolomite reaction boundary. *American Mineralogist* **89**, 1142-1147 (2004).
- 224 Doness, W. Crystal structure refinement of huntite, CaMg₂(CO₃)₄, with X-ray powder data. *American Mineralogist* **71**, 163-166 (1986).
- 225 Calvo, C. & Gopal, R. The crystal structure of whitlockite from the Palermo Quarry. *Am. Mineral* **60**, 120-133 (1975).
- 226 Reeder, R. J., Lamble, G. M. & Northrup, P. A. XAFS study of the coordination and local relaxation around Co²⁺, Zn²⁺, Pb²⁺, and Ba²⁺, trace elements in calcite. *American Mineralogist* **84**, 1049-1060 (1999).
- 227 de Jonge, M. D. *et al.* An energy and intensity monitor for X-ray absorption near-edge structure measurements. *Nuclear Instruments and Methods in Physics Research Section A: Accelerators, Spectrometers, Detectors and Associated Equipment* **619**, 154-156 (2010).
- 228 Panitz, J. Point-projection imaging of unstained ferritin clusters. *Ultramicroscopy* **7**, 241-247 (1982).
- 229 Panitz, J. & Ghiglia, D. Point projection imaging of unstained ferritin molecules on tungsten. *Journal of Microscopy* **127**, 259-264 (1982).
- 230 Panitz, J. A. Ferritin deposition on tungsten and its desorption in a high electric field. (Sandia National Labs., Albuquerque, NM (USA), 1981).
- 231 Harrison, P. M. & Arosio, P. The ferritins: molecular properties, iron storage function and cellular regulation. *Biochimica et Biophysica Acta (BBA)-Bioenergetics* **1275**, 161-203 (1996).
- 232 Shaw, J. A. *Biomineralisation processes in the radula teeth of the chiton Acanthopleura hirtosa (Mollusca: Polyplacophora)* Ph.D. thesis, Murdoch University, (2007).
- 233 Michel, F. M. *et al.* Reactivity of ferritin and the structure of ferritin-derived ferrihydrite. *Biochimica et Biophysica Acta (BBA) - General Subjects* **1800**, 871-885 (2010).

- 234 Lawson, D. *et al.* Solving the structure of human H ferritin by genetically engineering intermolecular crystal contacts. (1991).
- 235 Michel, F. *et al.* The structure of ferrihydrite, a nanocrystalline material. *Science* **316**, 1726 (2007).
- 236 Rancourt, D. & Meunier, J. Constraints on structural models of ferrihydrite as a nanocrystalline material. *American Mineralogist* **93**, 1412 (2008).
- 237 Manceau, A. Evaluation of the structural model for ferrihydrite derived from real-space modelling of high-energy X-ray diffraction data. *Clay Minerals* **44**, 19 (2009).
- 238 Michel, F. *et al.* Ordered ferrimagnetic form of ferrihydrite reveals links among structure, composition, and magnetism. *Proceedings of the National Academy of Sciences* **107**, 2787 (2010).
- 239 Pan, Y.-H. *et al.* Electron-beam-induced reduction of Fe³⁺ in iron phosphate dihydrate, ferrihydrite, haemosiderin and ferritin as revealed by electron energy-loss spectroscopy. *Ultramicroscopy* **110**, 1020-1032 (2010).
- 240 Stadermann, F. *et al.* in *Lunar and Planetary Institute Science Conference Abstracts*. 1595.
- 241 Development of State of the Art Techniques in Cement Manufacturing: Trying to Look Ahead (CSI/ECRA-Technology Papers). (World Business Council for Sustainable Development Cement Sustainability Initiative WBCSD-CSI and the European Cement Research Academy (ECRA) Düsseldorf, Germany and Geneva, Switzerland, 2009).
- 242 Cement Technology Roadmap. Carbon emission reductions up to 2050. (World Business Council for Sustainable Development Cement Sustainability Initiative WBCSD-CSI and the International Energy Agency (IEA), Geneva, Switzerland and Paris, France, 2009).
- 243 Cement Industry Energy and CO₂ Performance “Getting the Numbers Right”. (World Business Council for Sustainable Development Cement Sustainability Initiative, Geneva, Switzerland, 2009).
- 244 Mineral Commodity Summaries (U.S. Geological Survey (USGS), Reston, Virginia, 2012).
- 245 Taylor, H. F. W. (Thomas Telford, London, 1997).
- 246 Gartner, E. M., Young, J. F., Damidot, D. A. & Jawed, I. in *Structure and Performance of Cements* (ed J. Bensted and P. Barnes) (Taylor and Francis e-Library, 2008).
- 247 Bullard, J. W. *et al.* Mechanisms of cement hydration. *Cem. Concr. Res.* **41**, 1208-1223 (2011).
- 248 Stark, J. Recent advances in the field of cement hydration and microstructure analysis. *Cem. Concr. Res.* **41**, 666-678 (2011).
- 249 Richardson, I. Tobermorite/jennite-and tobermorite/calcium hydroxide-based models for the structure of CSH: applicability to hardened pastes of tricalcium silicate, β-dicalcium silicate,

- Portland cement, and blends of Portland cement with blast-furnace slag, metakaolin, or silica fume. *Cement and Concrete Research* **34**, 1733-1777 (2004).
- 250 Kelly, T. F. & Miller, M. K. Invited review article: Atom probe tomography. *Review of scientific instruments* **78**, 031101-031101-031120 (2007).
- 251 Gault, B. *et al.* Advances in the calibration of atom probe tomographic reconstruction. *Journal of Applied Physics* **105**, 034913-034913-034919 (2009).
- 252 Gault, B., Moody, M. P., Cairney, J. M. & Ringer, S. P. Atom probe crystallography. *Materials Today* **15**, 378-386 (2012).
- 253 Moody, M. P., Gault, B., Stephenson, L. T., Haley, D. & Ringer, S. P. Qualification of the tomographic reconstruction in atom probe by advanced spatial distribution map techniques. *Ultramicroscopy* **109**, 815-824 (2009).
- 254 Miller, M. K. The effects of local magnification and trajectory aberrations in atom probe analysis. *Journal De Physique* **48**, 565-570 (1987).
- 255 Tsong, T. T. Mechanisms and energetic of atomic processes in surface diffusion. *Physica a-Statistical Mechanics and Its Applications* **357**, 250-281, doi:10.1016/j.physa.2005.06.029 (2005).
- 256 Gault, B. *et al.* Spatial Resolution in Atom Probe Tomography. *Microsc. Microanal.* **16**, 99-110, doi:10.1017/s1431927609991267 (2010).
- 257 Vurpillot, F., Bostel, A., Menand, A. & Blavette, D. Trajectories of field emitted ions in 3D atom-probe. *European Physical Journal-Applied Physics* **6**, 217-221 (1999).
- 258 Gault, B. *et al.* Estimation of the reconstruction parameters for atom probe tomography. *Microsc. Microanal.* **14**, 296-305, doi:10.1017/s1431927608080690 (2008).
- 259 Miller, M. K., Cerezo, A., Hetherington, M. G. & Smith, G. D. W. *Atom Probe Field Ion Microscopy*. (Oxford University Press, 1996).
- 260 SURAM, S. K. & RAJAN, K. Calibration of Reconstruction Parameters in Atom Probe Tomography using a Single Crystallographic Orientation. *Ultramicroscopy* (Submitted).
- 261 Geiser, B. P., Kelly, T. F., Larson, D. J., Schneir, J. & Roberts, J. P. Spatial distribution maps for atom probe tomography. *Microsc. Microanal.* **13**, 437-447, doi:10.1017/s1431927607070948 (2007).
- 262 Vurpillot, F., Da Costa, G., Menand, A. & Blavette, D. Structural analyses in three-dimensional atom probe: a Fourier transform approach. *Journal of Microscopy* **203**, 295-302 (2001).
- 263 Vurpillot, F., Bostel, A., Cadel, E. & Blavette, D. The spatial resolution of 3D atom probe in the investigation of single-phase materials. *Ultramicroscopy* **84**, 213-224 (2000).

- 264 Vurpillot, F., De Geuser, F., Da Costa, G. & Blavette, D. Application of Fourier transform and autocorrelation to cluster identification in the three-dimensional atom probe. *Journal of Microscopy-Oxford* **216**, 234-240 (2004).
- 265 Yao, L. *et al.* Crystallographic structural analysis in atom probe microscopy via 3D Hough transformation. *Ultramicroscopy* (2010).
- 266 Suram, S. K. & Rajan, K. Refining Spatial Distribution Maps for Atom Probe Tomography via Data Dimensionality Reduction Methods. *Microsc. Microanal.* **18** (2012).
- 267 Gault, B. *et al.* Estimation of the Reconstruction Parameters for Atom Probe Tomography. *Microscopy and Microanalysis* **14**, 296-305, doi:doi:10.1017/S1431927608080690 (2008).
- 268 Cerezo, A., Warren, P. & Smith, G. Some aspects of image projection in the field-ion microscope. *Ultramicroscopy* **79**, 251-257 (1999).
- 269 Torres, K., Geiser, B., Moody, M., Ringer, S. & Thompson, G. Field evaporation behavior in [001] FePt thin films. *Ultramicroscopy* **111**, 512-517 (2011).
- 270 Sitzman, S. D., Banfield, J. F. & Valley, J. W. Microstructural characterization of metamorphic magnetite crystals with implications for oxygen isotope distribution. *American Mineralogist* **85**, 14-21 (2000).
- 271 Nudelman, F., Lausch, A. J., Sommerdijk, N. A. & Sone, E. D. < i> In vitro</i> models of collagen biomineralization. *Journal of structural biology* (2013).
- 272 Jacobs, J. J., Gilbert, J. L. & Urban, R. M. Current Concepts Review-Corrosion of Metal Orthopaedic Implants*. *The journal of bone & joint surgery* **80**, 268-282 (1998).
- 273 Albrektsson, T. & Johansson, C. Osteoinduction, osteoconduction and osseointegration. *European Spine Journal* **10**, S96-S101 (2001).
- 274 Everett, E. *et al.* Dental fluorosis: variability among different inbred mouse strains. *Journal of dental research* **81**, 794-798 (2002).
- 275 Weatherell, J., Deutsch, D., Robinson, C. & Hallsworth, A. Assimilation of fluoride by enamel throughout the life of the tooth. *Caries research* **11**, 85-115 (1977).
- 276 Yamashita, I. Fabrication of a two-dimensional array of nano-particles using ferritin molecule. *Thin Solid Films* **393**, 12-18 (2001).
- 277 Mann, S. *et al.* Crystallization at inorganic-organic interfaces: biominerals and biomimetic synthesis. *Science* **261**, 1286-1292 (1993).
- 278 Douglas, T. & Stark, V. Nanophase cobalt oxyhydroxide mineral synthesized within the protein cage of ferritin. *Inorg. Chem* **39**, 1828-1830 (2000).
- 279 Meldrum, F., Douglas, T., Levi, S., Arosio, P. & Mann, S. Reconstitution of manganese oxide cores in horse spleen and recombinant ferritins. *Journal of inorganic biochemistry* **58**, 59-68 (1995).

- 280 Rheinheimer, V. & Casanova, I. Hydration of C3S thin films. *Cem. Concr. Res.* **42**, 593-597, doi:10.1016/j.cemconres.2012.01.002 (2012).
- 281 Lea, F. M. & Nurse, R. W. Problems of Crystal Growth in Building Materials. *Discussions of the Faraday Society*, 345-& (1949).
- 282 Devaraj, A., Colby, R., Hess, W. P., Perea, D. E. & Thevuthasan, S. Role of Photoexcitation and Field Ionization in the Measurement of Accurate Oxide Stoichiometry by Laser-Assisted Atom Probe Tomography. *The Journal of Physical Chemistry Letters* **4**, 993-998 (2013).
- 283 Silaeva, E. P., Karahka, M. & Kreuzer, H. Atom Probe Tomography and field evaporation of insulators and semiconductors: Theoretical issues. *Current Opinion in Solid State and Materials Science* **17**, 211-216 (2013).
- 284 Vurpillot, F., Gaillard, A., Da Costa, G. & Deconihout, B. A Model to predict image formation in Atom probe Tomography. *Ultramicroscopy* (2012).
- 285 Karahka, M. & Kreuzer, H. Field evaporation of oxides: A theoretical study. *Ultramicroscopy* (2012).
- 286 Kanazawa, Y. & Sasaki, A. Structure of kamiokite. *Acta Crystallographica Section C: Crystal Structure Communications* **42**, 9-11 (1986).